UNIVERSITY OF CALIFORNIA SAN DIEGO

Extreme Laser-Driven Regimes in Covalently Bonded Planetary Materials

A Dissertation submitted in partial satisfaction of the requirements
for the degree Doctor of Philosophy

in

Materials Science and Engineering

by

Boya Li

Committee in charge:

Professor Marc A. Meyers, Chair
Professor Shengqiang Cai
Professor Javier Garay
Professor Vlado Lubarda

2025

The Dissertation of Boya Li is approved, and it is acceptable in quality and form for publication on microfilm and electronically.

University of California San Diego

2025

DEDICATION

To my parents.

TABLE OF CONTENTS

LIST OF FIGURES

LIST OF TABLES

ACKNOWLEDGEMENTS

I would like to acknowledge Professor Marc A. Meyers for his support as the chair of my committee. Through multiple drafts and many long days, his guidance has proved to be invaluable.

I also would like to acknowledge Professor Shiteng Zhao who laid the foundation for this line of research and instructed me during this course, Dr. Alex C. Li as my partner in the simulation sections of this work on diamond shock compression.

I am grateful for the continuous advice of my committee members, Professor Shengqiang Cai, Professor Javier Garay, and Professor Vlado A. Lubarda on my senate and dissertation.

I would like to thank Professor Olivia A. Graeve and the MATS Graduate Coordinator Taylor Nelson for granting me the UCSD MATS Dissertation Fellowship and Diversity Fellowship, which were vital for me to finish my degree.

I am thankful for the instructions on FIB and TEM and discussions with Mr. Ping Che Lee, UCSD Nano3 staff, Dr. Jeff Wu and Dr. Zhicheng Long, and Dr. Mingjie Xu at UCI IMRI. I appreciate Dr. Shu-Ting Ko of Professor Jian Luo's lab for letting me use their experimental facilities.

Chapter 1, in part, is a reprint of material as it appears in: B. Y. Li, A. C. Li, S. Zhao, and M. A. Meyers. Amorphization by mechanical deformation. Materials Science and Engineering: R: Reports 149 (2022): 100673. The dissertation author was the primary researcher and first author of this paper.

Chapter 1, in part, is a reprint of material as it appears in: A. C. Li, B. Li, F. González-Cataldo, R. E. Rudd, B. Militzer, E. M. Bringa, and M. A. Meyers. Diamond under extremes. Materials Science and Engineering: R: Reports 161 (2024): 100857. The dissertation author was the primary researcher and second author of this paper.

Chapter 1, in part, has been submitted for publication of the material as it may appear in: B. Li, S. Zhao, and M. A. Meyers. Plastic Deformation of $CaTiO_3$ Perovskite under Extreme Loading. The dissertation author was the primary researcher and first author of this paper.

Chapter 2, in part, has been submitted for publication of the material as it may appear in: B. Li, S. Zhao, and M. A. Meyers. Direct observation of plastic deformation in diamond under extreme loading. The dissertation author was the primary researcher and first author of this paper.

Chapter 2, in part, has been submitted for publication of the material as it may appear in: B. Li, S. Zhao, and M. A. Meyers. Plastic Deformation of $CaTiO_3$ Perovskite under Extreme Loading. The dissertation author was the primary researcher and first author of this paper.

Chapter 3, in part, has been submitted for publication of the material as it may appear in: B. Li, S. Zhao, and M. A. Meyers. Direct observation of plastic deformation in diamond under extreme loading. The dissertation author was the primary researcher and first author of this paper.

Chapter 4, in part, has been submitted for publication of the material as it may appear in: B. Li, S. Zhao, and M. A. Meyers. Plastic Deformation of $CaTiO_3$ Perovskite under Extreme Loading. The dissertation author was the primary researcher and first author of this paper.

Chapter 5, in part, is a reprint of material as it appears in: S. Zhao, B. Li, B. A. Remington, C. E. Wehrenberg, H. S. Park, E. N. Hahn, and M. A. Meyers. Directional amorphization of covalently-bonded solids: A generalized deformation mechanism in extreme loading. Materials Today 49 (2021): 59-67. The dissertation author was the second author of this paper.

Chapter 6, in part, has been submitted for publication of the material as it may appear in: B. Li, S. Zhao, and M. A. Meyers. Direct observation of plastic deformation in diamond under extreme loading. The dissertation author was the primary researcher and first author of this paper.

Chapter 6, in part, has been submitted for publication of the material as it may appear in: B. Li, S. Zhao, and M. A. Meyers. Plastic Deformation of $CaTiO_3$ Perovskite under Extreme Loading. The dissertation author was the primary researcher and first author of this paper.

VITA

2014 Bachelor of Science in Materials Science and Engineering, Xi'an Jiaotong University

2016 Master of Science in Materials Science and Engineering, University of Windsor

2025 Doctor of Philosophy in Materials Science and Engineering, University of California San Diego

PUBLICATIONS

B. Li, S. Zhao, and M. A. Meyers. Direct observation of plastic deformation in diamond under extreme loading. In revision.

B. Li, S. Zhao, and M. A. Meyers. Plastic Deformation of $CaTiO_3$ Perovskite under Extreme Loading. Submitted.

A.C. Li, **B. Li**, F. González-Cataldo, R.E. Rudd, B. Militzer, E.M. Bringa, and M.A. Meyers. "Diamond under extremes." *Materials Science and Engineering: R: Reports* 161 (2024): 100857.

A.C. Li, **B. Li**, R.E. Rudd, M.A. Meyers "Dislocation generation in diamond under extreme loading." *Matter* 6, no. 9 (2023): 3040-3056.

B. Y. Li, A. C. Li, S. Zhao, and M. A. Meyers. "Amorphization by mechanical deformation." *Materials Science and Engineering: R: Reports* 149 (2022): 100673.

S. Zhao, **B. Li**, B. A. Remington, C. E. Wehrenberg, H. S. Park, E. N. Hahn, and M. A. Meyers. "Directional amorphization of covalently-bonded solids: A generalized deformation mechanism in extreme loading." *Materials Today* 49 (2021): 59-67.

B. Li, O.A. Gali, M. Shafiei, J.A. Hunter, A.R. Riahi, Aluminum transfer buildup on PVD coated work rolls during thermomechanical processing, *Surface & Coatings Technology* 308 (2016) 244–255.

Li, Boya, "Material Transfer Buildup on PVD Coated Work Rolls during Hot Rolling of an Al Alloy." (2016).

ABSTRACT OF THE DISSERTATION

Extreme Laser-Driven Regimes in Covalently Bonded Planetary Materials

by

Boya Li

Doctor of Philosophy in Materials Science and Engineering

University of California San Diego, 2025

Professor Marc A. Meyers, Chair

Our study focused on two materials: diamond (component in exoplanets and National Ignition Facility capsules) and perovskite (predominant component of the Earth mantle). High-power, pulsed, laser-driven shock compression experiments conducted on [001] oriented single crystalline diamond reveal stacking faults, dislocations, nano-twins and amorphous bands, upon the recovery and characterization of the specimens. Three laser energy levels are applied to specimens encapsulated in impedance matched momentum traps, generating shock pressures of 69, 93, and 115 GPa at a pulse duration of approximately 1 ns. At the lowest laser energy level (generating a pressure of 69 GPa), the defect-free lattice is retained, and diamond only exhibits

elastic deformation. At the highest energy level (generating a pressure of 115 GPa) defects are generated in the structure to relax the deviatoric stresses resulting from the uniaxial strain compression of the lattice. The high shear stresses are relaxed by stacking faults, dislocations, twins, and amorphous bands. These shear-induced lattice defects on crystallographic slip planes are crucial to the onset of amorphization. Transmission electron microscopy reveals that the amorphous bands are extremely localized and as narrow as a few nanometers. This amorphization is consistent with other covalently bonded materials with negative Clapeyron behavior subjected to extreme loading. Consequently, shock-induced amorphization is proposed as a new deformation mechanism of diamond under extremely high strain rate deformation.

Laser shock compression was employed on [010] oriented $CaTiO_3$ under extreme pressure and temperature conditions comparable to those in the Earth's mantle. The shear stress generated by the 70 GPa shock stress was equal to approximately 20 GPa, assuming elasticity. This is significantly higher than the Peierls-Nabarro stress required to move dislocations, around 10 GPa. TEM also revealed the generation of profuse perpendicular dislocations in [110](001) and $[\bar{1}10](001)$ slip systems. Dislocation density ranged from 15×10^{12} m^{-2} to 2×10^{12} m^{-2} within 12 μm from the shocked surface. Additionally, antiphase domain boundaries along [010] and [100] were observed under the high-pressure shock conditions. $CaTiO_3$ deforms mainly through dislocation motion due to its positive Clapeyron slope and high atomic packing factor.

INTRODUCTION

1 Motivation

Amorphization of crystalline structures is a ubiquitous phenomenon in metallic alloys, intermetallic compounds, ionically and covalently bonded materials, and even biological materials. Although the amorphous phase generally has a higher Gibbs free energy than its crystalline counterpart, there are many methods by which amorphization can be generated. The requirement to create an amorphous phase from a solid crystalline one is to increase its free energy above a critical level which enables this transition. The deformation introduces defects into the structure, raising its free energy to the level that it exceeds the one of the amorphous phase, thus propitiating conditions for amorphization.

The goal of this study is to elucidate upon pressure-shear induced amorphization as a new plastic deformation mechanism. This is especially important for covalently-bonded materials, which have an open structure with a low atomic packing factor. In many cases, the molten phase has the same or higher density than the solid one, and this favors amorphization under shock compression. It has been demonstrated for two covalently-bonded elements (Si ad Ge) and compounds (SiC and B_4C) that high shear stresses with shock pressures are relaxed by the formation of amorphized bands at angles close to 45˚ to the shock front. This amorphization process is enabled by a negative Clapeyron slope or a small to negligible volumetric expansion of materials upon amorphization. These experiments are extended to diamond and two partially covalently-bonded solids, olivine and perovskite.

The high energy laser of Omega Laser Facility enabled the simulation of the extremely high pressure and temperature conditions of the Earth's interior (mantle pressures from 24 to 136 GPa), allowing us to probe the deformation mechanisms of geophysically relevant materials at

geophysically relevant conditions. These phase transformations are believed to have a significant effect on geophysical events and especially in some deep-focus earthquakes. High-pressure instabilities resulting from a phase transformation/amorphization have been proposed as a source of some deep-focus earthquakes. This collapse of the structure at high pressures is explored in our experiments. Although the primary focus of this study is experimental, the use of molecular dynamics simulations to enhance the significance of results has proven to be of great value. Lasers typically create stress pulses with a duration of ~1 ns and apply strain rates of ~10^7-10^9 s^{-1}. Molecular dynamics simulations are on the order of ps, while the strain rates are 10^8- 10^{10} s^{-1}. Thus, the two methods can provide comparable parameters.

Olivine and perovskite are the most abundant minerals in the Earth's upper and lower mantle. This study explores the deformation mechanisms and probes the mechanical behavior of these minerals of the Earth's mantle. Diamond is, by virtue of the directional covalent and the very strong sp^3 carbon-carbon bonding, the hardest natural material. It has been a fascinating material since its discovery, first as a decorative gem and more recently, for its numerous industrial uses such as cutting, drilling, polishing, and optical windows because of its extreme hardness, elastic modulus, and optical transparency. Its density, strength, chemical inertness, and specific heat make it one of the best materials for ablation and use as the capsules containing deuterium and tritium fuel in inertial confinement fusion research at the National Ignition Facility. Diamond is also believed to be the core of some carbon-rich exoplanets, e.g., 55 Cancri e.

When a shock wave passes through a crystalline solid, the material is compressed while plastic deformation is generated behind the shock front. Ductile materials such as metals may undergo generation of dislocations, twins, and phase transformations. However, for brittle materials defect-mediated plasticity is limited and fracture appears to be the dominant way to relax

the imposed strain energy, typically leading to a catastrophic failure. Each of the deformation mechanisms has a characteristic time scale and is therefore highly strain rate-dependent. On the other hand, the propagation of cracks is limited by Rayleigh wave speed. Since the duration of the shock wave determines the strain rates, one may pose the question: what if the duration of the stress wave is orders of magnitude shorter than the characteristic time scale for fracture in brittle covalently-bonded materials? What phase transitions do diamond, olivine, and perovskite, principal planetary materials interior of some exoplanets or the Earth, undergo at the pressures and temperatures they are subjected to? The pressures and temperatures inside exoplanets are important parameters in predicting the possibility of life. Plate tectonics are essential to maintaining the surface temperature. Shock compression subjects materials to a unique regime of high hydrostatic and coupled shear stresses. There are, additionally, attendant temperature increases and shock front propagation approaching sonic velocities, forcing the carriers of plastic deformation such as dislocations, twins, phase transitions, and amorphization in materials to nucleate and propagate.

2 Research Objectives and Methodology

Laser shock compression is now a well-established technique that enables the exploration of materials behavior under extreme regimes of pressures, temperatures, and strain rates. Whereas explosively-driven flyer-plate and gas-gun experiments have explored the high-pressure regimes of materials at times on the order of microseconds, high power laser can produce pulses with nanosecond, picosecond, and even femtosecond durations. We employed laser-induced shock compression to reveal, quantify, and analyze the deformation mechanisms in these extreme regimes. The timescale and physical processes involved in elastic-plastic, phase transformations, and amorphization are fertile fields to be explored. Thus, measurements of the dislocation density

and reconstruction of material on the lattice level are of great importance in promoting our understanding of the basic physical processes of shock propagation in solids.

We are continuing this line of research, investigating the laser-shock response of (partially) covalently bonded solids, namely diamond, olivine ($(Mg, Fe)_2SiO_4$), and an ionic solid perovskite ($CaTiO_3$) to verify the generality of amorphization as the deformation mechanism under extreme conditions.

Specially designed shock recovery experiments were conducted in ride-along campaigns at Omega Laser Facility, Laboratory of Laser Energetics, University of Rochester. Brittle partially covalently-bonded targets (diamond, olivine, and $CaTiO_3$) were encapsulated in corresponding impedance matched ductile metals, enabling successful shock recovery and subsequent characterizations. The microstructures of the post-shock samples were characterized by various techniques such as scanning electron microscopy (SEM), focused ion beam (FIB), transmission electron microscopy (TEM), and high resolution transmission electron microscopy (HRTEM).

Chapter 1 BACKGROUND

1.1 Literature Review on Amorphization

1.1.1 Introduction

There are four states of matter dictated by the fundamental state variables of pressure and temperature: solid, liquid, gas, and plasma. One phase can transform to another under certain conditions. Atoms in a solid have a restricted mobility. Every atom stays in the vicinity of one site in space, even though its position is not static; instead, it oscillates rapidly surrounding this fixed site. Although the frequency of this oscillation is weakly related to temperature, its amplitude has a well-established correlation with temperature. The atomic-scale structure of the solid is composed of the spatial configuration of these fixed sites. On the contrary, a liquid does not possess an enduring configuration of atoms. In the liquid state, they are mobile and continuously moving throughout the material.

A classic example is silicon dioxide, also known as silica. It has at least three crystalline forms, commonly referred to as polymorphs (quartz, cristobalite, tridymite, and others); its amorphous form is known as glass. It is not easy for quartz to crystallize, but the slow "geological" times are sufficiently long to obtain well-defined crystals. When molten silica is cooled, the very viscous melt, constituted of silicon and oxygen atoms, has difficulty reorganizing itself into a crystalline matrix, because of the strong covalent bonding; thus, this disordered structure of the molten state is retained in the solid state, leading to the formation of glass.

If one observes a glass blower at his trade, one can immediately see that glass has a unique property: it can be blown into a hollow sphere of an ever-increasing diameter at the end of the tube, whereas a metal would neck and fracture in tension. It can also be freely shaped if the temperature

is sufficiently high. There is one exception, that of superplastic metals. This property derives from the linear viscosity exhibited by glass, expressed as [1]:

$$\frac{\sigma}{\dot{\varepsilon}} = \eta \tag{1}$$

Where σ is stress, $\dot{\varepsilon}$ is strain rate, and η is constant known as the Newtonian viscous coefficient. This viscosity changes with temperature as:

$$\eta = \eta_0 exp \frac{Q}{RT} \tag{2}$$

where Q is the activation energy for flow and T is the temperature in K. Crystalline metals and ceramics have a mechanical response that is quite different and is governed by defect generation and motion and crack nucleation and growth.

The common equation that expresses the strain-rate sensitivity of metals is:

$$\sigma = k\dot{\varepsilon}^m \tag{3}$$

The value that differentiates glasses from metals and ceramics is the parameter m. For glasses, m ~ 1, giving it an extreme ability to undergo tensile extension. In metals and ceramics, on the other hand, this value is in the 0.01 range and instability sets in right away on tension. The absence of dislocations, twins and other defects in glasses, that are the agents of plastic deformation in crystals, is also responsible for another extraordinary property: glasses are often stronger than their equivalent crystalline counterparts.

The glassy form of silicates exists in nature, and obsidian is the prime example. It is produced when volcanic lava is rapidly cooled, thus bypassing crystallization. Its high hardness and sharp edges produced by a technique called ‘knapping’ have rendered it precious all the way from the Neolithic era. It has been used as arrow tips, knives, and surgical blades. The Maya used

it as a weapon and in their ritual sacrifices which included the extraction of the heart from the live victim.

The synthetic counterpart of obsidian, glass, has its birth in Syria, Mesopotamia, or Egypt around 3,500-2,000 BC. Although the technology of glass manufacturing reached a high level of development in the Twentieth Century, no metallic glass had been produced up to this point. In 1957, the fortuitous discovery by the brilliant Belgian scientist Duwez [2] opened the doors for research on metals that exhibit the properties of glasses and have an amorphous structure. This was accomplished by shooting a liquid pellet of a saturated solid solution into a flat target. The recovered splats showed an absence of diffraction spots upon being observed by X rays.

It is now recognized that amorphization exists in all kinds of materials and forms: metallic glasses, glassy minerals, stained glasses, polymers, food, and even pharmaceuticals [3].

Amorphous (or glassy) metals are preferentially formed as a random mixture of metallic and metalloid atoms with only short-range order defined as the first- or second-nearest neighbors of an atom. There exists short-range-order (clusters) and medium-range order (extended clusters), which are distinct (Figure 1.1) [4]. The cluster model is a short-range order model for amorphous materials. The solute atom is surrounded by solvent atoms. The atomic size ratio decides the coordination number of the solute atom. The extended cluster model is a medium-range-order model for amorphous materials. The solute atoms connect to form extended clusters or strings as the solute atom concentration increases. The coordination number is normally 3 to 7 [4].

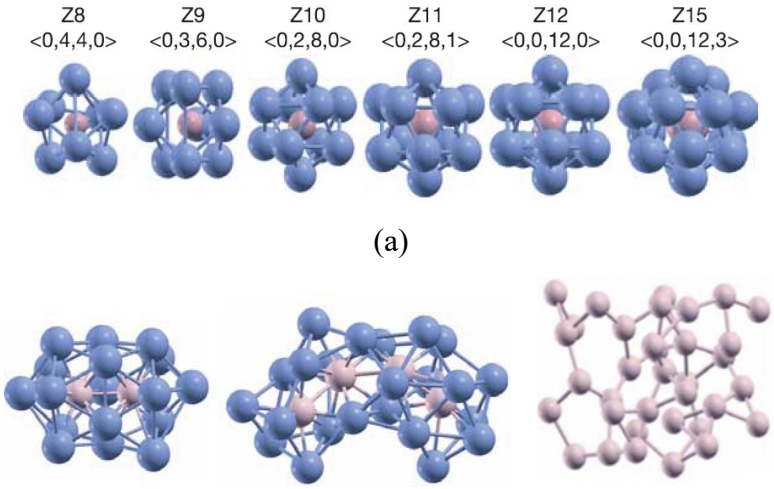

(a)

(b)

Figure 1.1 Examples of short and medium range order found through ab initio molecular dynamics simulations in various metallic glasses. (a) Kasper polyhedra show the types of short-range order for different coordination numbers Z (=8, 9, 10, 11, 12, and 15). (b) Lone pair cluster in $Zr_{80}Pt_{20}$, extended string cluster in $Al_{74}Ni_{25}$, and a solute network in $Ni_{63}Nb_{37}$ (from left to right), exhibit types of medium range order [4].

There are three atomic scale models for amorphous solids. The first one is the continuous random-network model [5] for covalent glasses such as amorphous silicon and various oxide glasses. The second one is the random-coil model [6] for quantities of polymer-chain organic glasses like polystyrene. The third one is the random close-packing model [7] for metallic glasses, which resembles a number of marbles compacted in a paper bag. The well-defined short-range order determines that amorphous solids are not as random as a gas although they all contain "random" in their name.

In glasses, each atom still has the nearest-neighbor atoms at the length of chemical bond, which is the same as in the corresponding crystalline material. However, the bond directions change as the distance goes farther away from an atom. Both crystalline and amorphous solids have short-range order at atomic scale as a result of chemical bonding, which holds the solid together.

It was previously believed that only a limited number of materials could be produced as glasses. These materials were known as glass-forming solids, including oxide glasses and organic polymers. It has now been realized that the amorphous solid state is generally universal in solid materials. Glass formation is a matter of bypassing crystallization (Figure 1.2 (a)). Nearly all materials can be produced with amorphous structure if cooled rapidly enough. Figure 1.2 (a) also shows how plastic deformation can increase the Gibbs free energy of the crystalline structure and lead to its transformation into the glassy one. This is indicated by the double-ended purple arrow in Figure 1.2 (a). This can also be expressed in terms of free energy vs. temperature (Figure 1.2 (b)). One can see that the amorphization is a second order transition because the slope does not have a discontinuity at the melting point. On the other hand, crystallization is a first-order transition. If deformation is imparted at a temperature T_d, the free energy is increased to the point where it reaches the one for the amorphous state and this can lead to the formation of the glassy form.

The melting and solidification between crystals and their corresponding liquids are first-order phase transitions, generating a sharp discontinuity in properties such as density. The glass transition, however, is a second-order transition, which does not have a discontinuous change in density nor does it have the latent heat of fusion. This is seen in both Figure 1.2 (a) and 1.2 (b). Nevertheless, heat capacity and thermal expansion of amorphous materials exhibit an abrupt change at glass transition temperature, making the accurate detection of crystalline to amorphous transition possible via differential scanning calorimetry [8].

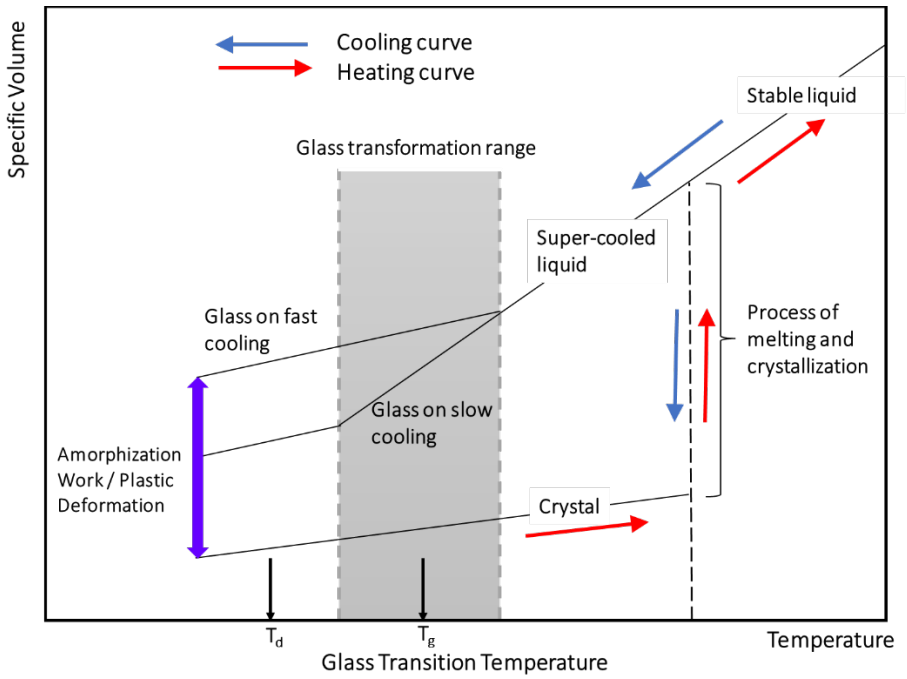

(a)

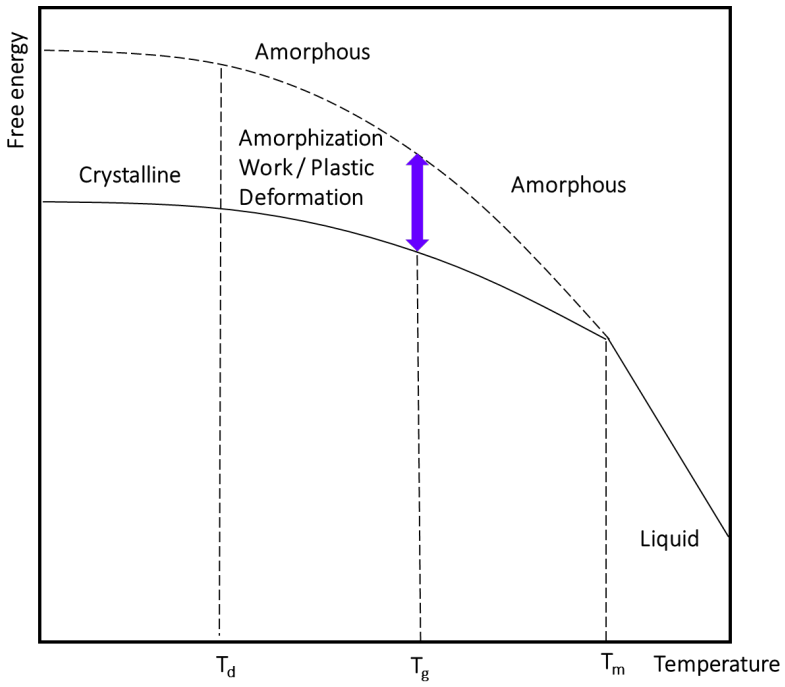

(b)

Figure 1.2 (a) Specific volume vs. temperature. (b) Free energy vs. temperature. (a) Generic specific volume vs. temperature showing crystallization and glass formation (on cooling) and difference in specific volume between crystalline and glassy phases. (b) Gibbs free energy vs. temperature showing crystalline and amorphous paths and difference in free energy between them.

In metals, the ordered crystal has higher packing efficiency, and so, the molar volume of the amorphous structure is larger than that of crystal. Therefore, the excess molar volume is a measure of disorder. This results in a positive Clapeyron slope for the boundary between solid and liquid phases in the T-P phase diagram. In contrast, many covalently bonded elements and compounds have open structures (e. g., Si, Ge, SiC, B_4C). For these solids, the densities of their amorphous phase are higher than their crystalline ones, resulting in a negative Clapeyron slope.

Metallic glasses are an important class of amorphous materials. Their microstructure is different from crystalline metals. Metallic glass is an alloy instead of a pure metal under most conditions. It is composed of atoms with significantly different sizes, resulting in low free volume in the liquid state, and thus has orders of magnitude higher viscosity in its molten state, restraining the atoms' motion to form an ordered crystalline matrix. This structure also leads to lower volume shrinkage during cooling, which is resistant to plastic deformation. The amorphous phase does not have grain boundaries, a potential vulnerability of polycrystalline materials, contributing to better wear and corrosion resistance. Metallic glasses have properties that exceed those of other structural metals. They can survive elastic or larger reversible deformations than crystalline alloys. They do not have defects such as dislocations to undermine their strength.

Figure 1.3 is a flow diagram of the fabrication of metallic glasses [9]. The fabrication processes are divided into direct casting and thermoplastic forming. Metallic glass can be formed into any shape like thermoplastic polymers upon heating.

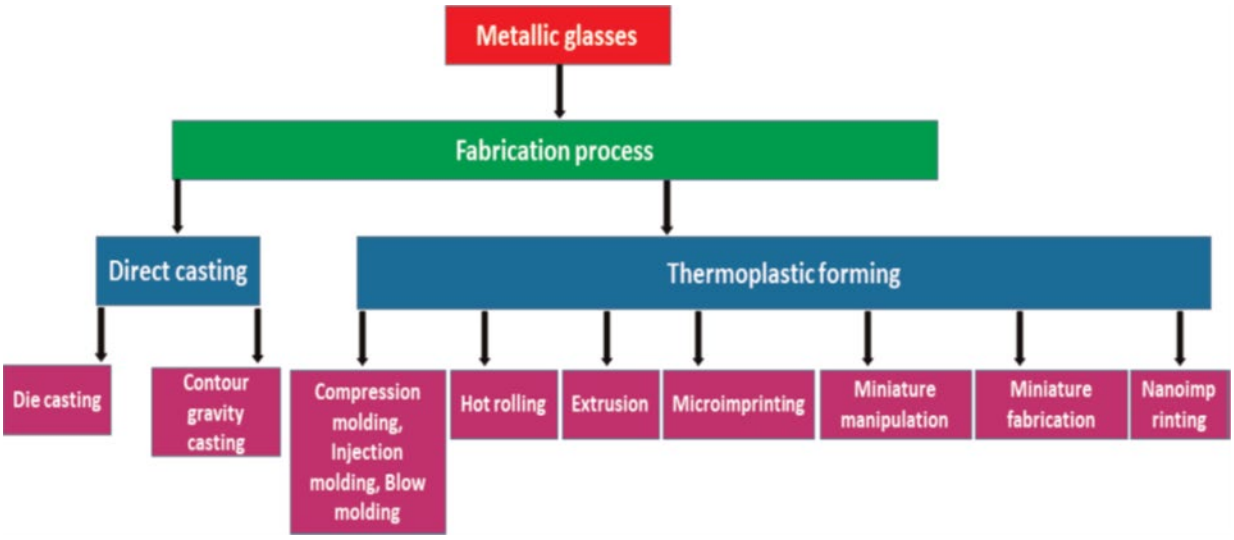

Figure 1.3 Flow diagram of the fabrication of metallic glasses with two major paths: casting from melt and thermoplastic forming [9]

Amorphization can be generated by a number of methods. The best known are rapid cooling (quenching), shock waves, mechanical deformation, focused ion beam, irradiation, vapor condensation techniques, moderate heating, solid state reactions, mechanical alloying; several other methods are summarized in Table 1.1 [10-47].

Table 1.1 Methods to generate amorphization

Rapid cooling (quenching) of a melt, low-temperature annealing, melt spinning, melt quenching
Mechanical deformation: micropillar compression deformation, high pressure torsion, pressure-induced, static compression or decompression of crystals, tribological load, (prolonged) ball milling, mechanical alloying, Vickers indentation, tension, static and shock high-pressure experiments, meteorite impact, and deformation by tectonic processes, shock waves
Focused ion beam, ion implantation
Microwave irradiation, electron beam irradiation, neutron and charged-particle irradiation, pulsed laser irradiation, ion irradiation, femtosecond laser pulses irradiation
Vapor condensation techniques: variations of the method include using an electron beam to vaporize the source or using the plasma-induced decomposition of a molecular species, laser-assisted chemical vapor deposition, magnetron sputtering
Moderate heating
Solid state reactions
Hydrogen absorption
Numerous other methods: lyophilization, spray drying, freeze-drying, dehydration of crystalline hydrates, above the crystallization temperature under an external magnetic field, followed by cooling accompanied with pulse current injection, impregnated in phosphoric acid

Table 1.2 lists the principal materials that have been amorphized by mechanical deformation. They are grouped into metals and alloys, intermetallics, covalent, ionic, and biological materials and will be discussed in detail in Sections 2 (metals and alloys), 3 (intermetallic compounds), 4 (covalently bonded solids), 5 (ionic materials), and 6 (biological materials). Mechanisms and kinetics of amorphization by mechanical deformation are given in Section 1.1.7. The fundamental deformation mechanisms in amorphous materials are presented in Section 1.1.8. Molecular dynamics has been extremely useful in studying the amorphization process by plastic deformation and in the simulation of the deformation mechanisms. The importance of amorphous materials can be gauged by the increasing number of publications, exemplified by the three-volume reference book edited by Taylor [48]. This compendium addresses three important components of amorphous materials: (i) chalcogenides, which have, in their glassy form, shown semiconducting properties; (ii) oxide glasses which consist of the major application of amorphous materials, and, although being known for thousands of years, present novel features; and (iii) thin film amorphous semiconductors, which have applications in solar cells and IR imaging, among others.

Table 1.2 Materials amorphized by mechanical deformation (in chronological order)

Metals and alloys			
Cu-Nb-(Si, Ge or Sn)	Mechanical alloying	Matsuki et al. [50]	1988
Nb_3Sn	Mechanical attrition	Cho et al. [51]	1991
Stainless steel	Hopkinson bar/shear band	Meyers et al. [52]	2003
Nanocrystalline nickel	Quasi-static compression	Han et al. [53]	2012
Graphite flakes in gray cast iron	Tribological loading (friction), Ball milling	Hinrichs et al. [54]	2018
$Fe_3Cr_2Al_2CuNi_4Si_5$ HEA	Mechanical alloying and consolidation	Yang et al. [56]	2019
Cantor high-entropy alloy of CrMnFeCoNi	Hopkinson bar/shear band	Zhao et al. [57]	2021

Table 1.3 Materials amorphized by mechanical deformation (in chronological order) (Continued)

Cantor high-entropy alloy of CrMnFeCoNi	In situ TEM tensile straining experiments	Wang et al. [125]	2021
Intermetallic compounds			
Ni-Zr	Mechanical alloying	Weeber and Bakker [62]	1988
Ni_xZr_y	Ball milling	Chen et al.[63]	1993
Ni_3Al	Mechanical milling	Jang et al. [64]	1990
NiTi	Cold rolling	Koike et al. [65]	1990
Ti/Ni	Explosive welding	Nishida et al. [66]	1995
NiTi	High-pressure torsion	Huang et al. [67]	2004
NiTi shape memory alloy	Local canning compression	Jiang et al. [73]	2013
NiTi shape memory alloy	Ultrasonic Nano-crystal Surface Modification (UNSM)	Ye et al. [74]	2016
Nanocrystalline NiTi shape memory alloy micropillars	Uniaxial compression	Hua et al. [75]	2018
ZrCu and $Zr_{50}Cu_{40}Al_{10}$	High pressure torsion	Tsuchiya et al. [76]	2011
$SmCo_5$	Nanoindentation	Luo et al. [77]	2019
Covalently-bonded solids			
Olivine	Shock compression	Jeanloz et al. [78]	1977
Si	Mechanical scratching	Minowa et al. [79]	1992
α-quartz	Compression	Kingma et al. [80]	1993
Cristobalite	Gas gun	Gratz et al. [81]	1993
α - quartz and α -berlinite $AlPO_4$	Diamond anvil cell	Cordier et al. [82]	1993
$CaSiO_3$	Pressure	Serghiou et al. [83]	1993
Serpentine	Pressure and temperature	Irifune et al. [84]	1996
B_4C	Ballistic impact	Chen et al. [86]	2003
B_4C	Vickers indentation	Subhash et al. [87]	2013
B_4C	Indentation	Subhash et al. [88]	2016
B_4C	Nanoindentation	Reddy et al. [89]	2021
Boron suboxide	Nanoindentation	Reddy et al. [90]	2014
Diamond	High pressure plus laser heating	Zeng et al. [91]	2017
Diamond	High pressure and high temperature	Shang et al. [92]	2021
Diamond	High pressure and high temperature	Tang et al. [93]	2021

Table 1.4 Materials amorphized by mechanical deformation (in chronological order) (Continued)

Si, Ge, SiC, B_4C	High energy laser shock compression	Zhao et al. [94]	2018
Forsterite	Static compression	Samae et al. [98]	2021
Ionic materials			
$Ca(OH)_2$	Static compression	Meade and Jeanloz [99]	1990
Calcium phosphates	Pressure	Vaidya et al. [100]	1999
Biological materials			
Dactyl club samples of mantis shrimp	Quasi-static indentation and microimpact tests	Huang et al. [101]	2020

1.1.2 Amorphization in metals and alloys

In this and subsequent sections, the observations of amorphization will be presented in a chronological order, following the sequence of Table 1.2. Amorphization in pure metals is very difficult to accomplish because of the extreme cooling rates required from the molten state. Similarly, it is very difficult to generate amorphization from mechanical deformation. However, different alloys including Cu-Nb-(Si, Ge or Sn) alloy systems, Nb_3Sn, stainless steel, graphite flakes in gray cast iron, Cantor and some other high-entropy alloys have been found to be amenable to amorphization by mechanical deformation.

Mechanical alloying (MA) is a solid-state powder processing method where a mixture of powders is subjected to high energy collision from milling balls in confined space; it involves repeated welding, fracturing and rewelding of powder mixtures to produce controlled, extremely refined microstructures [49]. It is a widely used technique to prepare amorphous alloys. Amorphous alloys such as Ni-Nb, Ni-Zr, Cu-Zr, Co-Zr and Fe-Zr have been produced by MA [50]. Pure elemental powders of copper, niobium and silicon, germanium or tin were ball milled then hot pressed. Bright field electron images and corresponding selected area electron diffraction patterns are shown in Figure 1.4 for $Cu_{44}Nb_{42}Sn_{14}$ powders made by MA after 4 h and 24 h milling.

A high density of tangled dislocations is distributed all over the bright-field micrograph (Figure 1.4 (a)). The corresponding diffraction pattern (Figure 1.4 (b)) is comprised mainly of completely linked reflection rings of bcc structure with only a few weak reflection spots of fcc copper phase, which indicates that the bcc phase is severely deformed and with small grain size. In addition, the lack of contrast characteristic of a crystalline phase (Figure 1.4 (c)) and broad diffuse rings in the selected-area diffraction pattern (Figure 1.4 (d)) confirm the formation of an amorphous phase. The particle size of the amorphous powders after 24 h milling was reduced to about 200 to 500 nm from the initial size of below 34 μm. It is proposed in this study that amorphization requires three conditions: (i) fast diffusive solute atoms, (ii) a negative heat of mixing in the amorphous alloys which provides the chemical driving force for the amorphization reaction, and (iii) this reaction must occur at sufficiently low temperatures to restrain the nucleation of crystallization.

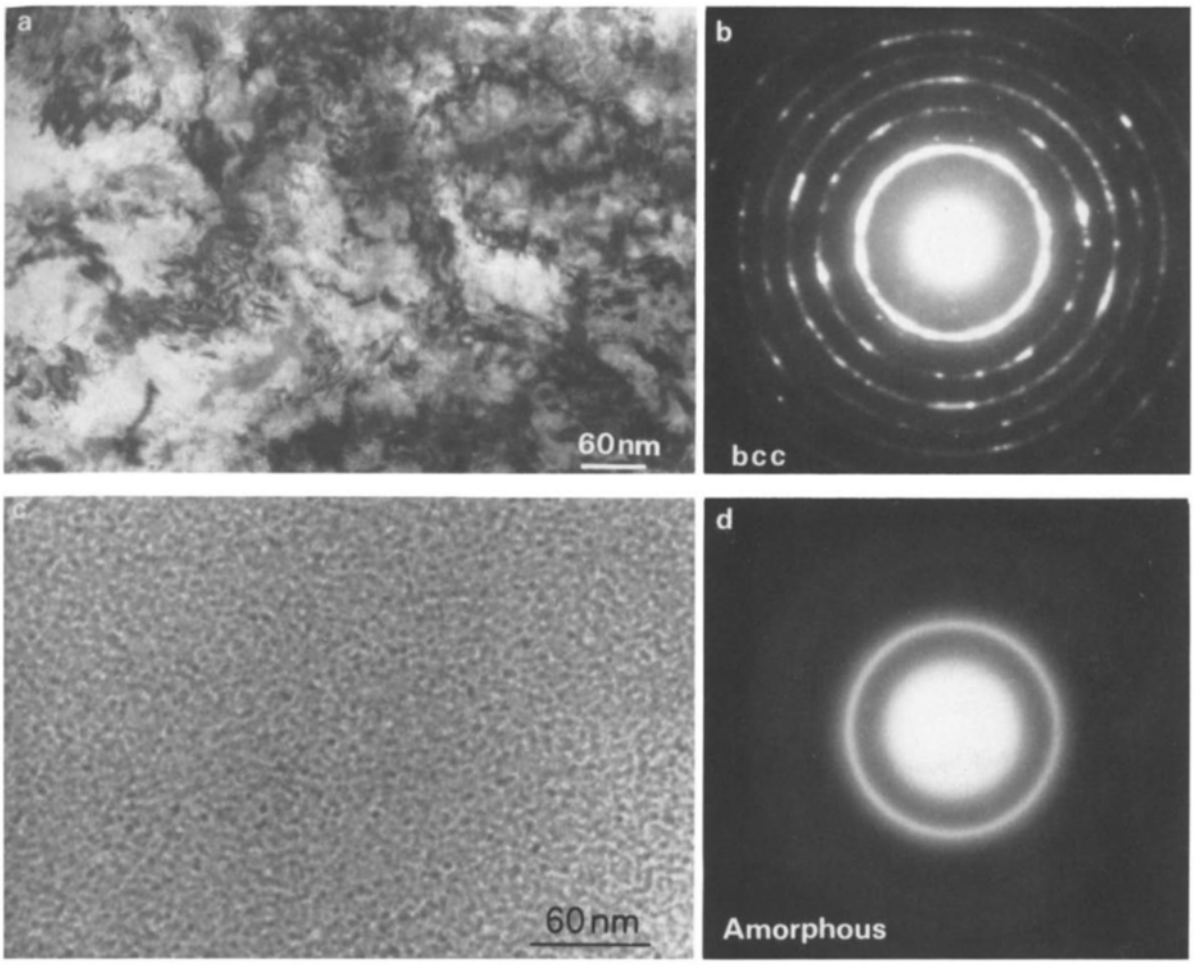

Figure 1.4 Bright field electron micrographs and selected area electron diffraction patterns of $Cu_{44}Nb_{42}Sn_{14}$ powders produced by mechanical alloying after 4 h ((a) and (b)) and 24 h ((c) and (d)) [50].

Amorphization by mechanical attrition was observed in the Nb_3Sn alloy when ball milling Nb + Sn, Nb + $NbSn_2$ or Nb_3Sn crystalline powder mixtures [51]. In starting powders of Nb + Sn and Nb + $NbSn_2$, milling first formed the A15 crystalline structure Nb_3Sn phase which then transformed to the amorphous structure. The ordered A15 structure Nb_3Sn disordered completely after 1h of milling, which was well before amorphization was first observed (5-6 h) (Figure 1.5). Estimation of the free-energy and enthalpy differences between the crystalline and amorphous Nb_3Sn phases indicates that the driving force for the crystalline-to-amorphous transition derives from the total energy, consisting of the disordering energy (about 5 kJ/mol) and the energy of the

defects induced by plastic deformation of the disordered crystalline Nb_3Sn (about 10 kJ/mol). The grain boundaries of the refined nanocrystallites are the possible source of the additional energy needed to initiate the amorphization transition process. The plastic deformation which occurs in the brittle A15 Nb_3Sn powder was confirmed by the work hardening and microstructures resulting from a considerable hydrostatic component of the stress state during ball milling.

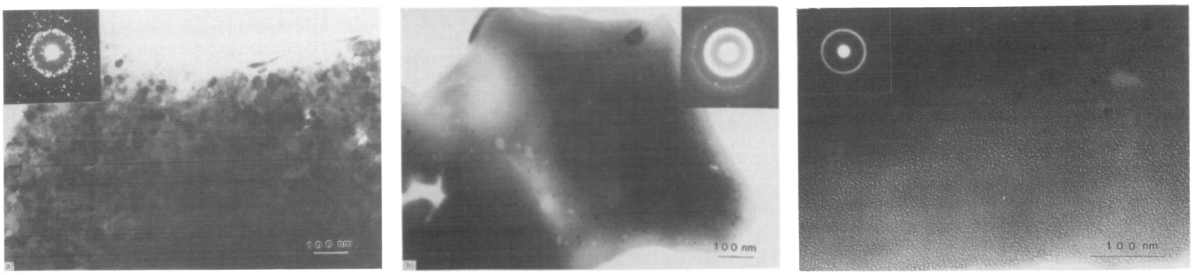

(a) (b) (c)

Figure 1.5 (a), (b) TEM images of 5 h milled Nb_3Sn: (a) larger grain sizes of 20-50 nm; (b) nanocrystallites of 6 nm grain size in an amorphous matrix. (c) amorphous Nb_3Sn after 8 h milling [51].

Hat-shaped AISI 304L stainless steel (Fe-18%Cr-8%Ni) specimens were compressed in a split Kolsky-Hopkinson bar at strain rates of about 10^4 s^{-1}, generating shear strains between 1 and 100 in a narrow region [52]. Shear bands are formed as a result of the compressive deformation, and both nanocrystalline and amorphous regions within the shear bands were observed by TEM and the corresponding electron diffraction patterns. The amorphization process was proposed to be achieved through a solid-state transformation. Outside the shear bands, stacking faults, twinning, and martensitic transformation were observed. Figure 1.6 (a) shows the amorphous region in the center and the nanocrystalline region in the periphery in the TEM micrograph. The two regions are separated by an interface which shows both crystalline and amorphous characteristics; Figure 1.6 (b) confirms the amorphous nature of this area.

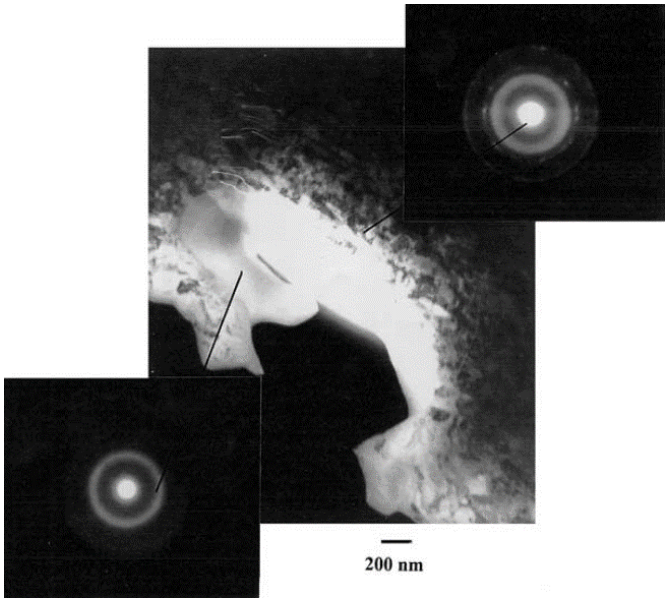

(a)

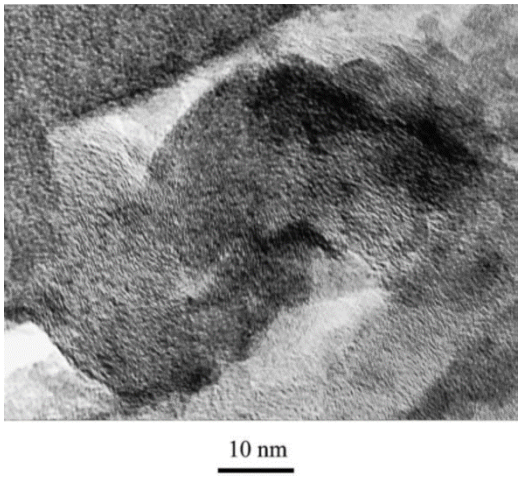

(b)

Figure 1.6 Amorphous region in the center and the nanocrystalline region in the periphery in the TEM micrograph. (a) Nanocrystalline and amorphous regions within a shear band and the corresponding electron diffraction patterns generated by high strain and high strain rate deformation in a shear band in AISI 304L stainless steel. (b) HRTEM images of amorphous region in the same specimen [52].

While amorphous structures have been observed in a variety of multi-component alloys, amorphization in pure metals has rarely been found. Localized solid-state amorphization in bulk nanocrystalline nickel generated by quasi-static compression at a strain rate of 10^{-5} s^{-1} at room temperature was observed by high-resolution TEM [53]. Figure 1.7 exhibits regions subjected to

severe deformation along the crack paths or surrounding the nano-voids. These nano-scale amorphous structures were found near the highly deformed regions, indicating that nanocrystalline structures can promote amorphization. This result may lead to new insights into the nature of the crystalline-to-amorphous transition and provide a possible method to produce elemental metallic glasses that have hardly been produced by rapid solidification so far. Figure 1.8 shows the dislocations around an amorphous band.

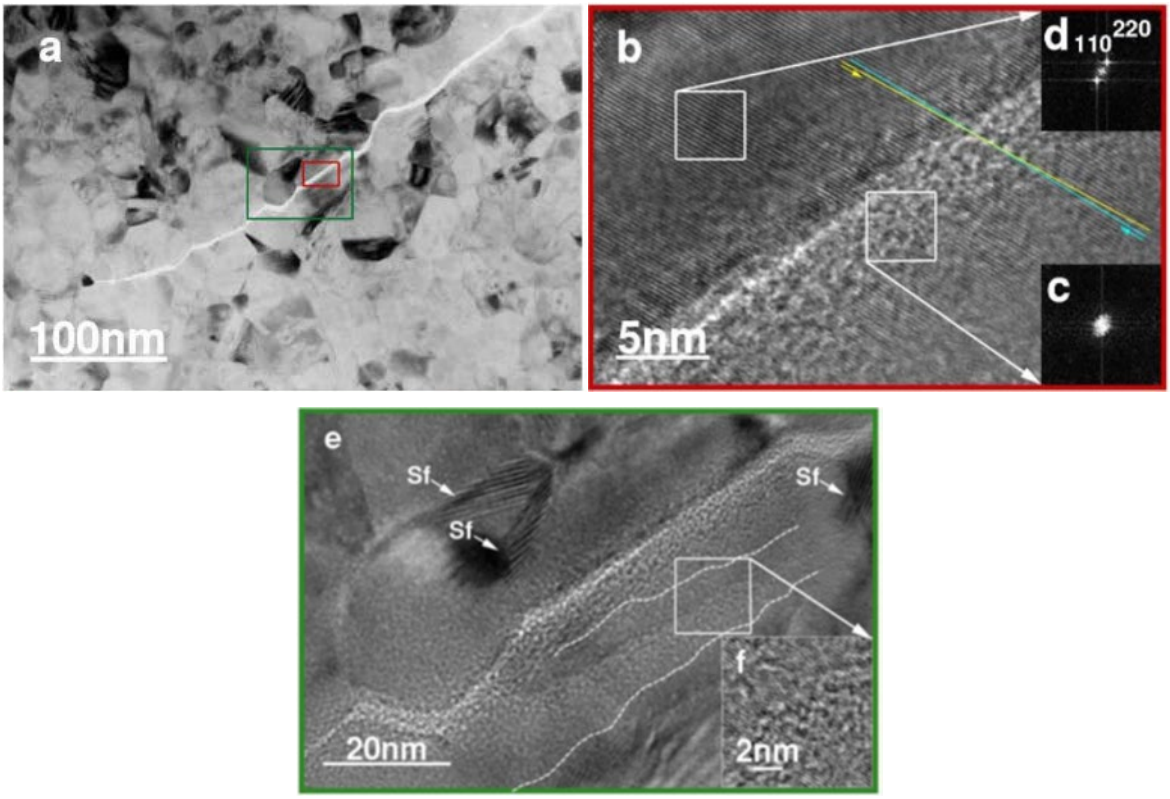

Figure 1.7 TEM micrographs of post-compression nanocrystalline nickel. (a) Bright-field image of crack-like damage areas. (b) HRTEM image of the red-boxed area in (a) exhibits a 3-5 nm wide band and a misalignment of about 1° of the lattice on both sides of the band. (c) Fast Fourier transform pattern from inside the band is an amorphous halo and (d) FFT pattern of the nearby crystalline region. (e) HRTEM micrograph of the green-boxed area in (a). Stacking faults are indicated by Sf, the two white dashed lines highlight a heavily deformed band. (f) A Fourier-filtered image from the white boxed area in (e) shows the heavily deformed band is composed of amorphous phase intertwined with nanocrystals [53].

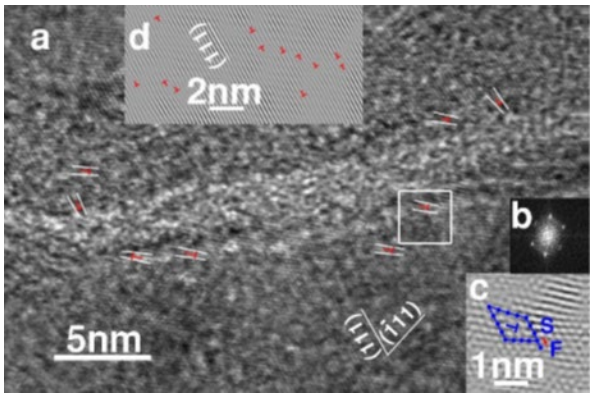

Figure 1.8 TEM micrographs of dislocations around an amorphous band. (a) HRTEM image exhibits a high density of dislocations around an amorphous band. (b) the FFT pattern of the white-boxed area in (a), revealing a crystalline orientation approximately along a <110> zone axis. (c) Fourier-filtered image of the white-boxed area in (a), showing the details of a a/2 <110> full dislocation. (d) A one-dimensional Fourier-filtered image near the amorphous band. Extra (111) half-plane dislocations are marked with a red "T" [53].

The energy-filtered transmission electron microscopy (EFTEM) images of amorphized graphite flakes in gray cast iron under tribological loading can be seen in Figure 1.9 [54]. The gray cast iron disc was subjected to a heavy-duty automotive brake test. Graphite layers were squeezed into the ferritic matrix, where oxygen could enter and subsequently form magnetite. The exfoliated few-layer graphene was heavily deformed. The Raman spectra revealed that the shear stresses on the brake surface induced disorder in a much more effective way than milling due to the additional compressive and impact forces exerted during the brake test. The high anisotropy of elastic moduli in the crystalline graphite structure and the low attraction between the graphene layers results in the exfoliation of wrinkled few-layer graphene under shear loading, leading to more defect-related bands in Raman spectra than by mechanical stresses during high energy milling. The high elastic modulus of graphite along the basal planes results in few-layer graphite batches that penetrate the soft iron matrix, causing iron nanoparticles to peel off. This low attraction between graphene layers allows the layers to be further wedged apart by micron sized iron or magnetite particles. This

mechanism explains the amorphization of graphite and formation of nano-scale magnetite in friction films during braking.

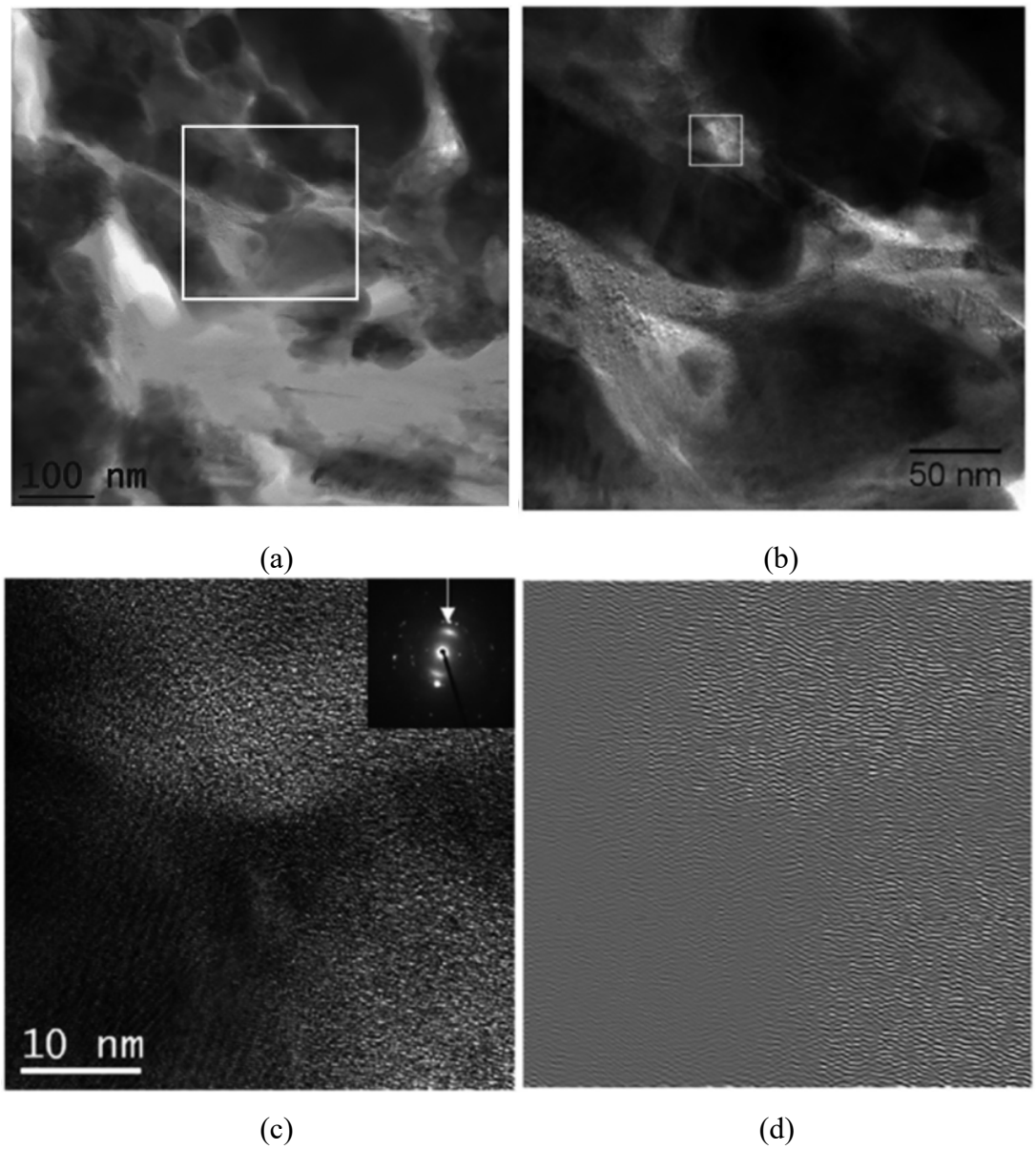

Figure 1.9 Amorphization of graphite flakes in a gray cast iron disc after heavy duty automotive brake test. (a) Energy Filtered TEM images of the cross section of the disc. Light gray ribbons are graphite, dark gray grains are iron, and blotched gray grains are magnetite. (b) Higher magnification of the white-boxed area in (a). (c) Higher magnification of the white-boxed area in (b). with SAED pattern inset. (d) Inverse fast Fourier transform (FFT) reconstructed image showing the graphite spots and that the planes are crumpled [54].

As mentioned earlier, metallic glasses (amorphous metals) are solid state materials which do not have a long-range atomic order. Most metals are crystalline and have a highly ordered atomic arrangement. Metallic glasses (MGs) present superior mechanical properties to crystalline alloys due to their glass-like microstructure. Most MGs are composed of two or more elements and the limited number of compatible principal elements restricts the development of MGs. HEAs have high configurational entropies which can significantly reduce the Gibbs free energy the alloy system and stabilize the interior structures. Some high entropy alloys (HEAs) have an amorphous phase, and have been called high entropy metallic glasses (HE-MGs) [55]. HE-MGs combine the properties of both HEAs and metallic glasses but not all HEAs can form amorphous structures. Usually, a single-phase solid solution or more complex compounds are formed instead. A high mixing entropy required for preparing HE-MGs can be achieved by using multicomponent alloys with equiatomic or near-equiatomic ratios. The $Fe_3Cr_2Al_2CuNi_4Si_5$ HE-MG was prepared by amorphous powder molding using mechanical alloying (MA) and ultrahigh pressure consolidation (UHPS), generating an amorphous matrix (Figure 1.10 (a)), with uniformly distributed nanoparticles (Figure 1.10 (b)) [56]. The UHPC is best performed at as low temperature as possible to retain the amorphous structure produced by MA. This technique can effectively suppress the crystallization process of the amorphous phase, thus providing a new way to prepare HE-MGs.

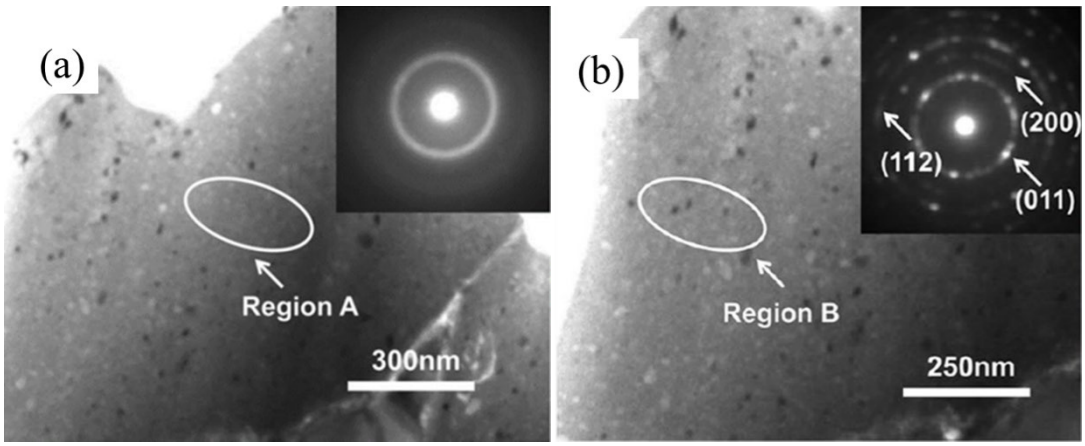

Figure 1.10 TEM images of $Fe_3Cr_2Al_2CuNi_4Si_5$ HE-MG, a novel non-equiatomic alloy. (a) inset shows the diffraction pattern for the amorphous matrix, (b) inset shows the diffraction pattern for the nanoparticles [56].

Figures 1.11 and 1.12 [57] show the microstructures of a pre-deformed high entropy CrMnFeCoNi Cantor alloy that underwent quasi-static uniaxial and dynamic uniaxial compression, and was subsequently subjected to dynamic shear experiments at a shear strain rate of 6×10^5 s^{-1} in the same hat-shape geometry as mentioned in the earlier experiments on stainless steel [52]. A dense structure composed of stacking faults, twins, crystalline transformation from fcc to hcp, and amorphization was observed. The coordinated growth of stacking faults and twins along {111} planes induced severely deformed regions, which can, at their intersection, rearrange into hexagonal packets; when the defect density reaches a threshold, they give rise to amorphous islands. As the deformation energy (defect density) increases, elastic deformation gives way to the generation and motion of dislocations, then to twinning, subsequently to phase transformations, and, in the end, in the extreme regime of high strain and high strain rate, to amorphization. The amorphization process can dissipate the large deviatoric stresses accumulated at the intersections of all kinds of crystalline imperfections, and thus inhibits the initiation and growth of nano cracks which could lead to failure. The amorphous phase should be harder than its crystalline counterpart because dislocations have no propagation path through the structure, a property also seen in bulk

metallic glasses [58] and crystalline/amorphous nanolaminates [59-61]. Thus, amorphization is proposed as a deformation mechanism which helps to release the imparted strain energy. The boundaries between different deformation mechanisms can be loosely depicted by critical defect densities. These regions may have superior mechanical properties which potentially strengthen or toughen the material under extreme loading conditions.

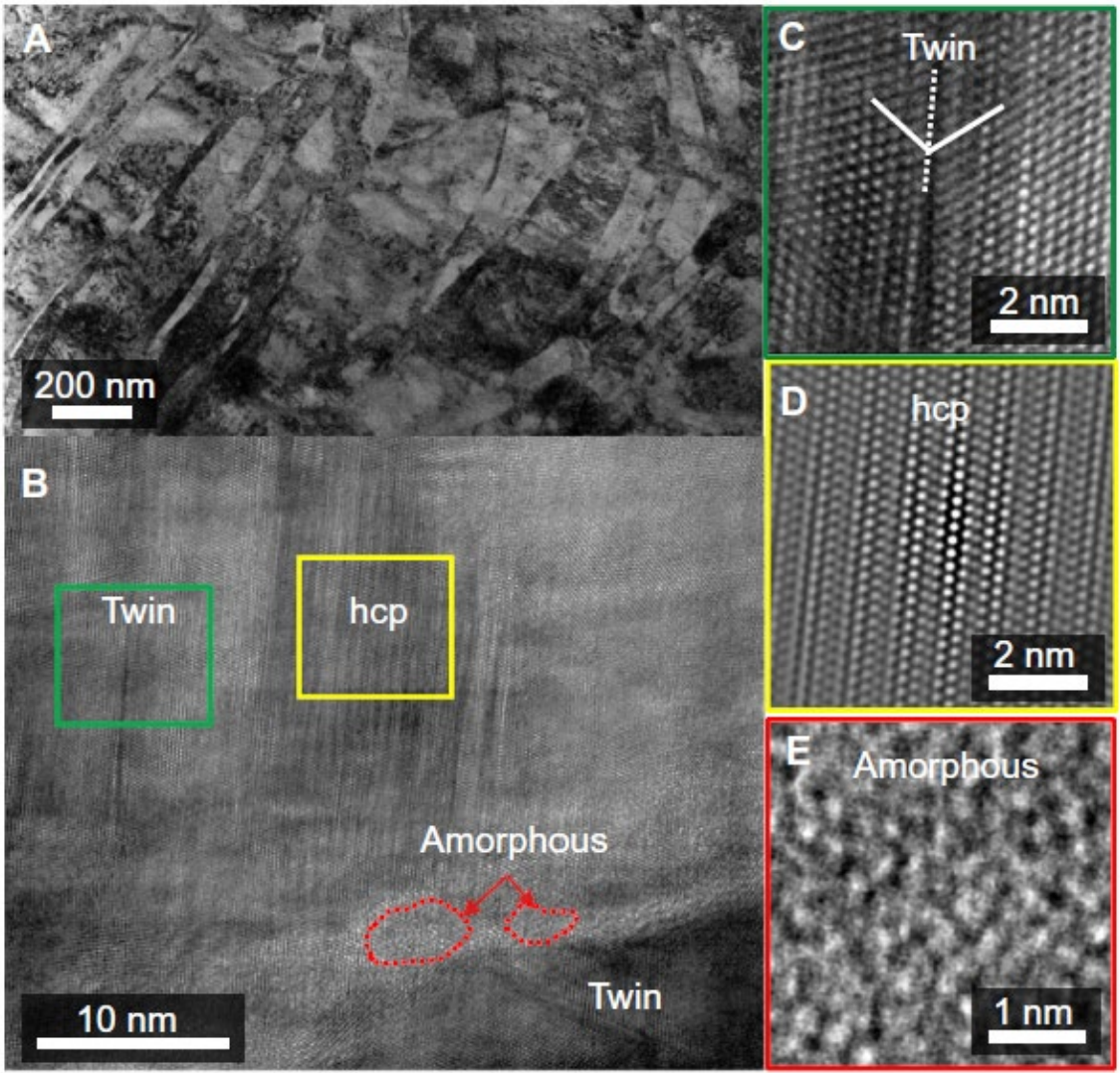

Figure 1.11 Complex deformation microstructure of the swaged CrMnFeCoNi HEA after quasi-static compression at a strain rate of 10^{-3} s^{-1}. (a) TEM bright-field image shows high density planar defects. (b) HRTEM micrograph of the heavily deformed regions of twinning, hcp phase, and amorphous regions as marked. (c) Close up view of the twinned region (d) Close up view of the hcp region, with Fourier transformation–filtered to maximize phase contrast. (e) Close up view of the amorphous region, formed at the intersection of hcp and twinned region [57].

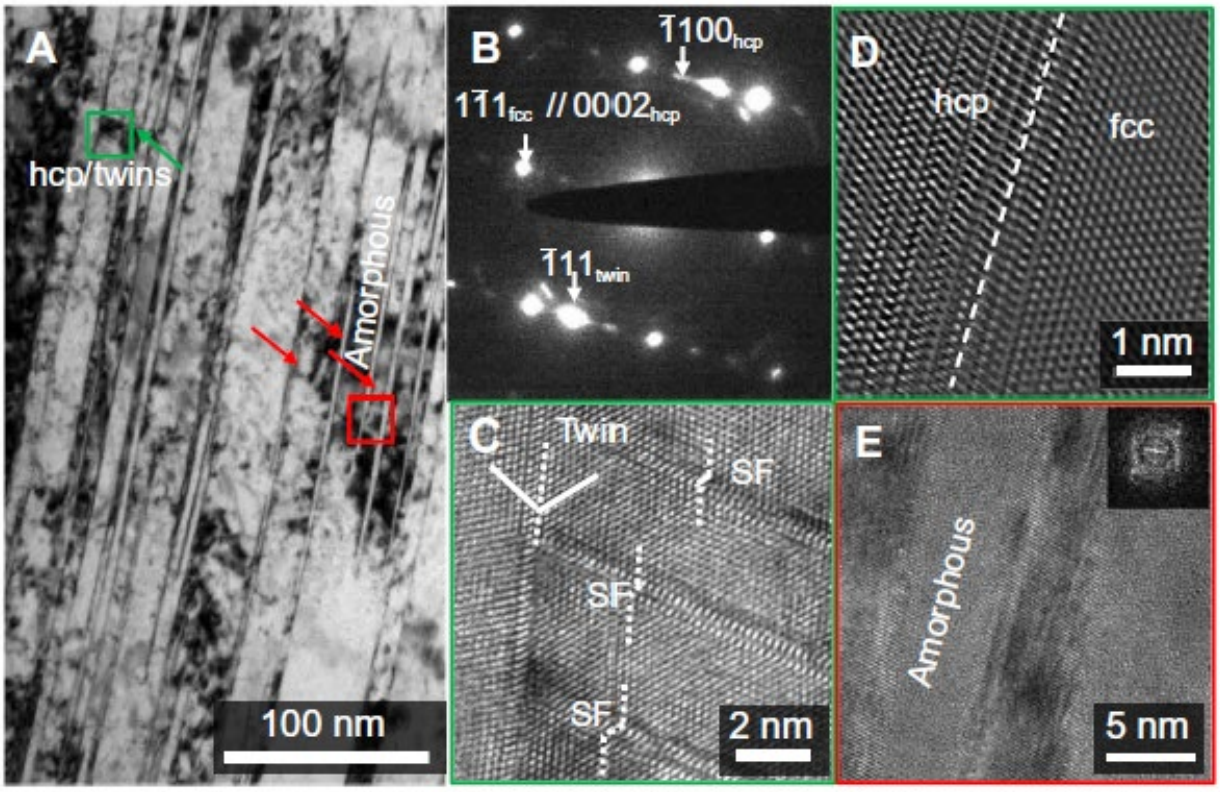

Figure 1.12 Complex deformation microstructure of the CrMnFeCoNi HEA after dynamic compression/shear. (a) Bright-field TEM image of the shear band with twins, stacking faults, hcp phase, and amorphous bands. (b) SAED pattern shows the existence of the fcc matrix, twinning spot, and the hcp structures. (c) HRTEM image shows the coexistence of twins and stacking faults (SF). (d) Fourier-filtered lattice image of the interface between hcp and fcc phases. (e) HRTEM image of the amorphous bands (red-boxed area in (a)) and the corresponding fast Fourier–transformed diffractogram [57].

1.1.3 Amorphization in intermetallic compounds

Amorphous alloys were formed by milling the crystalline $Ni_{50}Zr_{50}$ compound or the crystalline $Ni_{55}Zr_{45}$ alloy in a planetary ball mill [62]. In contrast, amorphous $Ni_{61}Zr_{39}$ can be generated by using a vibrating frame equipment. Thus, different milling methods can lead to different end products. The crystalline to amorphous transition of an alloy is an endothermic process. Milling can provide the energy required for this transition by introducing defects into crystalline compounds and breaking down crystallites in a powder particle, which increases their free enthalpy. When this free enthalpy exceeds that of the amorphous alloy, the crystalline

compounds transform into the amorphous phase. Figure 1.13 compares the enthalpy curves of the stable mixtures of two crystalline compounds and their amorphous alloy. The glass-forming range can be estimated from the difference in enthalpy between the two phases. When the increase in enthalpy is about 8 kJ/mol and Zr at.% is between about 40 and 50% amorphous alloys can be formed. Outside of this range the increase in enthalpy difference is not sufficient and a two-phase alloy consisting of amorphous and crystalline phases is formed.

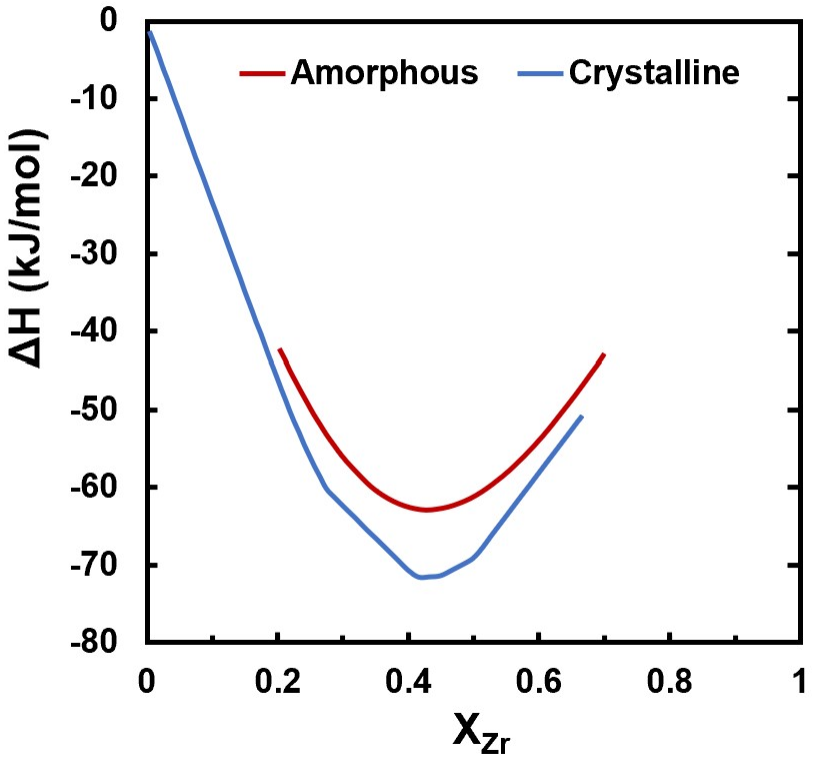

Figure 1.13 Enthalpy curves of crystalline (lower, blue) and amorphous (upper, red) Ni-Zr alloys/compounds [62].

Ni_xZr_y compounds [63] become fully amorphized when they are subjected to a milling intensity greater than a temperature and composition-dependent threshold. Milling intensity is defined as the amount of momentum transferred from the milling ball to the powder per unit mass per unit time. Below this threshold, a two-phase structure (crystalline and amorphous) is stable;

and above this threshold the proportion of the amorphous phase increases with the milling intensity and decreases with increasing milling temperature. The intensity threshold increases with temperature and decreases with the hardness of the initial crystalline compound, which also controls the amorphization rate and the steady-state phase fraction in the two-phase equilibria. During milling, the environment of an atom changes in time due to two parallel mechanisms: thermally activated point defect jumps, as in classical thermodynamic equilibrium, and forced deformation such as shearing, powders sticking along new surfaces, etc. In Figure 1.14 (a), the crystalline particles are distributed in an amorphous matrix, and the crystallites dissolve into the amorphous matrix until amorphization is fully achieved as milling time increases.

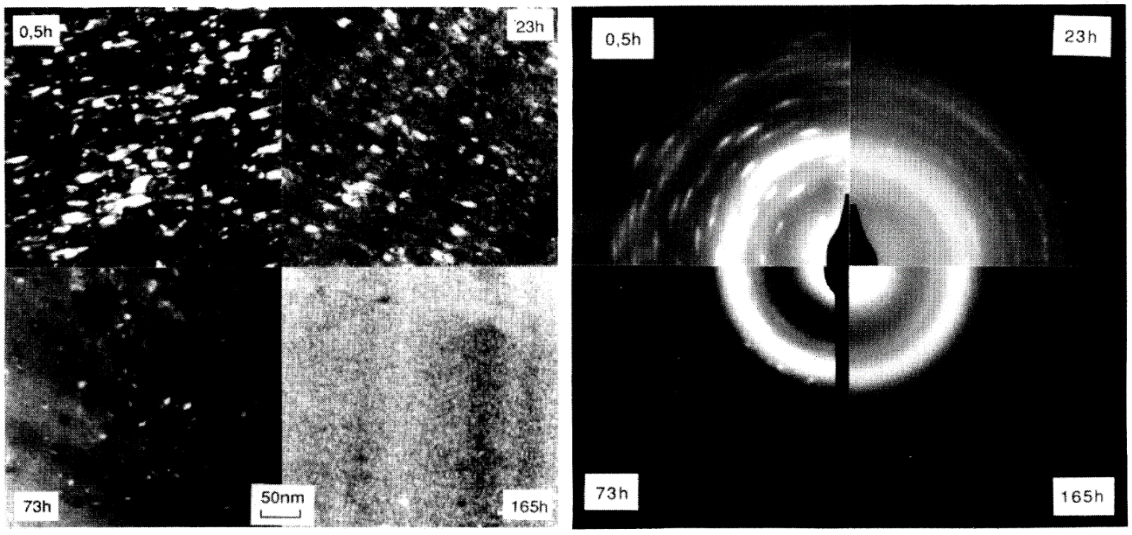

(a) (b)

Figure 1.14 (a) Dark field TEM micrographs of $Ni_{10}Zr_7$ milled at room temperature after 0.5 h, 23 h, 73 h, and 165 h; (b) corresponding electron diffraction patterns. Notice gradual amorphization [63].

The fcc intermetallic compound Ni_3Al was subjected to mechanical milling in a high energy ball mill [64]. It transformed from an ordered fcc structure to a disordered fcc solid solution, and then to mixed phases of nanocrystalline and amorphous structure after continued milling. Milling of the fcc solid solution was dominated by the formation of dislocation cell structures

which were refined into nanometer-sized crystallites. TEM (Figure 1.15) showed an average grain diameter of 2 ± 1 nm for Ni_3Al powder after 50 hours milling. This fine grain size is believed to lead to the crystalline-to-amorphous transition. The estimated free energy difference between the fcc and amorphous phases of Ni_3Al matched the calculated interfacial free energy of the grain boundaries.

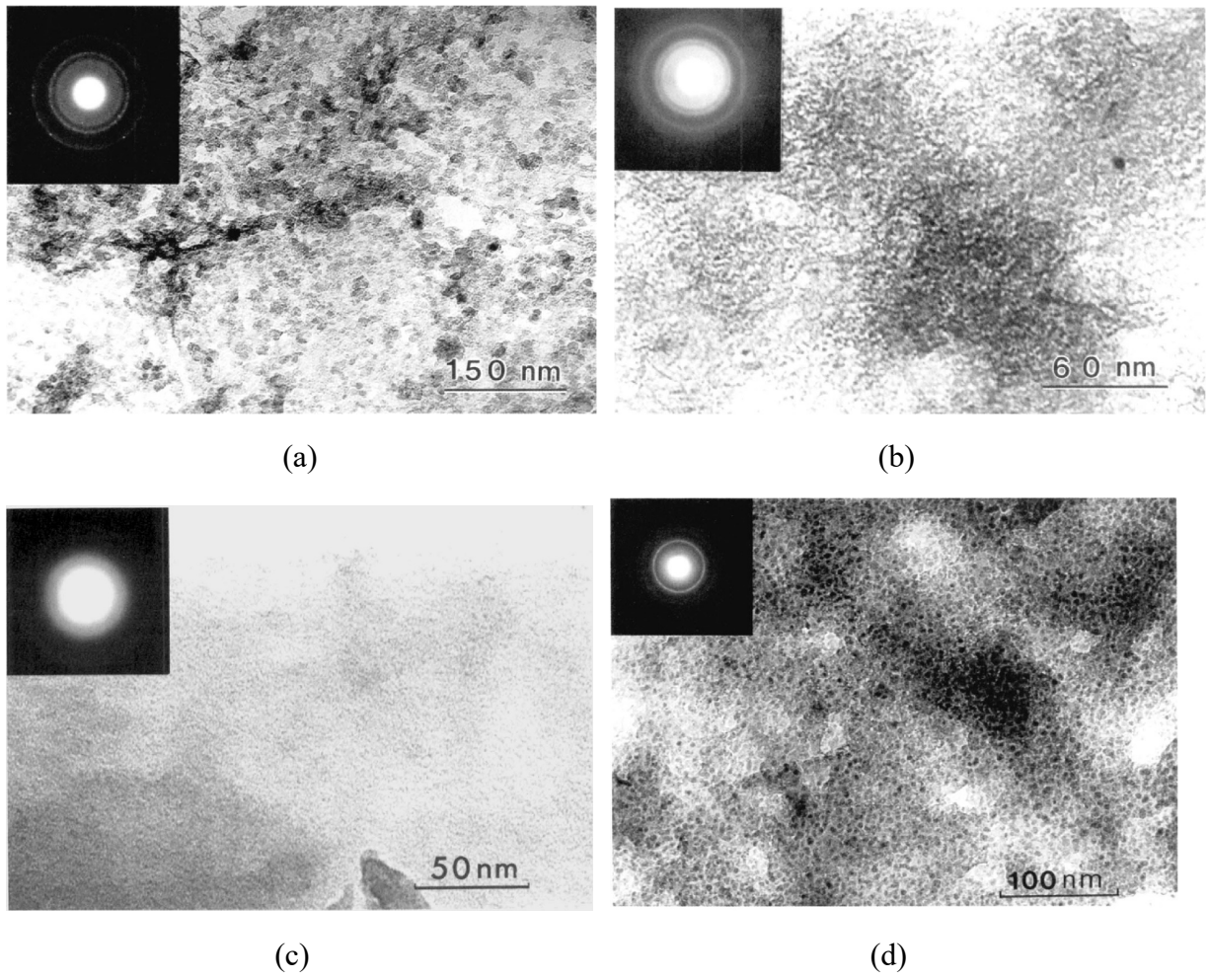

Figure 1.15 (a)-(d) Bright field TEM micrographs of Ni_3Al powders milled after 5 h, 23 h, 50 h, and 50 h and subsequently annealed for 0.5 h at 450 °C [64].

One advantage of solid-state amorphization over its rapid cooling counterpart is that it does not restrict the dimensions of the final product, enhancing the ease of producing bulk amorphous materials. Ni-49.2 at.% Ti alloy sheets were cold rolled at room temperature, generating a high

dislocation density between 10^{13} and 10^{14} cm^{-2}, and suggesting that the accumulation of dislocation is a major driving force for the amorphization process [65]. The 60% reduced sample showed amorphous bands within the finely twinned crystalline matrix. Above 65% reduction, the sample fractured; the straight fracture surface was inclined 30° to 50° to the compression direction. The TEM diffraction micrographs (Figure 1.16 [65]) show both polycrystalline spots and a diffuse ring pattern, confirming the coexistence of crystalline and amorphous phases. The amorphous bands only extended in one direction and were not dependent on the orientation of the original twinned grains. Similar morphologies were observed in other heavily cold-rolled metals, suggesting that amorphous phases form in the shear band due to mechanical instability caused by the shear stress.

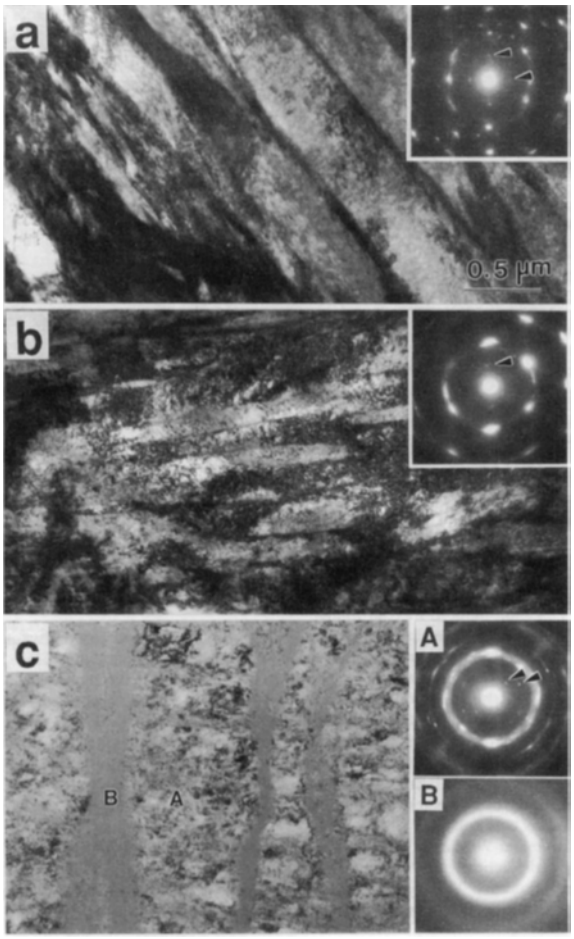

Figure 1.16 Bright-field TEM micrographs and the corresponding diffraction patterns of (a) as-received, (b) 20% reduced, and (c) 60% reduced NiTi [65].

Nonequilibrium phases such as amorphous (Figure 1.17) and intermetallic compound phases were produced and retained at the collision interface in the explosive welding of Ti/Ni clads [66]. There were crystalline particles D and E distributed in the amorphous phase identified by the diffraction patterns Figure 1.17 (d) and (e). These phases were formed by melting and rapid solidification of thin layers on the interface of both parent materials (Ti and Ni). The impact pressure generated by explosive welding promoted the formation of nonequilibrium phases such as the amorphous phase, indicating that shock processing has the combined features of rapid solidification, mechanical alloying, and combustion synthesis, all of which facilitate the formation of nonequilibrium phases.

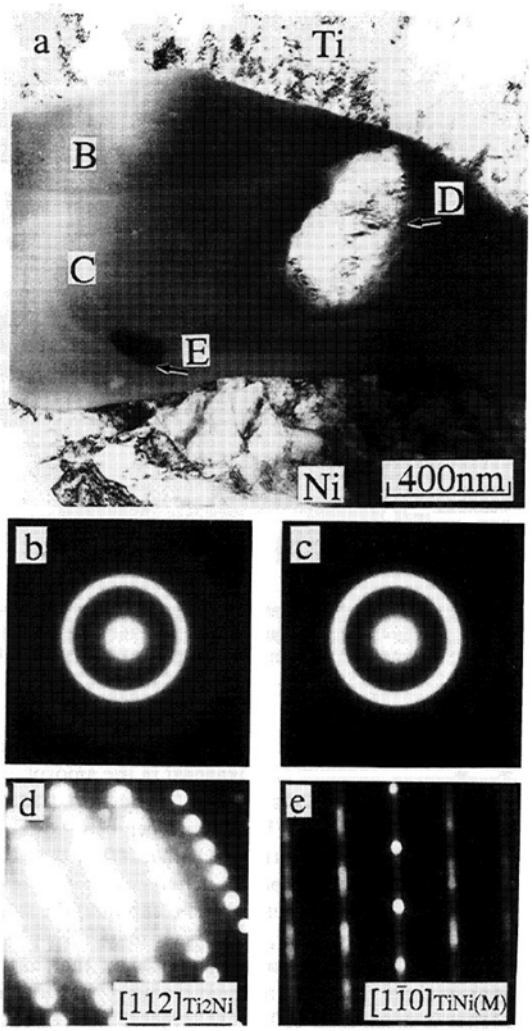

Figure 1.17 Nonequilibrium phases such as amorphous and intermetallic compound phases were produced and retained at the collision interface in the explosive welding of Ti/Ni clads. (a) Bright field TEM image of collision interface in explosively welded Ti/Ni clad, exhibiting the formation of amorphous and crystalline phases. (b) to (e) Electron-diffraction patterns of the corresponding areas B to E in (a); B and C show amorphous regions and D and E show crystalline regions [66].

Amorphization was also observed in Nitinol (TiNi) subjected to high-pressure torsion [67, 68], electron irradiation [69], ball milling [70], shot peening [71], and high-pressure extrusion [72]. High-pressure torsion (HPT) has been used as an effective method to produce bulk nanostructured materials with good mechanical properties [67]. As mentioned above, amorphization can be considered as an extreme case of refining grain size. The initial NiTi alloy (50.62 at.% Ni and 49.38 at.% Ti) disc sample had an austenite B2 (CsCl-type) structure with an average grain size of

30 μm. High pressure torsion was applied to the TiNi sample under a 5 GPa pressure to a true strain of 7. Figure 1.18 shows that most of the sample amorphized after the HPT. In agreement with the results obtained by Koike et al. [65], the sharp diffraction rings superimposed on an amorphous halo confirmed the presence of both nanocrystalline and amorphous phases, indicating that the amorphization transformation under HPT is not homogeneous (Figure 1.19). HRTEM micrographs show a disordered or amorphous phase originating from the dislocation core regions; amorphization was observed in both the interior of the grains and at the grain boundaries. This study concludes that the dislocations and grain boundaries both initiate the crystalline-to-amorphous transformation in TiNi.

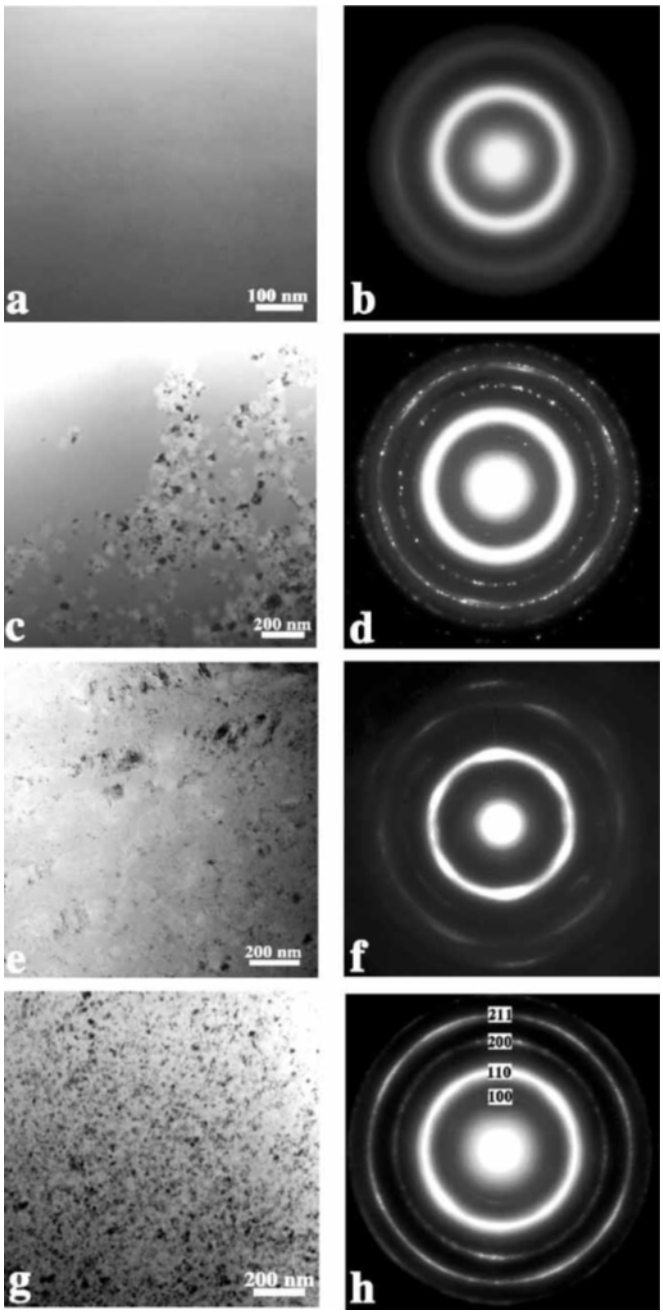

Figure 1.18 TEM micrographs and the corresponding EDPs showing the coexistence of the amorphous nanocrystalline phases in TiNi subjected to high-pressure torsion [67].

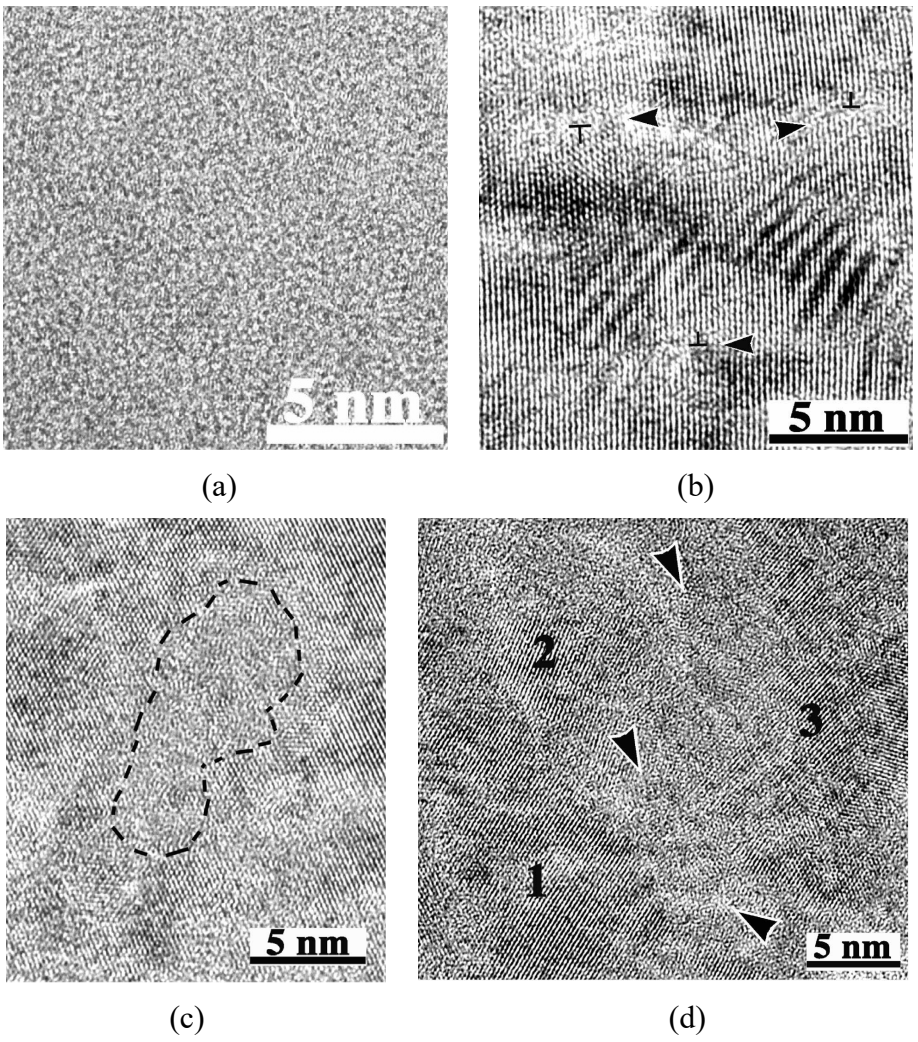

Figure 1.19 HRTEM images of inhomogeneous morphologies in TiNi. (a) Amorphous phase. (b) Disordered regions originated from dislocation cores. Arrowheads denote the disordered regions. T or inverted T indicate edge dislocations. (c) Amorphous phase in the interior of a grain. (d) Amorphous phase at the grain boundaries. The numbers denote three grains, and the amorphous regions are indicated by arrowheads [67].

Local canning compression of NiTi shape memory alloy subjected the material to a three-dimensional compressive stress state, which inhibited the initiation and propagation of micro-cracks and thus enhanced its plasticity [73]. Local canning compression can induce severe plastic deformation in NiTi alloy, leading to the formation of nanocrystallization or amorphization. At 25% reduction in height, dislocations and twins were observed. At 50% reduction in height, a small amount of nanocrystalline and amorphous phases occurred in the matrix of NiTi, where the

nanocrystalline phase was dominant. At 75% reduction in height, the amorphous and nanocrystalline phases were dominant, with a small amount of nanocrystalline phase distributed in the amorphous matrix (Figure 1.20). Jiang et al. [73], proposed a sequence of microstructural evolution leading amorphization (Figure 1.21). The sequence is essentially similar to other materials, with the added stress-induced martensite. Thus, one has the sequence austenite → stress-induced martensite→ deformation twinning→ dislocation slip→ nanocrystallization→ amorphization.

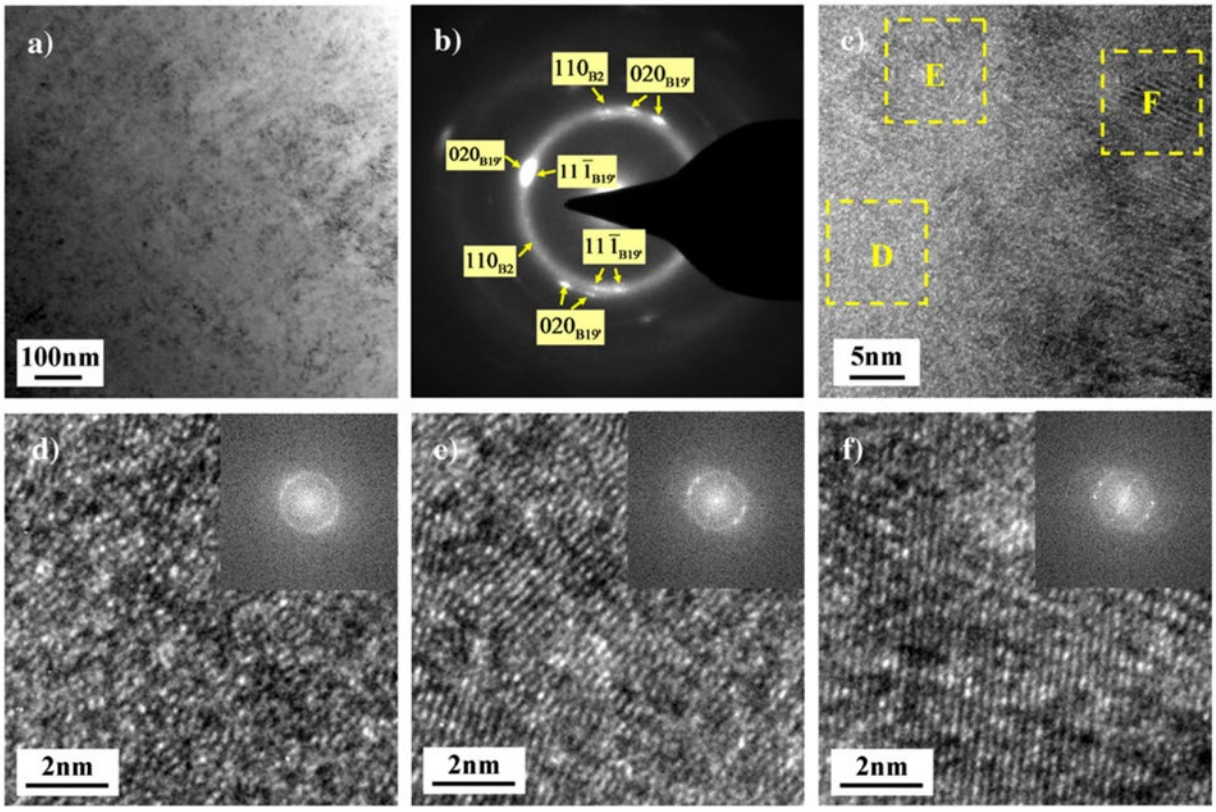

Figure 1.20 TEM images of NiTi specimen deformed by 75% in height: (a) bright field image; (b) SAEDP showing the coexistence of amorphous and nanocrystalline phases, B2 austenite and B19′ martensite; (c) HRTEM image exhibiting the retained nanocrystalline phase distributed in the amorphous matrix; (d) FFT of zone D in (c) revealing the amorphous nature; (e) FFT of zone E in (c) showing coexistence of amorphous and nanocrystalline phases; (f) FFT of zone F in (c) exhibiting dislocations and lattice distortion in nanocrystalline phase [73].

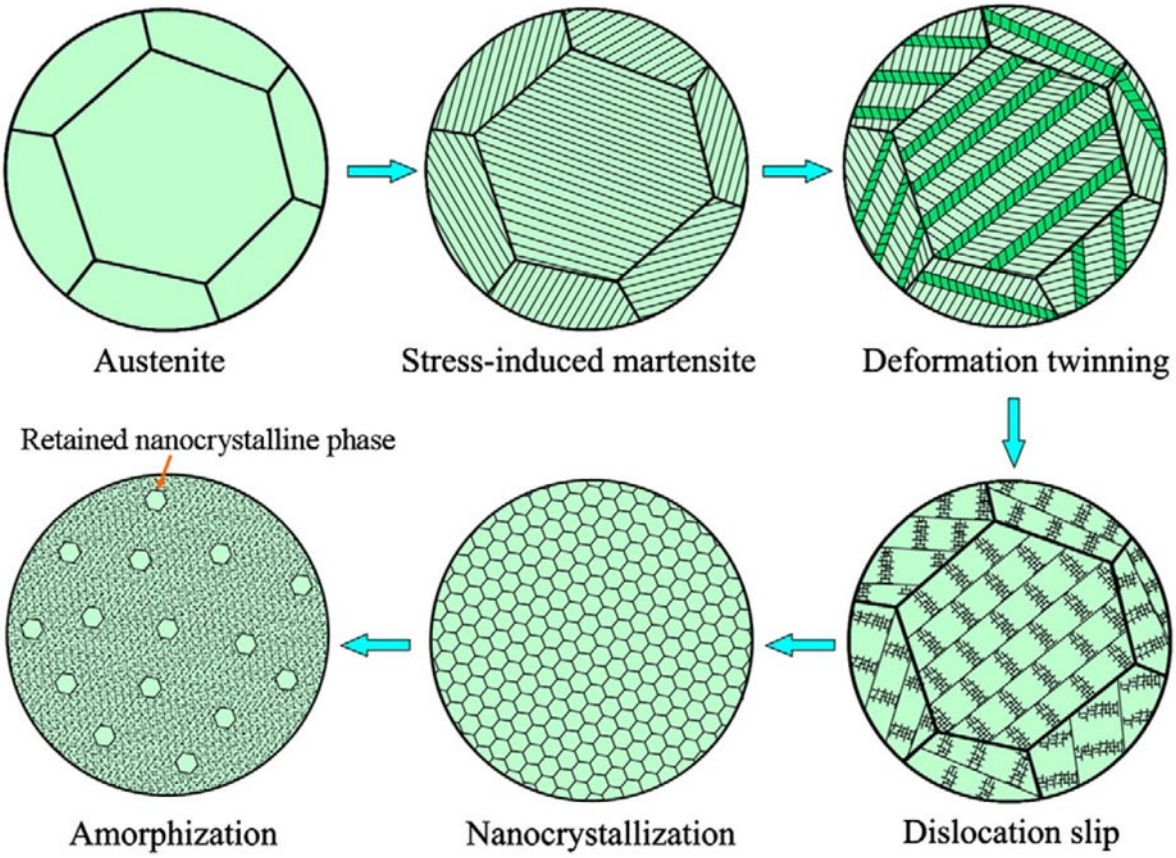

Figure 1.21 Schematic diagram of microstructural evolution of nanocrystallization and amorphization of NiTi specimen under local canning compression [73].

Ultrasonic Nano-crystal Surface Modification (UNSM) is a method where a tungsten carbide tip is forced against a sample surface and vibrates at a high frequency, which leads to severe surface plastic deformation. Surface amorphization of the NiTi shape memory alloy was achieved by UNSM [74], which improved its hardness and thus significantly enhanced its wear resistance. TEM (Figure 1.22) confirmed the amorphous nature by Fast-Fourier Transformation (FFT) and selected-area electron diffraction (SAED). Cell culture study also showed that the biocompatibility of the samples was not compromised by the UNSM process compared to the unprocessed samples. The high wear resistance and good biocompatibility suggests that UNSM is a potential process for creating better biomedical devices.

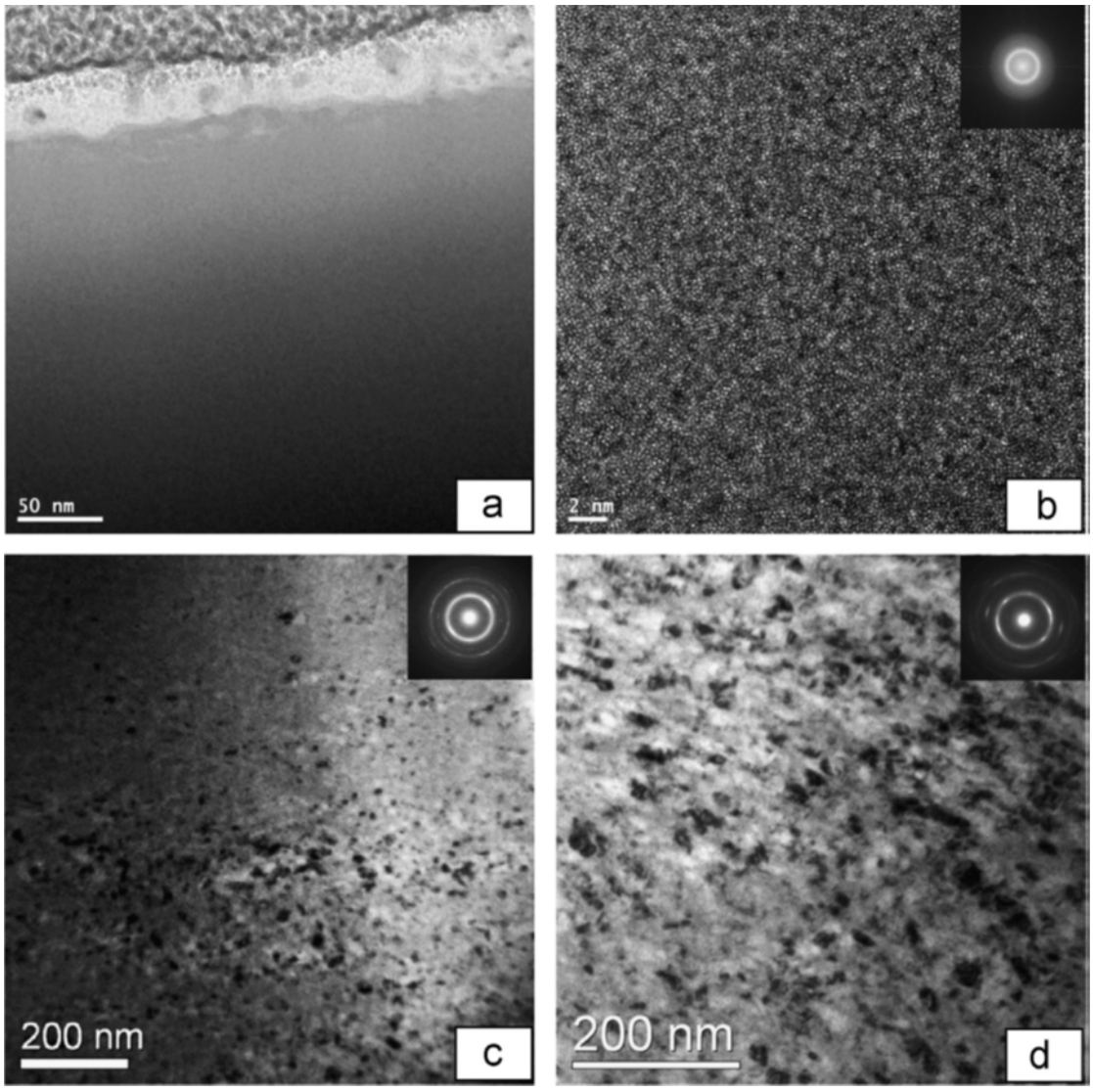

Figure 1.22 TEM images on or near the surface of NiTi shape memory alloy after Ultrasonic Nanocrystal Surface Modification (UNSM) processing. (a) Top surface low magnification image; little contrast can be seen. (b) Top surface high-resolution image with corresponding FFT pattern; no long-range order observed. (c) Bright field TEM image and corresponding diffraction pattern at 4 μm below surface; partially nanocrystalline and partially amorphous at 4 μm below the surface. (d) Bright field TEM image and corresponding diffraction pattern at 7 μm below surface. Nanocrystalline nature increases with depth, become fully nanocrystalline at 7 μm below [74].

Nanocrystalline NiTi micropillars under uniaxial compression underwent plastic deformation mainly through localized shear band formation accompanied by large strain bursts [75]. Grains inside the shear band were reduced from 65 nm to 11 nm and even amorphized. The microstructural changes in the NiTi micropillars resembled those of bulk materials processed via

macroscopic severe plastic deformation where a large plastic strain was imposed to obtain nanocrystallization. Figure 1.23 (a) shows the surface morphology of the micropillar by plastic-deformation. Figure 1.23 (b) is the bright-field TEM image, showing the shear band at 45° to the loading direction, which is the direction of the maximum shear stress. Inside the shear band (Figure 1.23 (c)), the microstructure is a mixture of amorphous phase and nanograins with as small as 11 nm, much smaller than the average grain size of the other parts of the micropillar (65 nm). The SADP of the shear band (Figure 1.23 (c)) shows the coexistence of austenite (B2 lattice), martensite (B19′ lattice), and amorphous phases. The refined 11 nm grains are more resistant to plastic deformation than the original 65 nm grains; as a result, the critical stress for bursts increases with the strain. Figure 1.23 (d) is the illustration of the localized plastic deformation of the nanocrystalline NiTi micropillar. The experimental results indicate that microfabrication by severe plastic deformation could be a potential manufacturing technique.

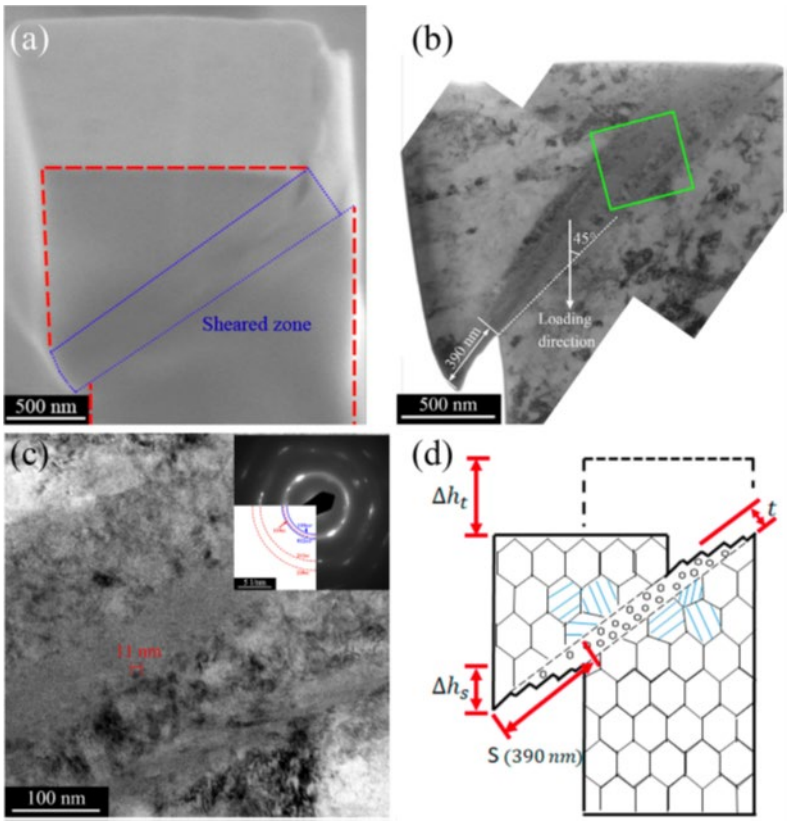

Figure 1.23 Surface morphology of the nanocrystalline NiTi micropillar by plastic-deformation. Surface morphology of the nanocrystalline NiTi micropillar by plastic-deformation. (a) SEM image of the NiTi micropillar by plastic deformation, (b) TEM image of the localized shear band, (c) TEM image and the SADP of the green-boxed area in (b), and (d) an illustration of the plastic deformation of the nanocrystalline NiTi micropillar (blue lines represent the residual martensite) [75].

High pressure torsion (HPT) is a suitable technique to deform brittle materials due to its quasi-hydrostatic loading condition which inhibits crack formation. In a ZrCu intermetallic compound [76], many shear bands nearly parallel to the shear direction were observed by optical microscopy after HPT deformation (Figure 1.24 (a)). X-ray diffraction and TEM observation confirmed the presence of partial amorphization, localized within the nano-scale shear bands (Figure 1.24 (b) and (c)). In the zone-melted $Zr_{50}Cu_{40}Al_{10}$, the amorphization was preferential in the ZrCu phase (Figure 1.25), indicating that the initial martensitic structures played an important role in the amorphization process.

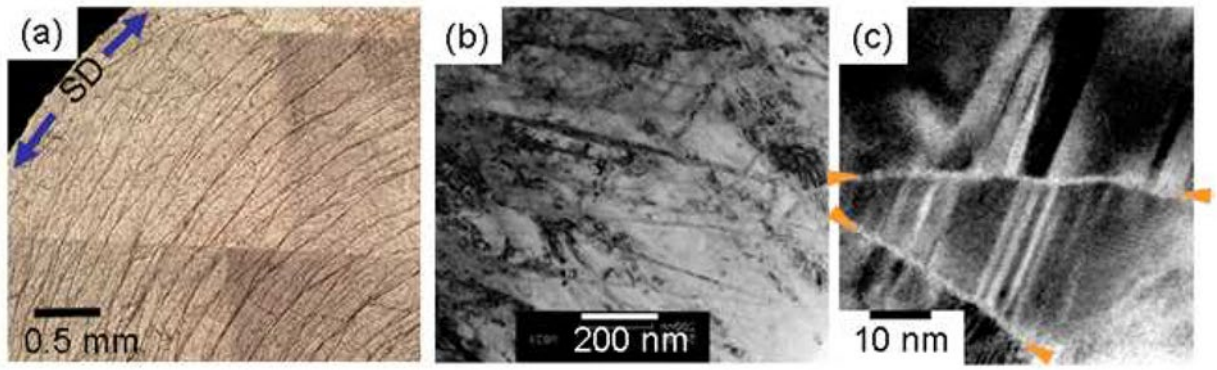

Figure 1.24 Microstructures of ZrCu after HPT deformation for 30 turns. (a) Optical microscopy image. (b) TEM bright field micrograph. (c) HRTEM micrograph [76].

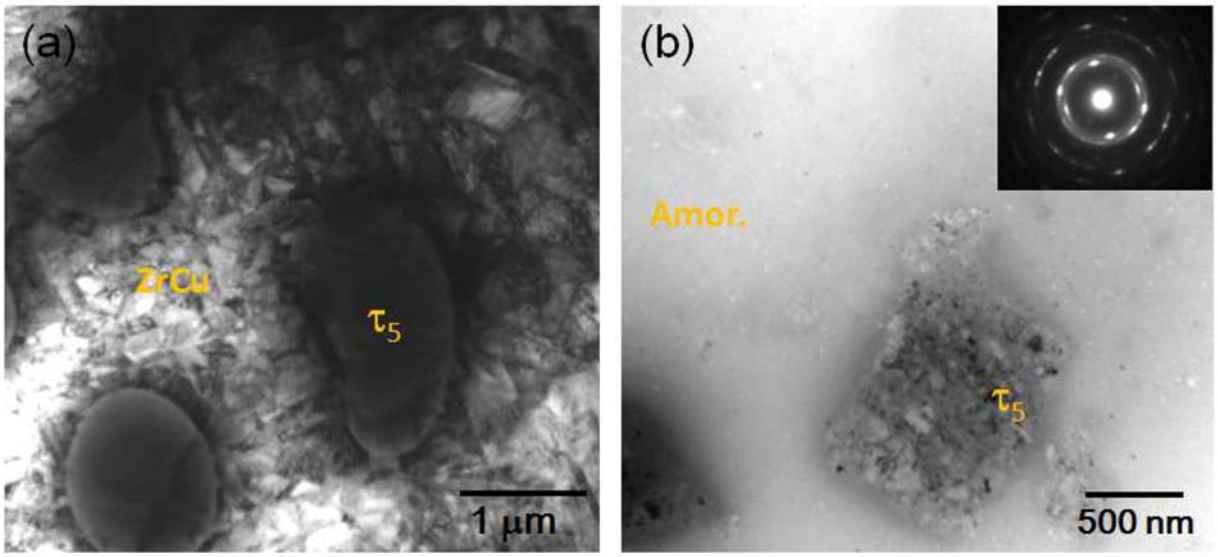

Figure 1.25 TEM images of $Zr_{50}Cu_{40}Al_{10}$. (a) Before HPT deformation. (b) After HPT deformation (N = 50). Amorphized region shown in (b) [76].

The interactions of dislocations with each other and other defects such as grain boundaries often results in strengthening of the material. Brittle failure occurs preferentially when dislocations are scarce. Another example of intermetallic compound is samarium–cobalt ($SmCo_5$) deformed by nanoindentation. For small grain sizes, the dominant deformation mechanism is grain boundary sliding, while for larger grain sizes, amorphous shear bands were found as well [77]. This unusual deformation mechanism leads to an inverse Hall-Petch (HP) relation of strength versus grain size which is opposite to the traditional HP relation observed in common metals. The HRTEM image

(Figure 1.26) shows a shear band without dislocations in its vicinity. FFT and its inverse patterns reveal that the shear band is amorphous while regions outside the band are crystalline. The amorphous shear band (about 2 nm thick) in this case is the primary carrier for plastic deformation and was able to propagate in the grains without crack initiation. These amorphous shear bands in $SmCo_5$ inhibit fracture and increase the plasticity of the material. Two features are important for this mechanism to release the strain in the intermetallic compound: a high-energy barrier for dislocation glide and a low-energy barrier for amorphization. This deformation mechanism can be generalized to other intermetallic materials which generate similar amorphous shear bands under deformed.

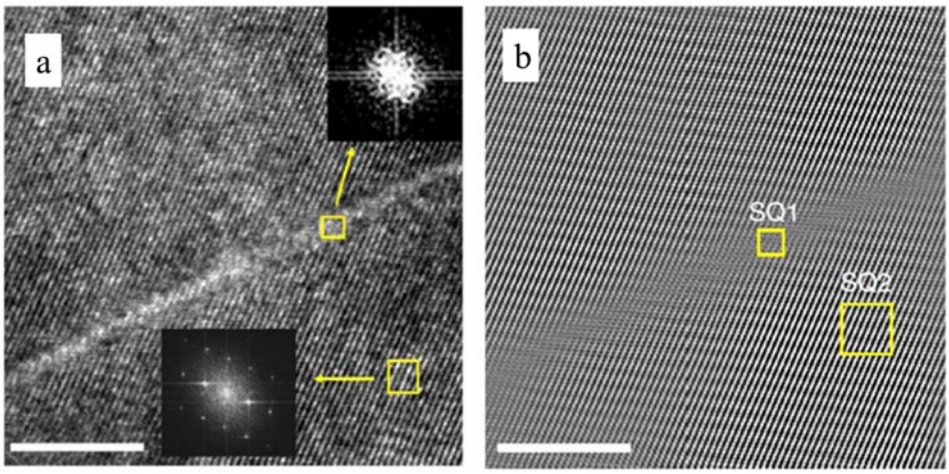

Figure 1.26 Amorphous shear bands in nanoindentation deformed $SmCo_5$. (a) HRTEM image of a shear band and its vicinity and the FFT patterns. (b) The inverse FFT image. A blurred band corresponds to the amorphous shear band. Scale bars are 10 nm [77].

1.1.4 Amorphization in covalently-bonded solids

Jeanloz et al. [78] were the first ones to observe, by TEM (Figure 1.27), an amorphous phase within the crystalline matrix with a high density of dislocations in a single crystal of natural olivine $(Mg_{0.88}Fe_{0.12})_2SiO_4$ disc sample subjected to 56 GPa shock pressure by multiple-reverberation for about 0.5 microseconds. The shocked sample had various degrees of deformation,

and the amorphous zones were found within regions with the highest density of dislocations. Thus, it was concluded that amorphous olivine glass may form at shock compression above 50 to 55 GPa.

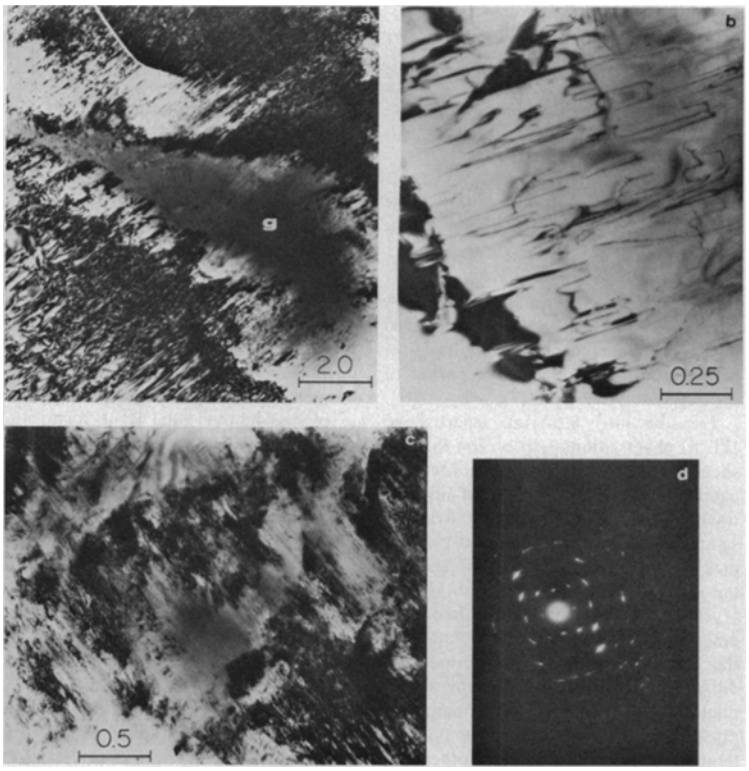

Figure 1.27 TEM images of shocked olivine. TEM images of shocked olivine. (a) 200 keV Bright-field TEM images of shocked olivine. The area marked with a (g) is a nondiffracting amorphous zone within crystalline olivine (light areas) and contains a high density of dislocations. (b) 1MeV Bright-field TEM image of shocked olivine showing dislocation densities as low-as 10^6 to 10^7 cm^{-2}, similar to those found in the starting material. (c) 1MeV Bright Field TEM image of shocked olivine with amorphous patches (dark, no contrast) mixed with crystalline material of a high density of dislocations. (d) Electron diffraction pattern of the area in (c). Scales in micrometers [78].

Dislocation-free Si crystalline specimens were scratched on the chemically polished (001) surfaces by a diamond stylus along the [110] with a load of 2 g at the speed of 10 mm/s at room temperature. The damaged zone consisted of a small amorphous zone distributed in a crystalline region with dislocations by TEM (Figure 1.28) [79]. The transformation from crystalline to amorphous silicon was abrupt, creating a rough interface, while no polycrystalline layers or cracks were observed near the interface. Dents were not detected on the surface, nor cracks found near

the scratch and the amorphous phase remained after removing the load. The driving force for the phase transformation is mainly the hydrostatic stress under high pressure testing. It was proposed that the very high shear stress generated by scratching resulted in the amorphization of the diamond cubic structure of the silicon crystal.

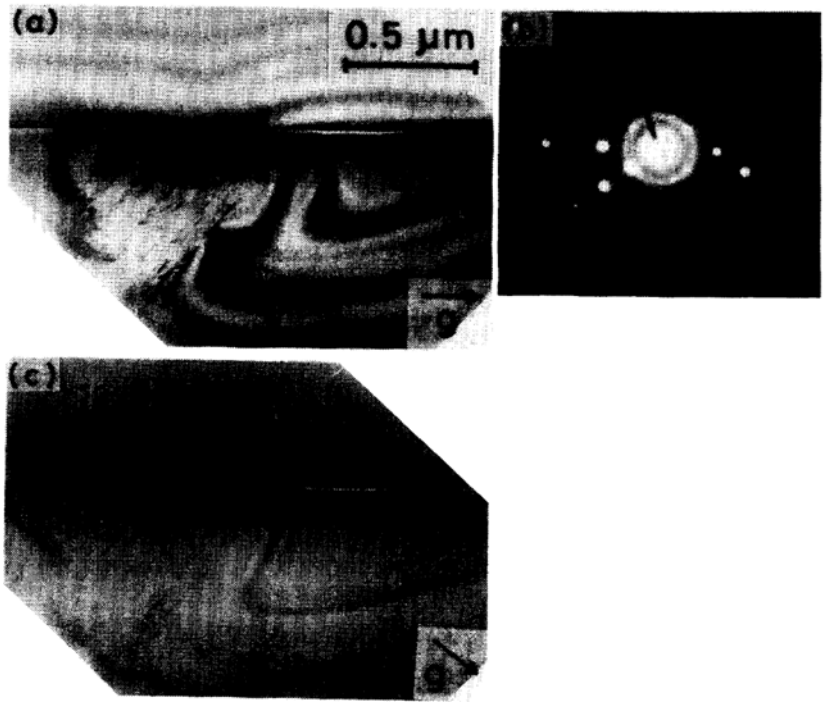

Figure 1.28 Cross-sectional TEM images of the damaged zone by scratching in Si. (a) diffraction vectors **g** [$\bar{2}$20] and (c) **g** [$\bar{2}$22]. (b) SADP of the damaged zone [79].

Figure 1.29 shows TEM images of how amorphization in α-quartz initiates with forming planar defects and continues by the propagation of amorphous silica phase at these defect sites [80]. The thickness of the amorphous lamellae ranges from 1 to 100 nm. Similar microstructures have been found in quartz subjected to quasi-hydrostatic and nonhydrostatic compression in diamond-anvil cells up to 40 GPa and from simple crushing as well. The geometric relationship between the crystalline and amorphous phases is consistent with the existence of a pressure-induced shear instability. The results suggest that there is a common deformation mechanism for

solid-state amorphization in static and shock compression, meteorite impacts, and deformation by tectonic processes in the earth interior.

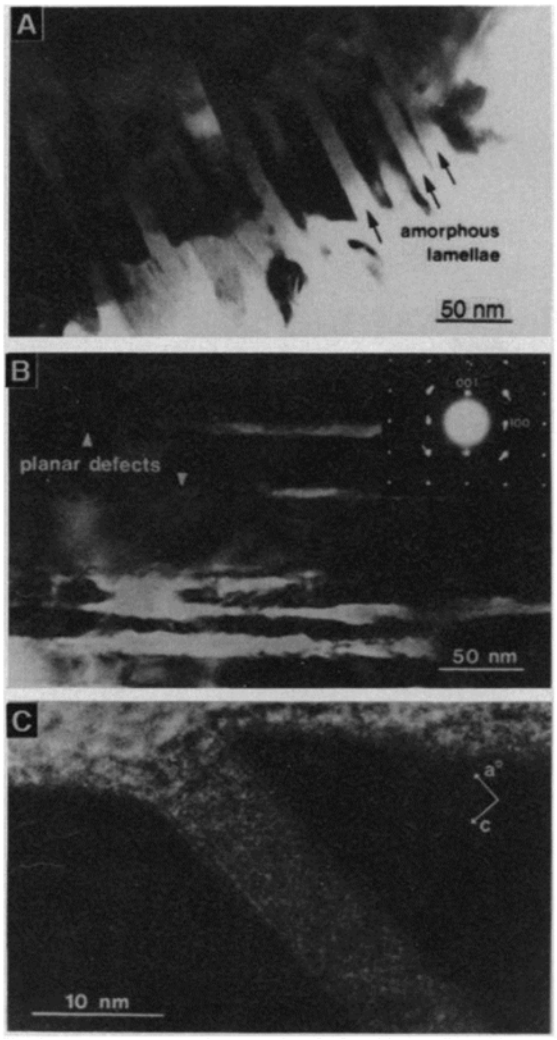

Figure 1.29 TEM images of stress-induced microstructures in quartz. Planar defects are bounded by quartz, and the thickness of amorphous lamellae ranges from 1 to 100 nm. (a) Bright-field image shows amorphous lamellae (light bands, three indicated) and crystalline phase (dark areas) by compression between 21 and 25 GPa. (b) Nucleation and propagation of amorphous lamellae (light areas) on planar defects. SAED inset shows streaking and multiple spots. (c) HRTEM of amorphous lamellae in a crushed particle [80].

Cristobalite and quartz are both polymorphs of silicon dioxide (SiO_2). While cristobalite completely amorphizes between 22 and 28 GPa, quartz fully amorphizes between 35 and 40 GPa [81]. Although lamellar amorphization is common in shock compression of quartz, it was not

detected in shocked cristobalite. Cristobalite is not available as large single crystals or aggregates, thus the experiments were performed on size-sorted powders with an average initial density of 62% encapsulated in a stainless-steel recovery capsule shocked by gas gun [81]. In Figure 1.30 (a), no evident Raman line shifts nor shock-induced features were found up to 22.9 GPa in cristobalite. TEM observations showed no sign of significant amount of glass. The decreased intensity and line broadening in the XRD and Raman spectra are probably due to the increase in twin density and extreme lattice bending. The specimen shocked at 28.2 GPa almost completely amorphized, with only less than 0.1% crystallinity. This specimen had a broader and weaker amorphous hump in XRD at $2\theta \approx 21^{\circ}$ (Figure 1.30 (b)), corresponding to a 0.40 nm interplanar lattice spacing. In contrast to shocked quartz, no distinctive shock-induced defects were observed in the shocked crystalline cristobalite grains. Figure 1.31 shows the interface between the crystalline and amorphous regions. Cristobalite amorphization did not follow twin boundaries, indicating twin strain energy did not have a large effect on amorphization. Both amorphous cristobalite and quartz have similar properties such as refractive indices and densities, as well as a similarly broadened Raman spectrum. They likely collapse to similar disordered structures under shock compression.

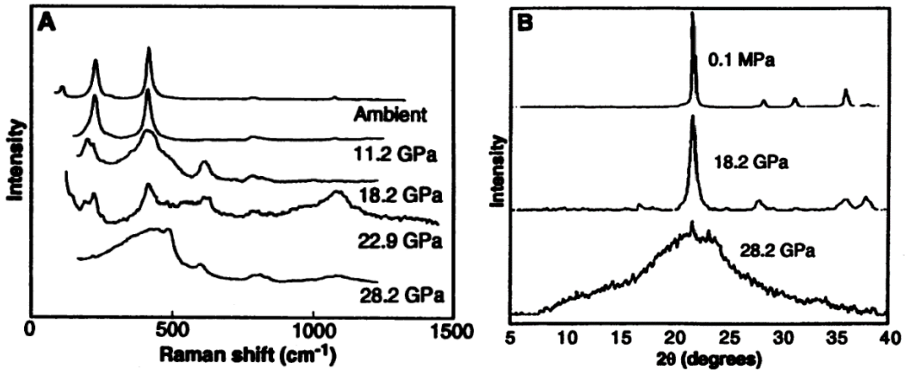

(a) (b)

Figure 1.30 (a) Raman spectra and (b) XRD patterns of cristobalite. Below 28.2 GPa, no significant line shifts or signs of amorphization in Raman or XRD with only a broadening and weakening of the characteristic peaks. At 28.2 GPa, broadened Raman lines and an amorphous hump in XRD pattern, indicating amorphous phases formed [81].

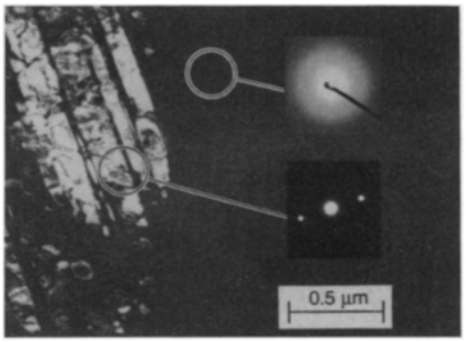

Figure 1.31 Crystalline-amorphous border in cristobalite shocked at 28.2 GPa. Diffraction patterns show the sharp contrast between crystalline and amorphous regions separated by boundary of a few hundred nanometers. No amorphous lamellae are observed, which typically exist in shocked quartz [81].

Another study investigated single crystals of α-quartz and α-berlinite ($AlPO_4$) compressed at different pressures at room temperature in a diamond anvil cell (DAC) [82]. Single crystal thin foils ~30 µm thick of quartz and berlinite were optically polished before compression of different crystal orientations in DAC. There is a large pressure gradient, from ambient pressure at the rim to more than 30 GPa in the center. In quartz, the rim region remained crystalline with no signs of plasticity up to 5 GPa but some thin straight 10 nm amorphous lamellae were observed. At 10 GPa, quartz transformed to a two-phase mixture: the crystalline matrix had microcracks with inhomogeneous density, with the second phase thicker and more densely arranged lamellae with 50-60 nm thickness (Figure 1.32 (a)). Above 15 GPa, regions close to the center of the samples were mostly amorphous (Figure 1.32 (b)). The crystalline regions were characterized by the bend contours and gradually vanished at the boundaries (Figure 1.32 (c)). Upon release, radial cracks formed. TEM images (Figure 1.32 (d) and (e)) show veins filled with amorphous silica throughout the area. Berlinite was more ductile than quartz, with abundant dislocation activity induced by DAC. The recovered samples were heavily fractured, and diffraction patterns with spots and radial streaking indicated slightly (up to ~ 10º) misoriented domains (Figure 1.33 (a)). The diffuseness around the spot indicated that amorphization might occur. Indeed, thin amorphous lamellae were

detected at lower pressures (2-5 GPa) in Figure 1.33 (b). At larger pressures (5-10 GPa), thicker amorphous lamellae were observed. Above 10 GPa, most of the material was amorphous and slabs with sharp crystal-amorphous boundaries (Figure 1.33 (c)) were formed. For quartz, this led to a two-stage amorphization process where shear lamellae first nucleated, then amorphized by the mechanical instability in the crystal. For berlinite compressed at certain crystal direction, optical microscopy exhibited a large density of straight and thin lines throughout the specimen (Figure 1.33 (d)). TEM showed that these lines were actually plastic slip lines caused by substantial dislocation density of up to 5×10^{13} m^{-2} (Figure 1.33 (e)). At about 10 GPa in berlinite, thick amorphous lamellae developed in the densely dislocated area, and eventually coarsened to complete amorphization. The lamellae orientation appeared to be crystallographically controlled and nucleated along planes with high shear stress because some of them became weakened under the shear stresses induced by the high pressure in both samples.

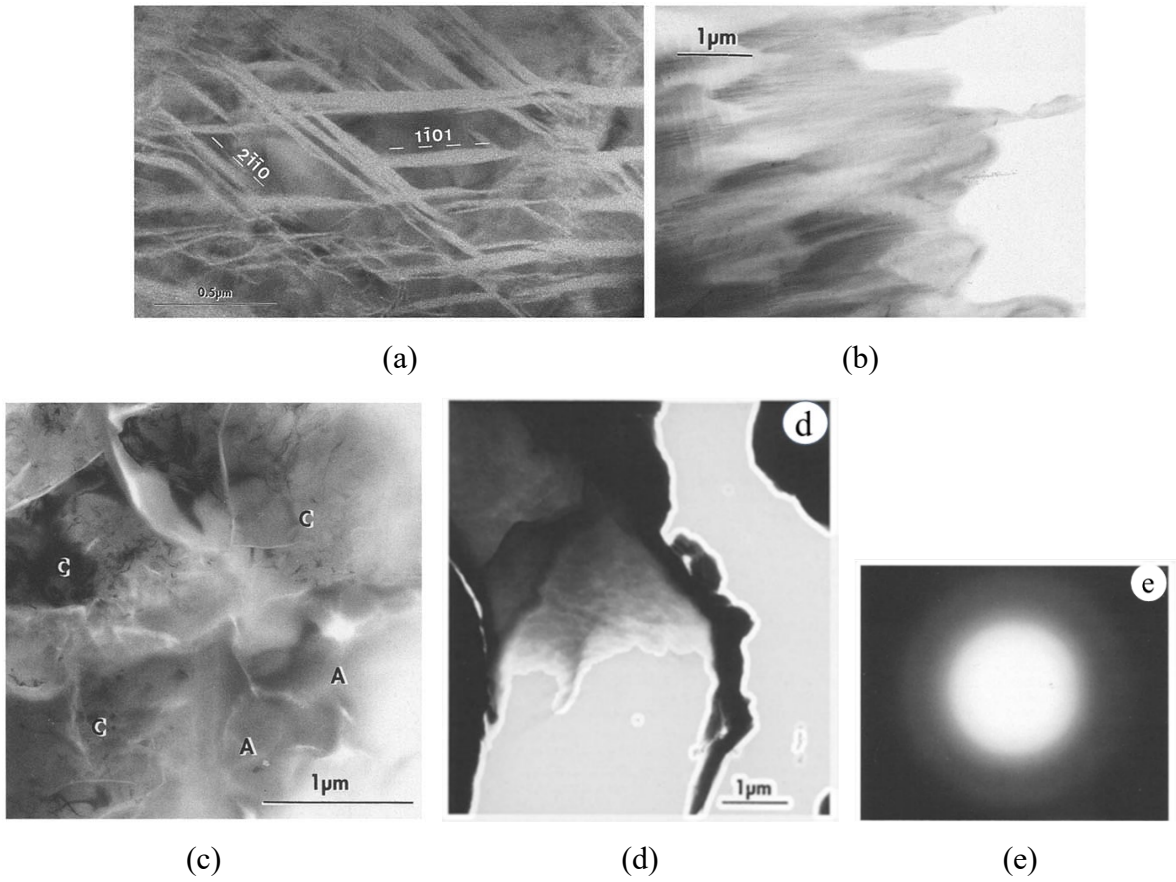

(a) (b)

(c) (d) (e)

Figure 1.32 TEM micrographs of quartz. (a) Dark field image. Amorphous lamellae appear in white. (b) Bright field image. Completely amorphized region. (c) Transition zone between amorphous and crystalline phases. Crystal region is characterized by the bend contours that vanished at the crystalline-amorphous boundaries. "C" for crystalline and "A" for amorphous. (d) Bright field image. Amorphous region with a radial crack. (e) Diffraction pattern of (d) [82].

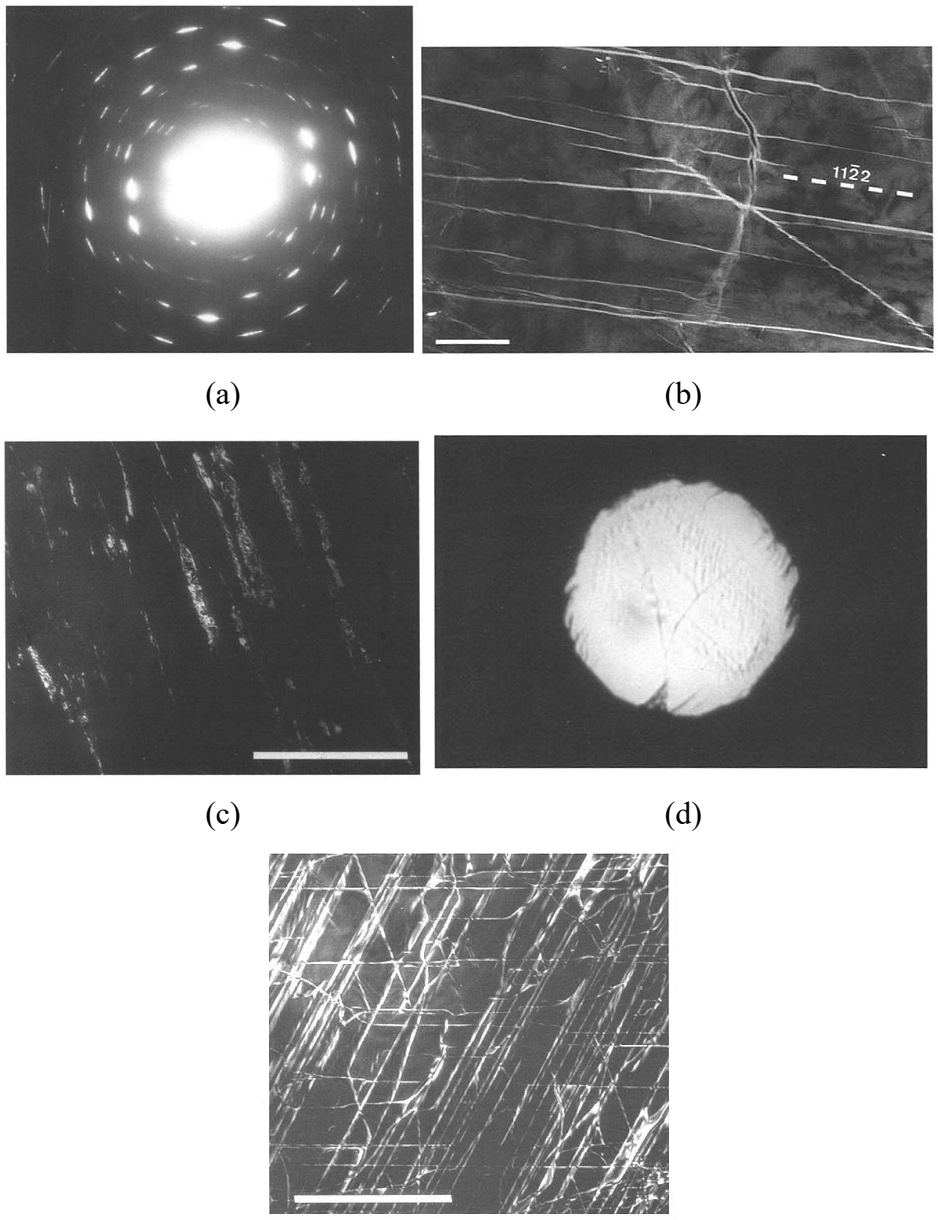

Figure 1.33 TEM micrographs of berlinite. (a) EDP shows misoriented domains with diffraction spots surrounded by radial streaking. The diffuse central spot indicates the presence of amorphous phase. (b) Dark field image of thin amorphous lamellae with amorphous zone in white. Scale bar: 0.5 μm. (c) Dark field image of largely amorphized area with crystalline zone in white. Scale bar: 1 μm. (d) Optical microscopy image. (e) Dark field image of dislocations. Scale bar: 1 μm [82].

The mineral wollastonite ($CaSiO_3$) was found to amorphize at a pressure of 25.6 GPa at 300 K [83]. Energy dispersive x-ray diffraction and Raman spectroscopy results showed the behavior of $CaSiO_3$. At high pressure and high temperature, the phase transition from crystalline

wollastonite to perovskite was kinetically inhibited; therefore amorphization occurred instead (Figure 1.34). It was also found that the perovskite phase $CaSiO_3$ became amorphous when released from high temperature and high pressure conditions. The activation energy barrier for this transformation prevented the formation of the wollastonite phase upon pressure release.

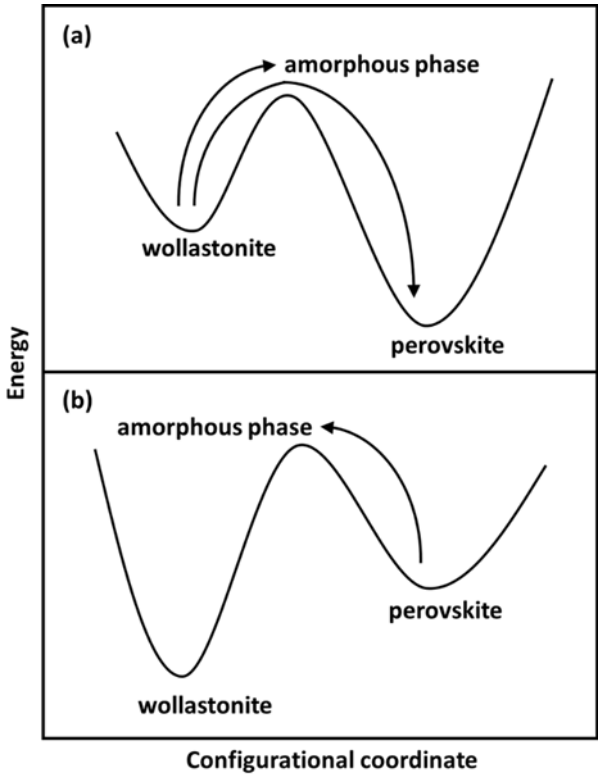

Figure 1.34 Energy vs configurational coordinate diagram of the relative stabilities of the wollastonite and perovskite phases of $CaSiO_3$. (a) At pressures> 17 GPa, perovskite is stable. Wollastonite transforms to perovskite at high pressures and high temperatures, indicated by the long arrow. (b) At ambient pressure, wollastonite is stable. When release the pressure and at ambient temperature, perovskite becomes amorphous because the transformation to wollastonite is inhibited, indicated by the short arrow in (b) [83].

Serpentine, a common rock-forming hydrous magnesium iron phyllosilicate ($(Mg,Fe)_3Si_2O_5(OH)_4$) mineral, was observed with synchrotron radiation to undergo pressure-induced amorphization at 14 to 27 GPa and 200°C to 300°C in a multianvil apparatus (Figure 1.35) [84]. When the temperature increased to 400°C the mineral samples rapidly crystallized into high-pressure phases. This transformation is likely enhanced by high differential stress, which is similar

to the effects of shear stress upon pressure-induced phase transitions found in olivine. It was concluded that amorphization of serpentine was unlikely a mechanism leading to deep-focus earthquakes because the temperature of subducting slabs was much higher than the temperature at which the rapid crystallization was observed in these experiments [85].

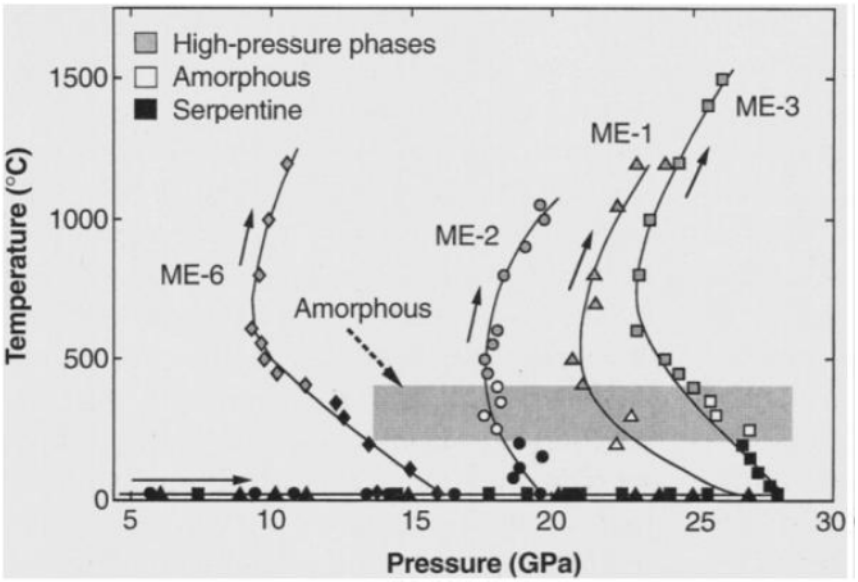

Figure 1.35 Summary of the experiments on the amorphization of serpentine. Amorphous zone indicates the T-P conditions where amorphization of serpentine was observed with no high-pressure crystalline phases formed. Initial materials were Antigorite for ME-1, ME-2 and ME-6, and lizardite for ME-3 [84].

Chen et al. [86] were the first to observe shock-induced amorphization in boron carbide (B_4C) during ballistic testing. Armor-piercing projectiles with velocities between 750 and 1000 m/s impacted the B_4C composite laminates, producing pressures between 19 and 25 GPa. TEM micrographs (Figures 1.36 and 1.37) show the impact tests results at 907 m/s (23.3 GPa) and 793 m/s (20.3 GPa), respectively. At higher impact velocity and pressure, amorphous bands were observed, while at lower velocity and pressure, planar faults such as microtwins and stacking faults were found instead of amorphous zones. These bands were 1 to 3 nm thick and only one band was observed in each grain, suggesting the complete amorphization was not achieved. Higher pressures may be required to complete the amorphization process, but the ballistic loading and resulting

release of compression appeared to impede this process. The amorphous bands aligned closely with cracks and the uncracked bands extended into the B_4C grains, indicating that these amorphous zones may serve as crack paths for cleavage-like failure.

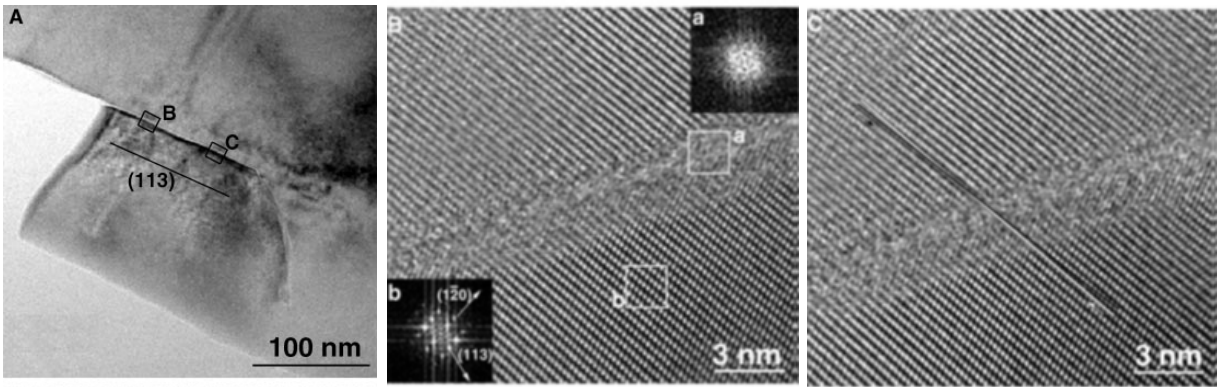

Figure 1.36 TEM images of B_4C fragment produced by ballistic test at 907 m/s (23.3 GPa). (a) Bright-field image shows a planar defect from a corner of the fracture surface. (b) HRTEM image of the amorphous band and surrounding region in (a). The lattice corresponds to [101] direction of crystalline B_4C. The loss of lattice fringes in the band indicates localized amorphization. FFT inset patterns also confirms the presence of an amorphous phase. (c) HRTEM image of the boxed area C in (a). The width and appearance of the amorphous zone are the same as in (b). Arrows represent sight lines of lattices across the band. Misalignment of the lattice fringes on two sides of the amorphous band was 1°, ruling out rebonding of two cracked surfaces. Absence of observed melting indicates this amorphization was a solid-state transition caused by development of a shear instability and elastic collapse of the lattice due to the high pressure and impact rates of the ballistic test [86].

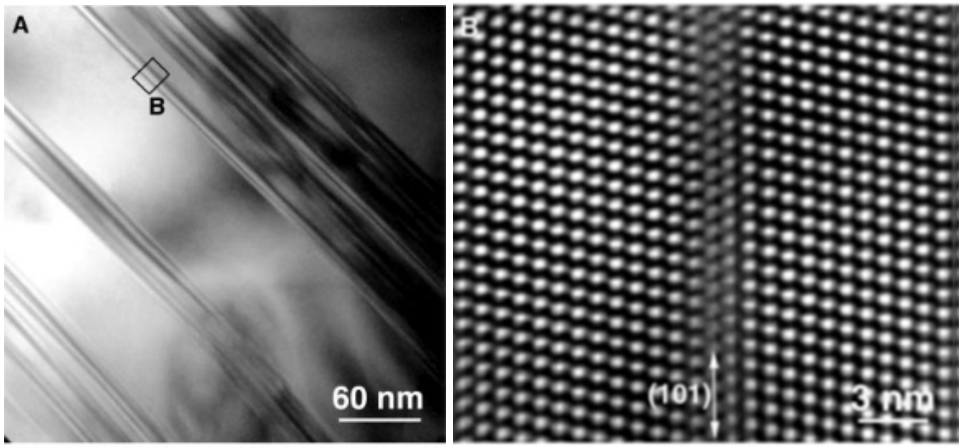

Figure 1.37 Boron carbide fragments produced by ballistic impact at 793m/s (20.3 GPa). (a) Bright-field TEM image showing planar defects. (b) HRTEM image of the area marked in (a) shows that these planar defects are microtwins and stacking faults. As the impact velocity was subcritical, no amorphous bands were formed [86].

Another study on B_4C used quasistatic indentation to generate amorphization. Fine metallographic polishing and Raman spectroscopy were combined to measure the spatial distribution of the amorphous zone under Vickers indentation (Figure 1.38) [87]. The maximum amorphization intensity occurred just beneath the contact surface and decreases farther from the center The amorphized zone was significantly smaller than the plastic zone, indicating that the threshold stress to initiate amorphization is higher than that for plastic deformation. It was argued that the amorphization in B_4C under a sharp indenter undermines the accuracy of its true crystalline strength as the area under the indenter immediately amorphizes upon contacting the indenter resulting in the measurement of a mix of amorphous and crystalline phases. The measured hardness values are lower than the true values for boron carbide because the amorphous B_4C is weaker and less resistant to penetration than the crystalline B_4C.

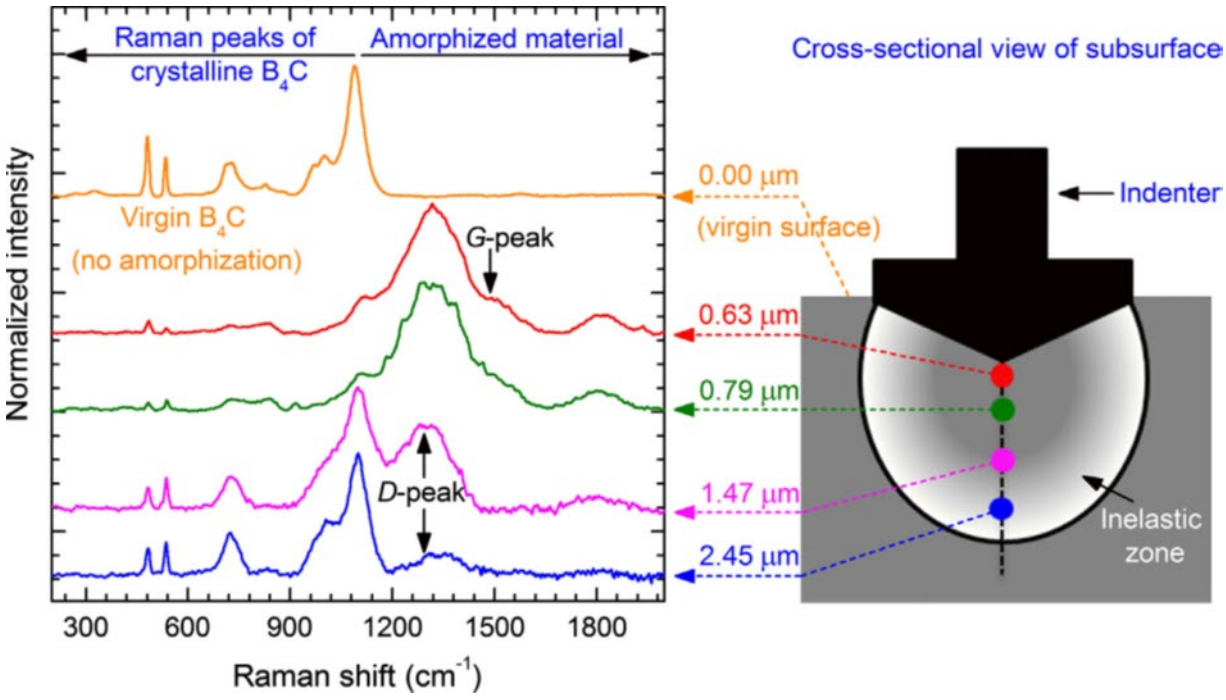

Figure 1.38 Raman spectra from the original surface and subsurface regions at different depths after Vickers indentation in B_4C of a 0.98 N load. The intensity of amorphization is the maximum directly beneath the indenter and decreases deeper into the sample [87].

Although boron carbide has many superior mechanical properties, pressure-induced amorphization can disturb its crystalline order and weaken its shear strength [88]. Figure 1.39 shows TEM observations of amorphous bands and a crack beneath indentation on a B_4C sample. Dislocations and lattice rotation were found near the amorphous zones. When grain sizes were refined, the tendency for amorphization was reduced, providing a potential method to minimize the effects of amorphization in B_4C.

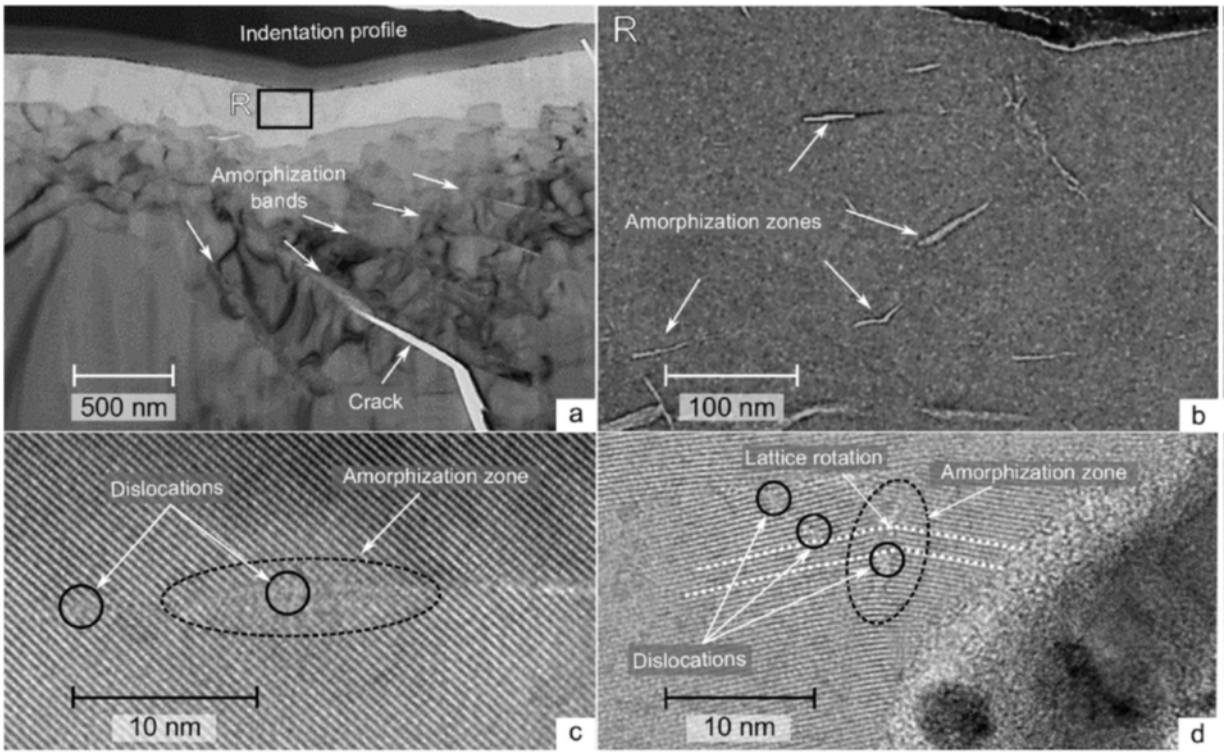

Figure 1.39 TEM of amorphous zones generated by indentation in B_4C. (a) Thin and micrometer-length amorphous bands and a crack beneath the indented surface. (b) Magnified region (R) showing several nanometer-sized amorphization zones. (c) and (d) Higher magnifications at the amorphous zones in (b). Dislocations and lattice rotation in the vicinity of amorphous zones. Solid circles indicate lattice dislocations [88].

Another study on B_4C examined the failure state related to stress-induced amorphization [89]. Microscopic observations showed that the shear localized amorphization normally coexisted with stacking faults and twins. HRTEM micrographs (Figure 1.40) support the amorphization deformation mechanism in B_4C and can probably be extrapolated to other ultrahard covalent

materials. Dislocations have lower energy barrier for nucleation than that of the first-order phase transition; creating new dislocations or stimulating existing ones under high nonhydrostatic pressures is favored. Dislocation movements due to conventional lattice sliding were prevented by strong covalent bonds, and instead amorphization was initiated at the highly distorted symmetry-breaking dislocation cores. Figure 1.41 is an illustration of this dislocation-mediated amorphization in B_4C, rather than direct phase transition from crystalline to amorphous structures. The measured activation volumes, activation energies, and nucleation rates of two single-crystal B_4C samples were consistent with those of dislocation nucleation and significantly lower than that of the crystalline-amorphous phase transition. This mechanism could facilitate understanding failure in other ultrahard covalently-bonded materials under extreme loading conditions.

The combined results of the studies discussed above suggest that these localized amorphous bands can be another mechanism for high-rate deformation in B_4C and other materials.

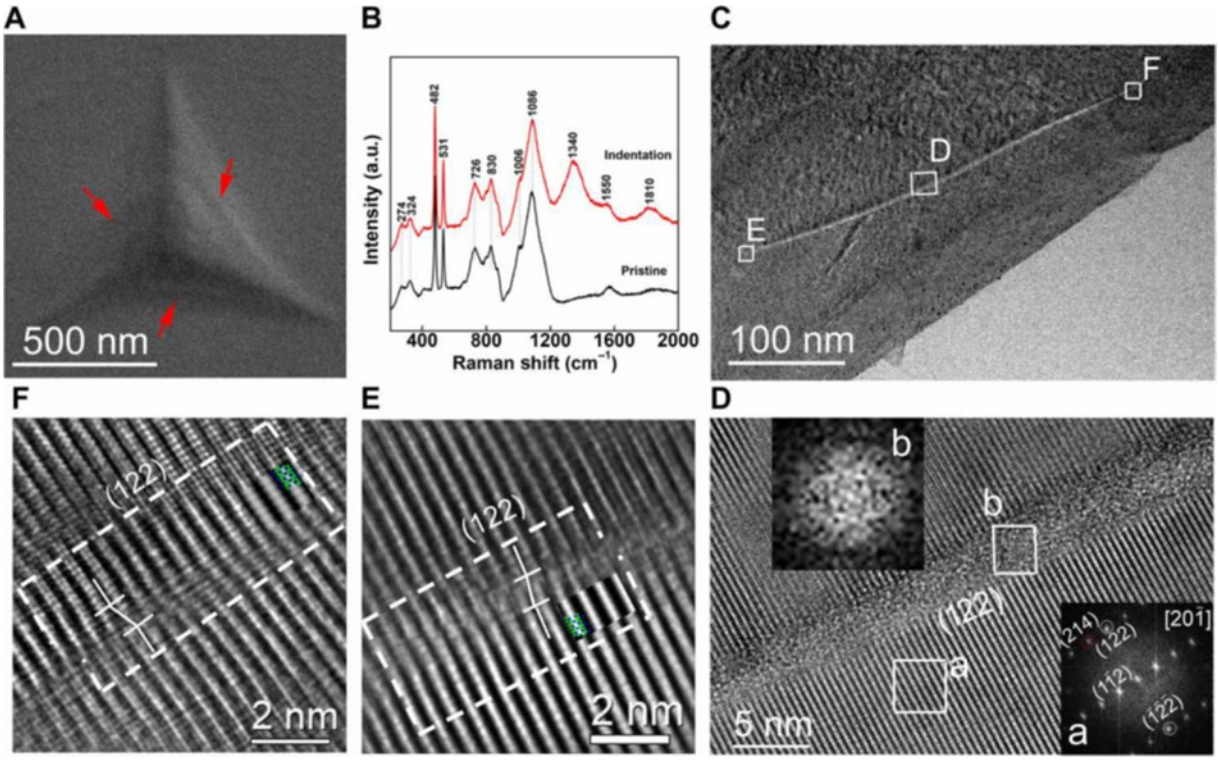

Figure 1.40 Characterization of (214) single crystal B_4C after nanoindentation. (a) Scanning electron microscopy (SEM) image of nanoindentation after 25 mN load. No cracks observed. (b) Raman spectra of initial sample (black curve) and indented (red curve) of samples. Extra peaks at 1340, 1550, and 1810 were found in the indented sample, corresponding to the characteristic Raman modes for amorphous B_4C. (c) TEM image the cross section of indented region showing a shear band with ~300nm length and ~1-4nm width. (d) HRTEM of boxed area D shows the lack of crystal lattice within the shear band along the (122) plane. FFT (inset b) within band showed the amorphous diffuse halo ring, compared to the FFT (inset a) of the crystalline material on either side of the $[20\bar{1}]$ zone axis. (e) HRTEM image shows the shear displacement at the origin and the tip of the amorphous shear band. (f) HRTEM image of the terminal end of the amorphous band showing the shear displacement. The shear displacements in both (e) and (f) can be characterized by a pair of dislocation dipoles [89].

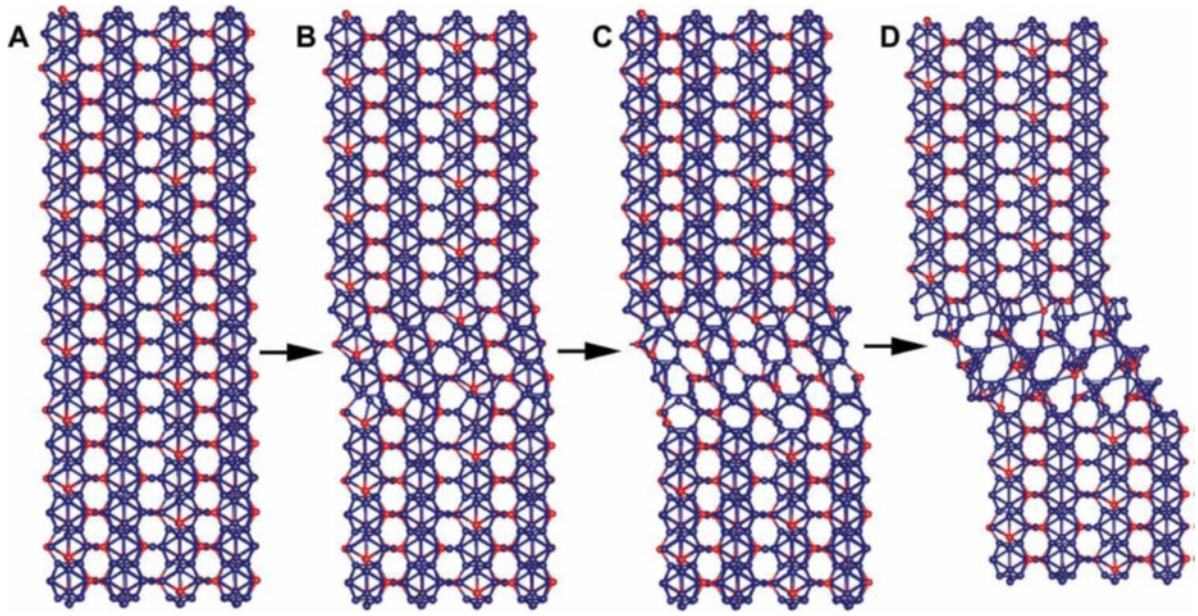

Figure 1.41 Diagrammatic representation of dislocation-mediated amorphization in B_4C. (a) Perfect lattice before deformation. (b) Shear deformation distorted the perfect crystal. (c) Dislocation kink formed by shearing. (d) Amorphization developed from dislocation under shear deformation [89].

Reddy et al. [90] reported shear-induced localized amorphization in boron suboxide generated by nanoindentation. The amorphous bands were orientated along the $(0\ \bar{1}\ 1\ 1)$ crystal plane and had widths between 1 and 3 nm and lengths between 200 and 300 nm. Figure 1.42 shows the STEM images of B_6O under the indented regions, with crack regions and shear bands indicated by black and white arrowheads. Many dislocations, rarely seen in the initial samples, were found near the deformation bands and microcracks, indicating that they likely play a role in the deformation process. The FFT pattern exhibited a diffuse halo, confirming the amorphous nature of the shear band. Inherent defects usually cause brittle failure of covalently-bonded materials with little plasticity. However, under extreme loading conditions such as shock or indentation, cracking is inhibited, and the material deforms through dislocation plasticity or phase transitions. Super-hard materials such as diamond, B_4C and B_6O have high Peierls stresses due to their strong covalent bonds, substantially inhibiting dislocation motion at low temperatures and leading to low

fracture toughness. Even when crack propagation is inhibited it is difficult for these materials to deform plastically due to the inflexible covalent bonds. They may slip with dislocations and shear on relatively weak atomic planes, resulting in localized shear amorphization from the break in the local order and translational symmetry. The brittleness is not because of the rigid bonds breaking but shear-induced structural instability. While in other materials shear deformation usually produces plastic strains and reinforces a material's ductility, in highly anisotropic materials the sliding along weakly bonded crystallographic planes results in a collapse of the local structure and even failure.

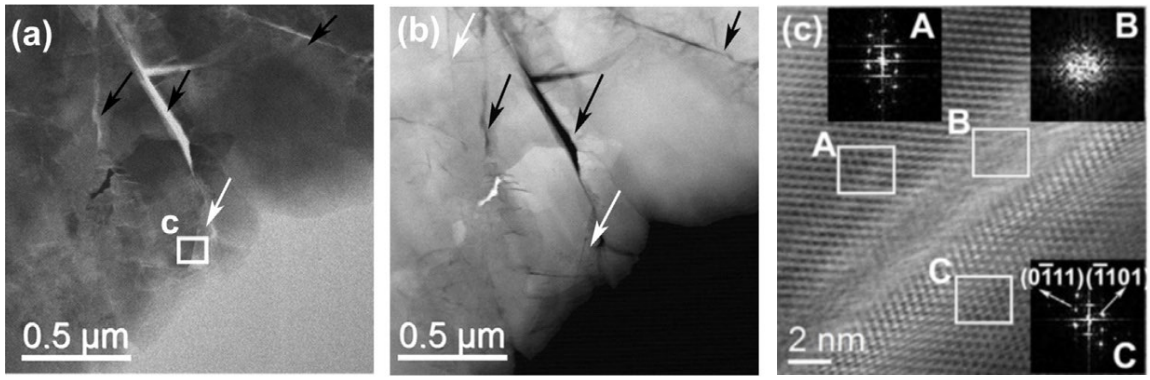

Figure 1.42 STEM images of boron suboxide (B_6O) subjected to nanoindentation. (a) Bright-field and (b) Dark-field micrographs show cracks (black arrowhead) and shear bands (white arrowhead) under the indented region. (c) Magnified BF-STEM image of the amorphous band along the (0 $\bar{1}$ 1 1) direction (inset FFT pattern A). The loss of lattice fringes indicates the amorphization (inset FFT pattern B) [90].

Glassy carbon subjected to 50 GPa at room temperature in a diamond anvil cell and subsequently heated in situ via laser to 1800 K converts into transparent "quenchable amorphous diamond" [91], which remains recoverable at ambient condition. Nanocrystalline diamond was observed at temperatures above ~2100 K. The initial glassy carbon was composed of randomly orientated fragments of curved carbon sheets. The high pressure and low temperature condition supply the energy for the sp^2-to-sp^3 transition. The resulting local tetrahedral structure cannot form long-range tetrahedral order due to the low temperatures but forms the sp^3-bonded amorphous

diamond structure instead. During laser heating, when the sample transformed to transparent amorphous diamond, the temperature immediately decreased as a result of the poor laser absorption of the transparent phase, suppressing high temperature annealing which would lead it to the return to a crystalline phase. XRD, HRTEM (Figure 1.43), and electron energy-loss spectroscopy (EELS) were used to confirm the material's sp^3 bonding state and amorphous structure. This transparent amorphous diamond has the highest known density of amorphous carbon materials, with elastic stiffness comparable to crystalline diamond. The amorphous diamond was an isotropic, dense, transparent, super strong, and possibly superhard material.

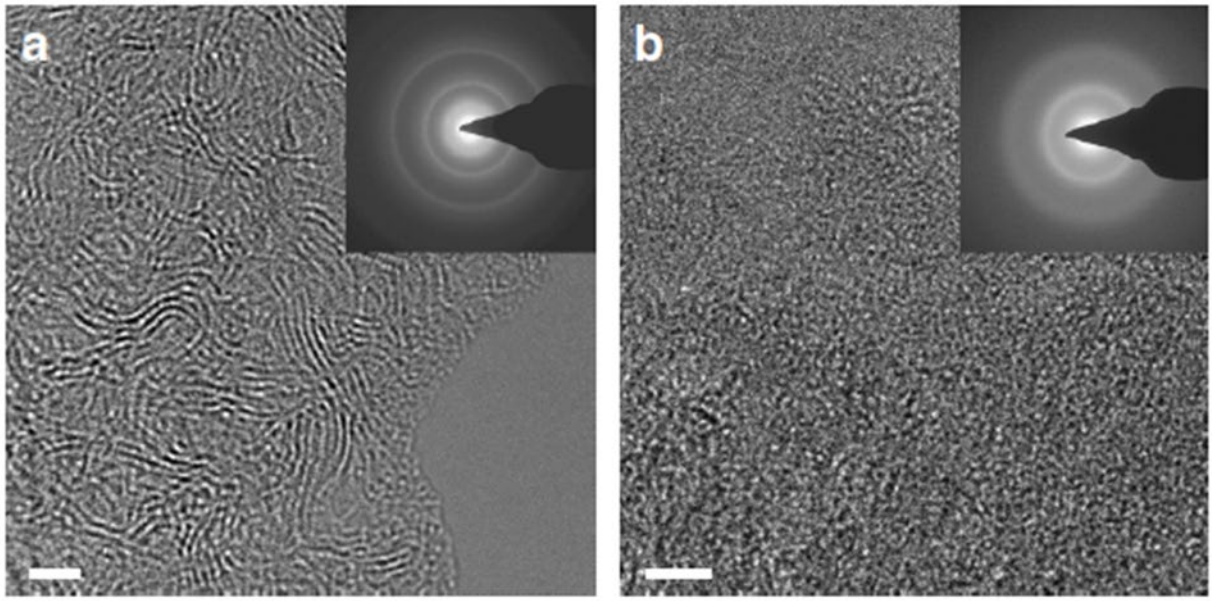

Figure 1.43 TEM images of amorphous diamond produced by high pressure and in situ laser heating from glassy carbon. (a) HRTEM and selected area electron diffraction (SAED) patterns of glassy carbon (b) HRTEM and SAED images of the recovered amorphous diamond confirm its disordered amorphous nature. The scale bars in (a) and (b) are 2 nm [91].

Amorphous diamond with sp^3 bonding was also formed by laser heating glassy carbon at 50 GPa in DAC or shock compression of C_{60} to 55 GPa and 2,000 K. By compressing C_{60} at about 27 GPa and 900–1000 °C, millimeter-sized amorphous carbon nearly completely sp^3-hybridized was produced [92]. XRD patterns of carbon samples subjected to 20–27 GPa at 1000 °C show two

broad and diffuse peaks, different from those of the starting fcc C_{60} precursor. Electron energy loss spectroscopy (EELS) spectra also confirms the sp^3-hybridized nature of the sample. Figure 1.44 (a) is a low-magnification TEM micrograph of the jagged edge of an amorphous carbon sample, which has a similar fracture behavior to bulk glass. Figure 1.44 (b) shows the HRTEM image of three-dimensionally organized carbon atoms with no long-range order. Amorphous features are characterized by diffuse halos of SAED patterns in the inset. In Figure 1.44 (c), the inverse FFT of the HRTEM image shows many medium-range order (MRO) clusters randomly distributed in the sp^3 matrix, indicated by the orange boxes. The white dashed lines mark the 'crystal-plane-like' fringes of MRO structures similar to crystalline diamond in the inset. A larger interplanar spacing of ~2.2 Å than that of diamond (2.06–2.19 Å) reveals lattice distortion in the sample. The phase transition from collapsed fullerene to sp^3 amorphous carbon by heating is achieved by changing pressure and temperature conditions. Rapid quenching (about 500 °C s^{-1}) is also crucial to synthesize high-quality sp^3 amorphous carbon. In this study, the isotropic sp^3 amorphous carbon exhibits superior mechanical and physical properties, making it a potential candidate in different fields for amorphous solids.

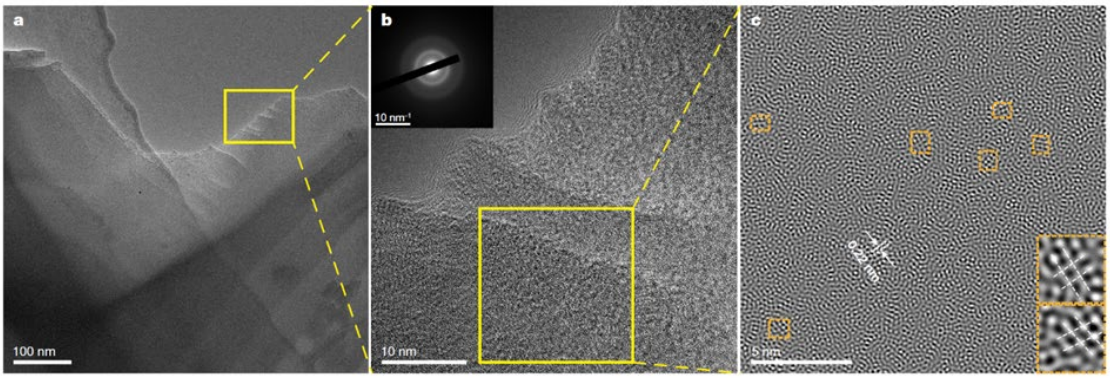

Figure 1.44 TEM images of the amorphous diamond sample. (a) At low magnification. (b) HRTEM image of the yellow boxed region in (a). Inset is the corresponding SAED pattern. (c) Inverse FFT image of the yellow boxed area in (b). Orange boxed regions exhibit randomly oriented MRO clusters of interplanar spacing of ~ 2.2 Å similar to that of diamond. Insets show diamond-like intersecting angles between the 'crystal-plane-like' stripes [92].

Paracrystalline diamond has a well-defined crystalline medium-range order (MRO) of a few atomic shells. The paracrystalline state of diamond is distinct from both the crystalline or amorphous structures, consisting of sub nanometer crystals. It can be prepared with fcc C_{60} under high pressure and high temperature conditions [93]. The paracrystalline diamond is formed due to intensive nucleation sites in compressed C_{60} and by the second-nearest-neighbor short-range order of sp^3 bonding in amorphous diamond. Nanosized paracrystallites were distributed in the amorphous matrix as the crystalline MRO. In this study, an fcc fullerene C_{60} was compressed to 30 GPa at 1200–1800 K. HRTEM images show no long-range order nor lattice fringes, suggesting the disordered structure of the samples at about 1 nm (Figure 1.45). Its amorphous nature is confirmed by the diffuse haloes in the FFT patterns. HRTEM images reveal a large number of ordered clusters of 0.5–1.0 nm size for samples annealed at 1400–1600 K. Lattice fringes approximately along the [110] and [010] zone axes of cubic and hexagonal diamond are identified within a 1 nm scale. The FFT patterns of the selected regions match cubic and hexagonal diamond, although both are highly distorted as indicated by the deviation of inclusive angles. The morphology of this paracrystalline diamond is different from amorphous diamond, characterized by the dominant formation of crystalline MRO clusters. Continuous random network type amorphous diamond has strong short-range order in the first two atomic shells, which substantially helps the development of MRO and diamond paracrystallites. The orientational sp^3 bonds between C_{60} units provide abundant nucleation sites, and the single-walled carbon nanotubes with well-arranged carbon bonds may supply sufficient sp^3 bonding sites for the formation of paracrystalline diamond. The unique MRO structures of paracrystalline diamond contribute to new mechanical and physical properties and oxidation resistance, suggesting potential new applications for ultrahard materials.

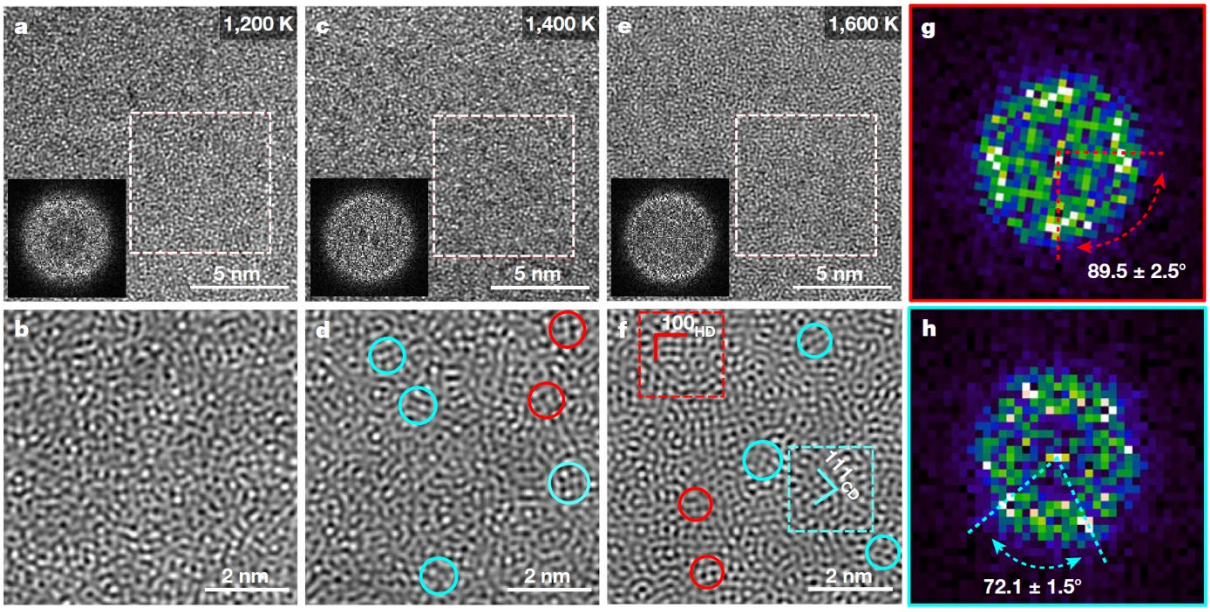

Figure 1.45 HRTEM micrographs of diamond samples recovered from 30 GPa and 1200 to 1600 K. (a)–(f), HRTEM images and corresponding inverse FFT images. Insets are FFT patterns of the white boxes (7.0 × 7.0 nm^2) in (a), (c) and (e). The cyan and red circles in (d) and (f) exhibit some of the MRO clusters. In (f), the lattice fringes marked by the cyan and red solid lines match (111) and (100) crystal planes of cubic and hexagonal diamond. (g) and (h) are FFT patterns of the red and cyan boxes (2.0 × 2.0 nm^2) in (f). The brighter spots on these diffuse haloes marked by the arrows confirm cubic and hexagonal diamond like MRO clusters in (f) [93].

Four covalently bonded materials (Si, Ge, SiC, and B_4C) were shocked using high energy lasers by Zhao et al. [94,95]. All four solids exhibited amorphization at pressures above certain thresholds. These four materials all have a negative Clapeyron slope, with the liquid having a higher density than the solid phase. The same effect should apply to amorphization, which is aided by both hydrostatic compression and shear. The rationale proposed by Patel and Cohen [96] and further developed by Levitas [97] was applied to the amorphization and the thermodynamics was explained. The post-shock TEM images (Figure 1.46) reveal that the newly formed amorphous materials have a shear band like morphology, which suggests that shear stress dominates this process. The threshold for amorphization depends on the strength of the material. The thickness of these shear bands is in the nanometer range, compatible with the extreme short durations of the shock pulses created by lasers (1-3 ns).

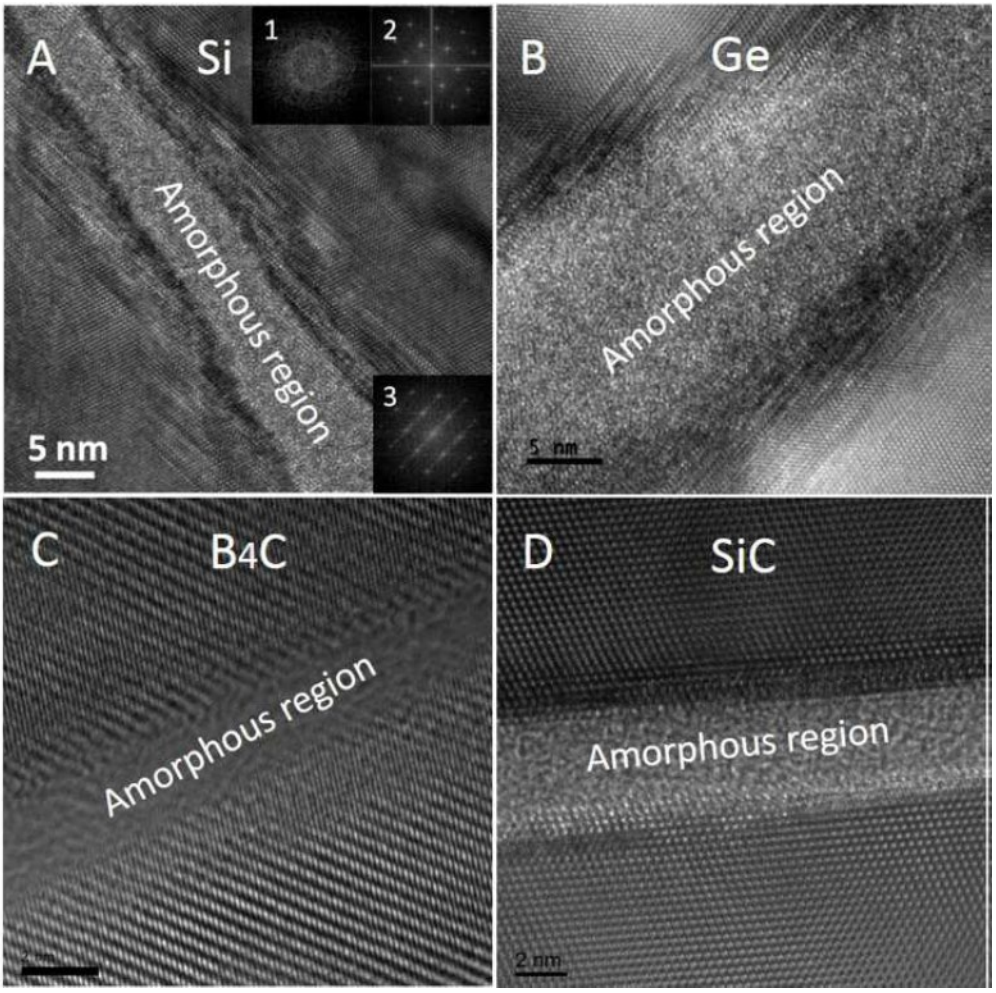

Figure 1.46 HRTEM images of amorphous bands in four covalently bonded solids: (a) Si, (b) Ge, (c) B_4C, and (d) SiC. High density of stacking faults was found at the interface between crystalline and amorphous phases in Si and Ge while not at the interface in B_4C and SiC [94].

The mechanical coupling between Earth's lithosphere and asthenosphere depends on the mechanical properties of olivine-rich rocks of its upper mantle. In conventional crystalline materials, dislocation motion plays an essential role in plastic deformation. However, olivine does not have sufficient slip systems to accommodate all the strain conditions; thus, supplementary deformation mechanisms are required. Figures 1.47 and 1.48 [98] show that in forsterite, the magnesium-rich end member of olivine solid solution series, amorphization form at grain boundaries under static compression; the onset of its ductility was attributed to the activated

mobility of grain boundaries in these amorphized layers. This could be one mechanism for plastic deformation of rocks deep within the Earth where such high stress conditions occur.

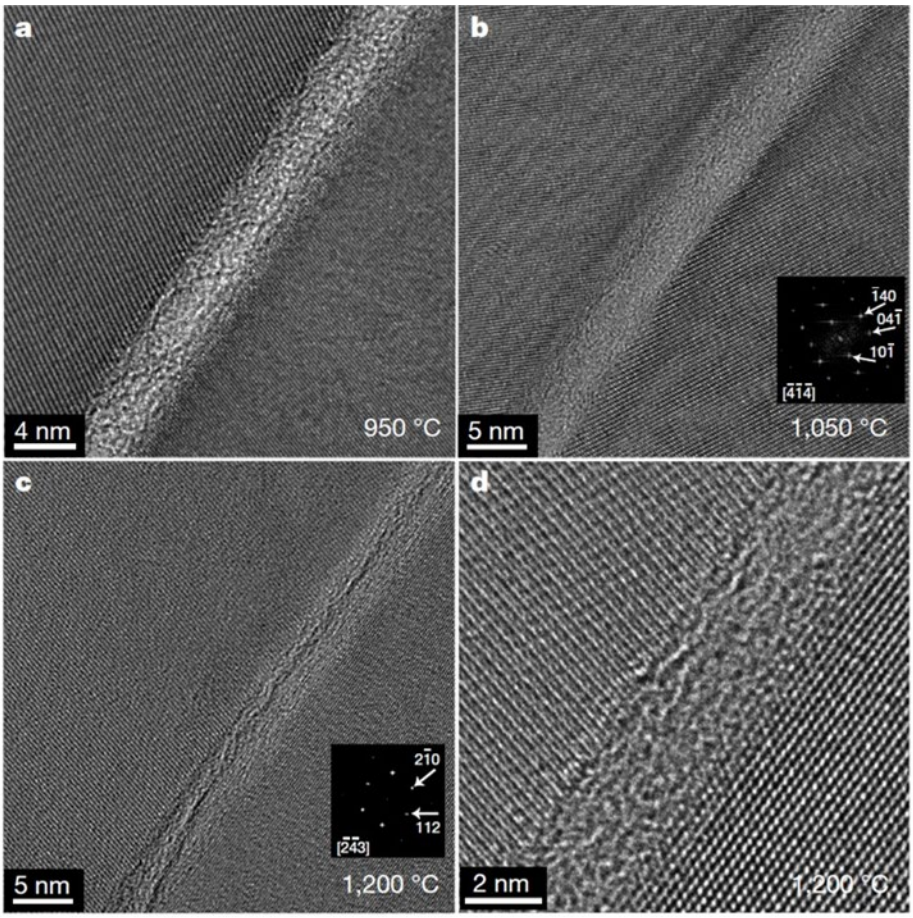

Figure 1.47 HRTEM images of two different grain boundaries in forsterite specimens by static compression in a Paterson press at 0.3 GPa at (a) 950°C, (b) 1050°C, (c) and (d) 1200°C. At 950 and 1050°C boundaries show presence of intergranular amorphous layer. At 1200°C amorphous layers were still present but much less frequent, about ten times less. FFT insets of (b) and (c) confirm the crystal structure of forsterite [98].

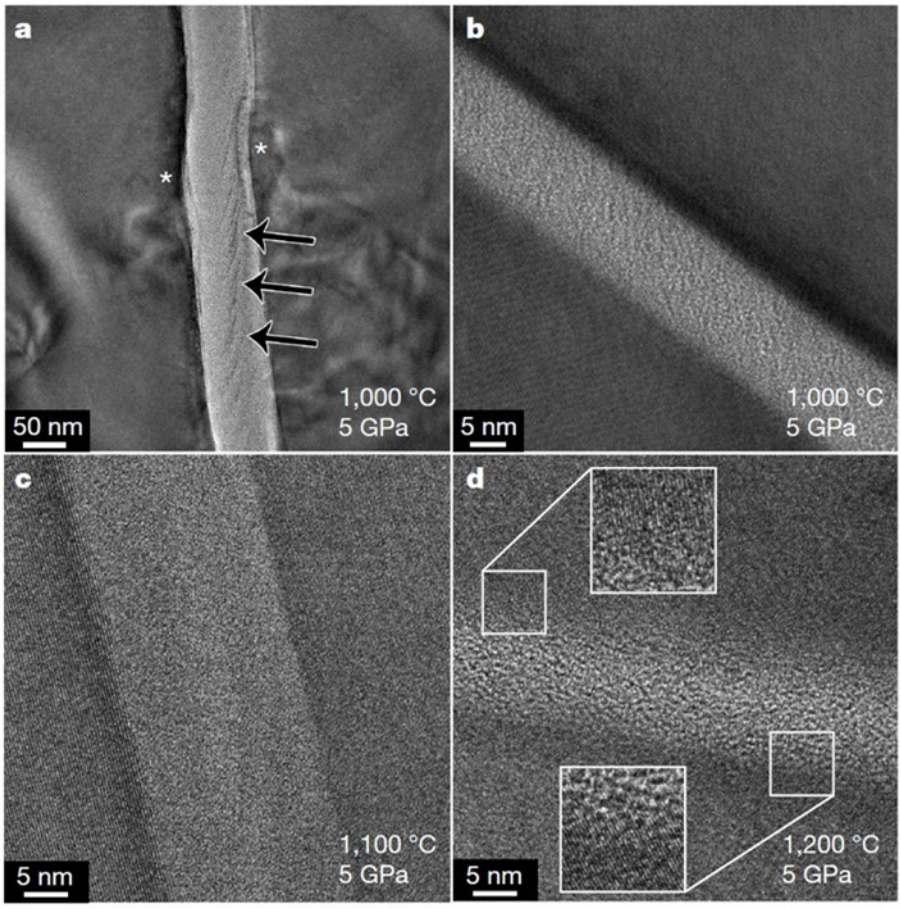

Figure 1.48 HRTEM images of forsterite specimens by static compression in the multi-anvil press. (a) 5 GPa, 1000 °C. (b) 5 GPa, 1000 °C. (c) 5 GPa, 1100 °C. (d) 5 GPa, 1200 °C. (a) The asterisks indicate the displacement of the amorphous lamella; the black arrows denote shear bands. Insets in (d) show maginified views of the glassy film and lattice interface [98].

1.1.5 Amorphization in ionic materials

Several ionically bonded compounds exhibit amorphization. Among them, $Ca(OH)_2$, commonly used to produce lime aggregate (by adding sand) and as a flocculant in the food industry, and resulting from the reaction of CaO and water, is attractive. Static compression of this simplest structure, among hydrous minerals, produces amorphization. $Ca(OH)_2$ portlandite samples were compressed up to 37.6 GPa in a diamond anvil cell at room temperature [99]. In Figure 1.49, between 10.7 and 15.4 GPa, the x-ray scattering disappeared, which indicates that amorphization occurred. At pressures above 10.7 GPa, a diffuse, low-intensity amorphous hump at 2θ of about

14º appears. This amorphous structure is retained up to 37.6 GPa. Upon the release of compression, the diffraction lines reappear between 5.1 and 3.6 GPa, revealing a reversible crystal-amorphous transition although with considerable hysteresis. The **c** direction is most compressible from 0 to 10.7 GPa due to the highly anisotropic elastic properties of crystalline $Ca(OH)_2$. $Ca(OH)_2$ is composed of sheets of $Ca(OH)_6$ octahedra with hydroxyls hexagonally close packed surrounding the Ca^{2+} cations. The bonding between these sheets is weak hydrogen bonds. Strain in the **a** direction requires the Ca-O bonding to be compressed; however, the **c** direction can accommodate all strains by compressing the OH···O bonds for hydrogen bonds are weaker than ionic or covalent bonding of the same bond length. Hydrogen bonding can lead to large anisotropies in the elasticity of hydroxides, and therefore limits the understanding of the compression mechanisms in other complicated hydroxides prepared at high pressures.

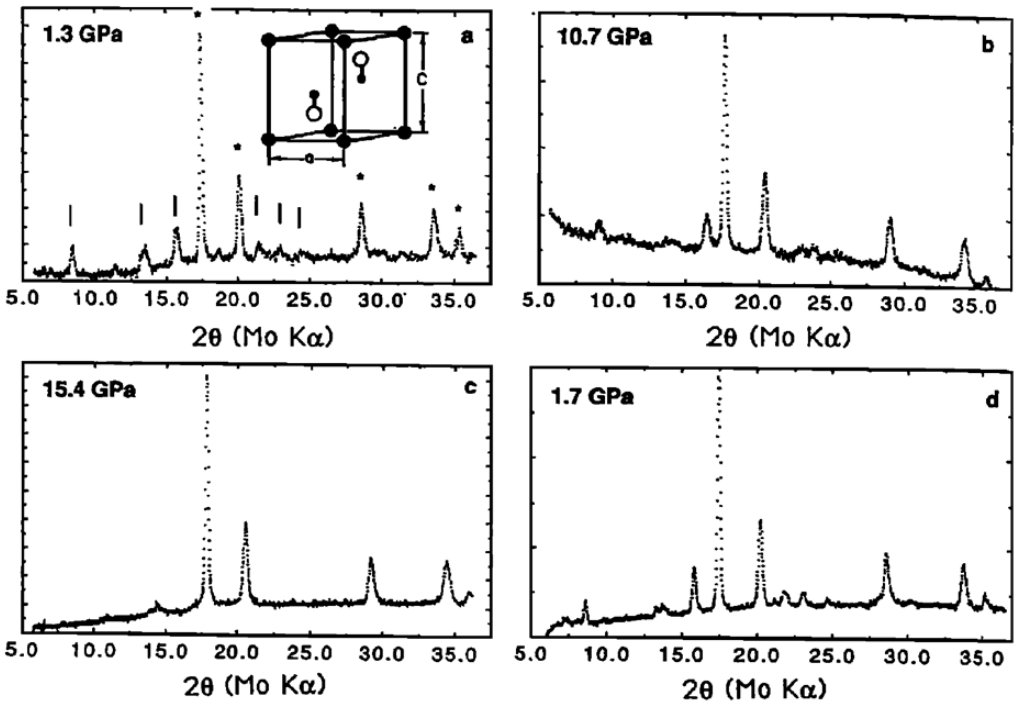

Figure 1.49 Powder x-ray diffraction of $Ca(OH)_2$ and Au in the diamond cell on increasing pressure. (a) The lines corresponding to $Ca(OH)_2$ and Au. The inset is a (110) projection of the $Ca(OH)_2$ unit cell. (c) At 15.4 GPa, $Ca(OH)_2$ has amorphized according to the broad feature at 14º. (d) Upon release, $Ca(OH)_2$ recrystallizes between 3.6 and 5.1 GPa [99].

Calcium phosphates are valued clinical and biocompatible materials and have been used widely in dentistry, prosthetics, and bone augmentation fields. Calcium phosphates are comprised of loosely packed polyhedra at ambient pressure, in different formations. In hydroxyapatite (HA), hydrated tricalcium phosphate (HTCP), and α tricalcium phosphate (α TCP), the polyhedra are arranged in chains. In dicalcium phosphate dihydrate (DCPD), they are in a layered structure, and in dicalcium phosphate anhydrous (DCPA) they are arranged as interconnected chains. The phosphate groups do not share corners or edges but are instead held together by cations and H_2O molecules. Calcium phosphate samples of 0.45 mm thick discs were compressed up to 10 GPa for 72 hours in a Bridgman anvil; then x-ray diffraction (XRD) and Fourier transform infrared (FTIR) spectroscopy [100] were applied. These compounds amorphized at a 10 GPa pressure, with significant changes in the infrared spectra except DCPA. These changes are due to the lowering of site symmetry upon amorphization. At high pressures, HTCP, HA and α TCP began to collapse along their chain axes. HA and α TCP amorphized at around 10 GPa, while HTCP amorphized at only 2 GPa. These three compounds exhibit similar infrared spectra of the PO_4 group. The sheet structure of DCPD and DCPA collapsed in the sheet plane during the amorphization process, exhibiting low symmetry and similar PO_4 absorption bands.

1.1.6 Amorphization in biological materials

We have seen previously that many synthetic materials amorphize in extreme regimes such as high strain rate and high strain conditions. Section 5 discusses HAP amorphization; there is one example of a biological material undergoing amorphization: biogenic hydroxyapatite (HAP).

The impact surface of the fast-striking dactyl club of the mantis shrimp is a rare example of a natural material undergoing such extreme conditions [101]. Its dactyl club can generate forces up to 1500 N via acceleration above 10000 g and velocity of 23 m/s. The clubs experience

extremely high loadings and need to remain intact during the shrimp's feeding activities. It has evolved the special structure to localize damage and avoid catastrophic failure from high-speed impact. The outermost layer, i.e., the impact surface, of densely packed (about 88 volume%) ~65 nm bicontinuous hydroxyapatite (HAP) nanoparticles distributed within an organic framework is worn away on impacts and serves as the primary way to dissipate energy. Dactyl club samples were impacted at high strain rates (about 10^4 s^{-1}) with and without the outer protective layer. In the sample without the protective layer, penetration depths were twice compared to the one with it. It is possible that chitin and proteins interpenetrating in the nanoparticles harden, resulting in the localization of the failure and nanoparticles, therefore limiting the propagation of cracks. In this way, the organic network enables additional toughening and abundant damping. Although quasi-static indentation does not change the size and shape of HAP particles, they rotate, translate, and fracture into smaller primary grains of sizes between 10 and 20 nm whereas the nanocrystalline networks crack at low-angle grain boundaries, generate dislocations, and then amorphize to dissipate some impact energy. Figure 1.50 shows the TEM images of the impact surface of dactyl club samples and the illustration of its toughening mechanisms. This localized fracture and amorphization minimize the damaged zone to the renewable outer surface nanoparticle coating of the dactyl club.

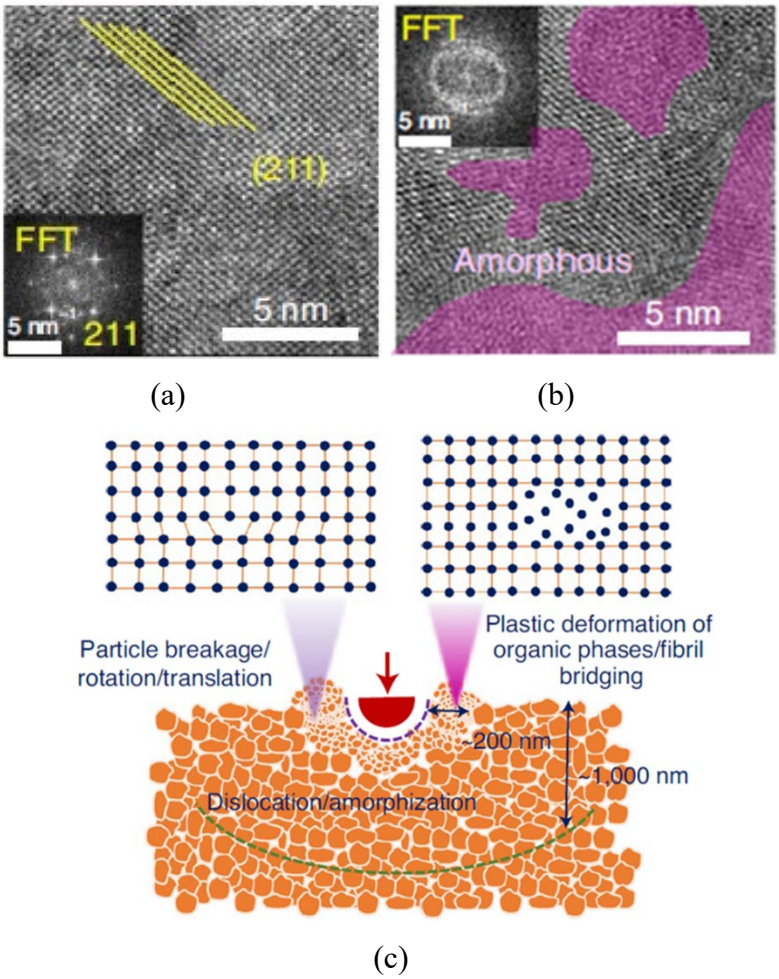

Figure 1.50 Dactyl club samples after impact tests. (a) Perfect (211) plane in crystalline matrix. (b) Impact-induced amorphization. (c) Different toughening mechanisms of surface nanoparticles from high-strain-rate impact [101].

1.1.7 Thermodynamics and Kinetics of Amorphization by Deformation

We mention in Section 1 the different methods by which mechanical loads can be applied to metals in order to amorphize them. In this section we will present a general framework for amorphization by mechanical means. A simple criterion is:

$$G_c + G_d > G_a \tag{4}$$

where the subscripts c and a refer to the crystalline and amorphous form, respectively, and d corresponds to defects (from deformation or radiation effects). Figure 1.13 of enthalpy vs.

composition for the Ni-Zr alloys shows the difference between the amorphous (higher) and crystalline (lower) enthalpies. This difference is around 8 kJ/mol. However, Koch [102] estimated that the dislocations only account for about 1-2 kJ/mol. Thus, other effects must be considered. An important one is the destruction of order in intermetallic compounds due to plastic deformation. Phase transitions have thermodynamic parameters associated with them, as do internal interfaces formed by deformation and phase transitions. Thus, a more general expression is:

$$G_c + G_d + G_o + G_{gb} + \Sigma G_{pt} > G_a \tag{5}$$

Where G_o is the free energy of disordering, G_{gb} is the energy of the additional interfaces generated by deformation or radiation, and ΣG_{pt} is the free energy increase from phase transitions.

External parameters are the stresses applied to the material, which can be decomposed into hydrostatic and deviatoric (or shear). In a more general formalism, we also need to consider the activation energy that represents the height of the energy that has to be overcome for amorphization to take place.

There exist theoretical analyses of this class of structural transitions in different degrees of complexity. The Patel-Cohen [96] and Eshelby [103,104] treatments provide an underlying energetics justification for the combined effects of hydrostatic and shear stresses on the thermodynamics. Levitas [105] provides a comprehensive theoretical framework for this effect, incorporating the effects of external, internal, and transformation (Eshelby) stresses and strains on the structural changes. Indeed, the shear strains produced by shear stresses generate greater relative atomic motions than hydrostatic stresses and strains in shock compression. The expression for the work per unit volume, W, of a transformation for a stress state where only normal stresses operate in the unit cube aligned with the deformation direction [95] can be written as:

$$\mathrm{W} = \sigma_0 \varepsilon_\mathrm{t} + \tau \varepsilon_\mathrm{s} + G_d + G_o + G_{gb} + \Sigma G_{pt} + \gamma A \geq \Delta G_a(T) \tag{6}$$

where ε_t is the spherical compression strain generated by the change of crystalline to amorphous phase and ε_s the deviatoric component of strain in a stress-free transformation, σ_0 is the hydrostatic stress ($(\sigma_{11}+\sigma_{22}+\sigma_{33})/3$), ε_s is the shear strain generated by the change of crystalline to amorphous phase. The term G_d represents the energy per unit volume of the local defect structure ($=\rho^d Gb^2/2$, where ρ^d is the local density of dislocations prior to amorphization, G is the shear modulus, and b is the Burgers vector). Several terms are added to Levitas' equation: the energy change for phase transitions, the energy of the grain boundaries produced by extreme deformation, G_{gb}, as well as γ, the interfacial energy (A being the interfacial area between the amorphous and crystalline region). Here, ΔG_a (T) is a critical temperature-dependent value of the energy per unit volume that has to be overcome for the transformation to take place (activation energy). We apply it here to amorphization.

There is no unanimity nor need to be about the relative importance of the various contributions presented above. It is known that the extensive plastic deformation taking place during the deformation of powders of different compositions in ball milling, forming multilayers with high density of defects is an attractive method to generate amorphous compounds through the reaction of the elements. This was first done by Yermakov [106] and later by Koch et al. [107]. There are two classes of experiments, according to Koch [102]: mechanical alloying, where powders of different metals are milled together. At some critical deformation, diffusion couples form between the thin slivers that are highly deformed.

Cho and Koch [51] used ball milling to generate amorphous Nb_3Sn from crystalline Nb+Sn, Nb+$NbSn_2$, and Nb_3Sn. They conclude that the free energy of disordering contributed ~5 kJ/mol whereas the energy of the grain boundaries for a grain size of 5 nm contributed ~7 kJ/mol. These two contributions almost reach the 15 kJ/mol difference between the amorphous and crystalline

structures. Donovan et al. [108] measured the enthalpies of the crystalline to amorphous transition in Si and Ge and obtained values of 11.6 and 11.9 kJ/mol. Weeber and Bakker [62] calculated the difference in enthalpy for Ni-Zr alloys and obtained values around 8 kJ/mol at the composition $Ni_{50}Zr_{50}$. These values are shown in Figure 1.13. These values for the enthalpies of amorphization are consistent and provide a good guideline for the energy input required to amorphize materials.

Szlufarska et al. [109], using MD, predict that amorphization under a nanoindenter in SiC was the result of dislocation interaction, specifically the coalescence of loops generated by the high stresses. The experimental results by Wu et al. [110] are somewhat different: they observe a direct amorphization of 6H-SiC under the nanoindenter coinciding with the first 'pop-in' of the loading curve. Subsequent 'pop-ins' are the result of amorphization triggered by dislocations.

One may argue that the deformation is not homogeneous but distributed in bands that have high dislocation densities, whose energy can locally reach high levels. This is accentuated by the intersections of these slip bands, essentially doubling the energy.

Although the exact mechanism of deformation-induced amorphization is not yet known, some thoughts, applicable to low stacking-fault energy materials, are advanced below. Figure 1.51 [57] shows a general deformation sequence in a low stacking-fault energy alloy or compound starting with the generation of stacking fault packets (A) which then form on different planes (B) and intersect (C), forming phase transitions (D) which eventually amorphize (E). This example shows that dislocation energy and the increase due to a phase transition can generate sufficient energy to overcome the energy barrier ΔG_a in Equation (6) and can promote amorphization. Idrissi et al. [111] comment at length on possible sequences leading to deformation-induced amorphization, including grain-boundary sliding. Thus, our knowledge in this domain is far from complete.

Kinetics of amorphization

There are no theoretical or experimental efforts, to the authors' knowledge of the kinetics of deformation-induced amorphization. One sequence that lends itself to analysis is the one depicted in Figure 1.51 and that is characteristic of low-stacking fault FCC alloys, such as stainless teel or HEAs. The situation depicted in Figure 1.51 is amenable to quantitatively predict the fraction amorphized as a function of externally applied strain and temperature. In low stacking-fault energy alloys and compounds, plastic deformation is often not homogeneous and generates profuse deformation bands composed of stacking faults, twins, and martensite. Our model presented here, based on the Olson-Cohen model [112] for the kinetics of strain-induced martensitic nucleation, assumes that the hierarchy of deformation leads from the γ phase to ε martensite and then to amorphization since ε martensite has a higher free energy than the original γ phase. The derivation was originally presented in the Supplementary Information section of [57]. Both ε-martensite and twins are generated by the coordinated motion of partial dislocations, shown in Figure 1.51 (a) and (b), respectively. The principal difference is that twinning is generated by the movement of partial dislocations on consecutive close packed {111} planes, producing a shear strain of 0.707, whereas the γ to ε transformation involves the movement of partial dislocations on alternate {111} planes, with an associated shear strain of 0.354. In this model, we assume that the fraction of material in the deformation bands, f_{db}, increases with strain γ as:

$$\frac{df_{db}}{(1-f_{db})} = \alpha d\gamma \tag{7}$$

where α is a constant that relates the increase in the fraction of material, df_{db}, occupied by deformation bands to the increase by the imparted plastic strain, $d\gamma$. The fraction of undeformed material decreases with plastic strain. It is represented by term (1-f_{db}) in the denominator. Integration of Equation (7) gives rise to:

$$f_{db} = 1 - \exp(-\alpha\gamma) \tag{8}$$

This accounts for the gradual exhaustion of material in which deformation bands can develop. The number of deformation bands per unit volume, N_{db}, is related to the fraction transformed through:

$$N_{db} = \frac{f_{db}}{V_{db}} \tag{9}$$

V_{db} is the volume of a deformation band, which is equal to its thickness t_{db} multiplied by the area $A_{db.}$

Each deformation band is comprised of ε martensite, twins, and partial dislocations; the first two contribute with their characteristic shear strains: $\gamma_\varepsilon = 0.354$ and $\gamma_t = 0.707$. The third strain, f_{pd}, is variable and dependent on the number of partial dislocations. Hence:

$$\gamma_{db} = f_\varepsilon\gamma_\varepsilon + f_t\gamma_t + f_{pd}\gamma_{pd} \tag{10}$$

where f_ε, f_t, and f_{pd} are the fractions of ε, twins, and partial dislocations in the deformation bands and $f_\varepsilon + f_t + f_{pd} = 1$. The fractions of these deformation mechanisms are dependent on strain, strain rate, and temperature. They determine the total shear strain in a deformation band and therefore the parameter α in Equation (8).

A simplified picture is presented in Figure 1.51 (c) in which only one fully formed ε martensite packet is shown. The intersection of ε martensite packets (Figure 1.51 (d)) generates additional strain. As mentioned above, each packet has a thickness t_{db} (shown in Figure 1.51 (d)). We assume that the volume of the amorphous region is determined by the thickness of the intersecting ε martensite packets which, on its turn, is equal to $f_\varepsilon t_{db}$. The amorphized region is shown in Figure 1.51 (e). Assuming the amorphization occurred at the intersection of the deformation bands which is power law proportional to the number density of the band itself, one

can eventually arrive at a sigmodal relationship of the amorphous volume fraction as a function of strain,

$$f_a = K[1 - \exp(-\alpha\gamma)]^n \quad (11)$$

The proportionality constant K incorporates various material (stacking-fault energy, fraction of ε martensite in the deformation packets, probability of nucleation of amorphous region at band intersections, thickness of the deformation bands, and others) and external (strain rate and temperature) parameters presented in [57]. Equation (11) can serve as a framework for a theory on the kinetics of deformation-induced amorphization. The determination of the various parameters requires systematic experimentation, which has not been conducted yet. Other materials will exhibit different deformation sequences which are also amenable to analysis.

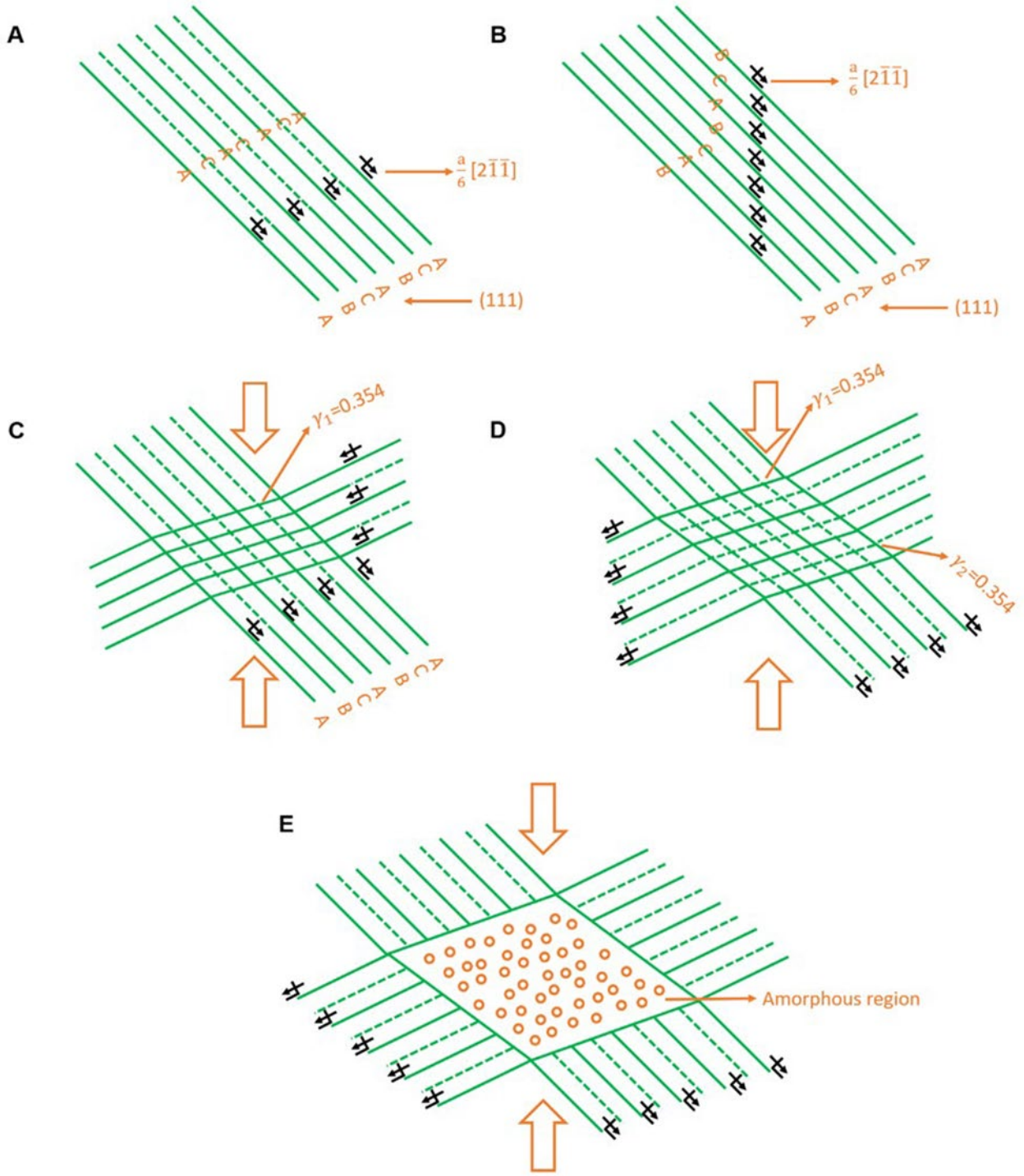

Figure 1.51 A general deformation sequence in an alloy or a compound with low stacking-fault energy. (a) Stacking fault packets are generated, (b) form on different planes, (c) intersect, (d) form phase transitions, and (e) eventually amorphized [57].

1.1.8 Fundamental mechanisms of deformation in amorphous materials

This section presents the principal mechanisms of plastic deformation which can lead to amorphization. Many amorphous materials have superior mechanical performance under specified circumstances. Previous attempts to reconcile dislocation theory with plastic deformation of glasses have failed, so new mechanisms had to be postulated. These theories fall into two groups: free volume (initially proposed by Spaepen [113]) and shear transformation zones (initiated by Argon [114]). These theories are being corroborated by molecular dynamics simulations and advanced characterization techniques. Generally, as the deformation energy from a defect density increases, elastic deformation yields to dislocation multiplication and movement, then to twinning, subsequently to phase transformations and finally, under the extreme conditions of high stress, high strain, and high strain rate, solid state amorphization can take place (Figure 1.52) [94].

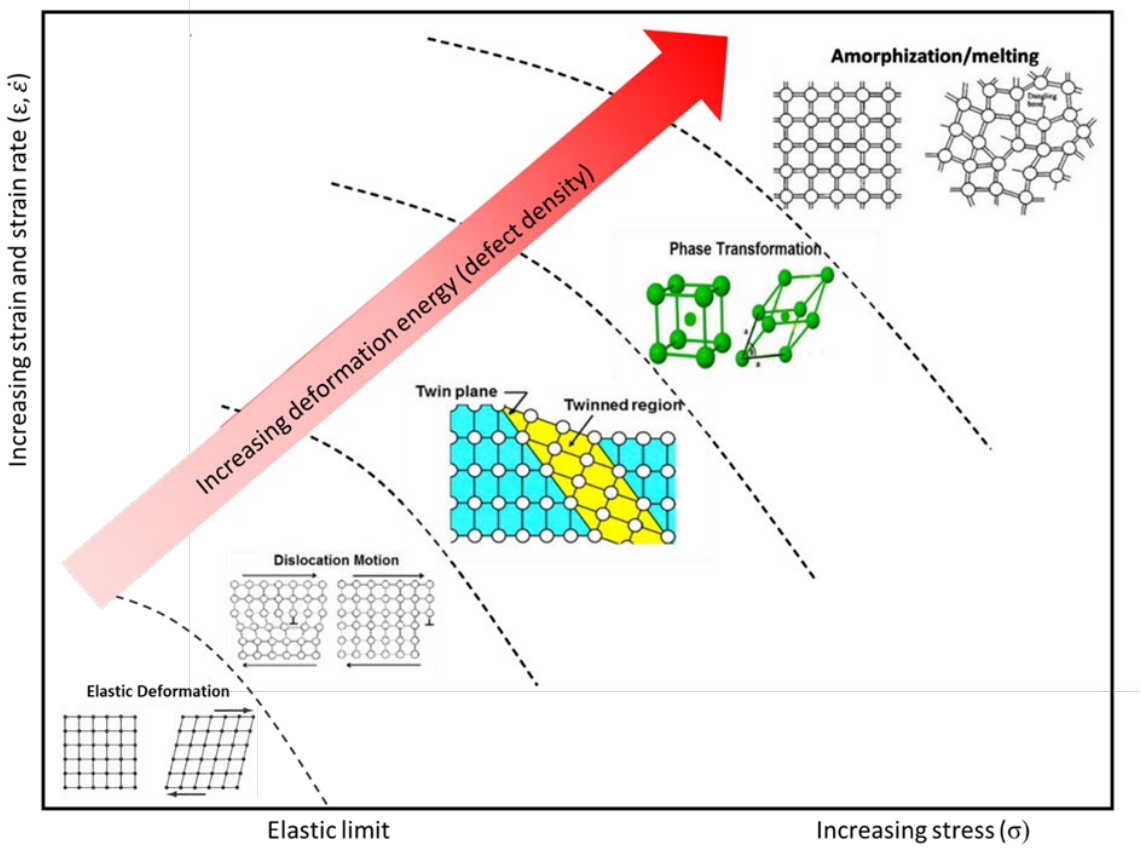

Figure 1.52 Evolution of deformation mechanisms as the strain and strain rate increase. The boundaries between domains highly depend on materials' properties [94].

Free volume theory

Free volume is defined as the empty space in a solid or liquid that is not occupied by molecules. When the temperature changes, the free volume also changes. In amorphous materials, free volume can be considered as the carrier for plastic deformation, in an equivalent role to dislocations in crystalline materials.

In free volume regions, inelastic relaxation through local atom rearrangements is possible due to the weak mechanical coupling to the surrounding atomic structure. These sites are called soft spots where amorphous structure destabilization preferentially initiates as a result of passing through the glass transition temperature or local shearing from applied stresses.

When shear stress is applied to crystalline materials, the initial volume during plastic deformation is unchanged because the periodicity of the crystal structure along slip planes leaves identical atomic positions and vicinities for the slipped material. In contrast, in amorphous materials the free volume increases during plastic deformation and some voids are left behind due to the randomness of their structure (Figure 1.53) [115]. The nano-voids are more likely to nucleate in tension rather than in compression, indicating that the hydrostatic pressure plays an important role in the nucleation of nano-voids.

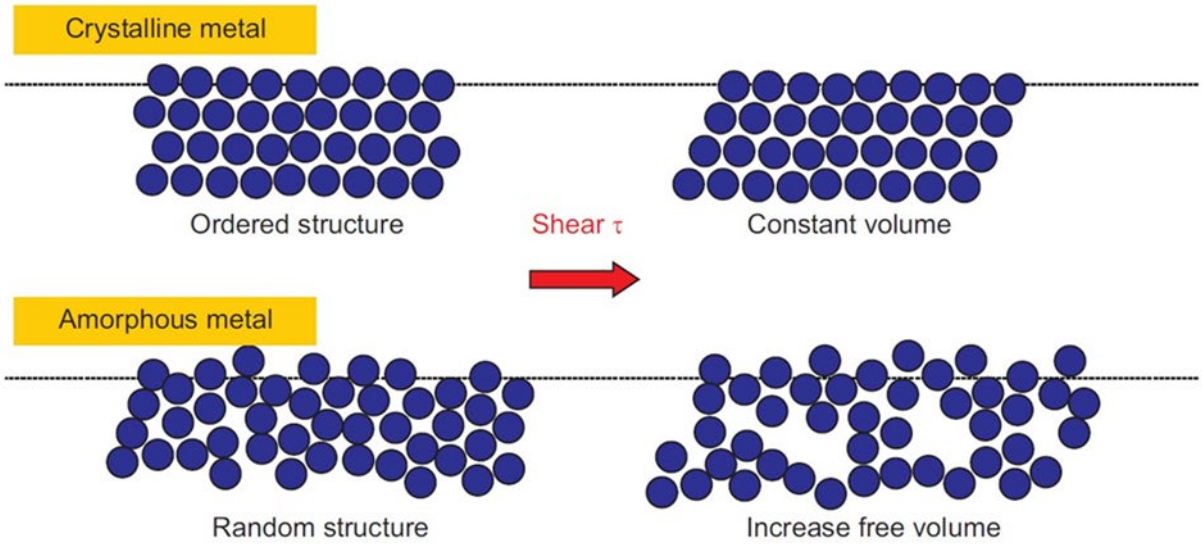

Figure 1.53 Spaepen's free volume theory in crystalline vs. amorphous metals [115].

Dislocations and shear bands are generated by different micro mechanisms in crystalline materials and amorphous metals by mechanical deformation, respectively (Figure 1.54) [115]. Shear banding in glassy materials plays a key role similar to dislocations in crystalline materials in mediating plasticity and failure.

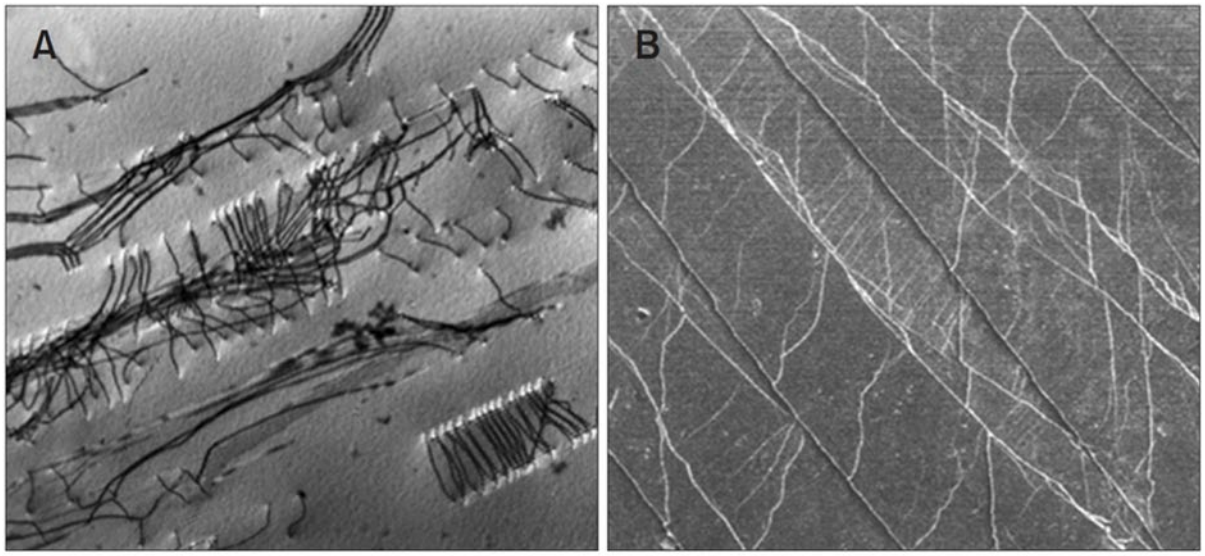

Figure 1.54 Micrographs show the dislocations in crystalline material and shear bands in amorphous material. (a) TEM image of deformed 316 stainless steel exhibiting dislocations and dipoles on (111) planes (b) SEM image of deformed bulk metallic glass with many shear bands [115].

Plastic flow in amorphous metals is initiated at some locally perturbed zones. The flow localizes as a result of strain softening from accumulated defects observed at the atomic scale (Figure 1.55) [115-117]. Amorphous metals tend to fracture abruptly along these shear band planes, especially when subjected to tensile loading. This mode of material failure has impeded their structural applications.

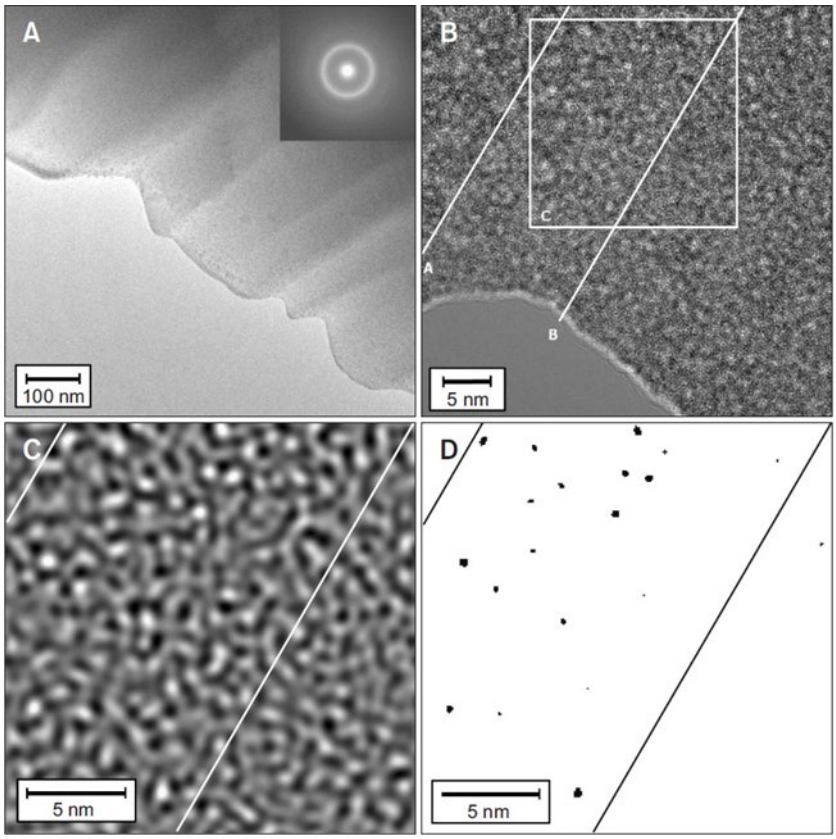

Figure 1.55 TEM micrographs of amorphous metals. TEM micrographs of amorphous metals. (a) Low magnification and (b) HRTEM micrographs of the shear band area induced by bending an amorphous metal. (c) FFT pattern. (d) Same image as (c) with black spots corresponding to white areas in (c), indicating regions of excess free volume. The free volume has preferentially accumulated and nanovoids (1 nm or less) are observed within the shear band [115-117].

Spaepen [114] proposed a single atom model (Figure 1.56 (a)) [115] for the formation of free volume in amorphous materials in 1977, characterizing it as the elastic energy required to push an atom into a small empty space. Macroscopic plastic flow is considered to be the sum of

these individual atomic jumps. The atoms tend to jump to the stress direction when an external stress is applied, forming the plastic flow in amorphous metals.

Shear transformation zone theory

The Shear Transformation Zone theory (STZ) was proposed by Argon in 1979 (Figure 1.56 (b)) [114,115] based on an atomic-analog bubble-raft model, explaining the shear deformation as spontaneous and cooperative rearrangements of small clusters of randomly close-packed atoms in amorphous solids. These clusters, up to around 100 atoms, are subjected to inelastic shear deformation from a lower energy configuration to a higher energy and volume configuration, resulting in stress and strain reconfiguration in the STZ region. Local motion of STZs around the free volume sites push apart surrounding atoms, leading to dilatation and strain softening in the vicinity.

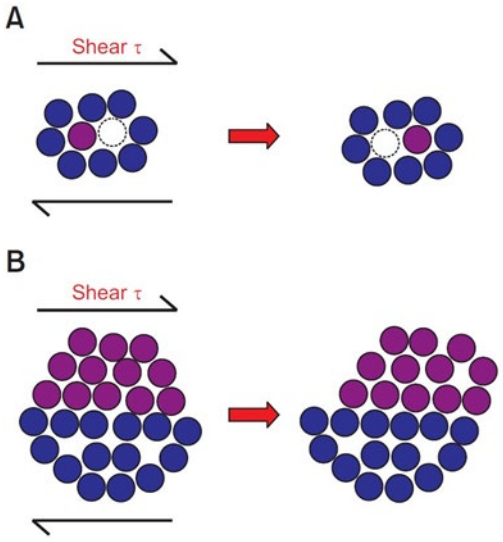

Figure 1.56 Two different atomic scale deformation mechanisms proposed for amorphous materials. (a) Spaepen [1977], free volume model, an individual atomic jump (macroscopic diffusion and flow). (b) Argon [1979], a shear transformation zone (spontaneous and cooperative rearrangement of a cluster of atoms) [115].

A number of simulation studies have recognized that single plastic events in amorphous metals can be illustrated by local stress fields with quadrupolar symmetry, analogous to Eshelby's

inclusions within an elastic continuum (Figure 1.57) [118]. Because of the mismatch between the sheared zones and the surrounding matrix, extra volume must be created when amorphous metals are sheared. These zones are softer, allowing the material to flow, and these nonaffine displacements cause particles within the shear plane to leave the glassy cage outward along a particular line from both ends, while pushing the particles perpendicular to the line inwards towards the center of the glassy cage from both directions, causing local density to change. As a result of an alignment of Eshelby-like quadrupoles, shear banding develops.

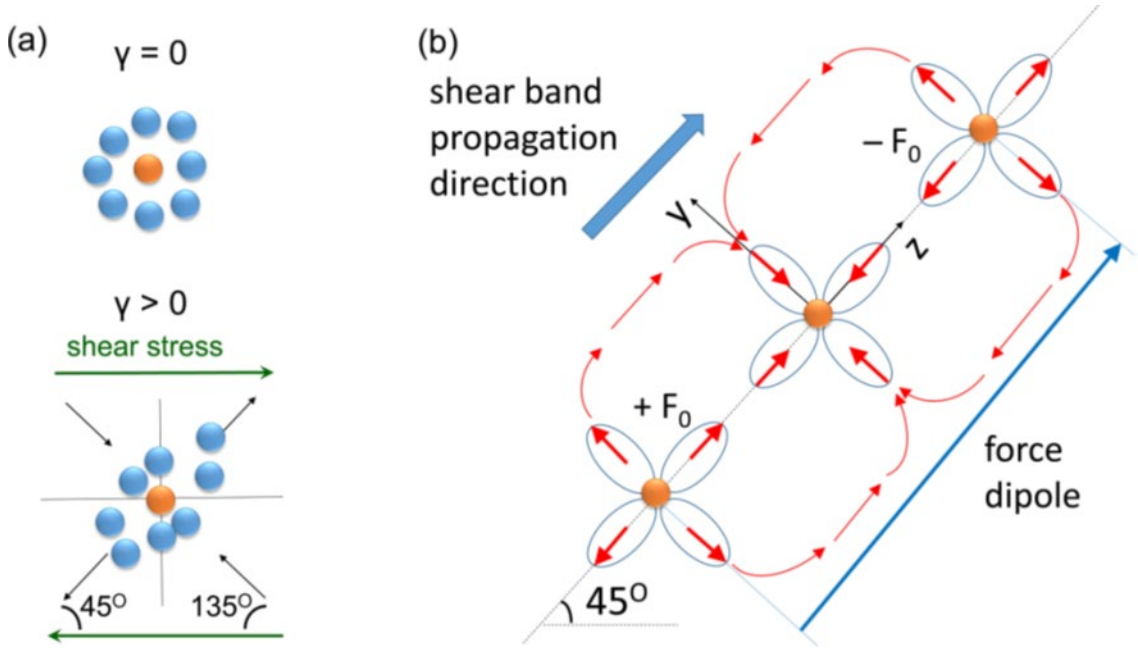

Figure 1.57 Simulation of shear deformation single plastic events in amorphous metals. Simulation of shear deformation single plastic events in amorphous metals. (a) Shear deformation in metallic glass renders particles within the shear plane to leave the glassy cage outward along the 45° line from both ends, meanwhile pushes the particles perpendicular to the line inwards towards the center of the glassy cage from both directions, thus local density changes. (b) Density change and shear band formation are caused by an alignment of Eshelby-like quadrupoles along the 45° direction [118].

Figure 1.58 [118] shows some high and low density regions within amorphous shear bands propagating along the direction of these shear bands in some metallic glasses. The periodicities vary between 135 and 163 nm. This alternating density due to the alignment of Eshelby plastic

events is considered as a response to plastic shear deformation in metallic glasses and may be postulated for other amorphous materials.

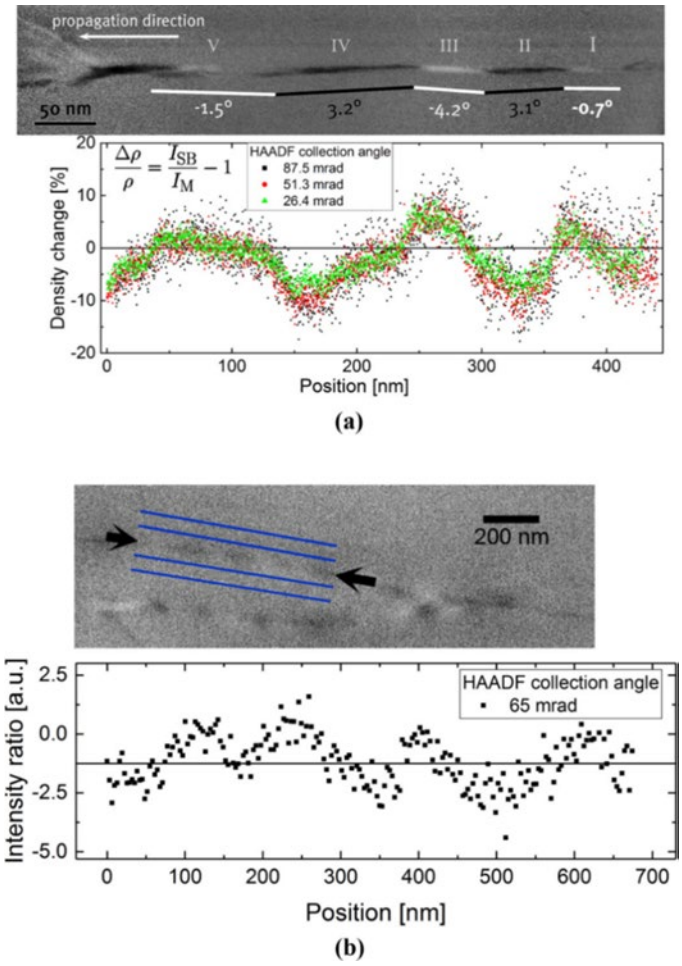

Figure 1.58 Regions with high and low density within amorphous shear bands propagating along the direction of these shear bands in some metallic glasses. (a) Top: High-angle annular dark-field (HAADF)-STEM image exhibits brightness contrast reversals in a shear band of $Al_{88}Y_7Fe_5$ metallic glass by cold rolling. Bottom: Corresponding quantified density oscillations along the shear band. (b) Top: HAADF-STEM image exhibits brightness contrast reversals in a shear band of a $Zr_{52.5}Cu_{17.9}Ni_{14.6}Al_{10}Ti_5$ BMG sample by compression. Bottom: Corresponding quantified density oscillations along the shear band [118].

Crystalline materials generally deform through the generation and propagation of lattice defects. However, nanoscale amorphization, which is defined as the formation of nanoscale amorphous regions in crystalline solids, is suggested as an alternative deformation mechanism

under extreme loading conditions. It is shown that nanoscale amorphization can facilitate the movement of plastic flow in crystalline nickel and silicon nanowires (Figure 1.59) [119].

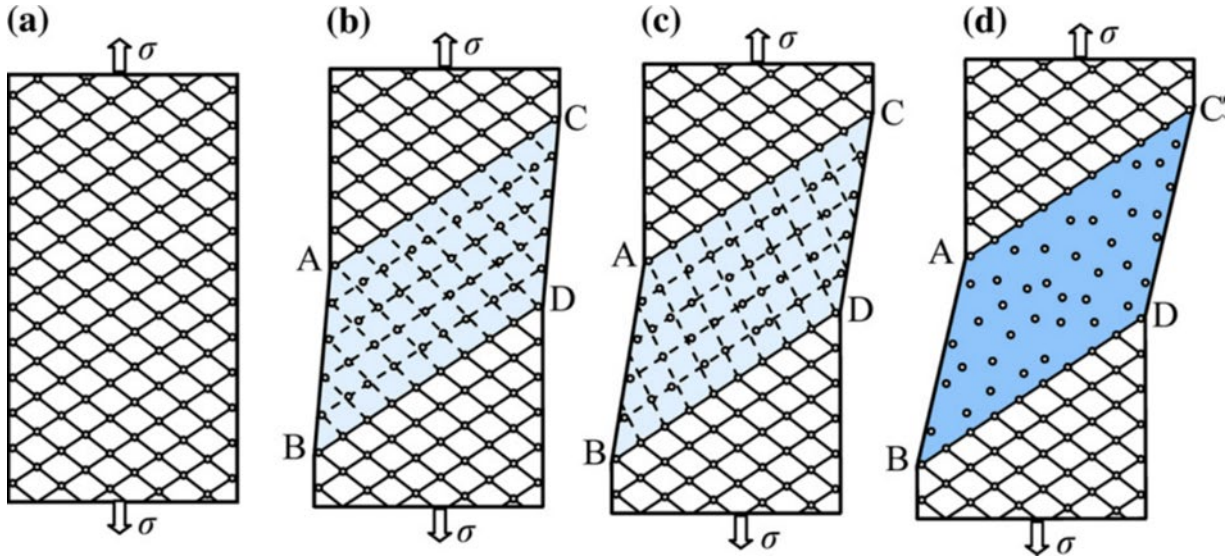

Figure 1.59 2D evolution of amorphization in the cross section of single crystalline fcc nanowire under tensile loading. (a) Initial state. (b) Spatially inhomogeneous multiplane shear is generated by shear stress within the region ABCD 45° from the loading direction. (c) The average shear stress keeps increasing until achieve the Burgers vector magnitude of twinning Shockley partials. Then 2D amorphous state forms in the crystallographic planes. (d) The conventional 3D amorphous phase forms within the plastically sheared region ABCD because of the elastic instability [119].

Figure 1.60 [120] compares the differences of microstructural defects between bulk metallic glasses and polycrystalline metals. While dislocations carry the plasticity in crystalline materials, bulk metallic glasses deform via the activation of shear transformations zones (STZs). A STZ's activation energy depends on its local composition and can be tuned by microalloying to modify its mechanical properties. Solutes in crystalline materials normally pin and impede dislocation motion. Precipitates and secondary phases can cause precipitation hardening in polycrystalline metals. In amorphous metals, the heterogeneous microstructure helps to stabilize the glass to avoid catastrophic failure. The interfaces separating glassy grains within nanoglasses prepared by cold compaction of glassy nanoparticles are found stable if local strain does not exceed the flow strain of the bulk metallic glass. These interfaces are characterized by an excess free

volume and lack of short-range order. Some experimental studies on iron- scandium nanoglass exhibited improved ductility in nanoindentation compression, and MD simulation of Cu–Zr nanoglasses showed that interfaces served as precursors for shear-band formation, restraining strain localization and contributing to more homogeneous deformation.

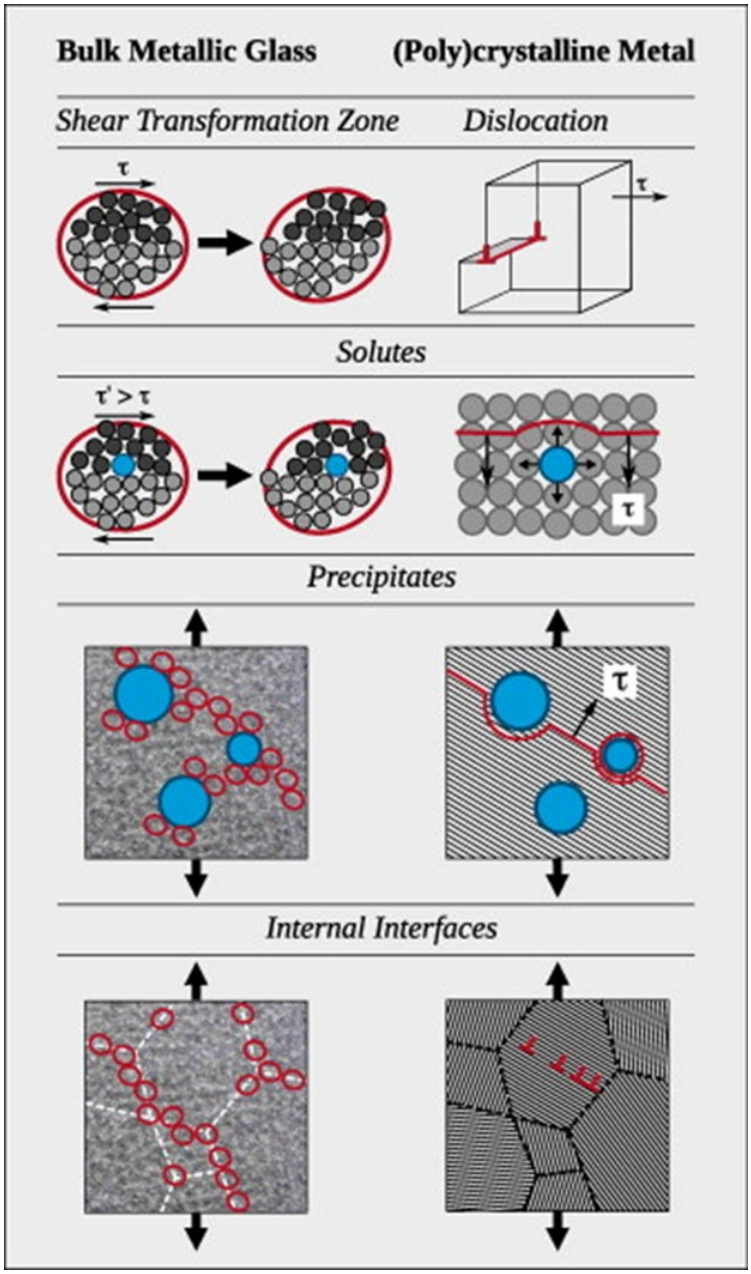

Figure 1.60 How different microstructural defects can modify mechanical properties in both polycrystalline metals and bulk metallic glasses. Although the micro-mechanisms are quite different, the same methods can be used [120].

1.2 Literature Review on Diamond

1.2.1 High Energy Density Physics Conditions and Planetary Interiors

High Energy Density Physics (HEDP) is a new field within the domain of condensed matter and radiation physics, where energy densities are sufficiently high such that conventional methods in chemistry and physics are inadequate to explain the behavior of matter. The HEDP regime is often defined by pressures exceeding 1 megabar, or 100 GPa. Such conditions exist in the interiors of planets and stars [121, 122]. In our solar system, large quantities of carbon are likely be stored in the ice giant planets Uranus and Neptune [123] even though the composition of their interiors is poorly constrained. Since these planets formed beyond the ice line, one assumes that massive amounts of the planetary ices, H_2O, CH_4, and NH_3 were incorporated into their mantles during formation. In the seminal paper [124], M. Ross proposed that methane decomposes into diamond and hydrogen at the high pressure conditions in the interiors of ice giants. The hypothesis of diamond formation has since again further support by results from diamond anvil cell experiments [125, 126], shock measurements [127] and computer simulations [128].

Mercury has recently been added to the list of carbon harboring planets. Based on measurements by NASA's MESSENGER spacecraft, a diamond layer has been proposed to exist on top of the Mercury's iron core [129].

Carbon-rich exoplanets are likely to exist in our galaxy as long as they formed out of a nebula that had a carbon-to-oxygen ratio greater than 0.8 [130]. In these environments, there is not enough oxygen available to form the typical magnesium silicates like $MgSiO_3$ or MgO that make up the bulk of the Earth's mantle. In such cases, the mantles of planets are predicted to be composed of diamond and silicon carbide [131]. *Cancri 55 e* was initially assumed to be such a diamond planet [132] but a more careful analysis of stellar spectra have called into question

whether *Cancri 55 e* formed in a carbon rich environment [133]. Instead it has been suggested to be a rocky planet with an atmosphere that is rich in CO and CO_2 [134].

Diamond transforms into graphite before melting at ambient pressure due to its thermodynamically unstable nature. The melting temperature of carbon under pressures of 0.6–1.1 TPa is probed by shock compression experiments on diamond. The melting curve has a negative Clapeyron slope, indicating that diamond melts to a denser, metallic fluid between 0.60 and 1.05 TPa, which agrees well with the first-principles calculation predictions. Diamond melts to a complex fluid at even higher pressures, and dissociates at pressures between 1.1 and 2.5 TPa when the temperatures are above 50,000 K.

Because of diamond's strength [135-137], a variety of extreme techniques such as gas guns, explosives, and pulsed lasers have to be used to allow it to reach the realm of temperature and pressure that may be defined as High Energy Density. Shock Hugoniot data of diamond from many sources is presented in Figure 1.61 [135, 136, 138–152]. The experimental results are very consistent up to 1 TPa; beyond that there is considerable scatter in data.

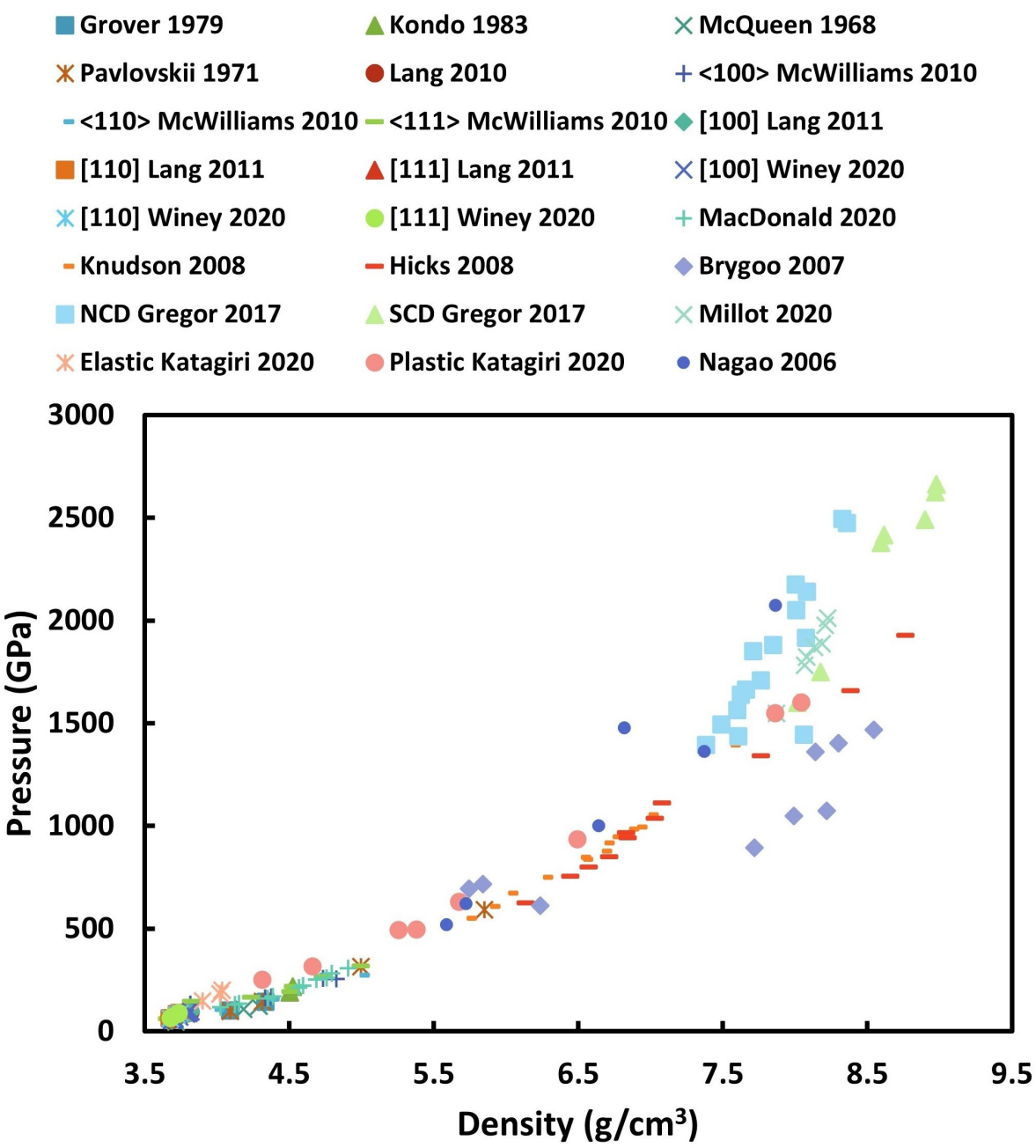

Figure 1.61 Diamond shock Hugoniot experimental data from different sources [135, 136, 138–152].

1.2.2 Diamond Hugoniot Elastic Limit and Strength

The Hugoniot elastic limit (HEL) is an essential property of materials under high strain rate shock compression. Below the HEL, the material is under uniaxial compression condition without permanent deformation; at HEL, solids undergo the highest shear stress under shock compression; above HEL the shear stress decreases and relaxes to hydrostatic compression condition, plastic deformation and material failure initiate [153]. This dissipation of stress is generally achieved in three forms: ductile-like by plastic flow, brittle by fracture, or phase transformation through atomic rearrangement [154]. The uniaxial strain state above the HEL has hydrostatic (isotropic) and deviatoric (anisotropic) stressed components; and the deviatoric component is a function of the strength of the material [145]. The HEL and strength measurements largely depend on the types, growth methods, density, and grain size of diamond samples used in experiments. Different initial imperfections in diamond can lead to a discrepancy of 10% - 20% on the measured values for HEL and strength. Table 1.3 presents HEL values for three orientations of single crystals diamond [138, 141, 155].

Table 1.5 HEL for Single Crystal Diamond

Authors	Year	<100> (GPa)	<110> (GPa)	<111> (GPa)
McWilliams et al. [138]	2010	80	81	60
Kondo et al. [141]	1983	110	63 ± 28	
Lang et al. [155]	2013	53 - 93.9	62.1 – 86.9	62 – 87.2

Single crystal diamond was shocked by plate impact experiments to about 900 GPa elastic impact stress (EIS, the stress obtained at impact, assuming purely elastic diamond response) to explore the elastic-inelastic response of [100], [110], and [111] orientations by Winey et al. [144]. A two-wave structure (elastic-inelastic response) was observed at ~900 GPa EIS at or near the melting stress along [110] and [111] directions while single (overdriven) waves were observed at

480 GPa EIS and above along [100]. The elastic wave velocities along [110] and [111] were much larger than those along [100]. The elastic wave amplitudes along [110] were much larger than those along [100] and [111]. And along [110] and [111], the elastic wave amplitudes rose significantly with increasing EIS, indicating strong orientation dependence. The two-wave structure and the large orientation dependence nature of elastic wave speeds and amplitudes illustrate that the response of single crystal diamond is not hydrodynamic up to shock stresses below the onset of melt [144].

The strength and nonlinear elastic response of natural and synthetic (type IIa) single crystal diamond were also measured by Lang et al. [136] through plane shock wave experiments of 60 ns duration along [100] direction to peak elastic pressures of 90 and 120 GPa. The maximum elastic wave amplitudes for both crystals are 89 ± 3 GPa, corresponding to shear stresses of 30 GPa for $(111)[1\bar{1}0]$ and 35 GPa ($\sim G/15$) for the $(111)[2\bar{1}\bar{1}]$ slip system. Under the higher peak stress, the elastic limit of 57 GPa was unexpectedly lower. The elastic constant C_{111} was determined to be -7804 ± 653 GPa. Particle velocity histories showed a sharp elastic wave which was followed by a second wave. Compression to stresses just above the HEL is linked to the formation of a two-wave shock structure, characterized by an elastic precursor propagating at a longitudinal sound speed which compresses the diamond to near its HEL and is followed by an inelastic wave which reaches the peak pressure. This two-wave structure is characteristic of a material which has a time-dependent, elastic-inelastic response.

Lang et al. [137] also explored the elastic-inelastic response of shocked single crystal diamond, including how crystalline anisotropy affects the elastic limit, strength, and deformation by plate impact experiments to ~120 GPa along [110] and [111] directions. Their HEL values are given in Table 1.3. Understanding and quantifying the strength or elastic limit of diamond single

crystals is significant for science and technology. The elastic limits exhibit highly orientational dependence under uniaxial strain conditions. The maximum resolved shear stress (MRSS) values reach the maximum ($\tau_{max} \sim G/15$) along the [110] and [100] orientations and minimum ($\tau_{max} \sim G/20$) along the [111] orientation, showing significant orientational dependence. The MRSS values calculated for the [110] and [100] directions correspond to 25% – 30% of the calculated theoretical shear strength for {111}<110> slip systems in perfect single crystal diamond. The MRSS values depend strongly on the resolved normal stress which is the stress component normal to the {111} slip planes, explaining the orientational dependence of strength in shocked single crystal diamond: [110] > [100] > [111]. The results show that the resolved normal stress can suppress the initiation of inelastic deformation in shocked single crystal diamond. The lower elastic wave amplitudes at higher shock stresses and the impact of stress normal to the slip planes indicate a highly time-dependent inelastic response which is typical in shocked brittle solids, rather than the dislocation slip mechanisms [137, 156–158].

Single-crystal diamond bridges, approximately 1 μm in length and 100 nm in width, were microfabricated and tested by Dang et al. [159]. These samples exhibited extremely large (sample wide), reversible, and uniform elastic strain deformation through in situ uniaxial mechanical tensile tests along the [100], [101], and [111] orientations at room temperature. A maximum tensile strain of up to 9.7%, approaching the ideal elastic limit [160], was achieved. The Young's modulus was measured to be around 1010 ± 70 GPa in the [111] direction, which is higher than the values of ~895 ± 65 GPa and ~850 ± 80 GPa for the [101] and [100] directions, respectively. These results are consistent with the expected ranking of orientation-dependent elastic moduli for bulk diamond [161, 162].

The strength of laser shocked polycrystalline diamond at stresses above the HEL was examined by x-ray diffraction with velocity interferometry at the Linac Coherent Light Source. Typically, brittle materials lose considerable strength above the elastic limit [163]; shocked diamond exhibits a unique elastic–inelastic response [138]. Both ramp compression [164, 165] and shock compression at [136, 137] and above [138] the HEL were conducted to probe the dynamic behavior of diamond. Diamond behaves in a brittle manner at ambient conditions like most materials with high initial strength, but it has a plastic response under shock compression condition [138]. The experimental results show that shock compressed diamond retains ~ 20 GPa of strength at 150 – 300 GPa longitudinal stresses, which gives valuable data for developing improved strength models of diamond. These models will promote simulations in inertial confinement fusion implosions and reduce the uncertainties in EOS [145].

1.2.3 Shock Compression

Shock-wave experiments up to 191 GPa and 217 GPa were conducted along the intermediate direction between <111> and <110> on diamond by Kondo et al. [141] (HEL measurements in Table 1.3). The highest post-shock density from about 200 GPa shock compression was 3.95 g/cm^3 while its initial density was 3.52 g/cm^3, indicating a transformation to a denser metallic carbon phase induced by shock or an elastic unloading process. The post-shock diamond metallic carbon phase is stable at the lower mantle and earth core, which is of geophysical interest [140, 141].

Cubic diamond is the strongest naturally occurring material, and is thermodynamically stable over a wide pressure and temperature range. At 172 GPa, a macroscopic flow similar to plastic deformation was observed at the tip of a diamond anvil at above 2000 K by Mao et al. [166]. Cubic diamond transformed to graphite when a sharp diamond indenter was pressed on its surface

[167]. Cubic diamond particles directly transformed into hexagonal diamond under shock compression in nanoseconds at only tens of GPa and hundreds of K, thermodynamically still within the stable cubic diamond phase domain. The transformation from cubic to hexagonal diamond is a kinetic solid-to-solid transition induced by shear stress and the increasing temperature generated by shock compression. Cubic diamond has the "*ABCABC*..." stacking sequence of identically packed carbon layers, while hexagonal diamond has the "*ABAB*..." stacking sequence. High shear stress is generated during shock compression due to the high stiffness of diamond under the uniaxial strain condition. The shear stress may induce stacking faults or multiple twin intersections, resulting in a transition of stacking faults from the "ABC" to the "AB" sequence. At the Hugoniot elastic limit (HEL), solids undergo the highest shear stress under shock compression; exceeding this, the shear stress decreases and plastic deformation initiates. The best shock pressure to produce hexagonal diamond is ∼70–80 GPa, which is about the HEL of cubic diamond (see Table 1.3), corresponding to a shear stress of around 30 GPa. This enhances the explanation of the importance of shear stress. High shear stresses combined with the temperature rise promote the formation of hexagonal diamond with shear stress. If the shear stress is high enough but the temperature is not high enough to form hexagonal diamond, cubic diamond transforms to disordered graphitic carbon. If the temperature is too high, it may lead to the graphitization of hexagonal diamond. Appropriate temperatures are required for the formation of hexagonal from cubic diamond, and approximately 500 K is favorable [168].

Decades of experiments show that the diamond–liquid melting line has a positive slope above the graphite–diamond–liquid triple point [169]. Theoretically, the melting curve of diamond should have a maximum at a higher pressure [170-173], because the sp^3 hybridization loses its stability in the fluid phase. High-pressure measurements conducted using laser shock along the

diamond shock Hugoniot indicate that crystalline diamond likely melts into a conducting fluid. The shocked diamond starts to melt at about 750 GPa. A negative volume discontinuity is observed at melting, indicating it has a negative melting slope at a maximum at 300–500 GPa on the melting curve. The presence of this maximum is due to the coordination change from two- and threefold at low pressure to tetrahedral in the fluid [174]. This change is due to the stabilization of diamond-like bonding at elevated pressures. But because the diamond-like bonding destabilizes, it becomes a more condensed fluid [148, 170-172]. This behavior is akin to silicon on melting, which also exhibits a negative Clapeyron slope. Si and C have the same covalent bonding configuration and crystal structure.

Magnetically accelerated flyer-plate experments on diamond were conducted at the Sandia Z machine [175] from 550 to 1400 GPa. There is evidence of a diamond-bc8-liquid triple point at the melting boundary. Under high pressure and density condition of the planet's ice layer, the free carbon may condense as diamond.

Diamond is used as an ablator material for inertial confinement fusion capsules. In the high energy density carbon phase diagram, the first slope change at 700 GPa pressure and 6.08 g/cm^3 density corresponds to the onset of melting of the diamond phase. The second slope change at pressures and densities between ~850 to 880 GPa and ~6.53 to 6.67 g/cm^3 corresponds to a triple point along the solid melting boundary. The third slope change at 1064 GPa and 7.01 g/cm^3 corresponds to the end of melting of a solid phase other than diamond. These values correlate well with the ab initio molecular dynamics (AIMD) simulations predictions for the triple point at 850 GPa and 6.52 to 6.62 g/cm^3 and for the onset and end of melting at ~680 GPa and ~1040 GPa, respectively [146].

The two-wave shock structure containing elastic and inelastic compression wave was discovered in laser shock compression on single crystal and polycrystalline diamond up to 800 GPa. The yield strength of single crystal diamond is about 1/3 of the theoretical predictions. The measurements demonstrate evident deviations from an elastic-plastic response following dynamic yielding, showing substantial relaxation to an isotropic stress state of at least 160 GPa. Features of melting at 700–800 GPa along the diamond Hugoniot may correlate to the shift from a two-wave to a single-wave structure, which supports the explanation that the onset of melting occurs at lower stresses, around 600 GPa, coinciding with the occurrence of a carbon phase with optical reflection. The yielding behavior of single crystal and polycrystalline diamond is measured by large-amplitude shock waves between 100 and 1000 GPa. Although diamond resists plastic flow and tends to yield by fracturing at ambient pressure and temperature [176], plastic flow has been detected under high pressures [177] and temperatures [176], albeit over considerably longer time scales than those investigated through shock compression. The diamond shock response varies from nearly elastic isotropic to nearly elastic-plastic, depending on initial sample properties. While the onset of melting implies that strength should not have an influence in this stress regime, the observations suggest that this is not accurate. Ramp-wave response reveals that solid diamond maintains considerable strength to ramp stresses up to 800 GPa [164], suggesting that it can play a similar role in shock compression experiments [138].

Shock compression on single crystal diamond along the [100], [110], and [111] orientations was used to determine its nonlinear elastic response to 120 GPa peak elastic stresses. The complete set of third order elastic constants is shown in Table 1.4 combining theoretical models, experimental data, and ab initio simulations at 0 K. Third-order elastic constants exhibit the lowest-order anharmonic and anisotropic response of a crystal, which quantify the nonlinear elastic

response of a solid. Anharmonicity plays a significant part in initiating solid to solid phase transformations [135].

Table 1.6 Third-order elastic constants of diamond (GPa)

Ref.	Grimsditch, 1978	Anastassakis, 1990	Cousins, 2003	Nielsen, 1986	Lang, 2011
C_{111}	-6260	-7367	-6475	-6300 ± 300	-7603 ± 600
C_{112}	-2260	-2136	-1947	-800 ± 100	-1909 ± 554
C_{123}	112	1040	982	0 ± 400	835 ± 1447
C_{144}	-674	186	115	0 ± 300	1438 ± 853
C_{166}	-2860	-3292	-2998	-2600 ± 100	-3938 ± 375
C_{456}	-823	76	-135	-1300 ± 100	-2316 ± 743

Hard x-ray free-electron lasers (XFELs) pulses were employed to investigate the evolution of an elastic wave in diamond with both high spatial (about 500 nm) and temporal (about 50 fs pulse duration) resolution. The elastic wave was generated by an intense optical laser pulse and imaged at various delay times. Figure 1.62 shows the phase-contrast images captured at 1.2 to 3.0 ns time delays, illustrating the decay of the elastic compression wave with the 3 ns duration. The contrast diminished at the longer time delays. Moreover, even though the front width of the elastic compression wave was atomic, the direct observation of the propagation of the front width for a material under shock pressures above HEL would lead to better understanding of the time scales involved in plastic flow under high strain-rate conditions above 10^9 s^{-1} [178].

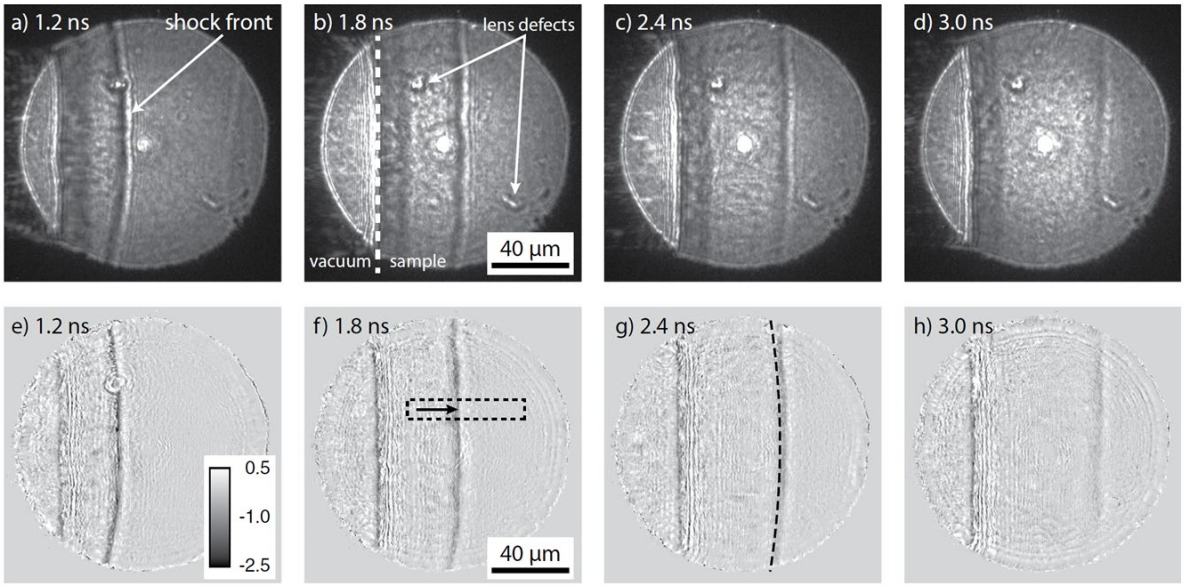

Figure 1.62 Phase-contrast images captured at 1.2 to 3.0 ns time delays, illustrating the decay of the elastic compression wave with the 3 ns duration. (a–d) Phase contrast images acquired from 4214 mm behind the specimen by a high-resolution x-ray detector marked by corresponding time delays. (e–h) Corresponding phase maps from iterative phase retrieval. (inset in Fig. e) Gray values illustrate the phase shift radians. The rectangular box in (f) can infer the compression of material [178].

The optical properties of single crystal diamond along <100> direction were examined by shock compression experiments from 60 to 550 GPa. Diamond can retain its transparency during both compression and the subsequent release process when the applied stress is below HEL. The transparency limit of diamond at 532 nm is about 170 GPa according to the experimental results. However, between HEL and the transparency limit pressure, diamond is transparent only in the compression process. McWilliams [138] reports HELs for diamond varying from 60 GPa (for [111]) to 80 GPa (for [100]). It loses its transparency gradually during the release process following shock. The refractive index of single crystal diamond along <100> is observed to increase as density increases to the transparency limit, while in static compression experiments the refractive index decreases when pressure increases up to 40 GPa [179]. The significance of these optical properties is for developing diamond as the premier material for shock impedance windows in

velocity measurements during dynamic compression experiments. When the shock pressure in diamond is below 170 GPa, diamond is transparent, which enables it to be used as an optical window. The shock compression state of a material can be explored by the density dependence of the diamond refractive index using a diamond window. Above 170 GPa, the formation and growth of defects lead to polycrystallization during the compression process, making diamond opaque in the early shock propagation stage. There are distinct differences between the polycrystallization process of diamond under shock compression below and above 170 GPa [180].

High pressures are believed to induce methane pyrolysis, resulting in the separation of carbon and potential formation of a diamond or metallic layer. The response of multi-layered diamond at pressures 300-900 GPa was studied by laser-driven planar shock compression under extreme high pressure and temperature conditions. The experimental results by Jakubowska et al. [181] show that a reflecting state of the material was generated by the shock propagation, which agrees well with 1D radiative hydrodynamic simulations using different EOS for diamond. No significant changes in shock velocity were observed although the shock pressure is not retained over time due to the short duration of the laser pulse. This reflecting state of diamond is due to electrons being thermally excited into the conduction band. These quasi-free electrons exhibit plasma-like behavior and can reflect the probe beam when the density is higher than the critical density associated with the VISAR laser wavelength [181].

The HEL is an essential measure of material strength under high strain rate shock compression [153]. As mentioned earlier, when subjected to a high amplitude shock stress higher than the elastic limit, the material transitions from a one-dimensional elastic deformation to a three-dimensional plastic deformation to rapidly dissipate shear stress [182]. The mechanical properties of a fine-grained polycrystalline bulk diamond differ significantly from those of a single crystal,

in spite of being the same material [1, 183]. The same phenomenon is characteristic of metals and is expressed through the Hall-Petch relationship. Bulk nanopolycrystalline diamond (NPD) has been reported to have the highest Vickers hardness [184] and HEL [150] of all diamonds. It is essential to know how nanograins deform under high strain rate compression for developing high-strength materials and their applications under extreme conditions. The laser shocked nano-grain reinforced polycrystalline diamond experiments were conducted using *in-situ* femtosecond XRD using an x-ray free electron laser (XFEL) beam [185] to understand its dynamic elastic-plastic transition deformation processes and strength evolution. Shock compressed NPD with an average grain size of 10-20 nm [184] is ideal to study how materials reinforced by grains lose their strength. Grain boundary strengthening is believed to play an important role because the strength of shock compressed NPD is larger than that of single crystal and micro polycrystalline diamond (MPD). Under shock compression, some brittle materials lose their strength immediately after the pressure exceeds the HEL [163, 186], while others have a brittle-ductile behavior [187]. Whether diamond behaves brittlely or ductilely under shock compression is largely unknown [138, 145]. However, NPD exhibits some ductility by showing considerable strength at applied stresses much higher than HEL until it finally reaches zero at ~700 GPa from XRD experimental results. Figure 1.63 shows transverse and longitudinal strains measured from the diffractions from (111) planes of shocked NPD and compares them with MPD [145, 188]. Whereas MPD tracks the strain in hydrostatic compression, NPD shows a considerably higher longitudinal than transverse strains. The ability of a material under high pressure to accommodate local shear stresses in different directions determines its brittle or ductile response. Figure 1.64 shows the strengths of shock compressed NPD, MPD [145, 188], and single crystal diamond [138]. The strength of NPD under shock compression in the volume deformed plastically is retained until the plastic wave exceeds

the elastic wave, producing a single shock wave which instantly compresses the material to the peak pressure. These conditions of overtaking suggest that the strength observed in the volume deformed plastically at lower pressures could be a remnant of the strength present in the prior volume deformed elastically. Even a strong material like diamond loses its strength so quickly that the original lattice transitions into complex dynamics under dynamical high pressure compression [189].

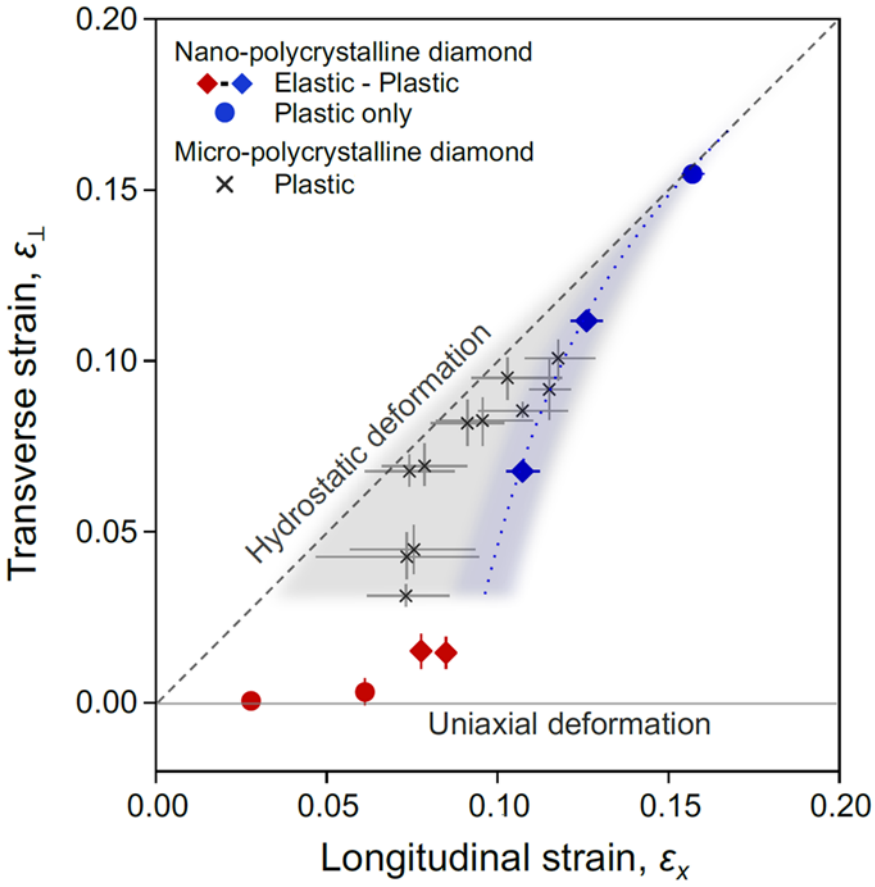

Figure 1.63 Evolution of transverse and longitudinal strains in diamond under shock compression. Purely elastic and plastic responses of shocked NPD are marked by red and blue circles, respectively. Continuous elastic-plastic deformations of NPD are marked by red and blue diamonds. Plastic deformation responses of MPD are marked by black crosses [145, 188]. Blue and grey shaded areas and the blue dotted curve indicate NPD and MPD are different [189].

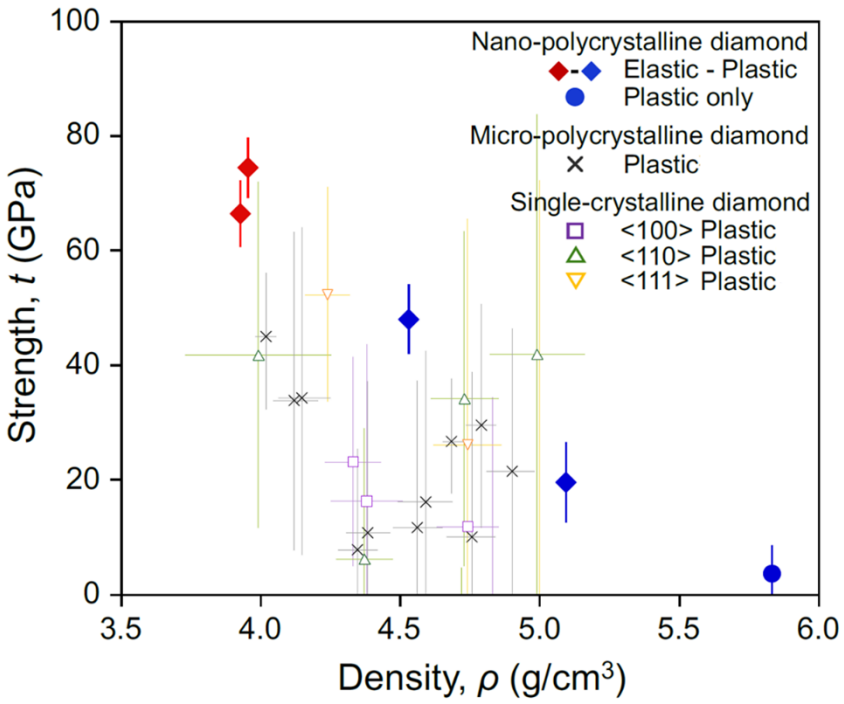

Figure 1.64 Strength of shock compressed diamond. The responses of single crystal diamond along three different directions are marked by open symbols: <100> (purple square), <110> (green triangle), and <111> (yellow reverse triangle) [138]. Other colored symbols are identical as in Figure 1.63 [189].

1.2.4 Dislocation Velocities in Extreme Deformation

Dislocation motion has been studied for over 60 years, but their maximum velocity is still unknown. Speed limits are suggested by models and simulations for dislocation motion, in the subsonic to transonic boundary, where the dislocation self-energy diverges. Nevertheless, these models do not exclude the potential occurrence of transonic dislocations. There is a second barrier in the transonic-supersonic boundary. The ultrafast dislocation movement in single crystal diamond generated by shock compression was tracked by femtosecond x-ray radiography [190,191]. The leading edges of partial dislocations move transonically as evidenced by the observation of stacking faults extending at speeds exceeding the slowest sound speed. It is important to understand the maximum mobility of dislocations in crystals for precise modeling,

prediction, and manipulation of their mechanical properties, particularly under extreme conditions [192, 193]. High strain-rate sensitivity is exhibited by many materials [194] even though dislocation-mediated plasticity is insensitive to the strain rate in some cases [195].

Materials deform by dislocation motion at near sound speed under the highest strain rates. Theoretical dislocation models suggest that the self-energy and dislocation stress diverge when a dislocation travels near the threshold velocities within a specific crystal [196–199], indicating that dislocations are forbidden to move beyond the limiting speeds. While the limiting speeds for dislocations are the same as the transverse and longitudinal sound speeds in isotropic single crystals [200, 201], they are on the same order of magnitude but not exactly the same for the anisotropic single crystals like diamond. Many theoretical models and MD simulations have demonstrated transonic or supersonic dislocation motion, suggesting that these limiting speeds may not be the upper limit for dislocation motion [196, 202–208]. Transonic and supersonic dislocations were discovered via MD simulations in silicon and germanium by Hahn et al. [209] and Zhao et al. [210]. However, transonic (between longitudinal (c_1) and two transverse ($c_1 \geq c_3$) sound speeds) or supersonic (faster than longitudinal (c_1) and two transverse ($c_1 \geq c_3$) sound speeds) motion of dislocations has not been found in a real crystal experimentally prior to the work by Katagiri et al. [190]. At strain rates higher than 10^7 s^{-1}, shock compression can generate dislocations whose initial speed exceeds the limiting speed due to the discontinuity of energy at the shock wavefront. Shock-induced transonic dislocation motion in single crystal diamond is demonstrated experimentally by femtosecond x-ray radiography [190]. The peak shock pressures were 184 ± 16 GPa and 92 ± 15 GPa along [100] and [110] orientations, respectively, which are high enough to induce yielding in diamond [138], resulting in strong shear stresses which trigger failure mechanisms. The shock wavefront splits into a preceding elastic front and a following plastic front

where dislocations propagate during shock compression. These are captured by x-ray radiography along the [110] orientation, moving across the diamond sample from the lower to the upper part of Figure 1.65. Shock induced amorphous bands diagonal to the shock wavefront were observed in other brittle materials [86, 94, 95, 210-213,]; however, the estimated temperature in shocked diamond is below 20% of the melting point, which is insufficient to induce amorphization. The possibility of phase transition is also minimal since the applied stress is significantly below the threshold of phase transformation [214, 146]. Transonic dislocations can be induced at energy or displacement discontinuities present at a shock wavefront [215, 216]. A perfect dislocation splits into partial dislocations under these conditions, resulting in a stacking fault in between which expands the plastically deformed volume [217, 218]. In Figure 1.66, the presence of stacking faults is in the form of discontinuous lines, suggesting that the dislocations propagate along with the plastic wavefront from the side of the diamond surface shocked by laser. Figure 1.65 shows in [110] shock direction, the bands do not appear in the plastic wavefront center, because the majority of the dislocations propagating with the plastic wavefront are from the limited region of the diamond surface shocked by laser. This suggests that the number of newly formed dislocations at the plastic wavefront is much less than those originated from the shocked diamond surface. In Figure 1.67, dislocation velocity (v_d) and longitudinal and transverse sound speeds (c_1, c_2, and c_3) of diamond are shown as a function of the density for the [110] orientation [219]. The dislocation velocities of [100] and [110] both are within the transonic regime (i.e., between c_1 and c_3). Such ultrafast dislocation motion has significant influence on the mechanical properties of materials. Since dislocation motion propagates with the plastic wavefront, increasing the shock stress to induce a faster plastic shock wave has the potential to accelerate dislocation motion even further. This opens the possibility for experimental studies of the existence of supersonic dislocations in a

real crystal. Microscopic dislocation motions could potentially impact macroscopic dynamics of elastic-plastic deformation. The experimental investigation of transonic dislocation motion gives insights into the ultrafast deformation mechanisms under extreme conditions [190, 220].

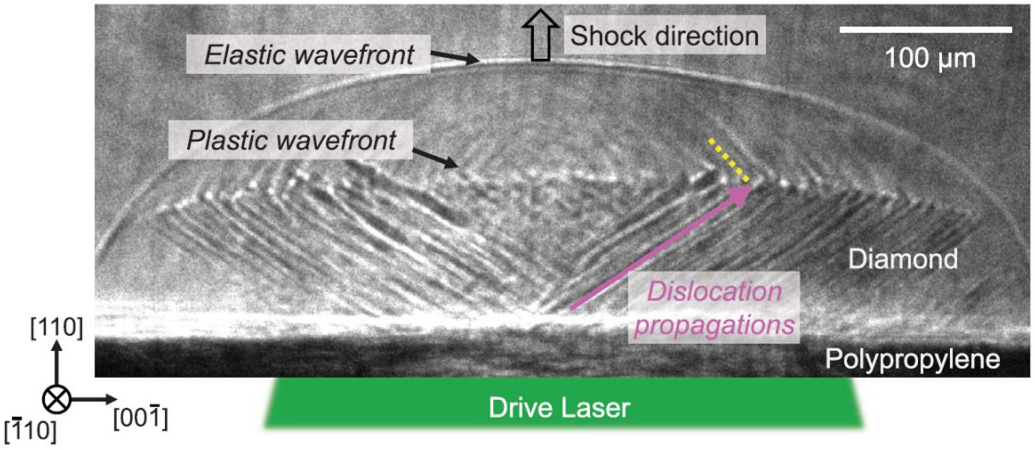

Figure 1.65 Femtosecond x-ray radiography image of diamond under shock compression. The elastic-plastic shock wavefronts travel in the shock direction. Dark and bright bands behind the plastic wavefront are stacking faults defined by partial dislocations propagating with plastic shock wavefront marked by the magenta arrow. The yellow dotted line highlights the phonon radiation [190].

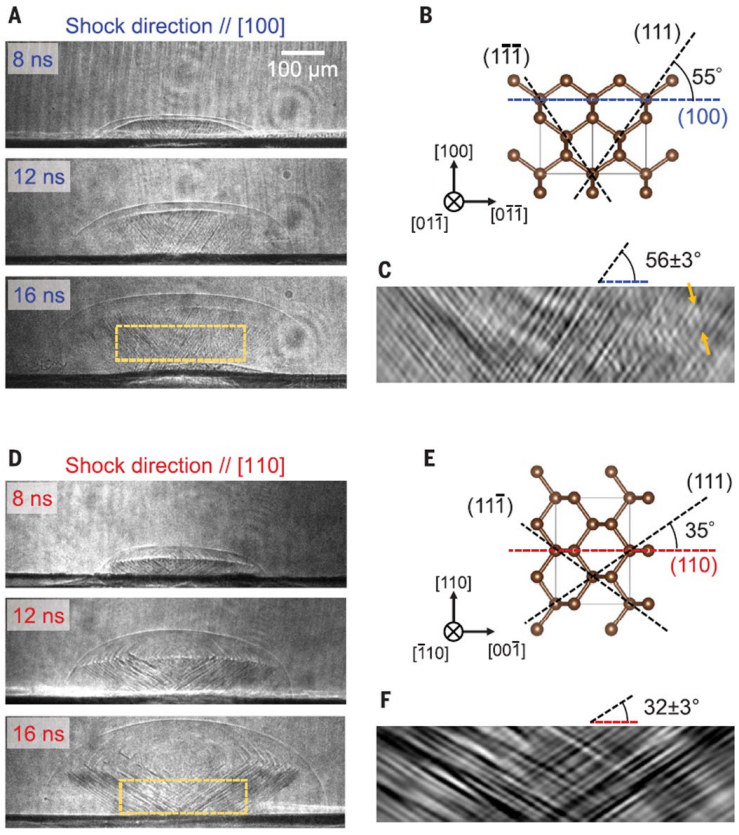

Figure 1.66 Illustration of stacking faults in shock compressed diamond. (A) X-ray radiography images of [100] shock orientation. The corresponding XFEL probe delay to the laser irradiation is marked on each image. (B) Lattice of diamond without distortion marked by corresponding plane orientations [221]. (C) Fast Fourier transform (FFT)–filtered image of stacking faults corresponding to the region marked by the yellow dashed rectangle at 16 ns in (A). The orange arrows highlight one of the bands nonparallel to 111 planes. (D) X-ray radiography images of [110] shock orientation. (E) Lattice of diamond without distortion exhibiting the plane orientations. (F) FFT filtered image of diamond shocked along [110] direction at 16 ns [190].

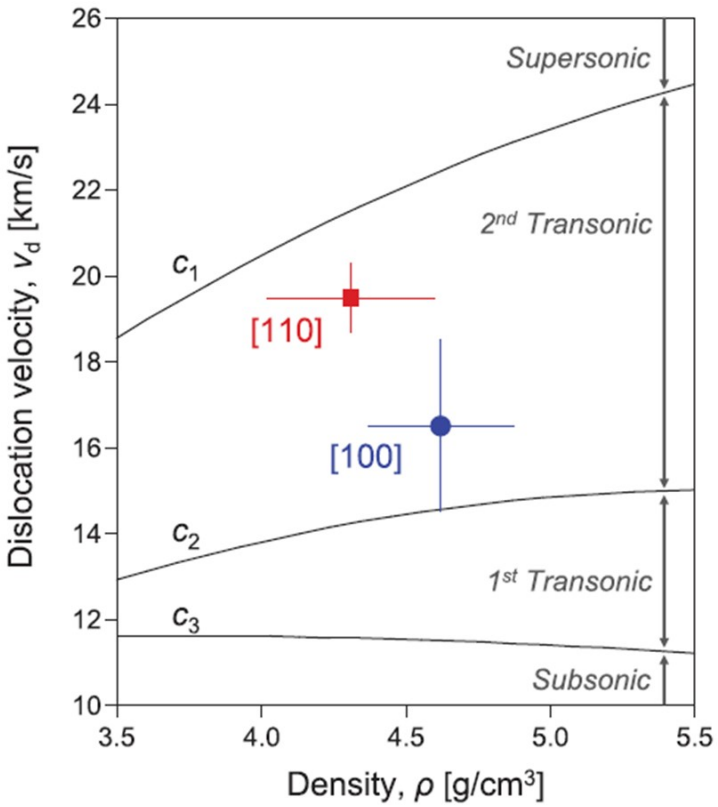

Figure 1.67 Calculated and experimentally determined dislocation velocity v_d and longitudinal and transverse sound speeds (c_1, c_2, and c_3) of [110] diamond versus the density. [190].

However, different interpretations of the claims of stacking fault formation and transonic dislocation motion emerged. It is argued that a brittle fracture response rather than dislocation-mediated plasticity for inelastic deformation prevails in laser shock compressed single crystal diamond [222]. Thus, brittle failure such as cracking would be an alternative deformation mechanism because direct imaging of stacking faults is too weak to be observed via the technique used by Makarov and Katagiri et al. [190, 191]. Hawreliak et al. [222] believes that the linear features in Figures 1.65 and 1.66 are not attributed to x-ray scattering caused by stacking faults or dislocations. Instead, they are due to the enhanced contrast from cracks along {111} planes via phase contrast imaging. However, this is an open question.

1.2.5 Ramp (Quasi-Isentropic) Compression

Shock compression can generate significantly higher pressure than static compression. But the temperature rise generated by shock is so significant that above hundreds of GPa typically only fluid properties are probed into. Ramp-wave compression methods (quasi-isentropic compression) extend the pressure range for solid-state physics into the TPa regime [165, 214, 223]. Diamond was ramp-compressed to a peak pressure of 1400 GPa, and the stress-density relation along this ramp compression path was examined up to 800 GPa. Brittle materials often lose strength catastrophically when shock compression exceeds the elastic yield. However, experimental results indicate that diamond is stable and still has significant strength under ramp compression to at least 800 GPa [164].

1.2.6 Static Compression

Dislocation mediated plastic deformation in submicron single crystal diamond pillars via in situ mechanical testing by transmission electron microscope (TEM) was observed at room temperature by Nie et al. [224]. Dislocation generation and propagation were induced by the confinement-free compression. Figure 1.68 shows the evolution of a diamond nanopillar under compression test. Atomic resolution images show that mixed-type dislocations slipping are activated in the non-close-packed planes {001} with Burgers vectors 1/2<110> uniaxially compressed along <110> (Figure 1.69A) and <111> orientations. As for the <100> orientation compression (Figure 1.69B), typical dislocations are activated in the {111} planes, exhibiting strong orientation dependence. These findings give novel insights into the mechanical response of diamond and prompt reconsideration of the fundamental deformation mechanism of diamond and in other brittle covalently-bonded materials at low temperatures. The {100}<110> slip system has hardly been identified in FCC crystals at room temperature. Figure 1.70 (A) shows the calculated

stress-strain curve which drops at 27% strain of diamond under [111] uniaxial compression, Figure 1.70 (B) exhibits its shear modulus $G_{[011](100)}$ and resolved shear stress $\tau_{[011](100)}$ for the {100}<110> slip system. The contrast between the brittle and ductile responses in diamond is explained by the competing mechanisms of Griffith cleavage [225] and plastic shear occurring at a crack tip. The strong C-C covalent bond must be broken to generate dislocations in diamond. At room temperature, breaking the C–C covalent bonds results in cleavage fracture rather than slip. In general, the initial dislocation density in diamond is several orders of magnitude lower than that in metals, making it extremely difficult to deform plastically before cleavage sets in at room temperature [162, 226]. The stress state of a material plays a significant part in plastic deformation. High hydrostatic pressure can inhibit propagation of microcracks and trigger dislocation slip in diamond [227, 228]. The hydrostatic pressure to initiate the plastic deformation is predicted to be as high as hundreds of GPa [227], which may be achieved by indentation [229, 230] and diamond anvil cell [231, 232]. Dislocations on the {111}<110> slip systems were observed near the Knoop indentation [230], though these dislocations might pre-exist in diamond before the indentation [233]. Developments of in situ mechanical tests via electron microscopy have enabled the investigation of elastic deformation [234–236] and the direct observation of microstructural evolution in real time [237]. Both {001}<110> and {111}<110> slip systems can be triggered along different orientations. It is surprisingly easier to initiate dislocations on {001}<110> slip systems than {111}<110>, even though {111}<110> is more common in most FCC crystals. The distinctive dislocation activities in diamond are not only due to its Schmid factor but are ascribed to its intrinsic nature such as lattice parameter and C–C bonds [224]. The lack of defect generation for diamond shocked up to 69 GPa in [001] direction in pulsed laser shock compression experiments is also corroborated by TEM results of Li et al. [238]. The crystallinity of the single

crystal diamond was perfectly preserved, with no plastic deformation observed and its corresponding electron diffraction pattern of the area confirmed the perfect crystalline order.

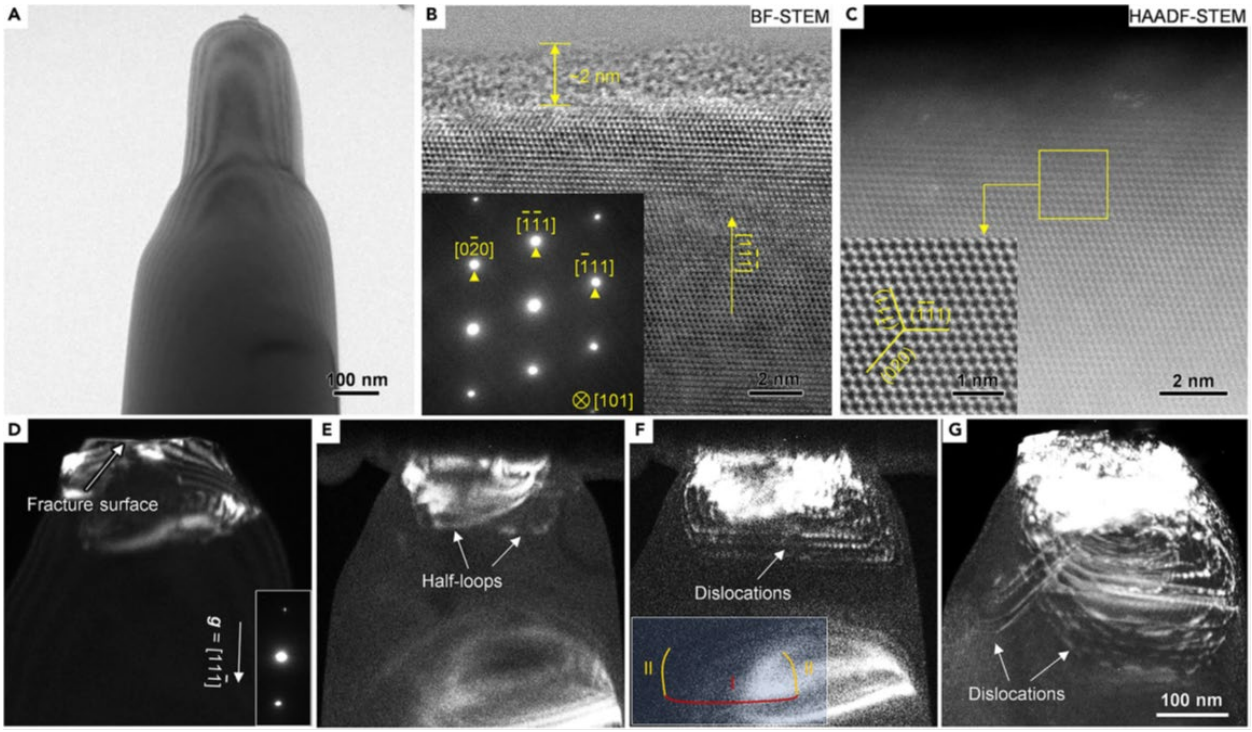

Figure 1.68 TEM images of a diamond nanopillar compressed along [111] direction. (A) Bright field image of a diamond nanopillar prior to compression test. (B) Atomic resolution bright field image. Inset of (B) is a selected area electron diffraction (SAED) pattern. (C) High-angle annular dark-field scanning TEM (HAADF-STEM) images. Inset of (C) is magnified atomic resolution HAADF image. (D)Weak-beam dark field TEM image of the diamond nanopillar after the thinner head of the nanopillar partially fractured from the thicker shoulder owing to stress concentration. (E) Dislocation half-loops originated from the fracture surface under compression. (F) Dislocation half-loops multiplied and propagated. Inset of (F) indicates half-loops with the head segment marked by red (I) and arm segment by orange (II). (G) Dislocations activated in multiple planes [224].

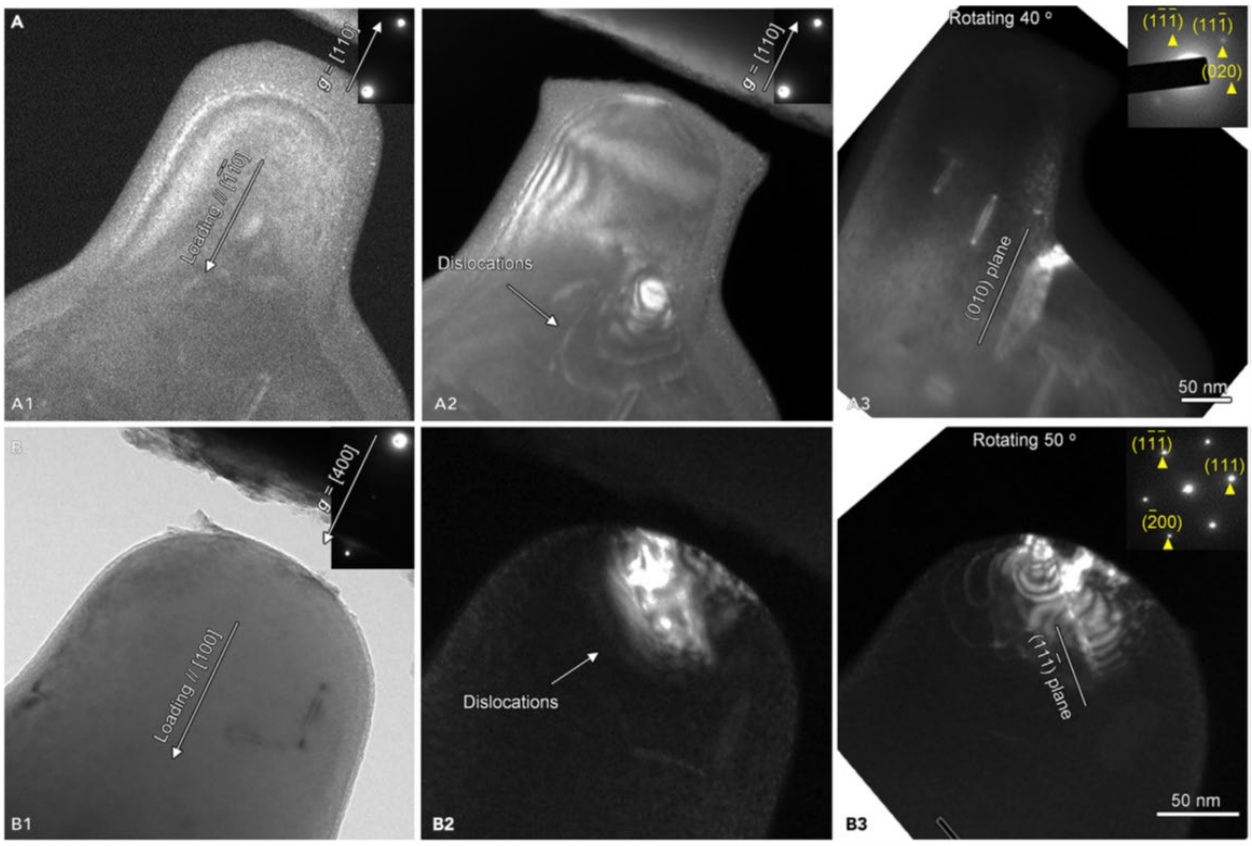

Figure 1.69 Dislocations under different loading orientations in diamond. (A) Dislocations are activated along <110> orientation (A1 and A2). The slip plane is rotated to present its edge-on view (A3) and identified as (010) plane. (B) Dislocations are activated along <100> orientation (B1 and B2). The slip plane is rotated to present its edge-on view (B3) and identified as (111) plane [224].

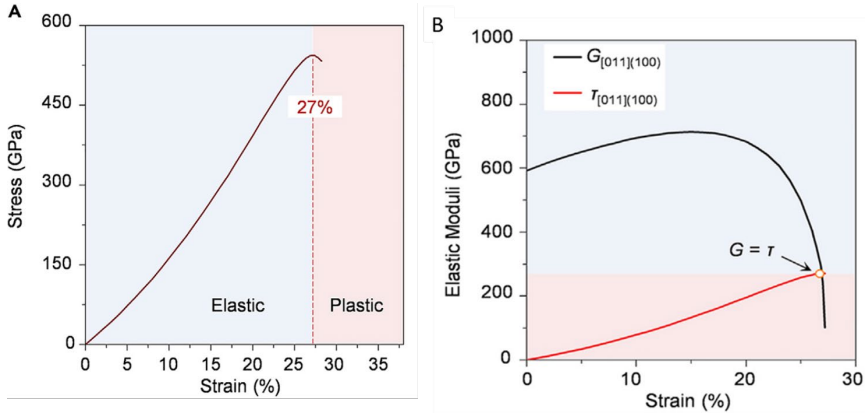

Figure 1.70 (A) Theoretical stress-strain curve of compressed diamond along [111] orientation. The first stress drop/plateau occurs at 27% strain and corresponds to the onset of plasticity. (B) Shear modulus $G_{[011](100)}$ and resolved shear stress $\tau_{[011](100)}$ of the {100}<110> slip system [224].

Table 1.5 is a summary of the shock, ramp, and static compression experiments.

Table 1.7 Shock, ramp (quasi-isentropic), and static compression of diamond

Authors	Method	Orientation	Pressure (GPa)	Year
Shock compression				
Kondo et al. [141]	Gas gun flyer plate	Intermediate direction between <111> and <110>	191 and 217	1983
He et al. [168]	Shock wave compression by the high velocity impact of an Al foil plate driven by a pulsed laser beam.	Polycrystalline with random orientation	54, 70, 80, 142, 196	2002
Brygoo et al. [148]	Laser shock	[100]	500 to 1500	2007
Knudson et al. [146]	Shock-wave experiments using a magnetically driven flyer-plate	Polycrystalline	550 to 1400	2008
Eggert et al. [239]	Laser shock	Single-crystal and polycrystalline, with little preferred orientation.	600 to 4000	2009
McWilliams et al. [138]	Laser shock	<100>, <110>, <111>, and polycrystalline	Up to 800	2010
Lang et al. [136]	Two-stage gun	[100]	~90 and ~120	2010
Lang et al. [135]	Powder gun or two-stage gun	[100], [110], and [111]	Up to 120	2011
Schropp et al. [178]	Laser shock	Polycrystalline	N/A	2015
Lang et al. [137]	Single-stage powder gun and a two-stage gun	[110] and [111]	Up to ~120	2018
MacDonald et al. [145]	Laser shock	Polycrystalline	Up to 300	2020
Winey et al. [144]	Plate impact experiments	[100], [110], and [111]	Up to ~900	2020
Katagiri et al. [150]	Laser shock	<100>	60 to 550	2020
Jakubowska et al. [181]	Laser shock	[100]	300 to 900	2021
Katagiri et al. [189]	Laser shock	Nanopolycrystalline	Up to 707	2022

Table 1.8 Shock, ramp (quasi-isentropic), and static compression of diamond (Continued)

Katagiri et al. [190]	Laser shock	[100], [110], and [111]	184 ± 16 and 92 ± 15	2023
Ramp (quasi-isentropically) compression				
Bradley et al. [164]	Ramp compression	Polycrystalline	Up to 1400	2009
Smith et al. [165]	Ramp compression	Polycrystalline	Up to 5000	2014
Lazicki et al. [214]	Ramp compression	Polycrystalline	Up to 2000	2021
Static compression				
Nie et al. [224]	Nanopillar confinement free compression	<100>, <110>, <111>	N/A	2020
Dubrovinsky [240]	Static DAC	-	Up to 600	2012

1.3 Literature Review on $CaTiO_3$ Perovskite

1.3.1 Introduction to $CaTiO_3$ Perovskite

The lower mantle makes up about 55% of the Earth's volume. The volume fraction of perovskite in the Earth lower mantle is estimated to be above 70% [241]. The major silicate perovskites are $(Mg, Fe)SiO_3$ (orthorhombic, bridgmanite) [242, 243] and $CaSiO_3$ (high-pressure phase known as davemaoite) [244], which are the primary components of the lower mantle and likely the most abundant minerals on the Earth [245, 246]. Plastic deformation in minerals of the lower mantle can lead to seismic anisotropy, and studying these mechanisms in perovskite as a function of pressure and temperature is therefore important for understanding the Earth's interior and deep geophysical processes [247].

The study of the mechanical properties and lattice defects of $(Mg, Fe)SiO_3$ perovskite under standard laboratory conditions is not feasible because this phase is unstable at ambient conditions and under the electron beam in TEM [248, 249]. The extreme conditions in the lower mantle make experiments on these minerals highly challenging. An alternative way is to use analogue materials

with similar crystallographic structures but different chemistry compositions, which are easier for experimental study. Insights from these analogues can be extrapolated to predict the response of the materials in the deep portion of the Earth. Typically, analogue materials have similar phase diagrams and cations charges but differ in their symmetries [250, 251]. Substitutions at both cation sites are common; consequently, natural perovskites can deviate significantly from ideal stoichiometry [252]. This method has proven effective in elasticity studies. It has been shown that materials with the same crystal structure and similar chemical bonding have similar mechanical response [253].

Perovskite has the ABX_3 structure with A and B cations having a variety of charges. The idealized perovskite structure is cubic (space group Pm3m), which has a network of corner-linked BX_6 octahedra with the large A cations located in the cavity formed by eight BX_6 octahedra. However, as the size of the A cation decreases, the B-X-B links have to bend to maintain contact between cations and anions because the A cations become too small to remain in contact with the anions in the cubic structure. This tilting of BX_6 octahedra is determined by the A and B cation sizes, described by the tolerance factor, and reduces lattice symmetry at lower temperatures [254]. Most oxide perovskites are cubic at high temperatures but distorted to lower-symmetry forms such as orthorhombic (Pbnm) at lower temperatures due to atomic displacements. $CaTiO_3$ is isostructural with $MgSiO_3$, as both are $A^{2+}B^{4+}O_3$ perovskites and thus have the same space group at ambient conditions, transitioning from orthorhombic to tetragonal and to cubic as temperature increases [245,249]. They exhibit similar distortions because the SiO_6 and TiO_6 octahedra have similar rotation angles, indicating that $CaTiO_3$ is a structural analogue for $MgSiO_3$ for dislocation glide [251]. The lattice parameters of the $CaTiO_3$ orthorhombic structure (space group Pbnm) used

in this study are a = 0.538 nm, b = 0.544 nm and c = 0. 7639 nm at ambient condition (from Crystallography Open Database).

$CaTiO_3$ transitions from the orthorhombic to the tetragonal structure at around 1385 K and then to cubic at about 1520 K, resulting in changes in its creep properties. The temperature dependence of lattice parameters supports these phase transitions. Thus, $CaTiO_3$ can act as a useful analogue for exploring the high-temperature deformation mechanisms of silicate perovskite due to its structural similarities and phase transition behavior [249].

First-principles calculations predict that the $CaTiO_3$ Pbnm orthorhombic perovskite structure transforms into a post-perovskite Cmcm $CaIrO_3$ phase at 32.7 GPa, and then transitions to a post-post–perovskite structure at 71.7 GPa as pressure increases [255]. Guennou et al. [256] demonstrated that $CaTiO_3$ retains its Pbnm perovskite structure up to 60 GPa under diamond anvil cell experiments at room temperature. However, Truffet et al. [257] proposed that $CaTiO_3$ dissociates into CaO and $CaTi_2O_5$ at pressures above 60 GPa and temperatures up to 4500 K instead of transforming into a post-perovskite phase.

Deep-focus earthquakes typically occur in depth from 300 to 700 km from Earth's surface, where minerals are subjected to extreme pressures and temperatures. Phase transformations, shear, and defect movements of minerals within subducted plates may be the causes of deep-focus earthquakes. This study may help to understand Earth's internal structure and behavior at such depths and decipher Earth's mantle dynamics with the shock waves involved in this process.

In summary, exploring $CaTiO_3$ within a pressure range suitable for experimental studies provides insights into ultra-high-pressure phenomena involved in planetary interiors, which are beyond the scope of experimental mineral physics. Thus, the main focus of the work presented

herein is to generate, through high amplitude pulsed lasers and use of a suitable simulant to (Mg, Fe)SiO_3 perovskite, a regime having similar pressure and temperature to the lower Earth mantle.

1.4 Literature Review on Olivine (Mg, Fe)$_2SiO_4$

1.4.1 Introduction to Olivine (Mg, Fe)$_2SiO_4$

Laser-induced shock compression was used to drive olivine to high pressures relevant to the Earth's mantle. Other covalent materials (Si, Ge, SiC, B_4C, and diamond) have been studied in similar conditions and were found to exhibit signs of pressure-induced amorphization. We continue this study of amorphization in covalently bonded materials to reveal a potentially new high pressure deformation mechanism. The materials and pressures of interest are comparable to the ones in the Earth' mantle. High-pressure instabilities resulting from a phase transformation/amorphization have been proposed as a source of some deep-focus earthquakes by Markenscoff [85]. This collapse of the structure at high pressures was explored to pressures of the earth mantle (24-136 GPa). Olivine has a strong covalent component of bonding and high Peierls-Nabarro stresses. These make the generation of dislocations difficult and therefore more likely to favor amorphization as an alternative mechanism.

Laser shock compression experiment conducted in a ride-along campaign was analyzed, showing that amorphization forms along preferred bands that correspond to concentrated plastic deformation. It is not likely that olivine melts and our calculations suggest that this is solid state amorphization [104, 258]. These experiments were conducted on four covalently bonded elements and compounds: Si, Ge, SiC, and B_4C. Atomic resolution transmission electron microscopy of the recovered specimens was also conducted for the four covalently bonded elements (Si, Ge) and compounds (SiC, B_4C). The amorphous bands are clearly seen for the four materials. This line of research is continued, with experiments followed by characterization and analysis.

Jeanloz et al. [78] were the first to observe that shock compression can amorphize olivine at a pressure above 56 GPa. This amorphization occurred in regions with high dislocation density. The thickness of these amorphous bands decreases with distance from the surface and eventually disappears at a certain depth, which is coincident with the decay of the shock wave and indicates that there might be a critical stress for the onset of amorphization.

Olivine is one of the most abundant minerals in the Earth's mantle. In the upper mantle (depth:< 410 km, pressure: < 14 GPa) olivine is the primary stable structure. Olivine has an orthorhombic structure. The structure of olivine is more complicated. It comprises silicate tetrahedra composed of silicon and oxygen atoms, and these silicate tetrahedra are surrounded by two different kinds of cations, one is magnesium cations, the other is divalent iron cations. Inside the silicate tetrahedra it is covalent bonding, while between these silicate tetrahedra and magnesium and iron cations, the bonding is ionic. Olivine has a negative Clapeyron slope, indicating its melting point decrease with increasing shock stress. This is due to its open structure, which collapses upon melting to a higher density. At larger depths and higher pressures (410-660 km, 14-24 GPa) olivine transforms to its higher-pressure polymorphs: wadsleyite and ringwoodite which have an orthorhombic and spinel structure, respectively. In the deepest region of the mantle (depth: 660-2900 km, pressure: 24-125 GPa) these polymorphs decompose into perovskite and post-perovskite at the highest pressure. Understanding how these materials deform at high pressures can help us explore the deformation mechanisms in the extreme conditions of the Earth's interior. In the upper mantle subduction zones are continuously pushing material into the Earth, causing enormous shear forces. As the material is pushed deeper, the temperature also rises, and mantle convection becomes predominant. All the mantle materials experience extreme deformation that induces phase transformations, anisotropy, and many other anomalies that are

constantly being debated [259]. There have been numerous experimental studies on olivine deformation [260]. These studies conclude that at low strain rates ($< 10^{-5}$ s^{-1}) the prevailing deformation mechanisms are transport of matter by diffusion, transport of shear with dislocations, and motion of grain boundaries. Furthermore, some other high-pressure polymorphs of olivine (wadsleyite and ringwoodite) have high critical resolved shear stress which suggests that there must be other deformation mechanisms that control their deformation in the Earth's mantle. Determining how exactly these materials are deforming at high pressure and high strain rate will help solve many unanswered questions in this field. Olivine is one of the more common minerals found in the Earth's mantle and uncovering its deformation mechanisms at high pressures will result in a stronger understanding of the Earth's interior.

Acknowledgements

Chapter 1, in part, is a reprint of material as it appears in: B. Y. Li, A. C. Li, S. Zhao, and M. A. Meyers. Amorphization by mechanical deformation. *Materials Science and Engineering: R: Reports* 149 (2022): 100673. The dissertation author was the primary researcher and first author of this paper.

Chapter 1, in part, is a reprint of material as it appears in: A. C. Li, B. Li, F. González-Cataldo, R. E. Rudd, B. Militzer, E. M. Bringa, and M. A. Meyers. Diamond under extremes. *Materials Science and Engineering: R: Reports* 161 (2024): 100857. The dissertation author was the primary researcher and second author of this paper.

Chapter 1, in part, has been submitted for publication of the material as it may appear in: B. Li, S. Zhao, and M. A. Meyers. Plastic Deformation of $CaTiO_3$ Perovskite under Extreme Loading. The dissertation author was the primary researcher and first author of this paper.

Chapter 2 EXPERIMENTAL MATERIALS AND METHODS

High energy pulsed lasers can produce pressures up to hundreds of GPa in times on the order of nanoseconds. High energy density laser was used with specially designed recovery fixtures, enabling recovery and subsequent characterization of the shock-compressed targets. To maintain the integrity of the samples, the duration of the stress pulse needs to be shorter than the characteristic time for crack propagation generally on the microsecond scale. The short duration of the stress pulse and impedance matched encapsulation ensured the integrity of the specimen by suppressing the full development of cracks and enabled post-shock microstructure characterization. Using this methodology, shock-induced amorphization has previously been reported in Si, Ge, SiC, and B_4C.

2.1 Materials

Our Type IIas single crystal diamond cylinders were synthesized via high pressure and high temperature (HPHT) growth by Almax easyLab, with a diameter of 2 mm and a height of 3 mm. Gold and molybdenum capsules and foils were purchased and processed in the UCSD Campus Research Machine Shop (Figure 2.1). Our single crystal $CaTiO_3$ perovskite cylinder was synthesized by SurfaceNet GmbH, with a diameter of 3 mm and a height of 5 mm. Copper capsule and foil were purchased and processed at the UCSD Campus Research Machine Shop (Figure 2.2). Our Olivine $(Mg, Fe)_2SiO_4$ were natural single crystal San Carlos Arizona peridot. Titanium capsule and foil were purchased and processed at the UCSD Campus Research Machine Shop. $CaTiO_3$ perovskite, and olivine $(Mg, Fe)_2SiO_4$ have the same experimental setup.

2.2 Laser Shock Recovery Experiments

Figure 2.1 illustrates schematically the experimental set-up of the shock-recovery assembly. Specimen, capsule and recovery tube filled with Aerogel (a glass foam with a low-density of 1000 g/m^3) intended to decelerate and capture the specimen and recovery capsule. A cylindrical single crystal diamond target was encapsulated in gold and molybdenum cups. The target package consists of a 20 μm CH (polystyrene) ablator, 50 μm gold foil, Ø 2 × 3 mm cylindrical single crystal diamond target with the top and bottom surfaces lapped, and gold and molybdenum momentum traps. Before laser shock, diamond targets were encapsulated in the gold and molybdenum capsules by heating the capsules and inserting the diamond sample then allowing them to cool down to minimize the gap between the specimen and capsule, thereby confining the diamond single crystal. The acoustic impedance (product of density and longitudinal sound velocity) of gold (62.60 MPa·s/m) and molybdenum (63.12 MPa·s/m) is close to that of diamond (63.49 MPa·s/m). By matching acoustic impedances, reflected tensile shock waves are minimized while transmitted shock waves are maximized at interfaces/free surfaces. This reduces damage and limits fragmentation , thus ensuring the integrity of the specimens.

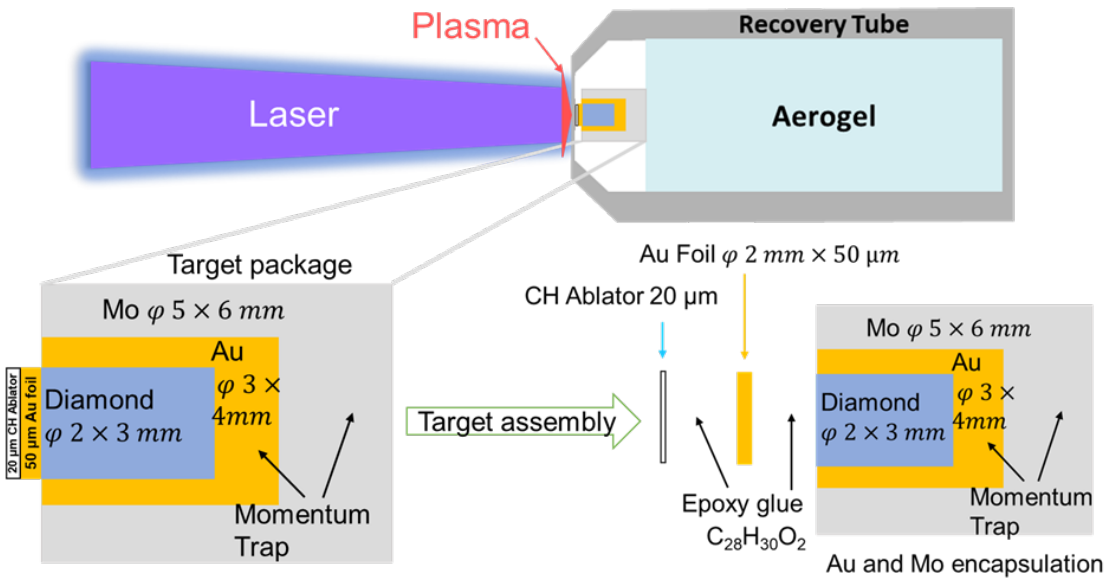

Figure 2.1 Overall experimental setup for laser shock of single crystal diamond showing the target package mounted in a recovery tube. Diamond single crystal cylinders are [001] oriented and have dimensions of Ø 2 mm × 3 mm. Magnification of the target package, showing a 20 μm CH ablator (polystyrene) and a 50 μm gold thin foil were stuck in front of the diamond sample, encapsulated in gold and molybdenum and backed by momentum trap.

The shock wave is produced by the following sequence of processes. First, the high-energy density laser, upon depositing onto the target package, vaporizes the polystyrene (CH) ablator into plasma, ablates and ionizes the gold foil on the surface. Second, the stress pulse rapidly builds up, transforms into a shock wave, and drives a compressive wave that propagates through the [001] single crystal diamond. The compression wave decays as it traverses the gold, finally arriving at the diamond target surface. This process is termed laser ablation. The ablation pressure is a function of laser parameters. The amplitude of the ablation pressure can be estimated by the analytical scaling law by Lindl [261],

$$P(GPa) = (42 \pm 3) \cdot \left(\frac{I\left(\frac{TW}{cm^2}\right)}{\lambda(\mu m)} \right)^{0.71 \pm 0.01} \quad (1)$$

where $I = E/At$ is the laser intensity, E, A, t, and λ are the laser energy, spot area, laser duration, and laser wavelength.

A high-power short-pulsed laser was used to conduct shock compression experiments on [001] oriented diamond single crystals. Laser shock experiments were conducted at Omega Laser Facility, Laboratory for Laser Energetics, University of Rochester. The sources are pulsed lasers of a 355 nm wavelength. Nominal laser energies for the experiment were 196.3, 296.5, and 401.4 J, each with a full width half max pulse duration of 1 ns and nominally square pulse shape in time. The laser spot size focused on the target package was 2.95 mm in diameter. The target was installed in a vacuum chamber and was pumped down to a pressure as low as 10^{-3} Pa during working conditions to prevent oxidation of the target and prevent absorption/scattering of the laser. The calculated shock pressures on the three diamond samples were 69, 93, and 115 GPa.

The Omega Laser Facility of Laboratory of Laser Energetics at University of Rochester was also used to shock brittle $CaTiO_3$ under extreme loading conditions. Figure 2.2 shows the sample, recovery capsule and tube filled with Aerogel. Before laser shock, a cylindrical single crystal $CaTiO_3$ target was encapsulated in a Cu cup by heating the cup and inserting the $CaTiO_3$ sample into it. They were allowed to cool down to minimize the gap between the sample and capsule, thus confining the $CaTiO_3$ cylinder. The 20 μm CH (polystyrene) ablator, 100 μm Cu foil, and Ø 3 × 5 mm $CaTiO_3$ cylinder single crystal sample were stuck together by a thin layer of epoxy glue. Shock compression subjects materials to a unique regime with a duration of nanoseconds under laser-driven loading.

The strain rate is determined by the duration of shock wave. Crack propagation is limited by the Rayleigh wave speed [262]. The ultrashort stress pulse duration (tens of nanoseconds including the shock release) is at least an order of magnitude shorter than the characteristic crack propagation time (microseconds) through the target. The impedance matched encapsulation retains

the sample's integrity by suppressing the full development of cracks, protecting it from catastrophic failure (e.g. fragmentation), thus enabling post shock characterization.

Copper was chosen as the encapsulation material due to its machinability and, more importantly, similar acoustic impedance (product of longitudinal sound speed and density) of 34.14 MPa·s/m, compared to $CaTiO_3$ of 30.3 MPa·s/m. Using this method, brittle $CaTiO_3$ was recovered without excessive cracking. Shock compression establishes a uniaxial strain state which can be decomposed into hydrostatic (elastic) stress and deviatoric (plastic) stress. The high energy laser of Omega can reach the extreme stress of the Earth's interior (mantle pressures from 24 to 136 GPa), enabling probing of the deformation mechanisms of geophysically relevant materials and conditions. Using the laser shock technique, unprecedented states with extremely high pressures, temperatures, and strain rates can be experimentally achieved.

The sources are pulsed lasers of a 355 nm wavelength. The nominal laser energy for the experiment was 200.5 J, with a full width half max pulse duration of 1 ns and square pulse shape. The laser spot size was 2.95 mm in diameter. Therefore, the initial peak shock pressure in the $CaTiO_3$ sample was 70 GPa along the [010] direction.

Olivine has the same experimental configuration and target assembly as $CaTiO_3$ (Figure 2.2). Similar acoustic impedance of titanium of 22.94 MPa·s/m, compared to olivine of 27.75 MPa·s/m was chosen.

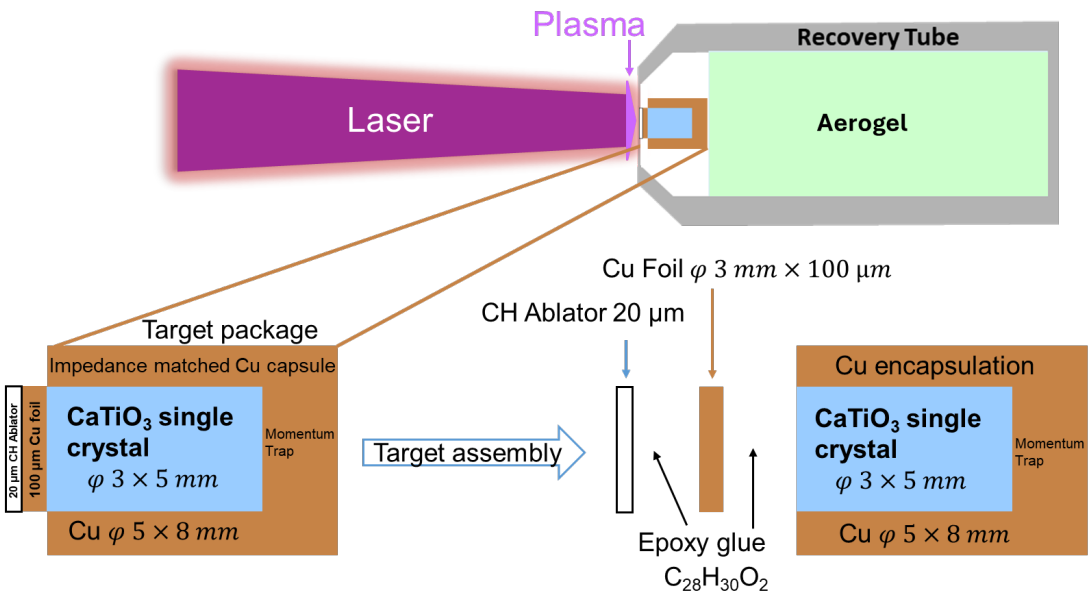

Figure 2.2 Overall experimental setup for laser shock on [010] single crystal $CaTiO_3$ illustrating the target package that is mounted in a recovery tube. Single crystal $CaTiO_3$ cylinder is [010] oriented and has dimensions of Ø 3 mm × 5 mm. Magnification of the target package, consisting of a 20 µm CH ablator (polystyrene) used to produce plasma under laser irradiation and a 100 µm Cu heat shield stuck in front of the $CaTiO_3$ sample, encapsulated in Cu cup and backed by momentum trap. The CH ablator, Cu foil, and $CaTiO_3$ sample were stuck together by epoxy glue.

2.3 Microstructure Characterization

We did not grind or polish the post-shock samples in order to protect the areas directly subjected to laser shock. Thus, the defect structure was preserved in this preparation procedure. Post-shock multi-scale microstructure analyses were carried out using different techniques.

Scanning electron microscopy (SEM) was used to characterize the surface morphology of the as-shocked samples by FEI Apreo and FEI Scios Dual Beam FIB/SEM at Nano3, UCSD.

Focused ion beam (FIB) was used to prepare very thin electron transparent foil specimens of about 100 nm for TEM. FEI Scios Dual Beam FIB/SEM was used with focused Ga ion beam for pattern/lamella milling cutting directly from the approximate center of the as-shocked surfaces at Nano3, UCSD. A thin Pt film of about 2 µm was deposited on the area of interest to protect the underneath sample. The TEM foils were ion milled at decreasing voltages of 30, 8, and 5 kV using

a Ga beam and finally polished at 2 kV to minimize damage. The defect structure survived in the procedure.

Transmission electron microscopy (TEM) is the ultimate tool to characterize materials at the nanometer scale. We used Thermofisher Talos 200X G2-S/TEM operated at 200 kV at Nano3, UCSD. Post-shock recovered microstructural characterization was carried out by conventional and high-resolution TEM (HRTEM) to study the deformation/failure mechanism of the shocked diamond, $CaTiO_3$, and olivine along the shock direction.

Acknowledgements

Chapter 2, in part, has been submitted for publication of the material as it may appear in: B. Li, S. Zhao, and M. A. Meyers. Direct observation of plastic deformation in diamond under extreme loading. The dissertation author was the primary researcher and first author of this paper.

Chapter 2, in part, has been submitted for publication of the material as it may appear in: B. Li, S. Zhao, and M. A. Meyers. Plastic Deformation of $CaTiO_3$ Perovskite under Extreme Loading. The dissertation author was the primary researcher and first author of this paper.

Chapter 3 LASER SHOCK COMPRESSION OF DIAMOND

3.1 Introduction

Diamond is an important material because of its outstanding hardness and optical properties. It has applications in far reaching technological areas, ranging from the capsules in inertial confinement fusion to cutting and polishing. Enhanced understanding of its response under extreme loading conditions is especially relevant. The high-power pulsed laser facilities, such as the Laboratory for Laser Energetics and the National Ignition Facility provide platforms for subjecting materials to regimes not attainable by any other means.

High energy pulsed laser compression generates a uniaxial strain state of stress with combined high hydrostatic and deviatoric stresses; these extreme stresses are created in short timescales in the nanosecond range. Amorphization in diamond has been predicted by Molecular Dynamics (MD) simulations [263], but never heretofore observed experimentally. Previously only dislocations under static compression were observed experimentally by Nie et al. [224] and corroborated via MD simulations under shock loading by Li et al. [238]. MD simulations by Li et al. [238] explored only a very small volume (a few nanometers side) and ultrashort times (less than 20 picoseconds). Thus, no defects were observed for loading in the [001] direction. Diamond is an inherently brittle material, lacking dislocation activity under ambient conditions. Its fracture toughness is as low as that of ceramics, and it exhibits significant crystallographic anisotropy [264]. This brittleness at room temperature makes it challenging to examine its behavior under shock conditions and complicates post-shock microscopy analysis due to sample fragmentation. When crystalline solids subjected to quasi-static stress, dislocation slip, twinning, and phase transformations are the predominant mechanisms to dissipate the applied elastic energy [265]. Under shock compression, high hydrostatic and shear stresses rapidly build up at the shock front,

promoting fast energy dissipation mechanisms. Amorphization, which may only involve localized rearrangements of atomic structures, emerges as an additional potential candidate. Shock-induced amorphization has now been reported in various materials [94, 95, 210-213, 266, 267] and hence has been established as a deformation mechanism of crystals under high-strain-rate loading. The unique combination of coupled large hydrostatic and shear stresses generated under shock compression, by nature of the uniaxial strain state imparted, plays a critical role in this transformation.

When a shock wave travels through a crystalline solid, it compresses the material and usually induces plastic deformation both at and behind the shock front [153]. In ductile materials such as metals, this process involves the formation of dislocations, stacking faults, deformation twins, and/or phase transformations [268]. In extremely brittle materials, defect-mediated plasticity is so limited that fracture often becomes the primary way to dissipate the imposed strain energy, typically resulting in catastrophic failure. Each of these mechanisms has a characteristic threshold stress and kinetics and therefore is highly strain rate dependent. The crack propagation is limited by the Rayleigh wave speed [262]. Advancements in high-power pulsed lasers have enabled the generation of high amplitude (10s to 100s of GPa) shock waves with nanoseconds pulse duration, which made it possible to explore materials science in this unknown regime.

Sufficient evidence proves that shear promotes structural changes, including amorphization. As a result, solid-state amorphization has often been approximated as introducing “free-volume” into the crystalline structure [269]. The unit cells of Si, Ge, and diamond are based on tetrahedra within a diamond cubic structure, resulting in a much lower atomic packing factor (0.34) compared to the face centered cubic (0.74) and body centered cubic (0.68) structures typical of metals. Such ‘open’ structures are inherently vulnerable to collapse upon amorphization.

It is recognized that shear stresses superimposed on hydrostatic pressure play an important role in phase transformations and solid-state amorphization. Prior work inspired our research into covalently bonded materials as a whole and their tendency to form amorphous bands under extreme conditions. Thus, the results from this study on deformation mechanisms may contribute to a more comprehensive constitutive understanding not only of diamond but also of covalently bonded materials in general.

3.2 Direct observation of plastic deformation in diamond under extreme loading

Here we present successful recovery of laser shocked diamond and identify a range of defects which culminate in the directional amorphous bands. Figure 3.1 (a) presents diamond Shock Hugoniot data from different sources [135, 138, 140, 141, 143, 145, 150, 152] and experimental pressures achieved in this study (69, 93, and 115 GPa). The calculated temperature rise associated with shock compression is provided in Figure 3.1 (b). At 115 GPa, the highest pressure in the current experiments, the temperature reaches ~494 K. The calculational procedure is provided below. This temperature rise is modest and much lower than the melting point of diamond.

The temperature rise calculations are obtained from the Rankine-Hugoniot equations [153].

$$P = \frac{C_0^2(V_0 - V)}{[V_0 - S(V_0 - V)]^2} \quad (1)$$

$$T = T_0 \exp[(\frac{\gamma_0}{V_0})(V_0 - V)] + \frac{(V_0 - V)}{2C_v} P + \frac{\exp(-\frac{\gamma_0}{V_0}V)}{2C_v} \int_{V_0}^{V} P \cdot \exp(\frac{\gamma_0}{V_0}V)[2 - (\frac{\gamma_0}{V_0})(V_0 - V)]dV \quad (2)$$

Where T_0 = 300 K, ρ_0 = 3.52 g/cm^3, $V_0 = \frac{1}{\rho_0}$ = 0.2840909 *10^{-3} m^3/kg, γ_0 = 0.9, C_v = 474.6 J/kg•K, C_0 = 18×10^3 m/s, S = 1.

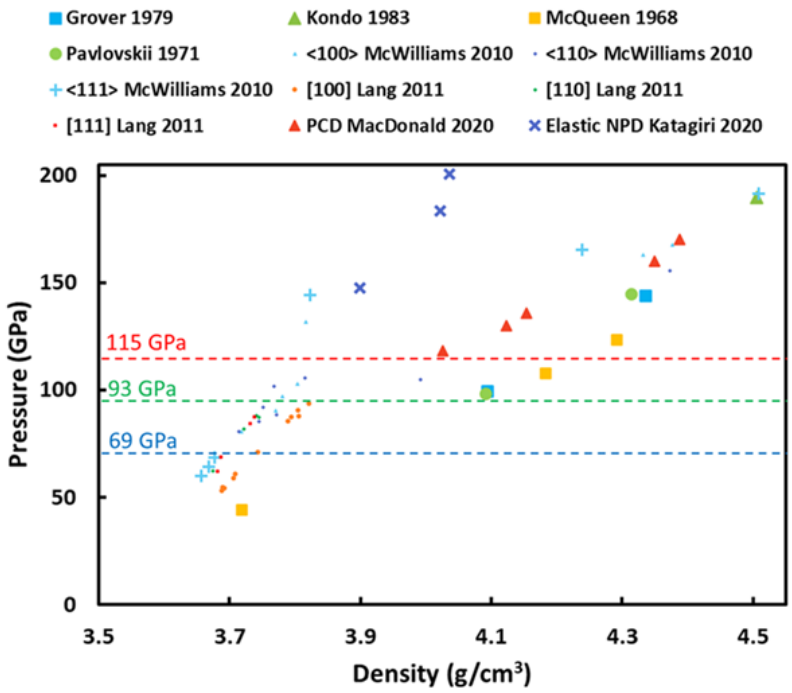

(a)

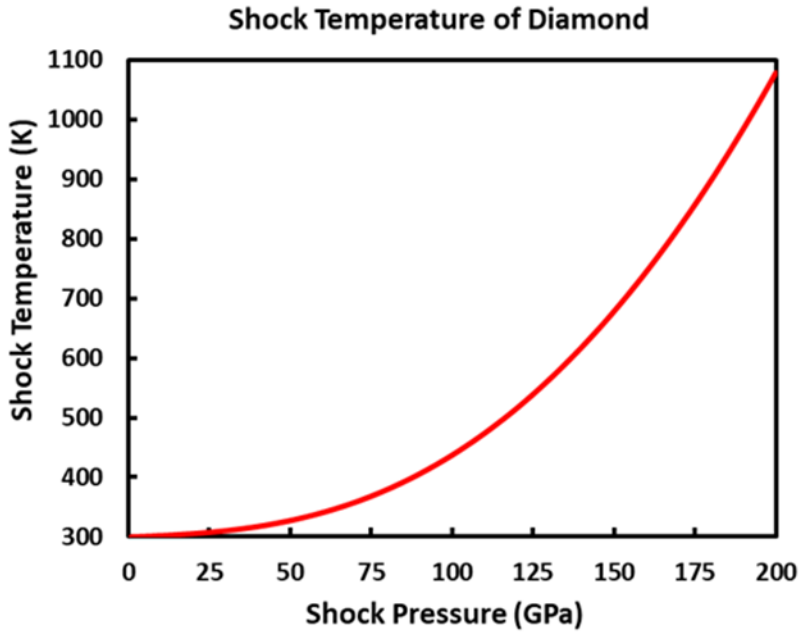

(b)

Figure 3.1 (a) Pressure vs. density for shock compression of diamond. Hugoniot data from different sources [135, 138, 140, 141, 143, 145, 150, 152] and experimental pressures achieved in this study (69, 93, and 115 GPa). (b) Calculated shock temperature as a function of shock pressure for [001] diamond.

Figure 3.2 shows SEM images of the surface appearances of [001] diamond single crystals shocked at (a) 69 and (b) 115 GPa. Micro-cracks were observed on the shock surface at 69 GPa in Figure 3.2 (a), with the crack network pattern exhibiting a clear preferential crystallographic orientation. {111} planes are the easiest cleavage planes in diamond, generating crack lines along mutually perpendicular $[1\bar{1}0]$ and [110] directions on the (001) shock surface. Although cracks formed on the surface, they did not have sufficient time to fully develop and coalesce, allowing the sample to retain its integrity.

In the sample shocked at 115 GPa (Figure 3.2 (b)), there is a crater in the center of the surface where the laser energy was concentrated. There is also an amorphous layer of tens of micrometers on the surface, which has a high concentration of O, probably from the epoxy layer to glue the gold foil to the diamond sample.

We used a high-speed diamond saw to cut near the middle of the diamond sample, and the amorphous layer was removed on one side. This enabled the extraction of a few FIB samples near the center of the surface from the edge of the crater which was cut by the high-speed diamond saw. There was a marked contrast between the structure in the edge and center of the 115 GPa specimen. The FIB samples from the edge of the specimen, below the amorphous oxidized layer, did not have any defects. This is because the laser energy is not uniform and is concentrated in the center of the specimen. This proves that the defects observed in the center are not introduced by the FIB procedure.

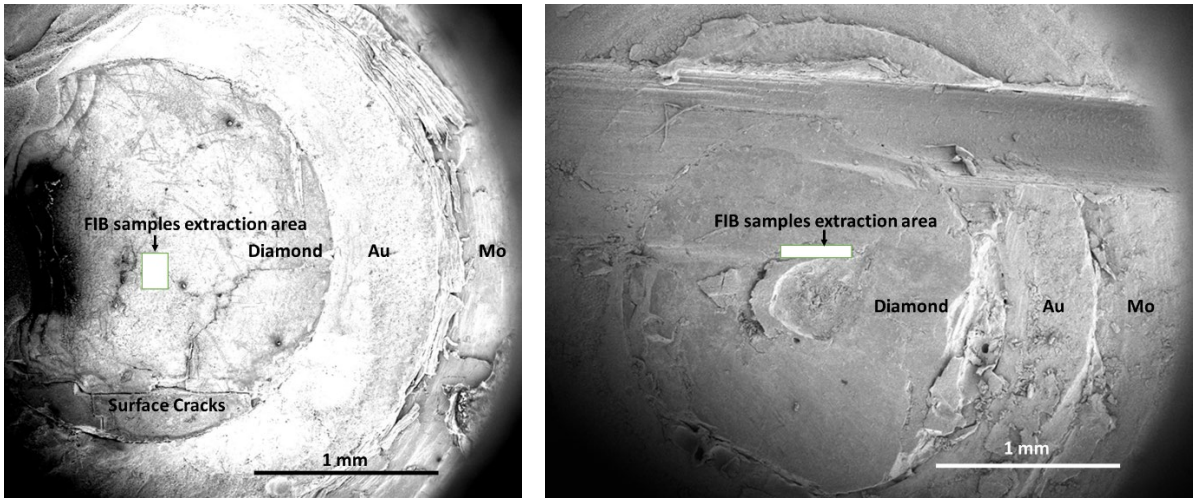

(a) (b)

Figure 3.2 SEM images of surface appearances of [001] diamond single crystals shocked at (a) 69 and (b) 115 GPa. The rectangles indicate the position of the TEM samples cut by FIB technique. The Au and Mo regions are lateral encapsulation that confine the diamond target and capture the reflected tensile pulses that would otherwise fragment the diamond.

At the lowest laser energy, 196.3 J (~ 69 GPa), diamond exhibits purely elastic behavior, i.e., neither phase transformations nor defects were observed. The significant difference in TEM images between the 69 GPa and 115 GPa samples confirms that subsequent observations in the latter are not artifacts from sample preparation by FIB. The virtually defect-free atomic structure of the 69 GPa sample is shown in Figure 3.3 (a).

The highest energy laser shock experiment generated an initial peak pressure, σ_s= 115 GPa, which is above the Hugoniot elastic limit (HEL) in the [001] direction, estimated to be in the range of 53-110 GPa [141, 138, 155]. Thus, the shear stresses are expected to be relaxed by inelastic processes. The following defects were observed and are documented in Figure 3.3 (b) to Fig. 3.4 (c).

Cleavage: {111} planes are the preferred cleavage planes in diamond, as shown in Figure 3.3 (b).

Dislocations: Figure 3.3 (c) and (d) are the bright and dark field images under the [$0\bar{2}2$] two-beam condition, showing arrays of dislocations down to 2 μm below the shock surface. These dislocations generally form in bands at orientations close to ~30˚ or ~45˚ to the shock direction [001].

Stacking faults: Figure 3.3 (e) and (f) show that sets of stacking faults are produced under applied stress and penetrate into the sample. The thickness of these planar faults varies from a few to tens of nanometers. These stacking faults intersect to generate regions of localized high strain energy. It has been reported for Si that stacking fault packets serve as precursors and favored nucleation sites for amorphization [211, 266, 267]. These planar faults nearly align with the maximum shear direction. Although most of these bands align mutually parallel, other variants are also present, often intersecting and bifurcating, to form a complex network.

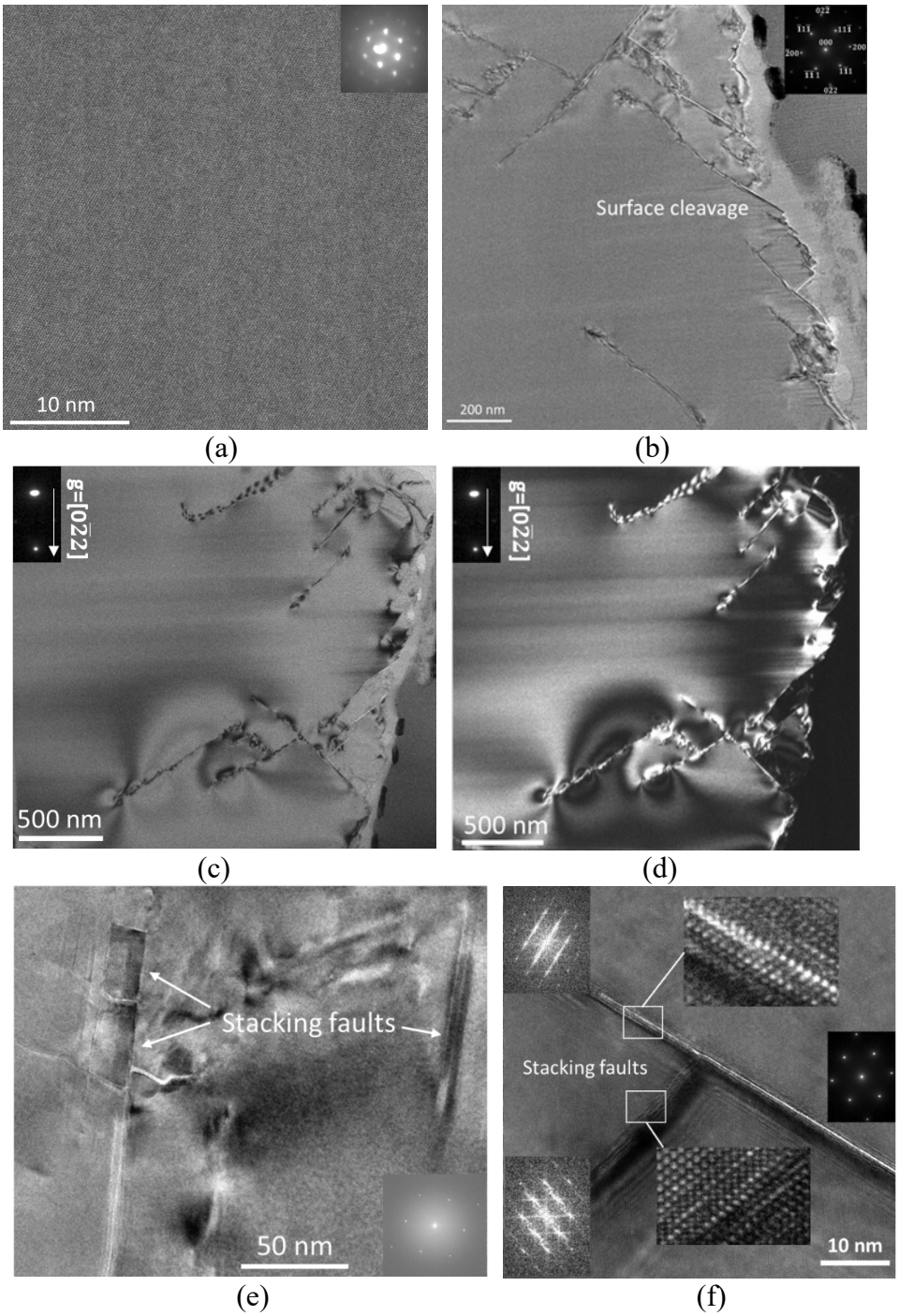

Figure 3.3 Characterization of laser shocked [001] single crystal diamonds. (a) TEM micrograph of laser shock recovered sample at 69 GPa; it is still almost purely a single crystal. The appearance of a (002) spot in the electron diffraction patterns is due to the strong double diffraction effect of {111} planes. (b-f) TEM images of laser shock recovered sample at 115 GPa. (b) Surface cleavage steps, (c) bright field image of dislocations imaged under two-beam condition, (d) dark field image of dislocations imaged under two- beam condition, (e) stacking faults at lower magnification, and (f) stacking faults at higher magnification. The faulted regions are highlighted showing the zigzag characteristic of these planar defects with corresponding FFT patterns.

Twinning: Nanotwins and stacking faults are observed near the amorphous/crystalline interface, displaying zigzag displacement as shown in the insets in Figure 3.4 (a). The faulted region is characterized by additional twin spots and streaking perpendicular to {111} reflections, aligning with the direction of stacking faults and nanotwins.

Bu et al. [270] recently demonstrated, in a comprehensive study, that deformation is significantly enhanced in [100] B_4C through mechanical twinning. They also observed a high density of deformation twins in [100] oriented diamond anvil tip at a stress of 360 GPa. They propose a new mechanism for twinning through the formation of transition layers. Observation of Figure 3.4 (a) suggests that similar layers are also present in our diamond.

Amorphization: In Figure 3.4 (b), a band of localized deformation exhibits clear amorphous characteristics, aligning approximately with the {111} slip plane of dislocations in diamond, which is close to the maximum shear surface, and forming a 45° cone. Additionally, Figure 3.4 (c) presents multiple variant bands with different orientations. Conventional TEM images and HRTEM micrograph, Figure 3.4, reveal an early stage of the formation of these amorphous bands in the crystalline lattice. The fast Fourier transformations (FFT) patterns of the amorphous, bulk crystalline and heavily faulted regions in the vicinity the amorphous bands are shown as insets in Figure 3.3 (f) and Figure 3.4. The number of bands observed is too small for a statistical analysis, and it is probable that the pressure slightly exceeds the threshold for amorphization; thus, their number is small.

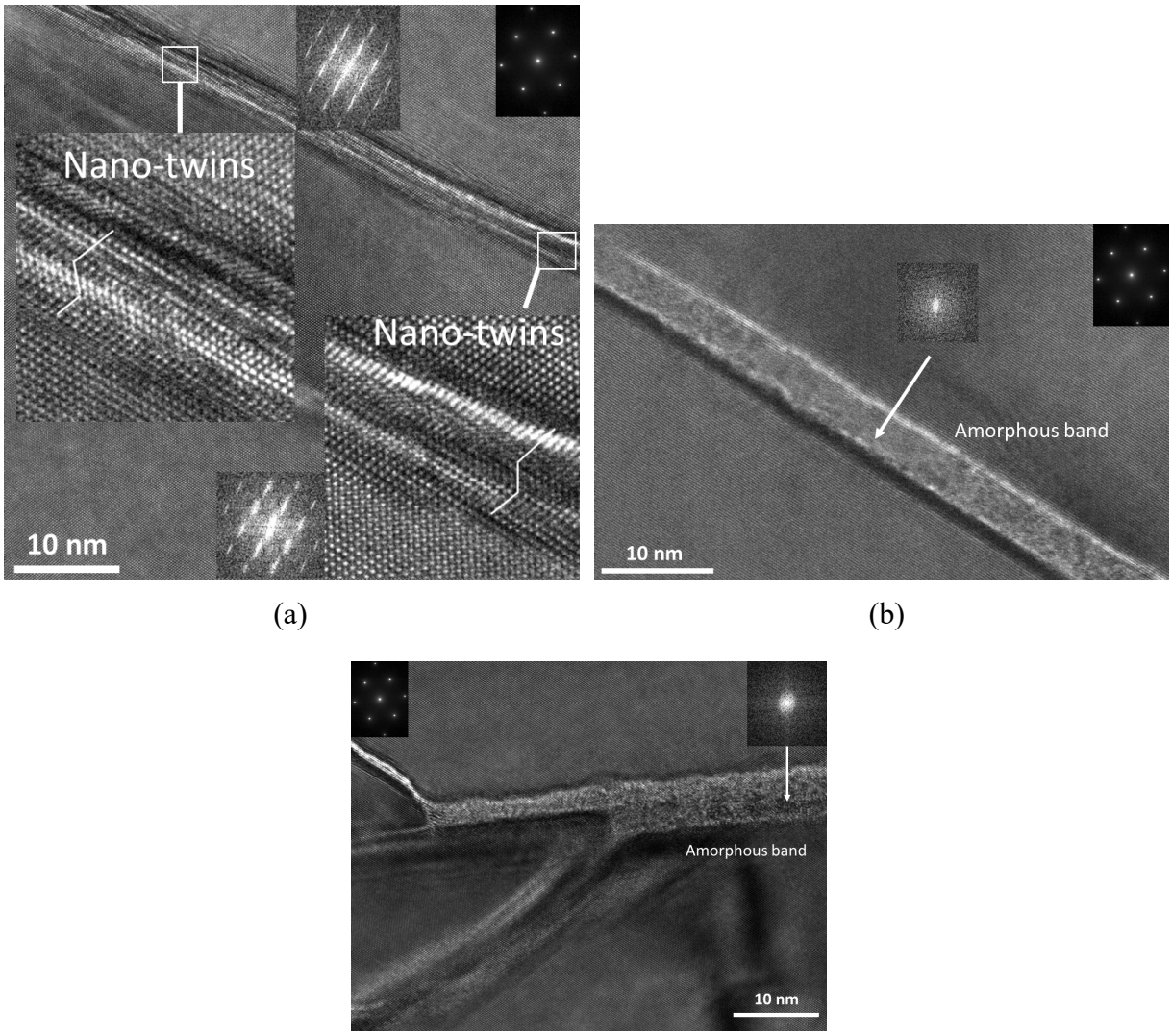

(a) (b)

(c)

Figure 3.4 Nanotwins and amorphous bands in diamond shocked at 115 GPa. (a) Nanotwins (b) a defect-free amorphous band with corresponding FFT pattern, (c) different variants of bifurcations found on the sides of a primary amorphous band. The insets show the FFT patterns of amorphous, crystalline and heavily faulted regions, respectively.

In crystalline regions, electron diffraction patterns show distinct spots corresponding to crystalline planes or sharp rings that are the result of nanocrystallization. The electron diffraction patterns exhibiting a diffused halo are characteristic of amorphous materials with no crystallinity. The contrast-less feature of the HRTEM image indicates a random atomic arrangement. In our

experiment, amorphous structures are preserved after unloading. Amorphous bands can be observed 2 μm below the shock surface, with widths ranging from about 2 to 5 nm. The shear strain within the amorphous region is much greater than its surroundings. Some amorphous bands are adjacent to nanocracks, indicating that amorphization may lead to the failure of diamond under shock compression. However, amorphous bands are not always consistently associated with cracks and appear to be distributed randomly throughout the sample.

Under quasi-static loading, heat is dissipated rapidly into the surrounding material without causing a significant temperature rise. The homogeneous temperature rise in shock compression is ~200 K at 115 GPa. Additionally, shock loading creates localized adiabatic shear, causing a localized temperature increase. The significant heating results in localized thermal softening which reduces the mechanical barrier and further facilitates amorphization [94].

The lattice undergoes uniaxial compression in the shock direction but cannot expand laterally because the lateral dimensions of the shocked region (~10^{-3} m) are sufficiently larger than the pulse length (~10^{-4} m). Thus, uniaxial strain state directly leads to high shear stresses.

The amplitude of the shear stresses τ_{max}, assuming elastic deformation in shock compression, is given by:

$$\tau_{max} = \frac{3}{4}(\sigma_{zz} - P) \tag{3}$$

Where σ_{zz} is the shock stress and P is the hydrostatic pressure.

When shock waves propagate in a solid material, a rapid uniaxial strain state is induced, with both high amplitude hydrostatic (pressure) and deviatoric (shear) stress components [153]. It is suggested that high shear stress, coupled with pressure generate amorphization. High shear stress reduces the threshold for pressure induced amorphization [80, 271], which is relaxed by the

formation of defects. Hydrostatic pressure alone does not generate line defects in cubic symmetry, whereas shear stresses account for plastic deformation and lattice defects.

The Peierls-Nabarro stress, τ_{PN}, which has to be overcome for dislocations motion and the associated dislocation energy are orders of magnitude higher in covalently bonded materials than in metals. This is the result of their high self-energy: very high shear stresses can build up in covalent materials, in contrast with metals where these stresses are readily relaxed by dislocation generation and motion. The amorphous bands are often preceded by dislocations and twins. These defects form along specific crystallographic planes with the maximum resolved shear stresses. The formation of these bands helps to reduce the local shear stresses and relax the overall stress state to near hydrostatic. Under dynamic loading, the temperature rise at the shock front may induce a lower τ_{PN}, thus makes dislocation motion easier although it is still much higher than that for metals. Consequently, the average dislocation velocities in covalently-bonded materials are orders of magnitude lower than that in metals under the same applied shear stress [272]. The tendency for amorphization is enhanced by three factors: (1) a higher τ_{PN} stress makes plastic deformation more difficult and thus allows deviatoric stresses to build up, which facilitates directional amorphization; (2) the high line energy of dislocations makes the dislocated regions energetically unfavorable and promotes amorphization; (3) higher stress states result in higher dislocation velocities (with possible supersonic dislocations [190] which eventually determines the kinetics of amorphization. The more open structures and stronger interatomic bonds in covalent materials make them more susceptible to amorphization. Covalent materials usually have a higher τ_{PN} stress that is approaching the theoretical strength of the material. This suppresses dislocation activity and leads to brittle fracture under quasi-static conditions. However, under confined high stress states or

during high strain rate deformation, amorphization becomes an alternative deformation mechanism to relax the deviatoric stress.

Acknowledgements

Chapter 3, in part, has been submitted for publication of the material as it may appear in: B. Li, S. Zhao, and M. A. Meyers. Direct observation of plastic deformation in diamond under extreme loading. The dissertation author was the primary researcher and first author of this paper.

Chapter 4 LASER SHOCK COMPRESSION OF $CaTiO_3$ PEROVSKITE

4.1 Plastic Deformation of $CaTiO_3$ Perovskite under Extreme Loading

$CaTiO_3$ is a perovskite material with various applications in electronics, biomedical, and photocatalytic fields, yet our current understanding of its mechanical response under extreme pressures and strain rates is far from complete. There is only a dearth of observations of the microstructural mechanisms of shock compressed $CaTiO_3$ due to the difficulty of sample recovery [273]. Figure 4.1 is the shock Hugoniot of $CaTiO_3$ up to 300 GPa [274]. The pressure P vs. relative density ρ/ρ_0 curve has an inflection at P~100 GPa. This is most probably due to a phase transition. Indeed, as mentioned above, there are reports of the orthorhombic to tetragonal and then to cubic transitions with increasing temperature. The pressure used in the current experiment, 70 GPa (marked in the plot), is below the threshold. The recovery technique used here enabled the capture of shocked $CaTiO_3$ with only minor cracks and therefore enabled characterization of the defect structure by TEM.

When a shock wave passes through a crystalline solid, it compresses it and usually induces plastic deformation due to shear stresses. In ductile crystalline solids, dislocation motion, twinning, and phase transformations are the predominant mechanisms to dissipate the imposed elastic energy. On the other hand, in brittle materials, defect mediated plasticity is often limited so that fracture becomes the dominant way to dissipate the imparted strain energy, resulting in catastrophic failure. Each deformation mechanism has a characteristic time scale and therefore is highly dependent on strain rate.

Laser shock generates a rapid uniaxial strain state with corresponding high hydrostatic pressure and shear stress components. The shear stresses directly result from the uniaxial strain condition; the lattice is compressed uniaxially along the shock propagation direction but cannot

expand laterally due to the sufficiently larger lateral dimensions of the shocked region compared to the pulse length.

From the generalized Hooke's Law,

$$\varepsilon_{xx} = \frac{1}{E}[\sigma_{xx} - \nu(\sigma_{yy} + \sigma_{zz})] \quad (1)$$

Shock compression subjects the material to uniaxial strain: $\varepsilon_{xx}=\varepsilon_{yy}=0$ and $\sigma_{xx}=\sigma_{yy}$. Thus:

$$\sigma_{xx} = \frac{\nu}{1-\nu}\sigma_{zz} \quad (2)$$

The amplitude of the deviatoric stresses τ_{max}, assuming elastic deformation during shock compression, is:

$$\tau_{max} = \frac{3}{4}(\sigma_{zz} - P) \quad (3)$$

Where σ_{zz} is the shock stress and P is the hydrostatic pressure. The latter is:

$$P = \frac{1}{3}(\sigma_{xx} + \sigma_{yy} + \sigma_{zz}) \quad (4)$$

So

$$P = \frac{\sigma_{zz}}{3}(\frac{1+\nu}{1-\nu}) \quad (5)$$

Therefore

$$\tau_{max} = \frac{\sigma_{zz}}{2}(\frac{1-2\nu}{1-\nu}) \quad (6)$$

Assuming a Poisson's ratio equal to 0.3 [275], one obtains, for elasticity: $\tau_{max} = 20$ GPa at $\sigma_{zz} = 70$ GPa. This is a very high value, and is a significant fraction of the shear modulus G of $CaTiO_3$ (101-107 GPa) [276-278].

The Peierls-Nabarro stress barrier (τ_{PN}) and dislocation energy are much higher in covalently and ionically bonded materials than in metals due to their high self-energy, leading to

very high shear stresses. Defects form on crystallographic planes with the maximum resolved shear stresses, reducing the local shear stresses and relaxing the stress state to nearly hydrostatic state. The shock induced temperature rise enhances defect mobility thus lowers τ_{PN}, although it is still much higher than in metals, resulting in lower dislocation velocities [190]. Slip occurs on close-packed planes to minimize energy loss. The τ_{PN} of perovskite approaches its theoretical strength limit (0.1 G) [95], which is about 10 GPa. Hence, laser shock generates shear stresses (~20 GPa) that exceed the Peierls-Nabarro stress (~10 GPa) and dislocations are generated. Since the Peierls-Nabarro stress τ_{PN} is the minimum shear stress that needs to be overcome for dislocations to move (10 GPa for perovskite), a critical shock stress of 35 GPa is required to enable the dislocation movements according to Equation (7), as marked in Figure 4.1.

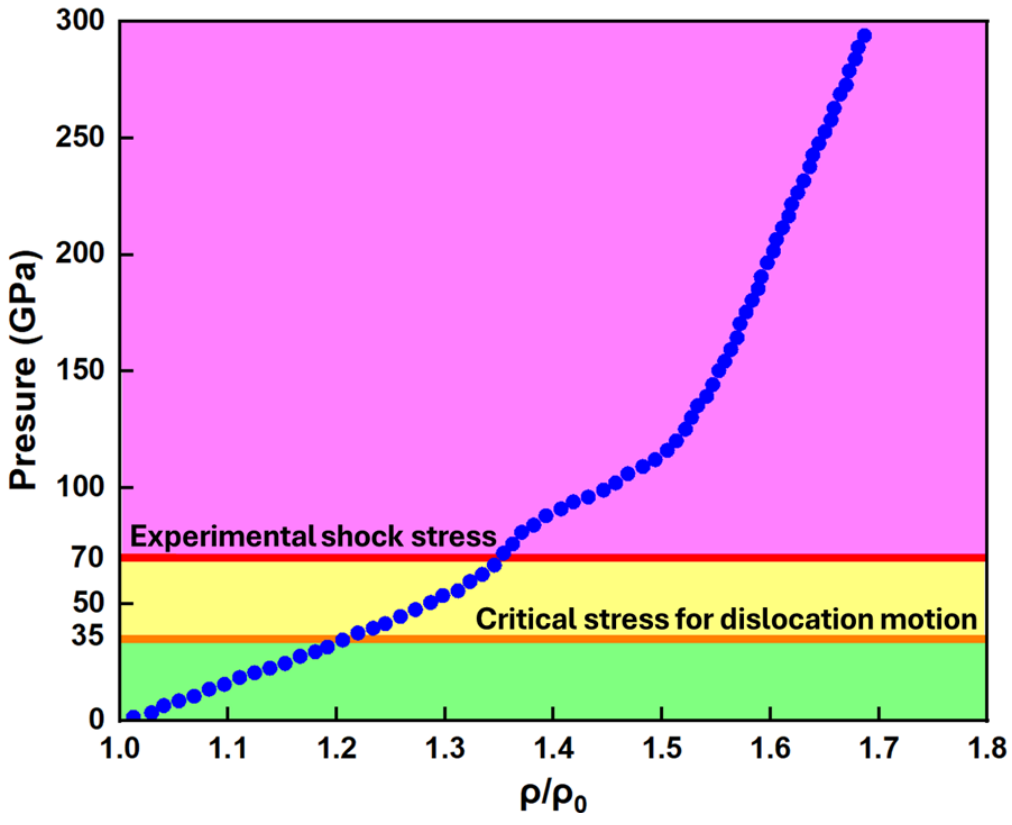

Figure 4.1 Shock Hugoniot curve Pressure vs ρ/ρ_0 for $CaTiO_3$ [273, 274]. The pressure used in the current experiment, 70 GPa, and the critical shock stress, 35 GPa, to initiate dislocation motion are marked in the plot.

Hydrostatic pressure alone does not generate line defects in crystals; in contrast, shear stresses play an important role in plastic deformation and lattice defects formation such as dislocations, stacking faults, and twinning. Point defect concentration, however, can be affected by both hydrostatic and deviatoric stresses. Shear stress plays a significant role in phase transitions and, in some instances, may even dominate the process [279- 281]. Driven by the high-amplitude stress pulse, these defects propagate inwards from the surface along specific crystallographic orientations. They intersect and generate additional defects and plastic work. Shear-induced plasticity induces localized heating which in turn produces localized thermal softening and reduces the mechanical barrier for further plastic deformation. Substantial evidence shows that shear promotes structural changes. Bridgman [279, 282] first proposed that shear stress superimposed on hydrostatic pressure lowers the threshold for structural phase transitions and accelerates their kinetics. Teller [280] and Enikolopian [283] indicated that shear strains significantly influence the reaction kinetics. Levitas [284] also reviewed the crucial role that shear plays in promoting phase transformations.

The conventional, bright-field and dark-field TEM, and HRTEM images in Figure 4.2 provide a baseline comparison of unshocked $CaTiO_3$ with a sample subjected to laser shock compression at 70 GPa. The unshocked sample exhibits a very low density of defects and anti-phase boundaries. The significant differences observed between the two samples confirm that the shock-induced features are not artifacts introduced during FIB preparation.

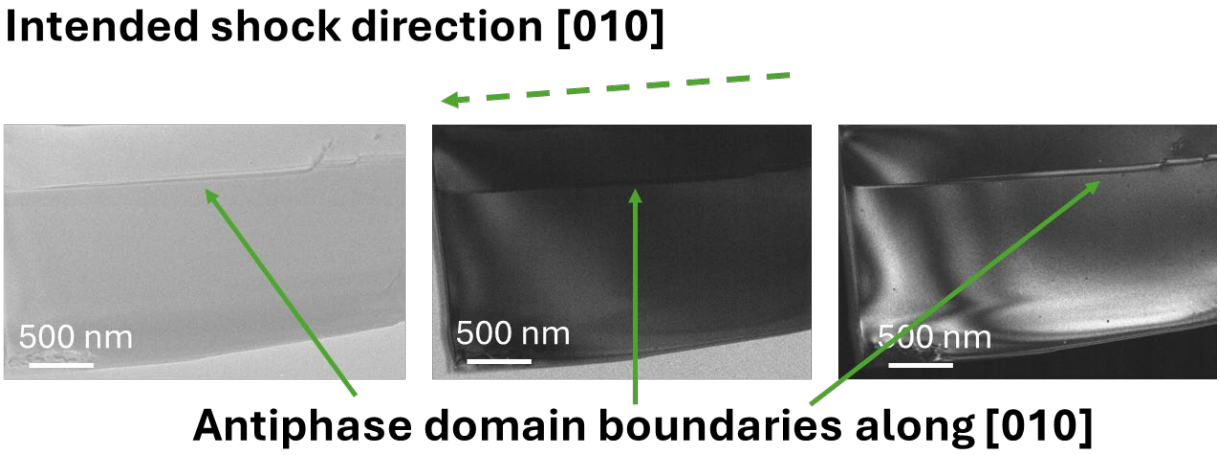

(a)

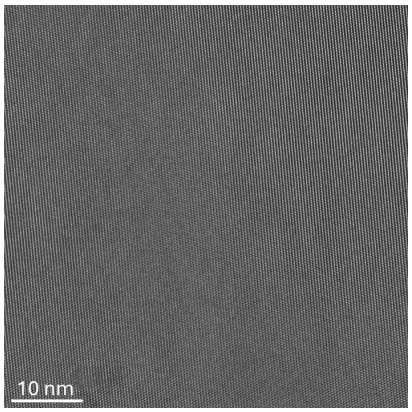

(b)

Figure 4.2 TEM micrographs of unshocked $CaTiO_3$. TEM micrographs of unshocked $CaTiO_3$. (a) Conventional, bright-field, and dark-field low magnification TEM images of unshocked $CaTiO_3$. It has a very low density of defects and antiphase boundaries. (b) HRTEM image of the unshocked $CaTiO_3$.

As illustrated in Figure 4.3, the shock direction is along [010]. The dislocations are aligned parallel to the [110] and [$\bar{1}$10] directions, while the slip plane is identified as (001) in the FIB-prepared sample. The subsequent figures (Figures 4.4–4.9) detail the shock-induced defects.

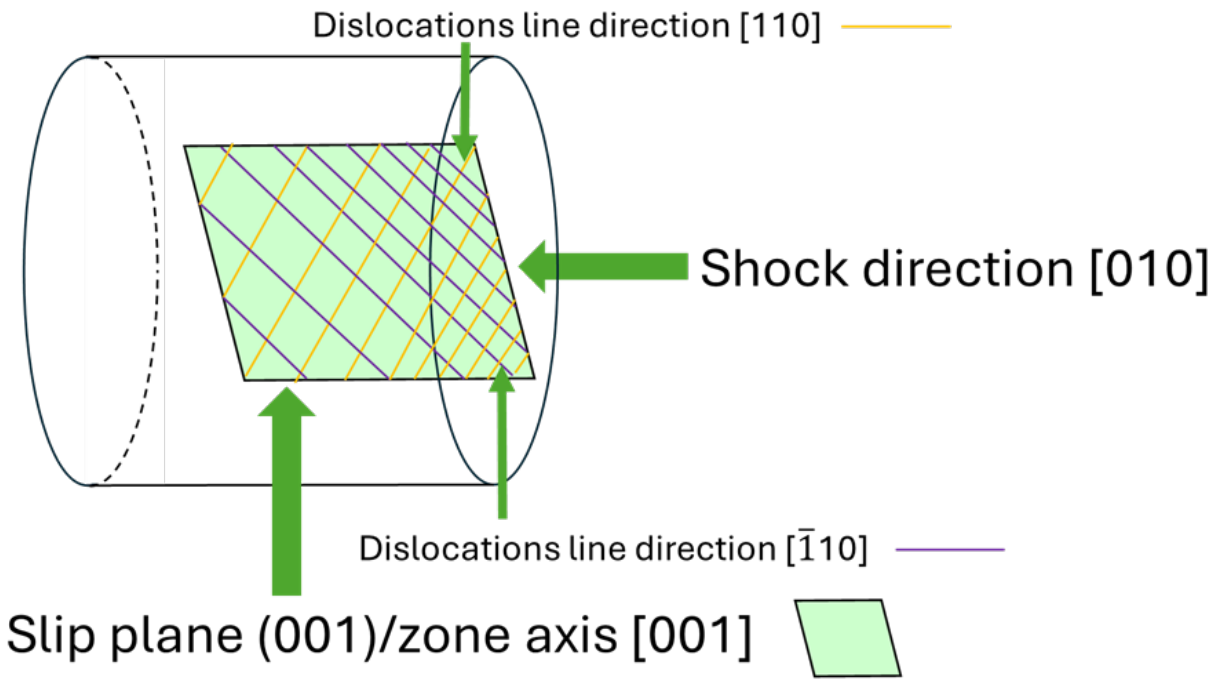

Figure 4.3 Illustration of the FIB sample prepared for TEM (not to scale). The shock direction is [010]. The dislocation lines are parallel along [110] and [$\bar{1}$10] directions and the slip plane is (001).

Two-beam bright-field and dark-field images (Figure 4.4) reveal a significantly higher density of defects in the 70 GPa shocked sample compared to the unshocked one (Figure 4.2). Perpendicular dislocations and antiphase domain boundaries, and shear band-like features are heavily entangled and intertwined.

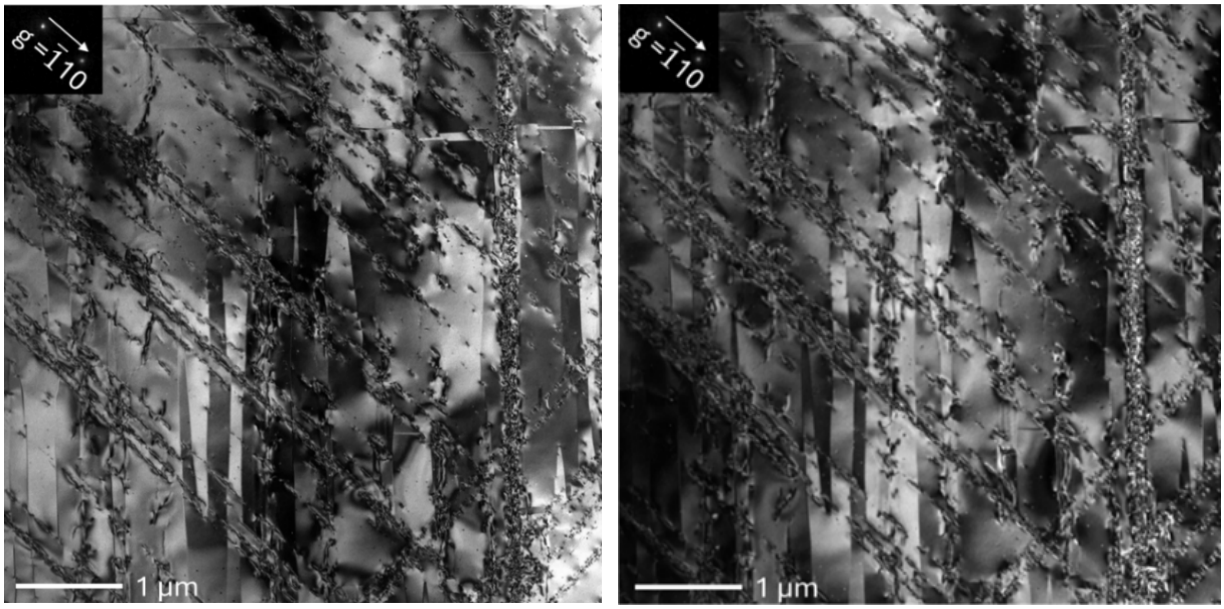

(a) (b)

Figure 4.4 Two-beam condition (a) bright-field and (b) dark-field TEM images of $CaTiO_3$ shocked at 70 GPa. Significantly more defects such as dislocations, antiphase domain boundaries, and shear band-like morphology are observed in the sample shocked at 70 GPa compared to the unshocked one.

Weak-beam dark-field TEM image (Figure 4.5) shows dislocations oriented at a 45° angle to the shock direction. The density of these dislocations decreases with distance from the shock surface, eventually disappearing at a certain depth. This gradient is consistent with the decay of the shock wave as it propagates away from the laser energy deposition surface. The dislocations are arranged in the (001) planes, with spacings ranging from approximately 20 nm to 350 nm.

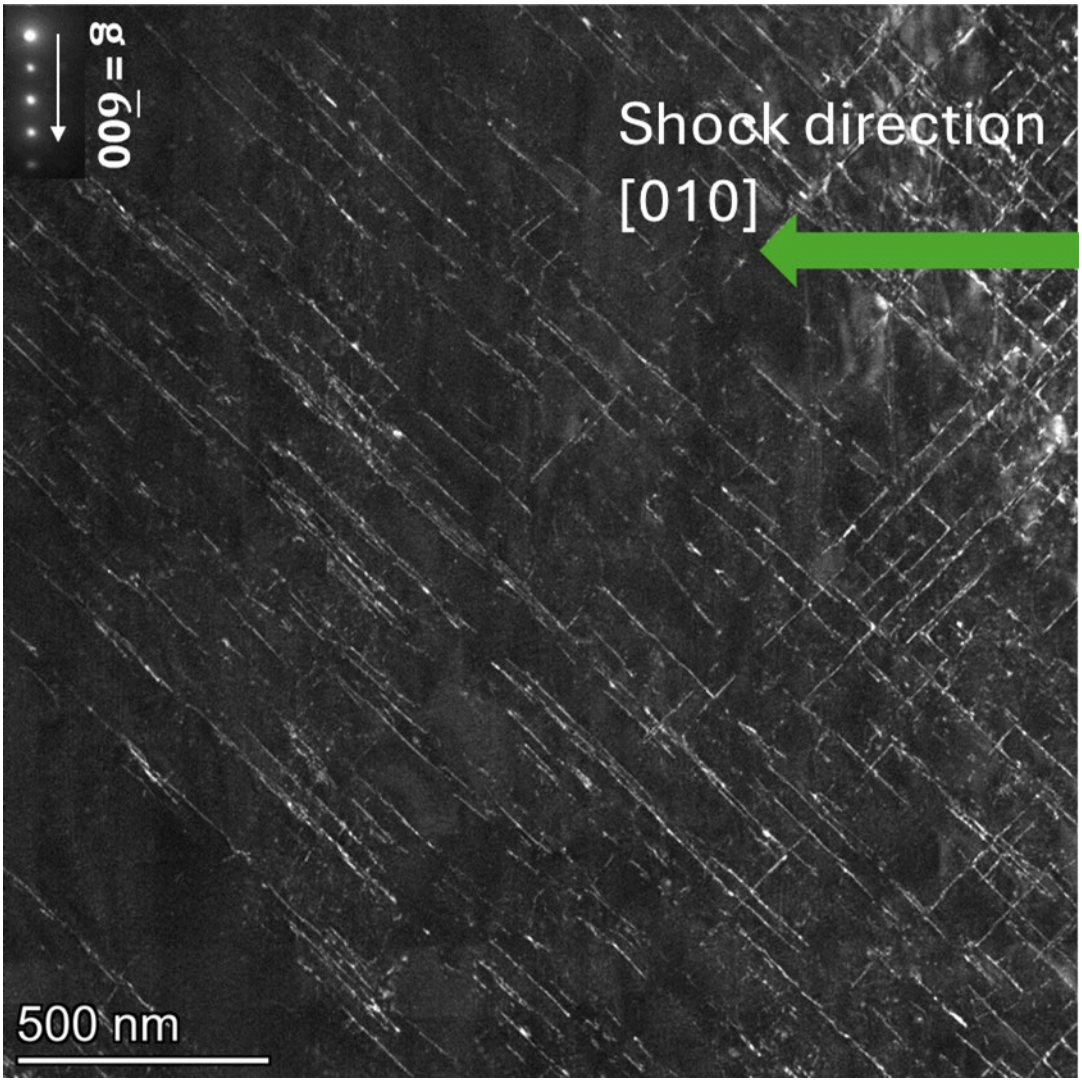

Figure 4.5 Weak beam dark field condition TEM image. Dislocations [110] and [$\bar{1}$10] are 45˚ from the shock direction down to 2 μm depth below the shock surface. Dislocation density generally decreases from the surface and eventually disappears at certain depth.

The dislocation density is shown in Figure 4.6 down to 12 μm depth below the shock surface; a general decreasing trend from ~15×10^{12} to ~2×10^{12} m^{-2} is observed. This dislocation density in the laser shocked $CaTiO_3$ sample is very high, close to that of the highly deformed metals (above the order of 10^{12} m^{-2}). The interactions between these defects are expected to occur under laser shock compression, resulting in high defect densities and localized effects, including the loss of atomic order, shear band formation, and plastic heating. The low-magnification

conventional, bright- and dark-field TEM images (Figure 4.7) show that the laser-shocked region has dislocations and antiphase boundaries (APBs) along [010] and [100] under the [010] shock direction. Two sets of dislocations appear to be crystallographically aligned along mutually perpendicular [110] and [$\bar{1}$10] directions on (001) planes, respectively. Isolated domain boundaries have widths of tens to hundreds of nanometers. Antiphase domains exhibiting similar morphology were observed by Wang and Liebermann in natural perovskite crystals [245]. Figure 4.8 illustrates the main slip system in the crystal unit cell of $CaTiO_3$, which shows the [110] and [$\bar{1}$10] dislocation lines on the (001) slip plane.

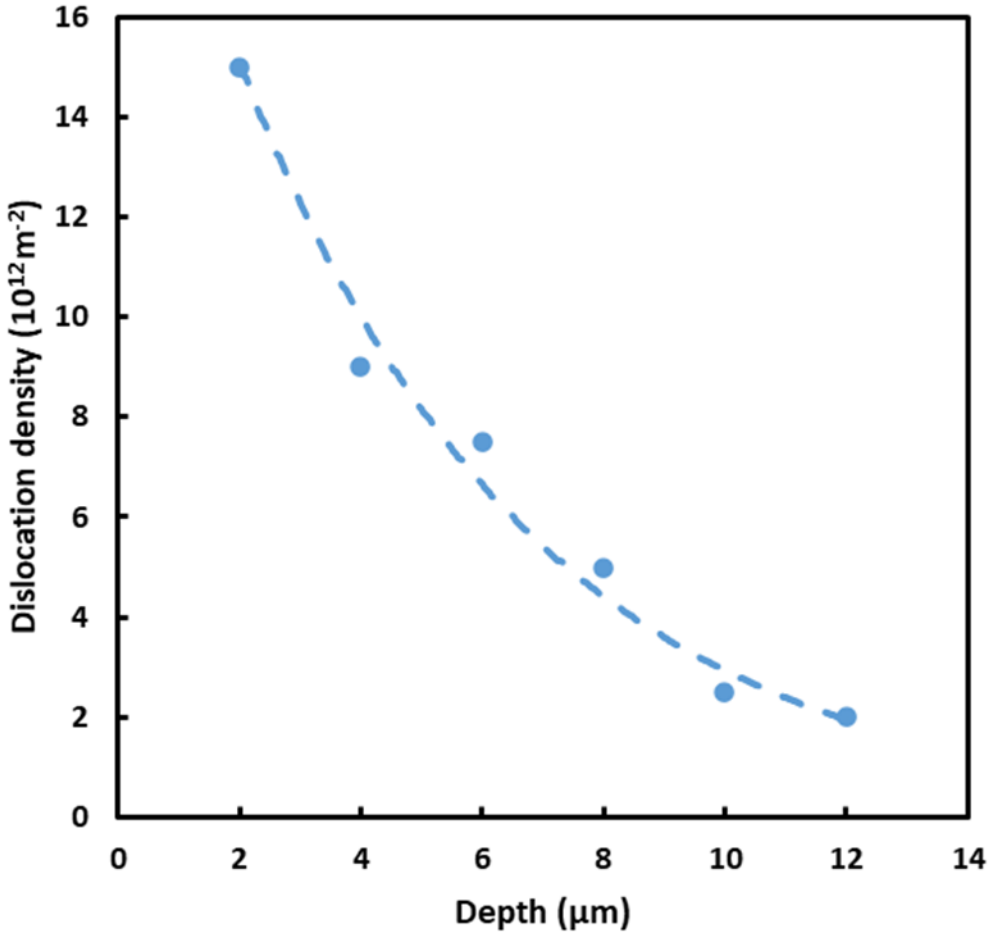

Figure 4.6 Dislocation densities in shocked $CaTiO_3$. Distance up to 12 μm depth below the shock surface, showing a decreasing trend from ~15×10^{12} to ~2×10^{12} m^{-2}.

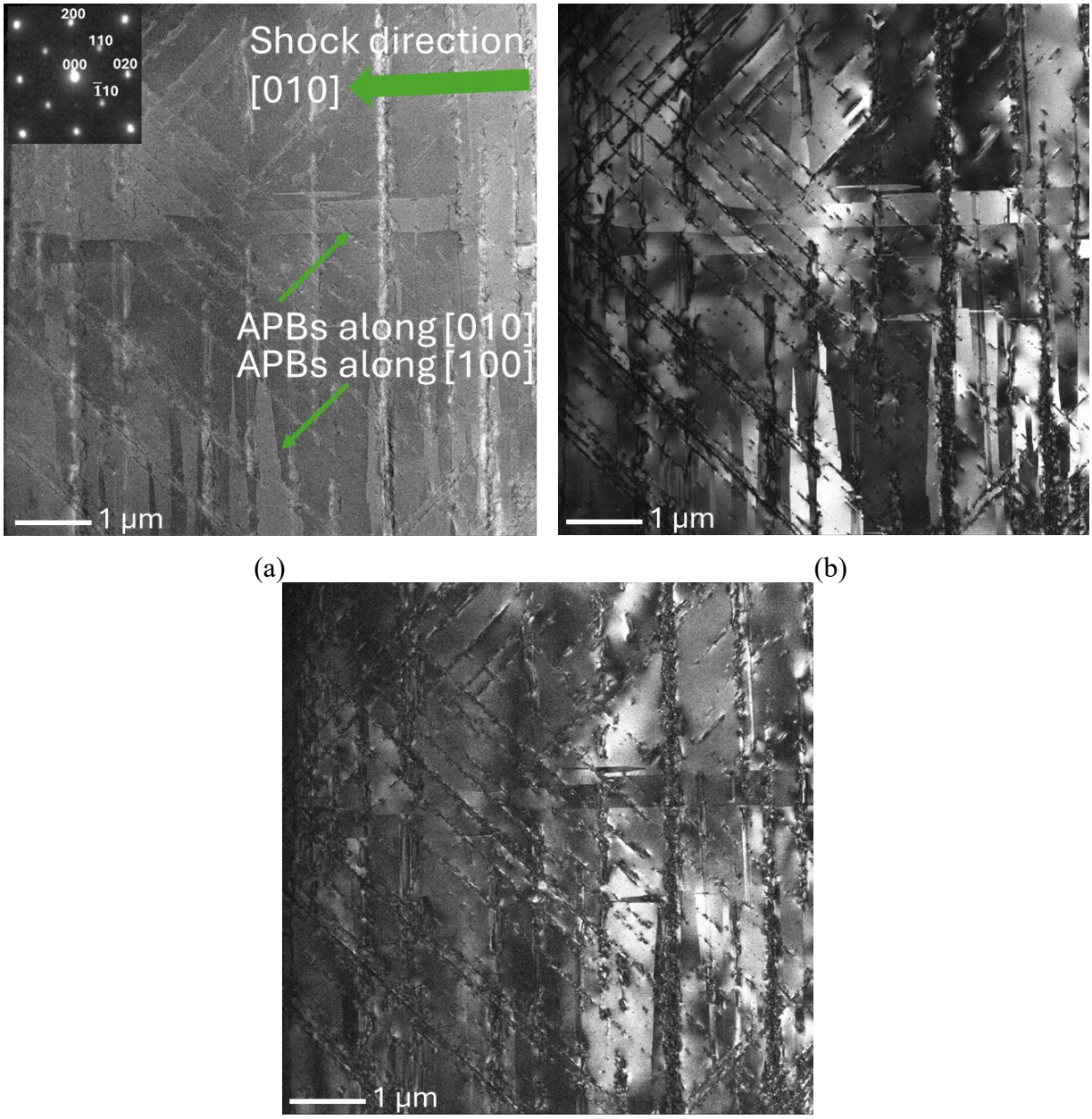

(a) (b)

(c)

Figure 4.7 Low-magnification conventional, bright- and dark-field TEM images of $CaTiO_3$ shocked at 70 GPa. (a) Antiphase domain boundaries are along [010] and [100] directions with corresponding SAED; (b) and (c) are its bright- and dark-field images showing the defect features. Dislocations are generally along mutually perpendicular [110] and [$\bar{1}$10] directions on (001) planes. Isolated domain boundaries have widths of tens to hundreds of nanometers.

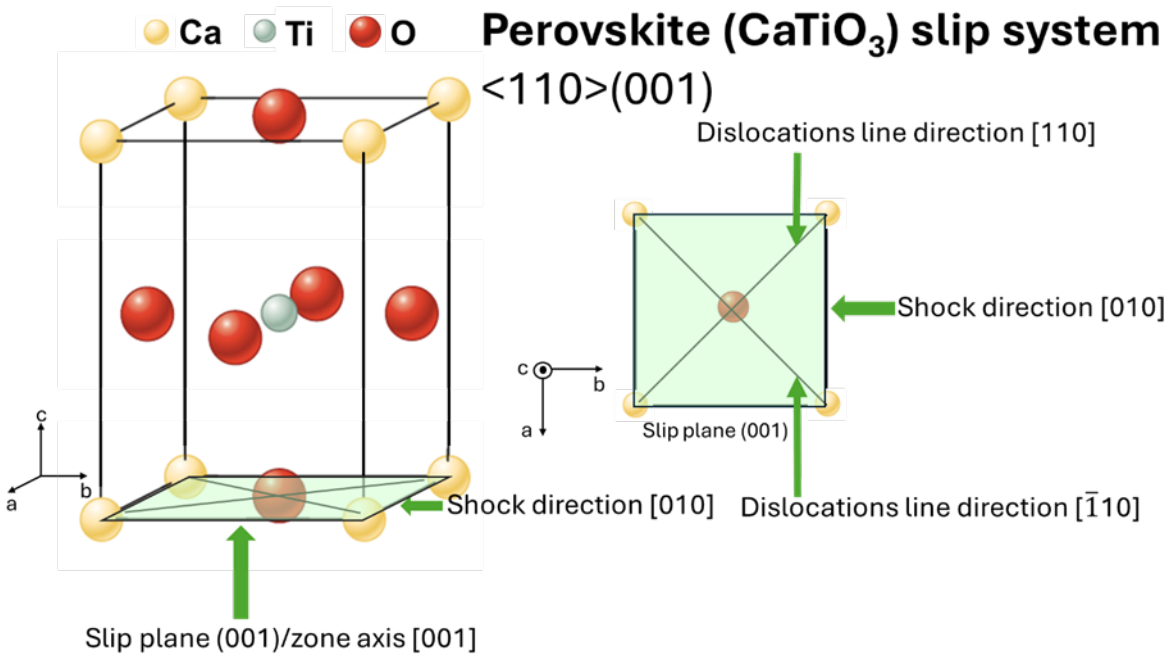

Figure 4.8 Slip system in crystal unit cell of $CaTiO_3$, showing the [110] and [$\bar{1}$10] dislocation lines on the (001) slip plane under the [010] shock direction.

In Figure 4.9, nanobeam electron diffraction and fast-Fourier transform (FFT) patterns in some regions exhibit extra spots which might result from double diffraction. There is another possible explanation for this phenomenon. The stacking nature of alternating neutral CaO and TiO_2 planes is regarded as the characteristic of perovskites [285]. However, the vulnerability to laser for CaO and TiO_2 planes might be different. Under laser shock compression, the complicated physical/chemical reactions might deplete or extract either CaO or TiO_2 planes so that the resulting layer defects might lead to the appearance of the extra spots in electron diffraction patterns. Nevertheless, whether this forms a second phase needs more investigation.

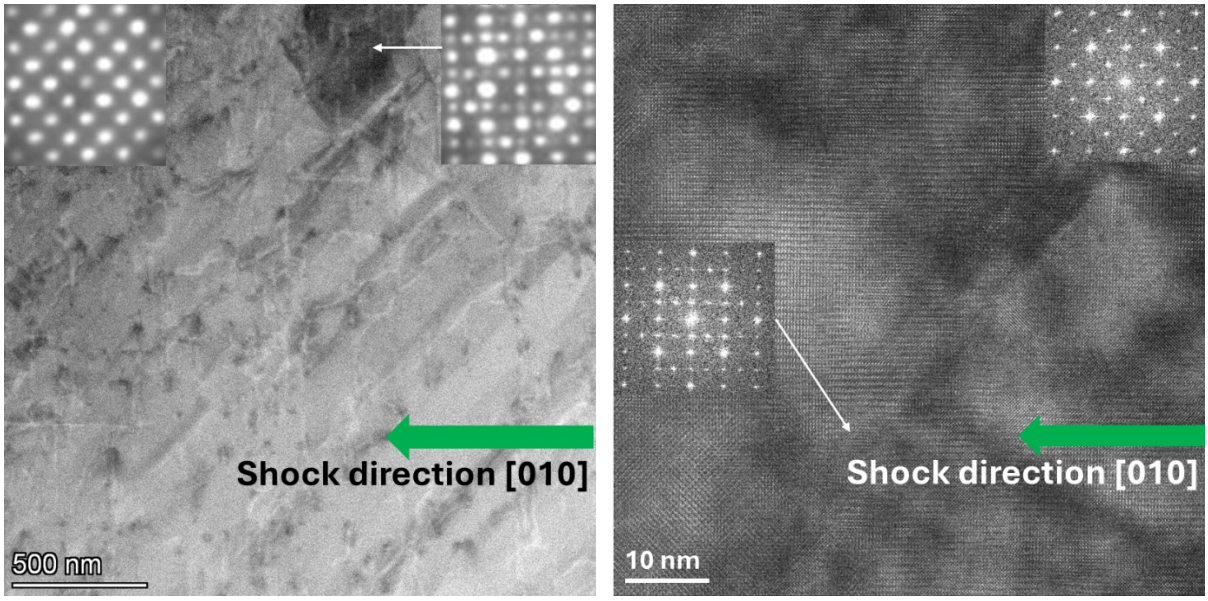

(a) (b)

Figure 4.9 Extra diffraction spots in some regions of shocked $CaTiO_3$ confirmed by (a) nanobeam diffraction pattern and (b) FFT.

We present below the results of several studies; many other slip systems are observed at different temperatures. The perovskite structure generally has dislocations with <110> or <100> Burgers vectors; <110> dislocations can be found both at room temperature and high temperatures whereas <100> dislocations are found predominantly at high temperatures [286]. Besson et al. [249] demonstrated using TEM that all the dislocations observed in deformed single crystal $CaTiO_3$ were of screw type. Poirier et al. [287] found that creep is controlled by dislocation gliding at high stresses and low temperatures. Mecklenburgh et al. [288] observed slip systems [110](001) and $[\bar{1}10](001)$ through torsion and compression experiments on $(Ca_{0.9}Sr_{0.1})TiO_3$ perovskite at temperatures between 1350 and 1550 K. Wang et al. [245] found that the heat treated and deformed natural perovskite crystal $CaFe^{3+}_{0.1}Nb^{5+}_{0.1}Ti^{4+}_{0.8}O_3$ exhibits the slip systems [110](001) and $[\bar{1}10](001)$, similar to our observations. Besson et al. [249, 289] discovered that [100] natural single crystal $CaTiO_3$ specimens compressed along the [100] direction favor the [001](110) slip system, and specimens compressed along the $[1\bar{1}0]$ direction favor the [100](010) slip system under creep tests

at temperatures up to 1973 K. Doukhan and Doukhan [248] found that the easy glide systems of $CaTiO_3$ are $[\bar{1}11](12\bar{1})$ by micro scratches at room temperature; although the corresponding Burgers vector <111> is not the shortest lattice translation, dislocation gliding on these systems can prevent bringing various cations too close to each other during dislocation glide.

Orthorhombic $CaTiO_3$ exhibits significantly higher normalized Peierls-Nabarro stress than cubic $SrTiO_3$, which demonstrates orthorhombic distortions. All dislocations undergo lattice friction; however, glide occurs more easily on $[\bar{1}10](001)$. While [100](010) and [010](100) are the easiest slip systems in cubic perovskite, they are accompanied by [110](001) easy glide system in orthorhombic $CaTiO_3$. Lattice friction increases as orthorhombic distortions increase [251]. In $CaTiO_3$, significant lattice friction is expected for any orientation of dislocation lines. Another notable effect of orthorhombic distortion is the presence of domains that persist at high temperatures and pressures. These domain boundaries also serve as obstacles to dislocation motion like grain boundaries. Phase transitions may give rise to APBs. These domain boundaries prefer to align with low indices planes parallel to {001} planes of minimum surface energy [248]. In contrast, very few APBs are present in the low-temperature samples as evidenced in our unshocked sample. Dislocations are common in minerals subjected to high stress, relatively high strain rate, and moderate temperature. In the shocked $CaTiO_3$ sample, [010] and [100] antiphase domains, which are rarely observed in the unshocked material, become dominant. This domain structure change is attributed to a structural phase transition in perovskite at temperatures below 1585 K. Dislocations are dominant in the material and often interact with these domain boundaries [245].

Under quasi-static loading, heat can be dissipated quickly to the surrounding without causing a temperature rise. In contrast, shock loading reduces material's volume, generating substantial work which is dissipated as heat and inducing a temperature rise at the shock front.

Elevated temperatures significantly increase defect mobility by lowering the energy barrier for plastic deformation, generating localized thermal softening and further facilitating this process [94]. If the temperature at the shock front exceeds the melting point of $CaTiO_3$ (2250 K), melting may occur; as a result, the material is unable to sustain shear stress.

Since $CaTiO_3$ has a positive Clapeyron slope [257] and a relatively higher atomic packing factor (0.58) than our previously studied materials (Si, Ge, SiC, B_4C, and olivine [95]) which have lower atomic packing factors (0.14 - 0.4), amorphization as the deformation mechanism under extreme loading conditions is not favored. $CaTiO_3$ behaves more like metals, responding to deformation mainly by dislocation motion rather than these covalently-bonded materials which amorphize under shock compression. This in turn confirms our previous conjecture.

This process is significant in planetary sciences as it may contribute to deep-focus earthquakes by generating stress waves. It is also relevant to meteorite impacts due to the role of shock waves.

Acknowledgements

Chapter 4, in part, has been submitted for publication of the material as it may appear in: B. Li, S. Zhao, and M. A. Meyers. Plastic Deformation of $CaTiO_3$ Perovskite under Extreme Loading. The dissertation author was the primary researcher and first author of this paper.

Chapter 5 LASER SHOCK COMPRESSION OF OLIVINE $(Mg, Fe)_2SiO_4$ AND OTHER COVALENTLY-BONDED MATERIALS

5.1 Directional Amorphization of Olivine $(Mg, Fe)_2SiO_4$ and Other Covalent Solids

We subjected five representative covalently bonded solids, two elements (Si and Ge) and three compounds [B_4C, SiC, and olivine $(Mg, Fe)_2SiO_4$] to shock compression in pursuit of understanding directional amorphization bands.

Powerful shear stresses can be generated in conjunction with the uniaxial shock compression, shown in Figure 5.1 (A) as a function of a normalized shock stress (divided by the bulk modulus, K). The ambient shear moduli for the materials studied are: G_{si}= 79 GPa [290, 291]; G_{Ge}= 67 GPa [290, 291]; G_{B4C}= 165-223 GPa [292, 293]; G_{SiC}= 161-192 GPa [294, 295]; and $G_{olivine}$=78 GPa [296, 297].

Although the ratios of shear stress to pressure decrease with pressure, they are still significant and are the principal contributors to shock-induced plastic deformation. They are relaxed by the generation of defects. The five materials investigated here exhibit a negative Clapeyron behavior; their melting points decrease with increasing pressure (Figure 5.1 (B)). This is a direct consequence of the open structures, which collapse upon melting to a higher density. In contrast, in metals the melting point typically increases with pressure, indicative of a positive Clapeyron relation. At a critical shock stress the sample temperature intersects the melting curve. This is the upper limit of our experiments because above this locus we have liquid and not solid-state amorphization.

Table 5.1 provides the melting pressures and experimental shock stresses. Each material was subjected to shock pulses at two or three pressures, except for SiC which was only subjected

to one pressure. It decomposes to Si and C at higher pressures. Throughout this paper, we use both the shock stress, σ_{zz}, and the hydrostatic pressure, P. They are related by:

$$\sigma_{zz} = P + \frac{4}{3}\tau_{max} \quad (1)$$

where τ_{max} is the maximum shear stress. In Figure 2, we use both P and σ_{zz}. σ_{zz} is slightly larger than P.

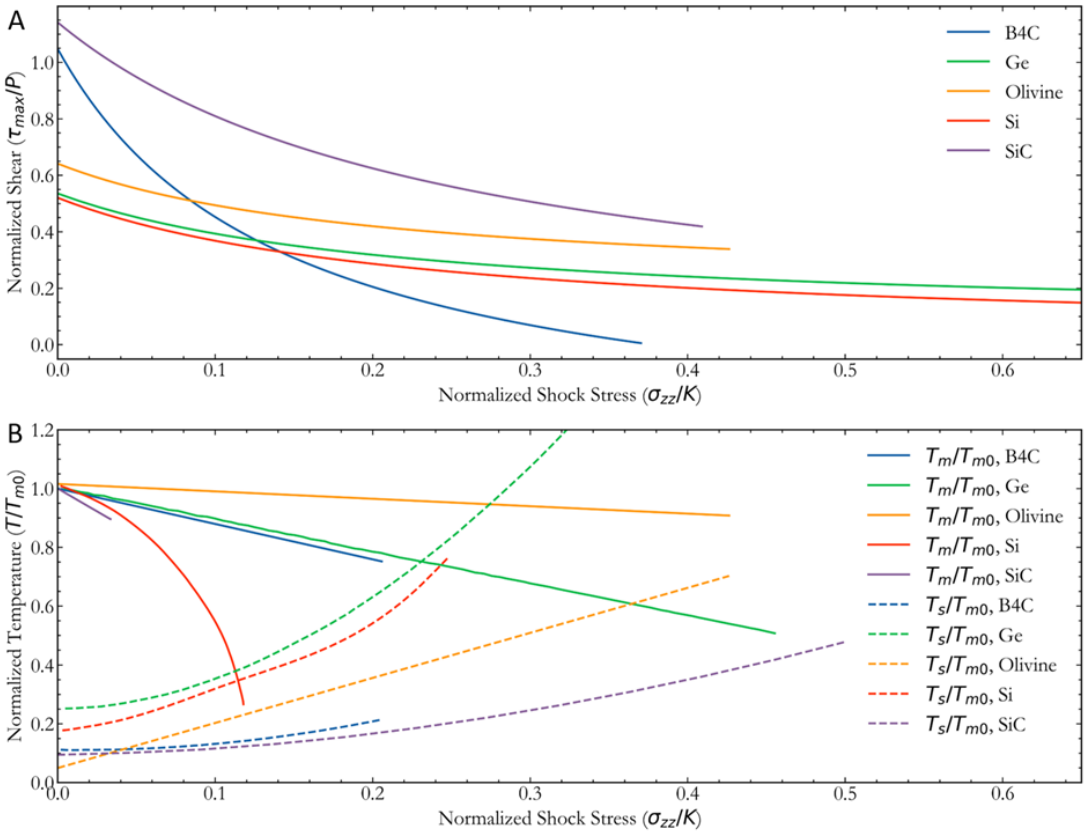

Figure 5.1 (A) Normalized shear vs. shock stress, (B) Normalized temperature vs. shock stress. (A) The ratio of shear stress, τ, to pressure, P, as a function of shock stress normalized by the bulk modulus, K, for Si, Ge, SiC, B_4C, and olivine; (B) Shock temperature/melting point (dotted lines) and melting point for materials with negative Clapeyron slope (solid lines) as a function of shock stress/bulk modulus.

Table 5.1 Parameters for the five materials investigated

Material	Melting pressure on the Hugoniot (GPa)	Experimental Shock Stress (GPa)	Shock threshold for amorphization (GPa)	Work of Amorphization, W (10^9J/m^3)		
				$\sigma_0\varepsilon_t$	$\tau\varepsilon_s$	$\rho_d Gb^2/2$
Si	11.5	4.1; 11; 22.3	11.2	0.548	2.063	0.013
Ge	26	13; 33	13	0.674	2.314	0.310
SiC	122	50	45-50	1.980	13.416	0.478
B_4C	100	45-50	25-50	0.489	15.950	0.182
$(Mg, Fe)_2SiO_4$	70	54; 56	50-55	0.219	0.918	1.373

Metals respond to shock compression primarily through three mechanisms: dislocation generation and motion, twinning, and displacive phase transformations. These structural changes and their formation have been quantified for the past eighty years and are amply documented. In covalently-bonded materials, such as Si or Ge, the dislocation velocity is 4-5 orders of magnitude lower than metallic-bonded material, such as Cu for the same applied shear stress [272]. The specimens were taken from different samples shocked at a much lower peak pressure.

Here are the preliminary TEM results of an unshocked olivine and olivine samples shocked at 20 and 40 GPa, respectively (Figures 5.2, 5.3, and 5.4). There are scarecly any defects in the unshocked natural single crystal olivine (Figure 5.2). The threshold to trigger amorphization in olivine is 50 to 55 GPa, so both were below the critical point. At 20 GPa (Figure 5.3), before amorphization, dislocations and shear bands are the predominant deformation mechanisms. The dislocations are dissociated. These dislocations generally have a Burgers vector of <100> and tend to group together and exhibit a band-like morphology. At 40 GPa (Figure 5.4), the amorphization process is not yet completed and we can still see the lattice vaguely in Figure 5.4 (B). But the crystalline lattice is heavily distorted near the amorphous band which is marked by red arrows in Figure 5.4 (C). Planar deformation features are observed. This shear band-like feature has a thickness of tens of nanometers, which suggests that the deformation is localized, and we suspect

that this dislocation activity forming planar deformation feature is the precursor to solid state amorphization in olivine. These TEM images show the morphologies of olivine below the threshold pressures of amorphization. High density of dislocations and stacking faults may be the precursors of amorphization for olivine.

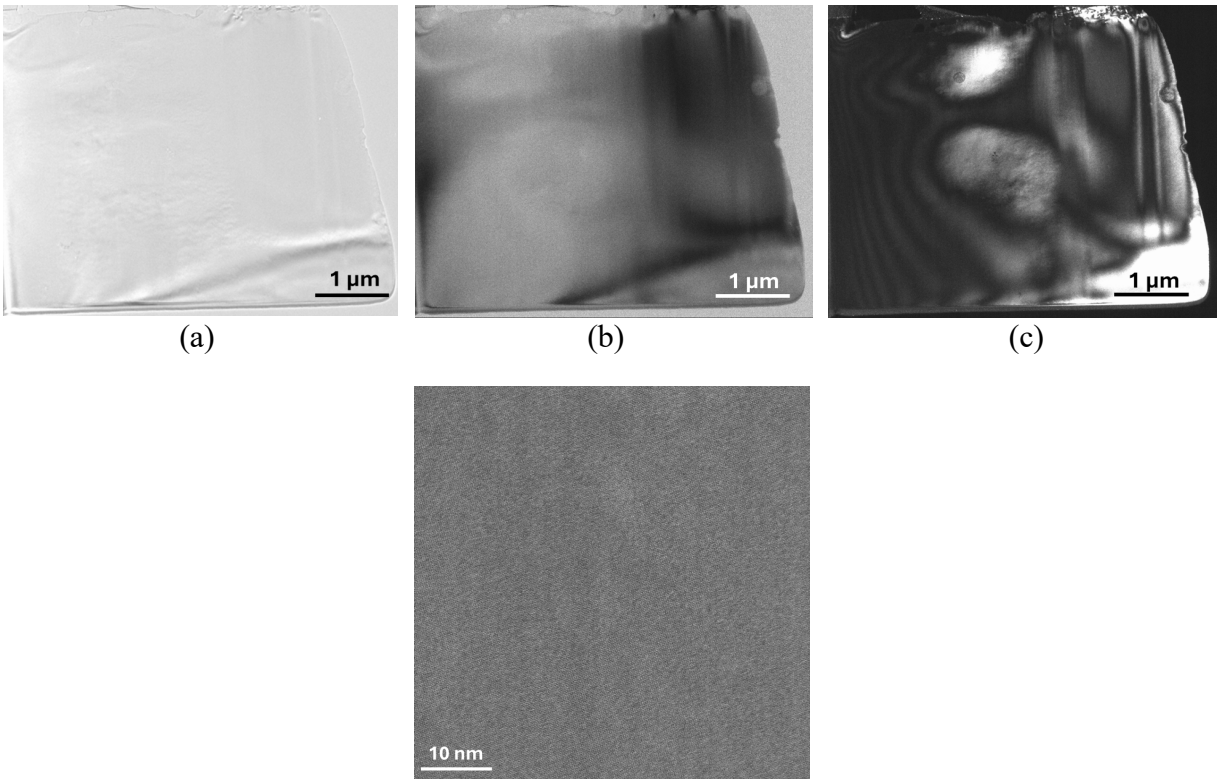

(a) (b) (c)

(d)

Figure 5.2 (a) Conventional, (b) bright-field, (c) dark-field, (d) high-resolution TEM images of unshocked olivine.

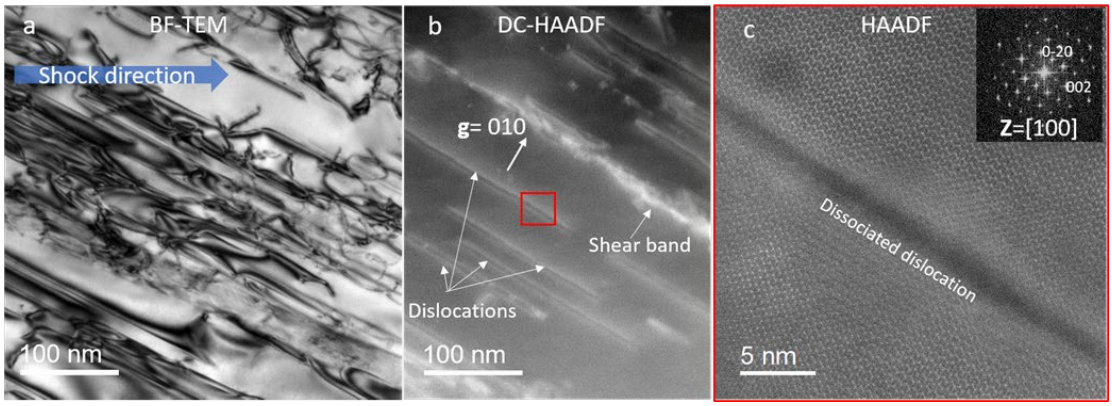

Figure 5.3 Post-shock olivine exhibits dislocations under shock pressure of 20 GPa.

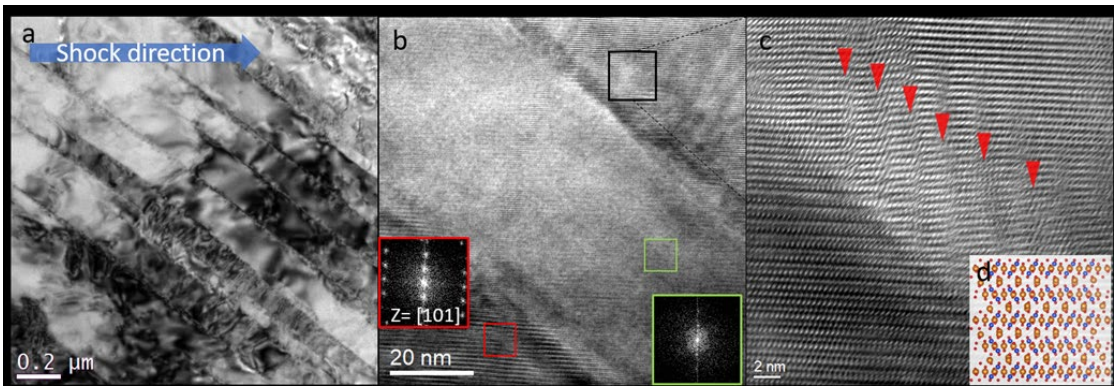

Figure 5.4 Shear faulting under shock pressure of 40 GPa.

Nevertheless, the morphological difference between dislocations and amorphous bands is reasonably convincing. They consist of parallel arrays of dislocations and stacking faults. However, for SiC no such dislocation arrays were observed and it is proposed that a high density of dislocations is not a prerequisite for amorphization.

Thus, another mechanism is responsible for plastic deformation above a critical stress, namely the formation of amorphous bands, as shown in Figure. 5.5 (A)-(E). These materials were shocked to pressures above the threshold for amorphization (provided in Table 5.1) and amorphous bands with widths in the nanometer range are generated. There is considerable similarity between the five covalent materials investigated, Si, Ge, B_4C, SiC, and olivine. This is the result of the high

Peierls-Nabarro stress necessary to move dislocations and of their high self-energy: very high shear stresses can develop in covalent materials, in contrast with metals where these stresses are readily relaxed by dislocation generation and motion.

These amorphous bands are usually preceded, at lower pressures, by dislocations and, in some cases, twins. These defects form along specific crystallographic planes which have the highest resolved shear stresses.

The formation of these bands decreases the local shear stresses and relaxes the overall stress state to a near hydrostatic state. The amorphous bands are further confirmed by the diffraction images of the recovered samples. The diffraction of crystalline structures typically shows the distinct sharp rings or dots which result from the crystalline planes; inside the bands, crystallinity is lost and the pattern shows only a diffused halo, the trademark of amorphization. This is illustrated here for silicon (Insets Figure 5.5 (F) and 5.5 (G) to Figure 5.5 (A)), with the other four structures exhibiting similar characteristic amorphous diffraction patterns. Our experiments show that the amorphous structures are retained after unloading. In terms of material properties, this is something under current investigation. The electronic band structure of silicon and germanium is altered by amorphization, which leads to different thermal/optical/mechanical/electrical properties.

The molecular dynamics (MD) simulation for Si shows in a clear fashion how the stacking faults serve, upon reaching a critical concentration level, as the nucleation sites for amorphization (Figure 5.5 (H)). Two packets of stacking faults are shown with a nascent amorphous region inside each of them. The stacking faults are shown in light blue and the amorphous region in grey. The simulations were conducted under shock compression produced by an infinite piston impact. The increase in temperature is incorporated into the calculations, which use a Tersoff potential. The

shock propagation direction is the same as the experiments: [001]. The 50 μm Al serves as both a heat shield and a medium to transfer the shock generated by the ablation of the very hot CH through to the covalent target. Especially for the short duration of the MD simulation, this means that the temperature at the Al/Si interface matches the ambient conditions, i.e., about 293K, which is the starting temperature of the silicon simulations. After that, the temperature evolves due to shock induced temperature rise. The identification of the diamond cubic vs disordered structure was completed using OVITO [298] using the built-in "identify diamond" method, which is an adaptation of the more common Common Neighbor Analysis (CNA) method to second nearest neighbors [299]. These stacking fault-defects provide the local stress fields that nucleate the amorphous phase. The process of amorphization is accompanied by an increase in density by virtue of the negative Clapeyron relationship and this is more clearly evident in MD-derived density plots (Figure 5.5 (I)). Note that the amorphous phase may also be a consequence of a virtual melting process, i.e., melting below the melting point, when a large nonhydrostatic stress is present [97]. Recent MD simulations in Si [300] under dynamic loading, show that dislocations can move at stresses much below the τ_{PN}. However, the accuracy of the estimation of τ_{PN} (or any other parameters related to the force field) using MD simulation is largely limited by the interatomic potential used. τ_{PN} is also temperature dependent. The temperature increase is not induced by laser directly, but by shock deformation. If the deformation temperature is reduced, for example, in a quasi-isentropic loading condition, amorphization should also occur. In fact, even in quasi-static loading conditions, silicon has been shown to undergo amorphization. The critical barrier should also vary as a function of temperature. This is because the mobility of defects is significantly increased by temperature. Under dynamic loading, the temperature rise at the shock front may generate a lower τ_{PN} and thus make dislocation motion easier. However, it is still much higher than

for metallically-bonded materials. High τ_{PN} is a characteristic of many covalently bonded materials. τ_{PN} and Gb^2 (at zero K) can be useful indicators of amorphization under extreme loading conditions, though the detailed mechanism is material dependent.

Figure 5.5 (J) shows in a schematic fashion arrays of stacking faults and/or dislocations below and above the threshold for amorphization. As the pressure is raised beyond a critical value P_c, the partial dislocation density increases and so does their interaction through intersection and pile ups, generating localized stresses that eventually trigger the nucleation of amorphized regions. Amorphous islands are formed within these regions of high defect concentration. Thus, the shock wave advances, generating in its wake stacking faults which, upon interaction, give rise to amorphization. This structural change takes place in bands at orientations close to 45° to the front, corresponding to the orientation of maximum shear stress τ_s. The dislocations have a periodic spacing which relaxes the shear stresses in the lattice.

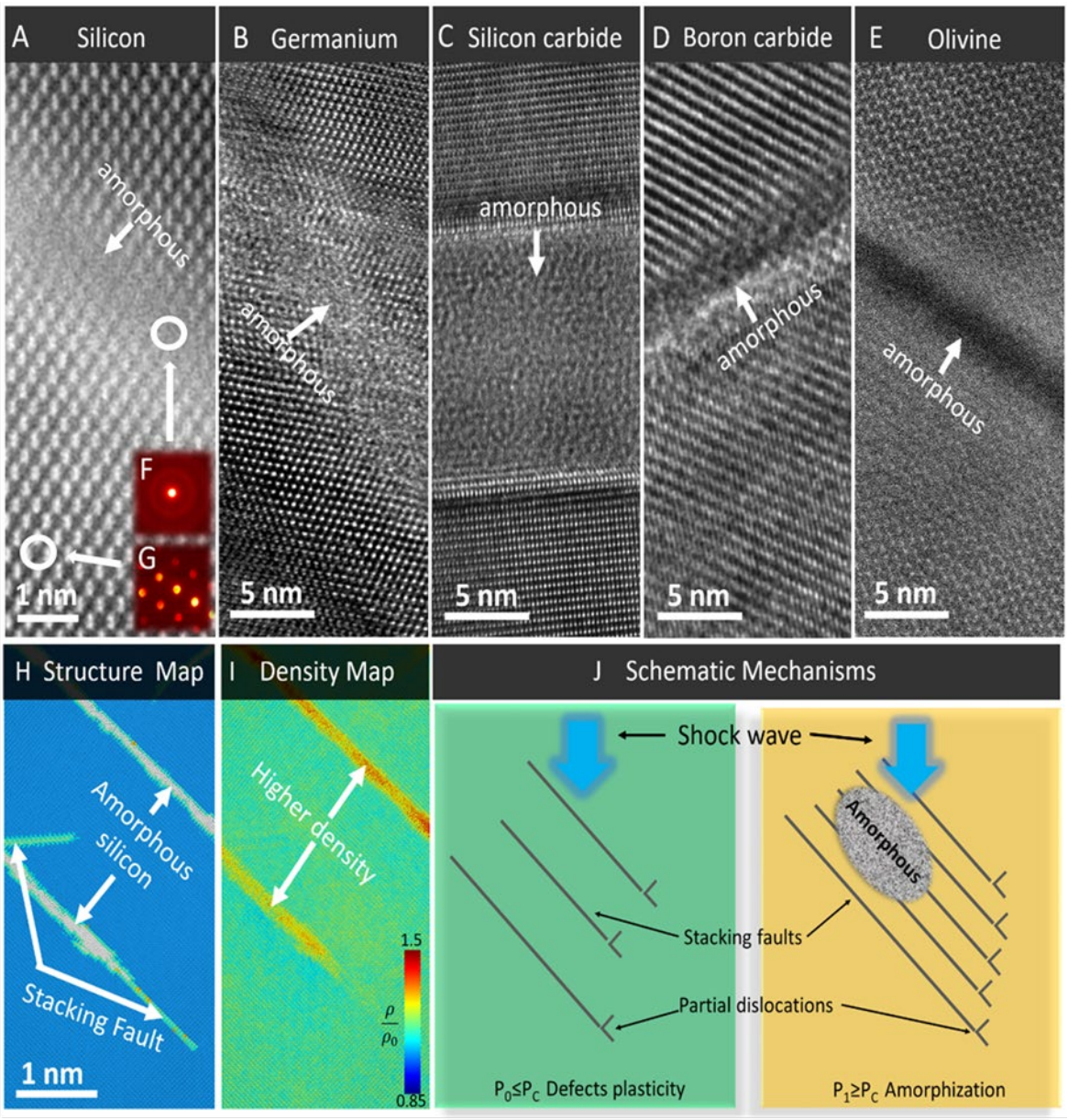

Figure 5.5 Amorphous bands produced by shock compression of (A) Si, (B) Ge, (C) SiC, (D) B_4C, (E) Olivine ($(Mg, Fe)_2SiO_4$). (F,G) Convergent electron diffraction patterns of amorphous and crystalline silicon, respectively. (H) Molecular dynamics simulation showing stacking faults (light blue) in Si and amorphous region (grey) forming between them. (I) Molecular dynamics simulation of density of the area simulated in 3H. The bands exhibit a higher density by virtue of amorphization. (J) Mechanism for formation of amorphous transformation: Schematic of partial dislocations propagating and leaving behind trailing stacking faults; shock stress is below (left, P_0) and above (right, P_1) a critical shock stress (P_c) for amorphization leading to the formation of amorphous island at $P_1 \geq P_c$.

There exist theoretical analyses of this class of structural transitions at different degrees of complexity. The Patel-Cohen [96] and Eshelby [103, 104] treatments provide an underlying energetics justification for the combined effects of hydrostatic and shear stresses on the thermodynamics. Levitas [105] provides a comprehensive theoretical framework for this effect, incorporating the effects of external, internal, and transformation (Eshelby) stresses and strains on the structural changes. Indeed, the shear strains produced by shear stresses generate greater relative atomic motions than hydrostatic stresses and strains in shock compression. The expression for the work per unit volume, *W*, for the transformation for a stress state where only normal stresses operate in the unit cube aligned with the shock propagation direction can be written as:

$$W=a_1\sigma_0\varepsilon_t+a_2\mathbf{S}\varepsilon_s+E_d+\gamma A \geq \Delta G_a(T) \quad (2)$$

where ε_t is the spherical compression strain and ε_s the deviatoric component of strain in a stress-free transformation, σ_0 is the hydrostatic stress ($(\sigma_{11}+\sigma_{22}+\sigma_{33})/3$), **S** is the deviatoric stress tensor, a_1 and a_2 are material parameters which dictate the evolution of one structure to the other. The term E_d, representing the energy per unit volume of the local defect structure ($=\rho_d\, Gb^2/2$, where ρ_d is the local density of dislocations prior to amorphization, G is the shear modulus, and b is the Burgers vector), is added to Levitas' equation as well as γ, the interfacial energy (A being the interfacial area). Here, $\Delta G_a(T)$ is a critical temperature-dependent value of the energy per unit volume that has to be overcome for the transformation to take place (activation energy). For $a_1=a_2=1$, Eqn. 1 reduces to the Patel-Cohen formalism. We apply it here to amorphization. In shock compression, the term ε_t is the strain generated by the change of crystalline and amorphous phase. As a first approximation, the shear strain is taken to be that for twinning, 0.707. We assume that when each slip plane has a partial dislocation, amorphization takes place. This results in that value, which can be calculated from the Burgers vector for partial dislocations. The shear strain for

twinning in fcc (and its derivatives) is 0.707 [211], and S is reduced to the local shear stress, τ (Fig. 2A). Thus, Eqn. 1 is reduced to:

$$W=\sigma_0\varepsilon_t+\boldsymbol{\tau}\varepsilon_s+\rho_d\, Gb^2/2\geq \Delta G_a\,(T) \qquad (3)$$

The corresponding results of energy calculations are presented in Table 1. For all five materials, the energy due to the relaxation of the shear stresses, $\tau\varepsilon_s$, is the largest. The elimination of shock-induced defects can also play a significant role. This analysis does not consider the interfacial energy, γA, because it is dependent on shape and volume.

Equation (2) indicates that the likelihood to form amorphous bands during plastic deformation is connected to the dislocation activity. The Peierls-Nabarro stress barrier, τ_{PN}, which has to be overcome for dislocations to move is higher, by orders of magnitude, in covalently bonded materials such as Si, ($\tau_{PN}/G\sim10^{-1}$), than in metallic face centered cubic materials such as Cu ($\tau_{PN}/G\sim10^{-5}$-10^{-4}) and body centered cubic ($\tau_{PN}/G\sim10^{-3}$-10^{-2}) materials such as Ta (here G is the shear modulus). Consequently, the average dislocation velocities for covalently-bonded materials such as Si are 4-5 orders of magnitude lower than for an fcc metal such as Cu for the same applied shear stress [272]. Figure 5.6 provides a graphical representation of the Peierls-Nabarro stresses for a number of materials [301]. The normalized Peierls-Nabarro stress (divided by the shear modulus, G) is plotted against the normalized dislocation energy per unit length, $Gb^2/2$, (where b is the Burgers vector), divided by the thermal energy at the melting temperature, kT_m. There is a clear correlation between these two parameters: as the dislocation energy per unit length, $Gb^2/2$, increases, so does the PN stress, τ_{PN}, until it saturates at the theoretical shear stress ($G/2\pi$). The correlation between the normalized τ_{PN} and a normalized dislocation energy per unit length is not for a single class of material (fcc, bcc, hcp, covalent) but for all materials. If one looks at the plot, one can see that each class occupies a small area indicated by its corresponding ellipsis.

Representative materials of each class are inserted into the ellipses. However, for the totality of materials, there is a definite trend with the curve saturating at the theoretical strength. While it is true that the high Peierls-Nabarro stress in covalent materials is well known, it is convenient to use this intrinsic property of the materials together with the dislocation line energy as a guiding principle to screen the materials which can undergo the amorphization. Both the energy of dislocations and the stress that has to be exerted on them to move (τ_{PN}) are much higher for covalently bonded materials than for metals. The amorphization tendency is enhanced by three factors: (1) a higher PN stress makes plasticity more difficult and thus allows higher deviatoric stresses to build up in the material, which, in turn, promotes directional amorphization; (2) once dislocations are generated, the higher line energy associated with them renders the dislocated area energetically less favorable; and (3) higher stress states lead to higher dislocation velocities (with possible supersonic bursts of dislocations) which eventually determines the kinetics of amorphization. The more open structures and higher interatomic bonds of covalent materials make them more amenable to amorphization.

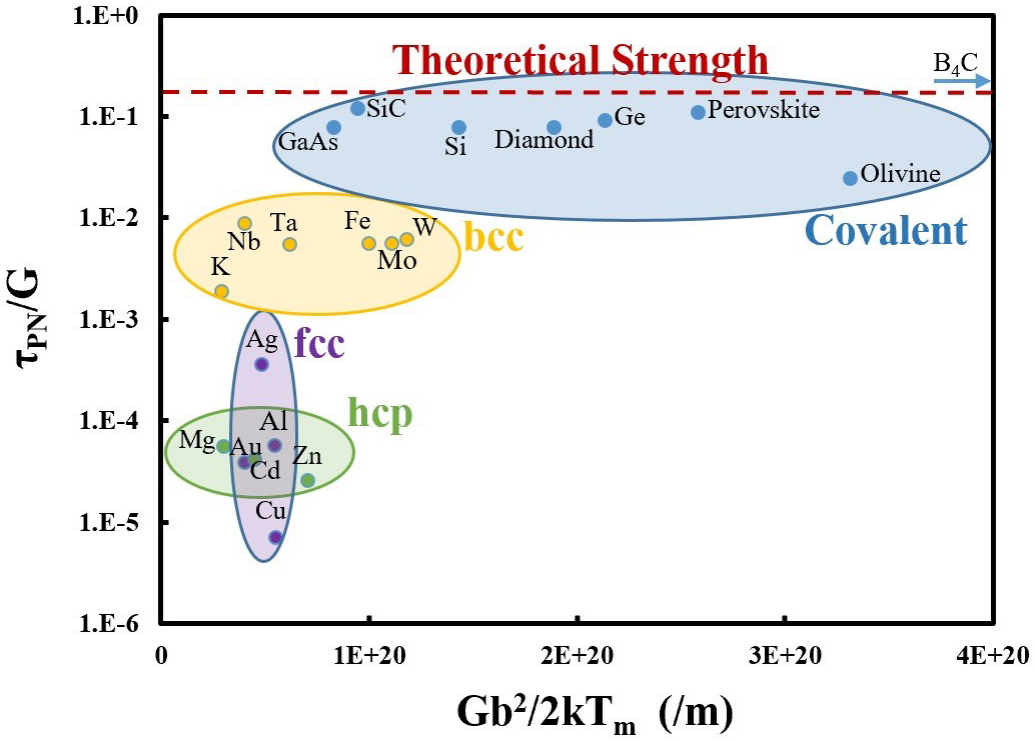

Figure 5.6 Paradigm of materials with different Peierls-Nabarro stresses (τ_{PN}) and dislocation line energies. Covalently bonded materials usually exhibit a higher τ_{PN} stress that is close to the theoretical strength of the material. This renders dislocation activity difficult and triggers brittle fracture under quasi-static conditions. On the other hand, when they are subjected to high stress states in confinement and/or during high strain rate deformation, amorphization emerges as an alternative deformation mechanism to release the applied deviatoric stress. Peierls-Nabarro stress for metals and covalently bonded materials are shown as a function of the ratio between dislocation energy and kT_m, where k is Boltzmann constant and T_m is the melting point (data from Kamimura et al. [301] and other sources).

Acknowledgements

Chapter 5, in part, is a reprint of material as it appears in: S. Zhao, B. Li, B. A. Remington, C. E. Wehrenberg, H. S. Park, E. N. Hahn, and M. A. Meyers. Directional amorphization of covalently-bonded solids: A generalized deformation mechanism in extreme loading. *Materials Today* 49 (2021): 59-67. The dissertation author was the second author of this paper.

Chapter 6 CONCLUSIONS AND PERSPECTIVES

6.1 Shock-induced Amorphization as a New Deformation Mechanism

Characterization of shock recovered [001] oriented diamond subjected to extreme pressures generated by pulsed laser at two amplitudes revealed that no defects are generated at 69 GPa and that dislocations, stacking faults, twins, and amorphous bands are observed at 115 GPa. This suggests that the threshold for these defects is in the 69-115 GPa region. Although there is substantial evidence in the literature for the formation of deformation-induced stacking faults, twins, and dislocations [224], the observation of amorphous bands in diamond is novel.

Amorphization has been observed in covalently bonded materials with negative Clapeyron slope: Si, Ge, SiC, B_4C, and olivine. In these materials there seems to be a threshold for the crystalline to amorphous transformation. Shear stresses play an important role in this process, as they induce large atomic displacements which can be relaxed by the formation of cracks, cleavage, dislocations, stacking faults, twins, and amorphization.

The amorphous bands typically follow specific crystallographic orientations, aligning with {111} slip planes although up to ~15˚ of deviation was observed. However, it remains unclear whether unloading will change the deformation microstructure. The synergy of high shear stresses associated with hydrostatic pressure, is proposed to generate amorphization in diamond under shock loading.

Our previous study demonstrated that five fully or partially covalently bonded materials (Si, Ge, SiC, B_4C, and olivine $(Mg, Fe)_2SiO_4$) [94, 95, 210 - 213, 266, 267] undergo shock-induced directional amorphization beyond their threshold stress. The results presented here show that diamond is also subjected to the same process. It is therefore confirmed that amorphization is a new deformation mechanism of covalently-bonded materials which have an open structure (with

low atomic packing factor) at ultrahigh strain rates (>10^7/s) when other mechanisms such as cleavage, dislocation slip, stacking faults, twinning, phase transformation, and fracture are kinetically less favorable.

The thermodynamic requirement for amorphization is that the energy gain of its crystalline to amorphous phase has to be sufficient to overcome the activation energy barrier for the amorphous phase to nucleate. In materials with well-defined slip systems such as Si and Ge, the amorphous bands initially align with the slip planes. However, after more generalized amorphization, the 45˚ orientation aligned with the maximum shear direction becomes dominant. In a material lacking well-defined slip systems, the amorphous bands predominantly align with this 45˚ maximum shear orientation. Most observations show that amorphous bands seem to align with slip planes of dislocations or twins and often deviate from the maximum shear cone, further indicating that crystalline defects are precursors to amorphization. The resemblance between the slip system and the amorphization pathway allows the material to accommodate shape changes without catastrophic failure. High density of stacking faults has been observed at the crystalline/amorphous interfaces in Si [211, 266, 267] and Ge [210], indicating that stacking faults act as the precursors to amorphization. However, the interfaces in $SmCo_5$ intermetallic [77], SiC [213] and B_4C [212] are relatively defect-free, revealing that amorphization can occur without the presence of lattice defects. Our current results do not indicate a clear association of defects with amorphization because of the scarcity of the latter. Higher pressure experiments are required to establish this connection.

Shock compression is not a prerequisite for amorphization, which has been identified in a wide range of materials under static, quasi-static, and dynamic loading conditions [269]. The role of defects in amorphization remains uncertain. Nevertheless, amorphization emerges as a new

deformation mechanism under extreme loading conditions, especially at high stresses, strains, and strain rates. In this study, amorphization is still in the initial stages due to the relatively low shock stress. Thicker amorphous bands/layers are expected at higher shock stress. Upon further heat transfer, the newly formed amorphous phase may recrystallize into energetically more favored crystalline phase, as previously observed in Si [211] and Ge [210].

$CaTiO_3$ was used as an analogue material for studying (Mg, Fe)SiO_3 and $CaSiO_3$ which are the most abundant minerals in the Earth mantle. Laser shock was applied to a [010] oriented orthorhombic single crystal $CaTiO_3$, subjecting it to a uniaxial strain state at a pressure of 70 GPa, characteristic of the Earth mantle. The corresponding maximum shear stress is ~20 GPa. This is significantly higher than the threshold for dislocation motion, the Peierls-Nabarro stress τ_{PN} (10 GPa for $CaTiO_3$). Materials with covalent and ionic bonding, such as $CaTiO_3$, are characterized by high Peierls-Nabarro stress (τ_{PN}), which increases resistance to dislocation motion. The high τ_{PN} of $CaTiO_3$ makes plastic deformation more difficult, resulting in the accumulation of higher deviatoric stresses within the material.

The laser shock generated a high density of defects in $CaTiO_3$. Most defects are mutually perpendicular dislocations. The dominant slip systems in our study are [110](001) and [$\bar{1}$10](001). The density of antiphase domain boundaries increased substantially after laser shock, along [010] and [100] directions. Dislocation density ranged from 15×10^{12} m^{-2} to 2×10^{12} m^{-2} within 12 μm from the shocked surface.

Because of its positive Clapeyron slope and higher atomic packing factor, $CaTiO_3$ behaves more like metals mainly by dislocation motion rather than covalently-bonded materials that respond by amorphization under shock compression, confirming our previous conjecture.

This profuse dislocation generation holds significance in planetary science, as it may provide insights into the mechanisms underlying deep-focus earthquakes and the effects of meteorite impacts.

6.2 Perspectives

Our experimental studies have proved shear-induced amorphization in diamond along [001] and olivine while high density of defects was observed in $CaTiO_3$ under laser shock compression. Molecular dynamics simulations have successfully corroborated shear-induced amorphization in Si. Thus, it is expected that MD simulations can be employed to confirm experimental results of shear-induced amorphization in [001] oriented diamond and olivine which has a more complex lattice structure and defects generated by shock compression in $CaTiO_3$.

Laser shock compression along [001] direction was approved to induce amorphization in diamond, however, our experiment at 115 GPa was only at the initial stage of amorphization. It is expected that the extent of amorphization in diamond will expand and recrystallization may occur at even higher pressures (with higher laser energy levels) along [001]. MD simulations [238] indicated that shock compressions along [011] and [111] directions in diamond can generate defects much easier (at lower pressures), therefore, more laser shock recovery experiments and post-shock characterizations on diamond along [011] and [111] directions can be conducted to corroborate these results of MD simulations [238].

Acknowledgements

Chapter 6, in part, has been submitted for publication of the material as it may appear in: B. Li, S. Zhao, and M. A. Meyers. Direct observation of plastic deformation in diamond under extreme loading. The dissertation author was the primary researcher and first author of this paper.

Chapter 6, in part, has been submitted for publication of the material as it may appear in: B. Li, S. Zhao, and M. A. Meyers. Plastic Deformation of $CaTiO_3$ Perovskite under Extreme Loading. The dissertation author was the primary researcher and first author of this paper.

REFERENCES

[1] Meyers, M.A. and Chawla, K.K., 2008. *Mechanical behavior of materials*. Cambridge university press.

[2] Klement, W., Willens, R.H. and Duwez, P.O.L., 1960. Non-crystalline structure in solidified gold–silicon alloys. *Nature*, *187*(4740), pp.869-870.

[3] Nicolas, A., Ferrero, E.E., Martens, K. and Barrat, J.L., 2018. Deformation and flow of amorphous solids: Insights from elastoplastic models. *Reviews of Modern Physics*, *90*(4), p.045006.

[4] Sheng, H.W., Luo, W.K., Alamgir, F.M., Bai, J.M. and Ma, E., 2006. Atomic packing and short-to-medium-range order in metallic glasses. *Nature*, *439*(7075), pp.419-425.

[5] King, S.V., 1967. Ring configurations in a random network model of vitreous silica. *Nature*, 213(5081), pp.1112-1113.

[6] Seymour, R.B., Mark, H.F., Pauling, L., Fisher, C.H., Stahl, G.A., Sperling, L.H., Marvel, C.S., Carraher, C.E. and Sperling, L.H., 1989. The "Katz Effect" on the Random Coil Model for Polymer Chains. *Pioneers in Polymer Science*, pp.41-46.

[7] Bernal, J.D., 1959. A geometrical approach to the structure of liquids. *Nature*, 183(4655), pp.141-147.

[8] Zheng, Q., Zhang, Y., Montazerian, M., Gulbiten, O., Mauro, J.C., Zanotto, E.D. and Yue, Y., 2019. Understanding glass through differential scanning calorimetry. *Chemical reviews*, *119*(13), pp.7848-7939.

[9] Patel, S.K., Swain, B.K., Behera, A. and Mohapatra, S.S., 2020. Metallic glasses: a revolution in material science. In *Metallic Glasses*. IntechOpen.

[10] Morrow, E.A., Terban, M.W., Thomas, L.C., Gray, D.L., Bowman, M.J., Billinge, S.J. and Schmidt, S.J., 2019. Effect of amorphization method on the physicochemical properties of amorphous sucrose. *Journal of Food Engineering*, *243*, pp.125-141.

[11] Misawa, M., Ryuo, E., Yoshida, K., Kalia, R.K., Nakano, A., Nishiyama, N., Shimojo, F., Vashishta, P. and Wakai, F., 2017. Picosecond amorphization of SiO2 stishovite under tension. *Science advances*, *3*(5), p.e1602339.

[12] Leide, A.J., Hobbs, L.W., Wang, Z., Chen, D., Shao, L. and Li, J., 2019. The role of chemical disorder and structural freedom in radiation-induced amorphization of silicon carbide deduced from electron spectroscopy and ab initio simulations. *Journal of Nuclear Materials*, *514*, pp.299-310.

[13] Darby, B.L., 2012. *Amorphization and solid phase epitaxial growth of germanium*. University of Florida.

[14] Chen, Z.Q., Wang, F., Huang, P., Lu, T.J. and Xu, K.W., 2013. Low-Temperature Annealing Induced Amorphization in Nanocrystalline NiW Alloy Films. *Journal of Nanomaterials*, *2013*(1), p.252965.

[15] Brant Carvalho, P.H., Mace, A., Bull, C.L., Funnell, N.P., Tulk, C.A., Andersson, O. and Häussermann, U., 2019. Elucidation of the pressure induced amorphization of tetrahydrofuran clathrate hydrate. *The Journal of Chemical Physics*, *150*(20).

[16] Richet, P. and Gillet, P., 1997. Pressure-induced amorphization of minerals: a review. *European Journal of Mineralogy-Ohne Beihefte*, *9*(5), pp.907-934.

[17] Tominaga, J. and Bolotov, L., 2018. Re-amorphization of GeSbTe alloys not through a melt-quenching process. *Applied Physics Express*, *12*(1), p.015504.

[18] Zarkadoula, E., Toulemonde, M. and Weber, W.J., 2015. Additive effects of electronic and nuclear energy losses in irradiation-induced amorphization of zircon. *Applied Physics Letters*, *107*(26).

[19] Romano, L., Jones, K.S., Sekar, K. and Krull, W.A., 2009. Amorphization of Si using cluster ions. *Journal of Vacuum Science & Technology B: Microelectronics and Nanometer Structures Processing, Measurement, and Phenomena*, *27*(2), pp.597-600.

[20] Deb, S.K., Wilding, M., Somayazulu, M. and McMillan, P.F., 2001. Pressure-induced amorphization and an amorphous–amorphous transition in densified porous silicon. *Nature*, 414(6863), pp.528-530.

[21] Qiang, W., Löbmann, K., McCoy, C.P., Andrews, G.P. and Zhao, M., 2020. Microwave-induced in situ amorphization: A new strategy for tackling the stability issue of amorphous solid dispersions. *Pharmaceutics*, *12*(7), p.655.

[22] Einfalt, T., Planinšek, O. and Hrovat, K., 2013. Methods of amorphization and investigation of the amorphous state. *Acta pharmaceutica*, *63*(3), pp.305-334.

[23] Pelaz, L., Marqués, L.A. and Barbolla, J., 2004. Ion-beam-induced amorphization and recrystallization in silicon. *Journal of applied physics*, *96*(11), pp.5947-5976.

[24] Ortiz, A.U., Boutin, A., Fuchs, A.H. and Coudert, F.X., 2013. Investigating the pressure-induced amorphization of zeolitic imidazolate framework ZIF-8: mechanical instability due to shear mode softening. *The journal of physical chemistry letters*, *4*(11), pp.1861-1865.

[25] Niknam, A.R., Hashemzadeh, M., Shokri, B. and Rouhani, M.R., 2009. Rarefaction shock waves and Hugoniot curve in the presence of free and trapped particles. *Physics of Plasmas*, *16*(12).

[26] Meldrum, A., Boatner, L.A. and Ewing, R.C., 2001. Nanocrystalline zirconia can be amorphized by ion irradiation. *Physical review letters*, *88*(2), p.025503.

[27] Meldrum, A., Boatner, L.A., Weber, W.J. and Ewing, R.C., 2002. Amorphization and recrystallization of the ABO3 oxides. *Journal of nuclear Materials*, *300*(2-3), pp.242-254.

[28] Mejdoub, R., Hammi, H., Khitouni, M., Sunol, J.J. and M'nif, A., 2017. Effect of amorphization degree on mechanical and microstructural properties of portland cement paste. *Journal of Materials in Civil Engineering*, *29*(6), p.04017019.

[29] Hurle, K., Neubauer, J. and Goetz-Neunhoeffer, F., 2017. Hydration enthalpy of amorphous tricalcium phosphate resulting from partially amorphization of β-tricalcium phosphate. *BioNanoMaterials*, *18*(3-4), p.20160016.

[30] Greaves, G.N., Meneau, F., Sapelkin, A., Colyer, L.M., Ap Gwynn, I., Wade, S. and Sankar, G., 2003. The rheology of collapsing zeolites amorphized by temperature and pressure. *Nature Materials*, *2*(9), pp.622-629.

[31] Fujita, M., Izawa, Y., Norimatsu, T., Miyanaga, N. and Izawa, Y., 2009, June. Laser wavelength dependences of amorphization and crystalization of Si by femtosecond laser pulses. In *The European Conference on Lasers and Electro-Optics* (p. CM_P21). Optica Publishing Group.

[32] Doreth, M., Hussein, M.A., Priemel, P.A., Grohganz, H., Holm, R., de Diego, H.L., Rades, T. and Löbmann, K., 2017. Amorphization within the tablet: Using microwave irradiation to form a glass solution in situ. *International Journal of Pharmaceutics*, *519*(1-2), pp.343-351.

[33] Djurabekova, F., Backholm, M., Backman, M., Pakarinen, O.H., Keinonen, J., Nordlund, K., Shan, T.R., Devine, B.D. and Sinnott, S.B., 2010. Amorphization of α-quartz and comparative study of defects in amorphized quartz and Si nanocrystals embedded in amorphous silica. *Nuclear Instruments and Methods in Physics Research Section B: Beam Interactions with Materials and Atoms*, *268*(19), pp.3095-3098.

[34] Grishin, A.M., 2020. Hardness, Young's modulus and elastic recovery in magnetron sputtered amorphous AlMgB14 films. *Crystals*, *10*(9), p.823.

[35] Cao, S., Bennett, T.D., Keen, D.A., Goodwin, A.L. and Cheetham, A.K., 2012. Amorphization of the prototypical zeolitic imidazolate framework ZIF-8 by ball-milling. *Chemical communications*, *48*(63), pp.7805-7807.

[36] Battaglia, A. and Campisano, S.U., 1993. Mechanisms of amorphization in crystalline silicon. *Journal of applied physics*, *74*(10), pp.6058-6061.

[37] Arora, A.K., Sastry, V.S., Sahu, P.C. and Mary, T.A., 2004. The pressure-amorphized state in zirconium tungstate: a precursor to decomposition. *Journal of Physics: Condensed Matter*, *16*(7), p.1025.

[38] Khulbe, P.K., Xun, X. and Mansuripur, M., 2000. Crystallization and amorphization studies of a Ge2Sb2. 3Te5 thin-film sample under pulsed laser irradiation. *Applied optics*, 39(14), pp.2359-2366.

[39] Akahama, Y., Mori, Y., Kobayashi, M., Kawamura, H., Kimura, K. and Takeuchi, S., 1989. Pressure-induced amorphization of quasi crystals. *Journal of the Physical Society of Japan*, *58*(7), pp.2231-2234.

[40] Motta, A.T., Lefebvre, F. and Lemaignan, C., 1991, January. Amorphization of precipitates in Zircaloy under neutron and charged-particle irradiation. In *Zirconium in the Nuclear Industry: Ninth International Symposium*. ASTM International.

[41] Douillard, L. and Duraud, J.P., 1996. Amorphization of α-quartz under irradiation. *Journal de physique III*, 6(12), pp.1677-1687.

[42] Jiang, T.T., Wang, J.J., Lu, L., Ma, C.S., Zhang, D.L., Rao, F., Jia, C.L. and Zhang, W., 2019. Progressive amorphization of GeSbTe phase-change material under electron beam irradiation. *APL materials*, *7*(8).

[43] Ewing, R.C., Meldrum, A., Wang, L. and Wang, S., 2000. Radiation-induced amorphization. *Reviews in mineralogy and geochemistry*, *39*(1), pp.319-361.

[44] Wang, K., Liu, R., Qiao, Y., Cui, J., Song, B., Liu, B. and Zou, B., 2015. Pressure-induced reversible phase transition and amorphization of CH3NH3PbI3. *arXiv preprint arXiv:1509.03717*.

[45] Hirayama, J., Kobayashi, H. and Fukuoka, A., 2020. Amorphization and semi-dry conversion of crystalline cellulose to oligosaccharides by impregnated phosphoric acid. *Bulletin of the Chemical Society of Japan*, *93*(2), pp.273-278.

[46] Kranjc, K., Thind, A.S., Borisevich, A.Y., Mishra, R., Flores, K.M. and Skemer, P., 2020. Amorphization and plasticity of olivine during low-temperature micropillar deformation experiments. *Journal of Geophysical Research: Solid Earth*, *125*(5), p.e2019JB019242.

[47] Carrez, P., Demyk, K., Cordier, P., Gengembre, L., Grimblot, J., D'Hendecourt, L., Jones, A.P. and Leroux, H., 2002. Low-energy helium ion irradiation-induced amorphization and chemical changes in olivine: Insights for silicate dust evolution in the interstellar medium. *Meteoritics & Planetary Science*, *37*(11), pp.1599-1614.

[48] Taylor, P.C., 2020. *World Scientific Reference Of Amorphous Materials, The: Structure, Properties, Modeling And Main Applications (In 3 Volumes)* (Vol. 15). World Scientific.

[49] Suryanarayana, C., 2001. Mechanical alloying and milling. *Progress in materials science*, *46*(1-2), pp.1-184.

[50] Matsuki, K., Inoue, A., Kimura, H.M. and Masumoto, T., 1988. New amorphous Cu Nb (Si, Ge or Sn) alloys prepared by mechanical alloying of elemental powders. *Materials Science and Engineering*, *97*, pp.47-51.

[51] Cho, Y.S. and Coch, C.C., 1991. Structural evolution in Nb3Sn during mechanical attrition. *Materials Science and Engineering: A*, *141*(1), pp.139-148.

[52] Meyers, M.A., Xu, Y.B., Xue, Q., Perez-Prado, M.T. and McNelley, T.R., 2003. Microstructural evolution in adiabatic shear localization in stainless steel. *Acta Materialia*, *51*(5), pp.1307-1325.

[53] Han, S., Zhao, L., Jiang, Q. and Lian, J., 2012. Deformation-induced localized solid-state amorphization in nanocrystalline nickel. *Scientific Reports*, *2*(1), p.493.

[54] Hinrichs, R., Vasconcellos, M.A.Z., Österle, W. and Prietzel, C., 2018. Amorphization of graphite flakes in gray cast iron under tribological load. *Materials Research*, *21*(4), p.e20171000.

[55] Wang, W.H., 2014. High-entropy metallic glasses. *Jom*, *66*, pp.2067-2077.

[56] Yang, X., Zhou, Y., Zhu, R., Xi, S., He, C., Wu, H. and Gao, Y., 2020. A novel, amorphous, non-equiatomic FeCrAlCuNiSi high-entropy alloy with exceptional corrosion resistance and mechanical properties. *Acta Metallurgica Sinica (English Letters)*, *33*, pp.1057-1063.

[57] Zhao, S., Li, Z., Zhu, C., Yang, W., Zhang, Z., Armstrong, D.E., Grant, P.S., Ritchie, R.O. and Meyers, M.A., 2021. Amorphization in extreme deformation of the CrMnFeCoNi high-entropy alloy. *Science advances*, *7*(5), p.eabb3108.

[58] Pekin, T.C., Ding, J., Gammer, C., Ozdol, B., Ophus, C., Asta, M., Ritchie, R.O. and Minor, A.M., 2019. Direct measurement of nanostructural change during in situ deformation of a bulk metallic glass. *Nature communications*, *10*(1), p.2445.

[59] Wang, Y., Li, J., Hamza, A.V. and Barbee Jr, T.W., 2007. Ductile crystalline–amorphous nanolaminates. *Proceedings of the National Academy of Sciences*, *104*(27), pp.11155-11160.

[60] Guo, W., Jägle, E.A., Choi, P.P., Yao, J., Kostka, A., Schneider, J.M. and Raabe, D., 2014. Shear-induced mixing governs codeformation of crystalline-amorphous nanolaminates. *Physical review letters*, *113*(3), p.035501.

[61] Wang, J., Zhou, Q., Shao, S. and Misra, A., 2017. Strength and plasticity of nanolaminated materials. *Materials Research Letters*, *5*(1), pp.1-19.

[62] Weeber, A.W. and Bakker, H., 1988. Amorphous NiZr powders by milling the crystalline alloys. *Journal of the Less Common Metals*, *141*(1), pp.93-102.

[63] Chen, Y., Bibole, M., Le Hazif, R. and Martin, G., 1993. Ball-milling-induced amorphization in Ni x Zr y compounds: A parametric study. *Physical Review B*, *48*(1), p.14.

[64] Jang, J.S.C. and Koch, C.C., 1990. Amorphization and disordering of the Ni3Al ordered intermetallic by mechanical milling. *Journal of Materials Research*, *5*(3), pp.498-510.

[65] Koike, J.I., Parkin, D.M. and Nastasi, M., 1990. The role of shear instability in amorphization of cold-rolled NiTi. *Philosophical magazine letters*, *62*(4), pp.257-264.

[66] Nishida, M., Chiba, A., Morizono, Y., Matsumoto, M., Murakami, T. and Inoue, A., 1995. Formation of nonequilibrium phases at collision interface in an explosively welded Ti/Ni clad. *Materials Transactions, JIM*, *36*(11), pp.1338-1343.

[67] Huang, J.Y., Zhu, Y.T., Liao, X.Z. and Valiev, R.Z., 2004. Amorphization of TiNi induced by high-pressure torsion. *Philosophical magazine letters*, *84*(3), pp.183-190.

[68] Peterlechner, M., Waitz, T. and Karnthaler, H.P., 2009. Nanoscale amorphization of severely deformed NiTi shape memory alloys. *Scripta Materialia*, *60*(12), pp.1137-1140.

[69] Thomas, G., Mori, H., Fujita, H. and Sinclair, R., 1982. Electron irradiation induced crystalline amorphous transitions in Ni Ti alloys. *Scripta Metallurgica*, *16*(5), pp.589-592.

[70] Yamada, K. and Koch, C.C., 1993. The influence of mill energy and temperature on the structure of the TiNi intermetallic after mechanical attrition. *Journal of materials research*, *8*, pp.1317-1326.

[71] Grant, D.M., Green, S.M. and Wood, J.V., 1995. The surface performance of shot peened and ion implanted NiTi shape memory alloy. *Acta Metallurgica et Materialia*, *43*(3), pp.1045-1051.

[72] Tatyanin, E.V. and Kurdyumov, V.G., 1990. Nucleation of the deformation induced amorphous phase at twin boundaries in TiNi alloy. *Physica status solidi (a)*, *121*(2), pp.455-459.

[73] Jiang, S., Hu, L., Zhang, Y. and Liang, Y., 2013. Nanocrystallization and amorphization of NiTi shape memory alloy under severe plastic deformation based on local canning compression. *Journal of non-crystalline solids*, *367*, pp.23-29.

[74] Ye, C., Zhou, X., Telang, A., Gao, H., Ren, Z., Qin, H., Suslov, S., Gill, A.S., Mannava, S.R., Qian, D. and Doll, G.L., 2016. Surface amorphization of NiTi alloy induced by Ultrasonic Nanocrystal Surface Modification for improved mechanical properties. *journal of the mechanical behavior of biomedical materials*, *53*, pp.455-462.

[75] Hua, P., Chu, K. and Sun, Q., 2018. Grain refinement and amorphization in nanocrystalline NiTi micropillars under uniaxial compression. *Scripta Materialia*, *154*, pp.123-126.

[76] Tsuchiya, K. and Ciuca, O., 2011, February. Nanostructure Formation and Amorphization in Intermetallic Compounds by Severe Plastic Deformation. In *Materials Science Forum* (Vol. 667, pp. 17-24). Trans Tech Publications Ltd.

[77] Luo, H., Sheng, H., Zhang, H., Wang, F., Fan, J., Du, J., Ping Liu, J. and Szlufarska, I., 2019. Plasticity without dislocations in a polycrystalline intermetallic. *Nature communications*, *10*(1), p.3587.

[78] Jeanloz, R., Ahrens, T.J., Lally, J.S., Nord Jr, G.L., Christie, J.M. and Heuer, A.H., 1977. Shock-produced olivine glass: First observation. *Science*, *197*(4302), pp.457-459.

[79] Minowa, K. and Sumino, K., 1992. Stress-induced amorphization of silicon crystal by mechanical scratching. *Physical review letters*, *69*(2), p.320.

[80] Kingma, K.J., Meade, C., Hemley, R.J., Mao, H.K. and Veblen, D.R., 1993. Microstructural observations of α-quartz amorphization. *Science*, *259*(5095), pp.666-669.

[81] Gratz, A.J., DeLoach, L.D., Clough, T.M. and Nellis, W.J., 1993. Shock amorphization of cristobalite. *Science*, *259*(5095), pp.663-666.

[82] Cordier, P., Doukhan, J.C. and Peyronneau, J., 1993. Structural transformations of quartz and berlinite AlPO4 at high pressure and room temperature: a transmission electron microscopy study. *Physics and chemistry of minerals*, *20*(3), pp.176-189.

[83] Serghiou, G.C. and Hammack, W.S., 1993. Pressure-induced amorphization of wollastonite (CaSiO3) at room temperature. *The Journal of chemical physics*, *98*(12), pp.9830-9834.

[84] Irifune, T., Kuroda, K., Funamori, N., Uchida, T., Yagi, T., Inoue, T. and Miyajima, N., 1996. Amorphization of serpentine at high pressure and high temperature. *Science*, 272(5267), pp.1468-1470.

[85] Markenscoff, X., 2021. “Volume collapse” instabilities in deep-focus earthquakes: a shear source nucleated and driven by pressure. *Journal of the Mechanics and Physics of Solids*, *152*, p.104379.

[86] Chen, M., McCauley, J.W. and Hemker, K.J., 2003. Shock-induced localized amorphization in boron carbide. *Science*, *299*(5612), pp.1563-1566.

[87] Subhash, G., Ghosh, D., Blaber, J., Zheng, J.Q., Halls, V. and Masters, K., 2013. Characterization of the 3-D amorphized zone beneath a Vickers indentation in boron carbide using Raman spectroscopy. *Acta materialia*, *61*(10), pp.3888-3896.

[88] Subhash, G., Awasthi, A.P., Kunka, C., Jannotti, P. and DeVries, M., 2016. In search of amorphization-resistant boron carbide. *Scripta Materialia*, *123*, pp.158-162.

[89] Reddy, K.M., Guo, D., Song, S., Cheng, C., Han, J., Wang, X., An, Q. and Chen, M., 2021. Dislocation-mediated shear amorphization in boron carbide. *Science advances*, 7(8), p.eabc6714.

[90] Reddy, K.M., Hirata, A., Liu, P., Fujita, T., Goto, T. and Chen, M.W., 2014. Shear amorphization of boron suboxide. *Scripta Materialia*, *76*, pp.9-12.

[91] Zeng, Z., Yang, L., Zeng, Q., Lou, H., Sheng, H., Wen, J., Miller, D.J., Meng, Y., Yang, W., Mao, W.L. and Mao, H.K., 2017. Synthesis of quenchable amorphous diamond. *Nature communications*, *8*(1), p.322.

[92] Shang, Y., Liu, Z., Dong, J., Yao, M., Yang, Z., Li, Q., Zhai, C., Shen, F., Hou, X., Wang, L. and Zhang, N., 2021. Ultrahard bulk amorphous carbon from collapsed fullerene. *Nature*, 599(7886), pp.599-604.

[93] Tang, H., Yuan, X., Cheng, Y., Fei, H., Liu, F., Liang, T., Zeng, Z., Ishii, T., Wang, M.S., Katsura, T. and Sheng, H., 2021. Synthesis of paracrystalline diamond. *Nature*, *599*(7886), pp.605-610.

[94] Zhao, S., Kad, B., Hahn, E., Chen, L., Yekaterina, O., More, K., Remington, B., Wehrenberg, C., LaSalvia, J., Yang, W. and Quan, H., 2018. Shock-induced amorphization in covalently bonded solids. In *EPJ Web of Conferences* (Vol. 183, p. 03027). EDP Sciences.

[95] Zhao, S., Li, B., Remington, B.A., Wehrenberg, C.E., Park, H.S., Hahn, E.N. and Meyers, M.A., 2021. Directional amorphization of covalently-bonded solids: A generalized deformation mechanism in extreme loading. *Materials Today*, 49, pp.59-67.

[96] Patel, J.R. and Cohen, M., 1953. Criterion for the action of applied stress in the martensitic transformation. *Acta metallurgica*, *1*(5), pp.531-538.

[97] Levitas, V.I. and Ravelo, R., 2012. Virtual melting as a new mechanism of stress relaxation under high strain rate loading. *Proceedings of the National Academy of Sciences*, 109(33), pp.13204-13207.

[98] Samae, V., Cordier, P., Demouchy, S., Bollinger, C., Gasc, J., Koizumi, S., Mussi, A., Schryvers, D. and Idrissi, H., 2021. Stress-induced amorphization triggers deformation in the lithospheric mantle. *Nature*, *591*(7848), pp.82-86.

[99] Meade, C. and Jeanloz, R., 1990. Static compression of Ca (OH) 2 at room temperature: observations of amorphization and equation of state measurements to 10.7 GPa. *Geophysical Research Letters*, *17*(8), pp.1157-1160.

[100] Vaidya, S.N. and Sugandhi, V., 1999. Pressure induced amorphization in calcium phosphates. *Journal of materials science*, *34*, pp.3769-3778.

[101] Huang, W., Shishehbor, M., Guarín-Zapata, N., Kirchhofer, N.D., Li, J., Cruz, L., Wang, T., Bhowmick, S., Stauffer, D., Manimunda, P. and Bozhilov, K.N., 2020. A natural impact-resistant bicontinuous composite nanoparticle coating. *Nature Materials*, *19*(11), pp.1236-1243.

[102] Koch, C.C., 1996. Amorphization of single composition powders by mechanical milling. *Scripta materialia*, *34*(1).

[103] Eshelby, J.D., 1956. The continuum theory of lattice defects. *In Solid state physics* (Vol. 3, pp. 79-144). Academic Press.

[104] Eshelby, J.D., 1957. The determination of the elastic field of an ellipsoidal inclusion, and related problems. *Proceedings of the royal society of London. Series A. Mathematical and physical sciences*, *241*(1226), pp.376-396.

[105] Levitas, V.I., Chen, H. and Xiong, L., 2017. Lattice instability during phase transformations under multiaxial stress: modified transformation work criterion. *Physical Review B*, *96*(5), p.054118.

[106] A. Yermakov, Y. Yurchikov, VA Barinov, *The Physics of Metals and Metallography* 52 (1981) 50–58.

[107] Koch, C.C., Cavin, O.B., McKamey, C.G. and Scarbrough, J.O., 1983. Preparation of ‘‘amorphous’’Ni60Nb40 by mechanical alloying. *Applied Physics Letters*, 43(11), pp.1017-1019.

[108] Donovan, 1.P., Spaepen, F., Turnbull, D., Poate, J.M. and Jacobson, D.C., 1985. Calorimetric studies of crystallization and relaxation of amorphous Si and Ge prepared by ion implantation. *Journal of Applied Physics*, *57*(6), pp.1795-1804.

[109] Szlufarska, I., Kalia, R.K., Nakano, A. and Vashishta, P., 2005. Atomistic mechanisms of amorphization during nanoindentation of SiC: a molecular dynamics study. *Physical Review B—Condensed Matter and Materials Physics*, 71(17), p.174113.

[110] Wu, Z., Liu, W., Zhang, L. and Lim, S., 2020. Amorphization and dislocation evolution mechanisms of single crystalline 6H-SiC. *Acta Materialia*, *182*, pp.60-67.

[111] Idrissi, H., Carrez, P. and Cordier, P., 2022. On amorphization as a deformation mechanism under high stresses. *Current Opinion in Solid State and Materials Science*, 26(1), p.100976.

[112] Olson, G.B. and Cohen, M., 1975. Kinetics of strain-induced martensitic nucleation. *Metallurgical transactions* A, 6, pp.791-795.

[113] Spaepen, F., 1977. A microscopic mechanism for steady state inhomogeneous flow in metallic glasses. *Acta metallurgica*, *25*(4), pp.407-415.

[114] Argon, A.S., 1979. Plastic deformation in metallic glasses. *Acta metallurgica*, *27*(1), pp.47-58.

[115] Park, E.S., 2015. Understanding of the shear bands in amorphous metals. *Applied Microscopy*, *45*(2), pp.63-73.

[116] Schuh, C.A., Hufnagel, T.C. and Ramamurty, U., 2007. Mechanical behavior of amorphous alloys. *Acta Materialia*, *55*(12), pp.4067-4109.

[117] Gu, X., Livi, K.J. and Hufnagel, T.C., 2002. Structure of shear bands in zirconium-based metallic glasses observed by transmission electron microscopy. *MRS Online Proceedings Library*, *754*, pp.1-6.

[118] Hieronymus-Schmidt, V., Rösner, H., Wilde, G. and Zaccone, A., 2017. Shear banding in metallic glasses described by alignments of Eshelby quadrupoles. *Physical Review B*, *95*(13), p.134111.

[119] Ovid'Ko, I.A., 2012. Nanoscale amorphization as a special deformation mode in nanowires. *Scripta Materialia*, *66*(6), pp.402-405.

[120] Albe, K., Ritter, Y. and Şopu, D., 2013. Enhancing the plasticity of metallic glasses: Shear band formation, nanocomposites and nanoglasses investigated by molecular dynamics simulations. *Mechanics of Materials*, *67*, pp.94-103.

[121] Saumon, D., Chabrier, G. and van Horn, H.M., 1995. An equation of state for low-mass stars and giant planets. *Astrophysical Journal Supplement v. 99, p. 713*, *99*, p.713.

[122] Guillot, T., 1999. Interiors of giant planets inside and outside the solar system. *Science*, 286(5437), pp.72-77.

[123] Hubbard, W.B., Nellis, W.J., Mitchell, A.C., Holmes, N.C., Limaye, S.S. and McCandless, P.C., 1991. Interior structure of Neptune: comparison with Uranus. *Science*, 253(5020), pp.648-651.

[124] Ross, M., 1981. The ice layer in Uranus and Neptune—diamonds in the sky?. *Nature*, 292(5822), pp.435-436.

[125] Ancilotto, F., Chiarotti, G.L., Scandolo, S. and Tosatti, E., 1997. Dissociation of methane into hydrocarbons at extreme (planetary) pressure and temperature. *Science*, 275(5304), pp.1288-1290.

[126] Benedetti, L.R., Nguyen, J.H., Caldwell, W.A., Liu, H., Kruger, M. and Jeanloz, R., 1999. Dissociation of CH4 at high pressures and temperatures: diamond formation in giant planet interiors?. *Science*, *286*(5437), pp.100-102.

[127] Kraus, D., Vorberger, J., Pak, A., Hartley, N.J., Fletcher, L.B., Frydrych, S., Galtier, E., Gamboa, E.J., Gericke, D.O., Glenzer, S.H. and Granados, E., 2017. Formation of diamonds in laser-compressed hydrocarbons at planetary interior conditions. *Nature Astronomy*, 1(9), pp.606-611.

[128] Cheng, B., Hamel, S. and Bethkenhagen, M., 2023. Thermodynamics of diamond formation from hydrocarbon mixtures in planets. *Nature Communications*, *14*(1), p.1104.

[129] Xu, Y., Lin, Y., Wu, P., Namur, O., Zhang, Y. and Charlier, B., 2024. A diamond-bearing core-mantle boundary on Mercury. *Nature Communications*, *15*(1), p.5061.

[130] Bond, J.C., O'Brien, D.P. and Lauretta, D.S., 2010. The compositional diversity of extrasolar terrestrial planets. I. In situ simulations. *The Astrophysical Journal*, *715*(2), p.1050.

[131] Wilson, H.F. and Militzer, B., 2014. Interior phase transformations and mass–radius relationships of silicon–carbon planets. *The Astrophysical Journal*, *793*(1), p.34.

[132] Madhusudhan, N., Lee, K.K. and Mousis, O., 2012. A possible carbon-rich interior in super-Earth 55 Cancri e. *The Astrophysical Journal Letters*, *759*(2), p.L40.

[133] Nissen, P.E., 2013. The carbon-to-oxygen ratio in stars with planets. *Astronomy & Astrophysics*, *552*, p.A73.

[134] Hu, R., Bello-Arufe, A., Zhang, M., Paragas, K., Zilinskas, M., van Buchem, C., Bess, M., Patel, J., Ito, Y., Damiano, M. and Scheucher, M., 2024. A secondary atmosphere on the rocky exoplanet 55 Cancri e. *Nature*, *630*(8017), pp.609-612.

[135] Lang Jr, J.M. and Gupta, Y.M., 2011. Experimental determination of third-order elastic constants of diamond. *Physical review letters*, *106*(12), p.125502.

[136] Lang, J.M. and Gupta, Y.M., 2010. Strength and elastic deformation of natural and synthetic diamond crystals shock compressed along [100]. *Journal of Applied Physics*, 107(11).

[137] Lang, J.M., Winey, J.M. and Gupta, Y.M., 2018. Strength and deformation of shocked diamond single crystals: Orientation dependence. *Physical Review B*, *97*(10), p.104106.

[138] McWilliams, R.S., Eggert, J.H., Hicks, D.G., Bradley, D.K., Celliers, P.M., Spaulding, D.K., Boehly, T.R., Collins, G.W. and Jeanloz, R., 2010. Strength effects in diamond under shock compression from 0.1 to 1 TPa. *Physical Review B—Condensed Matter and Materials Physics*, *81*(1), p.014111.

[139] Millot, M., Sterne, P.A., Eggert, J.H., Hamel, S., Marshall, M.C. and Celliers, P.M., 2020. High-precision shock equation of state measurements for metallic fluid carbon between 15 and 20 Mbar. *Physics of Plasmas*, *27*(10).

[140] Grover, R., 1979. Does diamond melt?. *Journal of Chemical Physics*, *71*(9), pp.3824-3829.

[141] Kondo, K.I. and Ahrens, T.J., 1983. Shock compression of diamond crystal. *Geophysical Research Letters*, 10(4), pp.281-284.

[142] Pavlovsky, M.N., 1971. Shock compressibility of six very hard substances. *Sov Phys Solid State*, *12*(7), pp.1736-1737.

[143] McQueen, R.G. and Marsh, S.P., 1967. *Hugoniots of Graphites of Various Initial Densities and the Equation of State of Carbon* (No. LA-DC-8411; CONF-670914-12). Los Alamos Scientific Lab., N. Mex..

[144] Winey, J.M., Knudson, M.D. and Gupta, Y.M., 2020. Shock compression response of diamond single crystals at multimegabar stresses. *Physical Review B*, *101*(18), p.184105.

[145] MacDonald, M.J., McBride, E.E., Galtier, E., Gauthier, M., Granados, E., Kraus, D., Krygier, A., Levitan, A.L., MacKinnon, A.J., Nam, I. and Schumaker, W., 2020. Using simultaneous x-ray diffraction and velocity interferometry to determine material strength in shock-compressed diamond. *Applied Physics Letters*, *116*(23).

[146] Knudson, M.D., Desjarlais, M.P. and Dolan, D.H., 2008. Shock-wave exploration of the high-pressure phases of carbon. *Science*, *322*(5909), pp.1822-1825.

[147] Hicks, D.G., Boehly, T.R., Celliers, P.M., Bradley, D.K., Eggert, J.H., McWilliams, R.S., Jeanloz, R. and Collins, G.W., 2008. High-precision measurements of the diamond Hugoniot in and above the melt region. *Physical Review B—Condensed Matter and Materials Physics*, *78*(17), p.174102.

[148] Brygoo, S., Henry, E., Loubeyre, P., Eggert, J., Koenig, M., Loupias, B., Benuzzi-Mounaix, A. and Rabec Le Gloahec, M., 2007. Laser-shock compression of diamond and evidence of a negative-slope melting curve. *Nature materials*, *6*(4), pp.274-277.

[149] Gregor, M.C., Fratanduono, D.E., McCoy, C.A., Polsin, D.N., Sorce, A., Rygg, J.R., Collins, G.W., Braun, T., Celliers, P.M., Eggert, J.H. and Meyerhofer, D.D., 2017. Hugoniot and release measurements in diamond shocked up to 26 Mbar. *Physical Review B*, *95*(14), p.144114.

[150] Katagiri, K., Ozaki, N., Umeda, Y., Irifune, T., Kamimura, N., Miyanishi, K., Sano, T., Sekine, T. and Kodama, R., 2020. Shock response of full density nanopolycrystalline diamond. *Physical Review Letters*, *125*(18), p.185701.

[151] Nagao, H., Nakamura, K.G., Kondo, K., Ozaki, N., Takamatsu, K., Ono, T., Shiota, T., Ichinose, D., Tanaka, K.A., Wakabayashi, K. and Okada, K., 2006. Hugoniot measurement of diamond under laser shock compression up to 2TPa. *Physics of Plasmas*, *13*(5).

[152] Pavlovskii, M.N., 1971. Shock compression of diamond. *Soviet Physics Solid State, Ussr*, *13*(3), pp.741.

[153] Meyers, M.A., 1994. *Dynamic behavior of materials*. John Wiley & Sons.

[154] McBride, E.E., Krygier, A., Ehnes, A., Galtier, E., Harmand, M., Konôpková, Z., Lee, H.J., Liermann, H.P., Nagler, B., Pelka, A. and Rödel, M., 2019. Phase transition lowering in dynamically compressed silicon. *Nature Physics*, *15*(1), pp.89-94.

[155] Lang Jr, J.M., 2013. *Mechanical and optical response of diamond crystals shock compressed along different orientations*. Washington State University.

[156] Gupta, Y.M., 1975. Stress dependence of elastic-wave attenuation in LiF. *Journal of Applied Physics*, *46*(8), pp.3395-3401.

[157] Hirth, J.P., Lothe, J. and Mura, T., 1983. Theory of dislocations. *Journal of Applied Mechanics*, *50*(2), pp.476-477.

[158] Gilman, J.J., 1969. *Micromechanics of flow in solids*. McGraw-Hill.

[159] Dang, C., Chou, J.P., Dai, B., Chou, C.T., Yang, Y., Fan, R., Lin, W., Meng, F., Hu, A., Zhu, J. and Han, J., 2021. Achieving large uniform tensile elasticity in microfabricated diamond. *Science*, *371*(6524), pp.76-78.

[160] Roundy, D. and Cohen, M.L., 2001. Ideal strength of diamond, Si, and Ge. *Physical Review B*, *64*(21), p.212103.

[161] Telling, R.H., Pickard, C.J., Payne, M.C. and Field, J.E., 2000. Theoretical strength and cleavage of diamond. *Physical Review Letters*, *84*(22), p.5160.

[162] Field, J.E., 2012. The mechanical and strength properties of diamond. *Reports on Progress in Physics*, *75*(12), p.126505.

[163] Grady, D.E., 1980. Shock deformation of brittle solids. *Journal of Geophysical Research: Solid Earth*, *85*(B2), pp.913-924.

[164] D. Bradley, D.K., Eggert, J.H., Smith, R.F., Prisbrey, S.T., Hicks, D.G., Braun, D.G., Biener, J., Hamza, F.A., Rudd, R.E. and Collins, G.W., 2009. Diamond at 800 gpa. *Physical Review Letters*, *102*(7), p.075503.

[165] R. Smith, R.F., Eggert, J.H., Jeanloz, R., Duffy, T.S., Braun, D.G., Patterson, J.R., Rudd, R.E., Biener, J., Lazicki, A.E., Hamza, A.V. and Wang, J., 2014. Ramp compression of diamond to five terapascals. *Nature*, *511*(7509), pp.330-333.

[166] Mao, H.K., 1978. High-pressure physics: sustained static generation of 1.36 to 1.72 megabars. *Science*, *200*(4346), pp.1145-1147.

[167] Gogotsi, Y.G., Kailer, A. and Nickel, K.G., 1999. Transformation of diamond to graphite. *Nature*, *401*(6754), pp.663-664.

[168] He, H., Sekine, T. and Kobayashi, T., 2002. Direct transformation of cubic diamond to hexagonal diamond. *Applied physics letters*, *81*(4), pp.610-612.

[169] Bundy, F.P., Bassett, W.A., Weathers, M.S., Hemley, R.J., Mao, H.U. and Goncharov, A.F., 1996. The pressure-temperature phase and transformation diagram for carbon; updated through 1994. *Carbon*, *34*(2), pp.141-153.

[170] Wang, X., Scandolo, S. and Car, R., 2005. Carbon phase diagram from ab initio molecular dynamics. *Physical review letters*, *95*(18), p.185701.

[171] Correa, A.A., Bonev, S.A. and Galli, G., 2006. Carbon under extreme conditions: Phase boundaries and electronic properties from first-principles theory. *Proceedings of the National Academy of Sciences*, *103*(5), pp.1204-1208.

[172] Grumbach, M.P. and Martin, R.M., 1996. Phase diagram of carbon at high pressures and temperatures. *Physical review B*, *54*(22), p.15730.

[173] Fried, L.E. and Howard, W.M., 2000. Explicit Gibbs free energy equation of state applied to the carbon phase diagram. *Physical Review B*, *61*(13), p.8734.

[174] Morris, J.R., Wang, C.Z. and Ho, K.M., 1995. Relationship between structure and conductivity in liquid carbon. *Physical Review B*, *52*(6), p.4138.

[175] Matzen, M.K., 1997. Z pinches as intense x-ray sources for high-energy density physics applications. *Physics of Plasmas*, *4*(5), pp.1519-1527.

[176] Field, J.E., 1992. *The properties of natural and synthetic diamond.* Academic Press.

[177] Eremets, M.I., Trojan, I.A., Gwaze, P., Huth, J., Boehler, R. and Blank, V.D., 2005. The strength of diamond. *Applied Physics Letters*, *87*(14).

[178] Schropp, A., Hoppe, R., Meier, V., Patommel, J., Seiboth, F., Ping, Y., Hicks, D.G., Beckwith, M.A., Collins, G.W., Higginbotham, A. and Wark, J.S., 2015. Imaging shock waves in diamond with both high temporal and spatial resolution at an XFEL. *Scientific reports*, 5(1), p.11089.

[179] Eremets, M.I., Struzhkin, V.V., Timofeev, J.A., Trojan, I.A., Utjuzh, A.N. and Shirokov, A.M., 1992. Refractive index of diamond under pressure. *International Journal of High Pressure Research*, *9*(1-6), pp.347-350.

[180] Katagiri, K., Ozaki, N., Miyanishi, K., Kamimura, N., Umeda, Y., Sano, T., Sekine, T. and Kodama, R., 2020. Optical properties of shock-compressed diamond up to 550 GPa. *Physical Review B*, 101(18), p.184106.

[181] Jakubowska, K., Mancelli, D., Benocci, R., Trela, J., Errea, I., Martynenko, A.S., Neumayer, P., Rosmej, O., Borm, B., Molineri, A. and Verona, C., 2021. Reflecting laser-driven shocks in diamond in the megabar pressure range. *High power laser science and engineering*, *9*, p.e3.

[182] Johnson, Q., Mitchell, A. and Evans, L., 1971. X-ray diffraction evidence for crystalline order and isotropic compression during the shock-wave process. *Nature*, 231(5301), pp.310-311.

[183] Madec, R., Devincre, B., Kubin, L., Hoc, T. and Rodney, D., 2003. The role of collinear interaction in dislocation-induced hardening. *Science*, *301*(5641), pp.1879-1882.

[184] Irifune, T., Kurio, A., Sakamoto, S., Inoue, T. and Sumiya, H., 2003. Ultrahard polycrystalline diamond from graphite. *Nature*, *421*(6923), pp.599-600.

[185] Ishikawa, T., Aoyagi, H., Asaka, T., Asano, Y., Azumi, N., Bizen, T., Ego, H., Fukami, K., Fukui, T., Furukawa, Y. and Goto, S., 2012. A compact X-ray free-electron laser emitting in the sub-ångström region. *Nature Photonics*, *6*(8), pp.540-544.

[186] Graham, R.A. and Brooks, W.P., 1971. Shock-wave compression of sapphire from 15 to 420 kbar. The effects of large anisotropic compressions. *Journal of Physics and Chemistry of Solids*, *32*(10), pp.2311-2330.

[187] Bavdekar, S. and Subhash, G., 2018. Comparison of pressure-sensitive strength models for ceramics under ultrahigh confinement. *International Journal of Impact Engineering*, *118*, pp.60-66.

[188] Margulies, L., Winther, G. and Poulsen, H.F., 2001. In situ measurement of grain rotation during deformation of polycrystals. *Science*, *291*(5512), pp.2392-2394.

[189] Katagiri, K., Ozaki, N., Dresselhaus-Marais, L.E., Eggert, J.H., Inubushi, Y., Irifune, T., Koenig, M., Matsuoka, T., Miyanishi, K., Nakamura, H. and Nishiyama, N., 2022. Strength of diamond beyond the elastic limit under dynamic compression. *arXiv preprint arXiv:2208.03416*.

[190] Katagiri, K., Pikuz, T., Fang, L., Albertazzi, B., Egashira, S., Inubushi, Y., Kamimura, G., Kodama, R., Koenig, M., Kozioziemski, B. and Masaoka, G., 2023. Transonic dislocation propagation in diamond. *Science*, *382*(6666), pp.69-72.

[191] Makarov, S., Dyachkov, S., Pikuz, T., Katagiri, K., Nakamura, H., Zhakhovsky, V., Inogamov, N., Khokhlov, V., Martynenko, A., Albertazzi, B. and Rigon, G., 2023. Direct imaging of shock wave splitting in diamond at Mbar pressure. *Matter and Radiation at Extremes*, *8*(6).

[192] Johnston, W.G. and Gilman, J.J., 1960. Dislocation multiplication in lithium fluoride crystals. *Journal of Applied Physics*, *31*(4), pp.632-643.

[193] Meyers, M.A., Jarmakani, H., Bringa, E.M. and Remington, B.A., 2009. Dislocations in shock compression and release. *Dislocations in solids*, *15*, pp.91-197.

[194] Fan, H., Wang, Q., El-Awady, J.A., Raabe, D. and Zaiser, M., 2021. Strain rate dependency of dislocation plasticity. *Nature communications*, *12*(1), p.1845.

[195] Zepeda-Ruiz, L.A., Stukowski, A., Oppelstrup, T. and Bulatov, V.V., 2017. Probing the limits of metal plasticity with molecular dynamics simulations. *Nature*, *550*(7677), pp.492-495.

[196] Gumbsch, P. and Gao, H., 1999. Dislocations faster than the speed of sound. *Science*, 283(5404), pp.965-968.

[197] Teutonico, L.J., 1961. Dynamical behavior of dislocations in anisotropic media. *Physical Review*, 124(4), p.1039.

[198] Teutonico, L.J., 1962. Uniformly moving dislocations of arbitrary orientation in anisotropic media. *Physical Review*, *127*(2), p.413.

[199] Blaschke, D.N., Chen, J., Fensin, S. and Szajewski, B.A., 2021. Clarifying the definition of 'transonic'screw dislocations. *Philosophical Magazine*, *101*(8), pp.997-1018.

[200] Weertman, J. and Weertman, J., 1980. *Dislocations in Solids, edited by FRN Nabarro, Moving Dislocations*, Vol. 3.

[201] Eshelby, J.D., 1949. Uniformly moving dislocations. *Proceedings of the Physical Society. Section A*, *62*(5), p.307.

[202] Tsuzuki, H., Branicio, P.S. and Rino, J.P., 2008. Accelerating dislocations to transonic and supersonic speeds in anisotropic metals. *Applied Physics Letters*, *92*(19).

[203] Jin, Z., Gao, H. and Gumbsch, P., 2008. Energy radiation and limiting speeds of fast moving edge dislocations in tungsten. *Physical Review B—Condensed Matter and Materials Physics*, *77*(9), p.094303.

[204] Peng, S., Wei, Y., Jin, Z. and Yang, W., 2019. Supersonic screw dislocations gliding at the shear wave speed. *Physical review letters*, *122*(4), p.045501.

[205] Gumbsch, P. and Gao, H., 1999. Driving force and nucleation of supersonic dislocations. *Journal of computer-aided materials design*, *6*, pp.137-144.

[206] Weertman, J., 1967. Uniformly moving transonic and supersonic dislocations. *Journal of Applied Physics*, 38(13), pp.5293-5301.

[207] Duong, T. and Demkowicz, M.J., 2023. Resonance with surface waves induces forbidden velocity bands in dislocation glide. *Journal of the Mechanics and Physics of Solids*, *180*, p.105422.

[208] Gurrutxaga–Lerma, B., Verschueren, J., Sutton, A.P. and Dini, D., 2021. The mechanics and physics of high-speed dislocations: a critical review. *International Materials Reviews*, *66*(4), pp.215-255.

[209] Hahn, E.N., Zhao, S., Bringa, E.M. and Meyers, M.A., 2016. Supersonic dislocation bursts in silicon. *Scientific reports*, *6*(1), p.26977.

[210] Zhao, S., Kad, B., Wehrenberg, C.E., Remington, B.A., Hahn, E.N., More, K.L. and Meyers, M.A., 2017. Generating gradient germanium nanostructures by shock-induced amorphization and crystallization. *Proceedings of the National Academy of Sciences*, 114(37), pp.9791-9796.

[211] Zhao, S., Hahn, E.N., Kad, B., Remington, B.A., Wehrenberg, C.E., Bringa, E.M. and Meyers, M.A., 2016. Amorphization and nanocrystallization of silicon under shock compression. *Acta Materialia*, *103*, pp.519-533.

[212] Zhao, S., Kad, B., Remington, B.A., LaSalvia, J.C., Wehrenberg, C.E., Behler, K.D. and Meyers, M.A., 2016. Directional amorphization of boron carbide subjected to laser shock compression. *Proceedings of the National Academy of Sciences*, *113*(43), pp.12088-12093.

[213] Zhao, S., Flanagan, R., Hahn, E.N., Kad, B., Remington, B.A., Wehrenberg, C.E., Cauble, R., More, K. and Meyers, M.A., 2018. Shock-induced amorphization in silicon carbide. *Acta Materialia*, *158*, pp.206-213.

[214] Lazicki, A., McGonegle, D., Rygg, J.R., Braun, D.G., Swift, D.C., Gorman, M.G., Smith, R.F., Heighway, P.G., Higginbotham, A., Suggit, M.J. and Fratanduono, D.E., 2021. Metastability of diamond ramp-compressed to 2 terapascals. *Nature*, *589*(7843), pp.532-535.

[215] Stroh, AN139306. "Steady state problems in anisotropic elasticity." *Journal of Mathematics and Physics* 41, no. 1-4 (1962): 77-103.

[216] Anderson, P.M., Hirth, J.P. and Lothe, J., 2017. *Theory of dislocations*. Cambridge University Press.

[217] Masuya, S., Hanada, K., Oshima, T., Sumiya, H. and Kasu, M., 2017. Formation of stacking fault and dislocation behavior during the high-temperature annealing of single-crystal HPHT diamond. *Diamond and Related Materials*, *75*, pp.155-160.

[218] Vandersall*, J.Y. and Wirth, B.D., 2004. Supersonic dislocation stability and nano-twin formation at high strain rate. *Philosophical Magazine*, *84*(35), pp.3755-3769.

[219] Núñez Valdez, M., Umemoto, K. and Wentzcovitch, R.M., 2012. Elasticity of diamond at high pressures and temperatures. *Applied Physics Letters*, *101*(17).

[220] Knudson, M.D. and Seagle, C.T., 2023. Damaging diamond with shock waves. *Science*, 382(6666), pp.37-38.

[221] Momma, K. and Izumi, F., 2011. VESTA 3 for three-dimensional visualization of crystal, volumetric and morphology data. *Applied Crystallography*, *44*(6), pp.1272-1276.

[222] Hawreliak, J.A., Winey, J.M., Sharma, S. and Gupta, Y.M., 2024. Comments regarding Transonic dislocation propagation in diamond by Katagiri, et al.(*Science* 382, 69-72, 2023). *arXiv preprint arXiv:2401.04213.*

[223] Bradley, D.K., Eggert, J.H., Hicks, D.G., Celliers, P.M., Moon, S.J., Cauble, R.C. and Collins, G.W., 2004. Shock compressing diamond to a conducting fluid. *Physical Review Letters*, *93*(19), p.195506.

[224] Nie, A., Bu, Y., Huang, J., Shao, Y., Zhang, Y., Hu, W., Liu, J., Wang, Y., Xu, B., Liu, Z. and Wang, H., 2020. Direct observation of room-temperature dislocation plasticity in diamond. *Matter*, *2*(5), pp.1222-1232.

[225] Griffith, A. A., 1921. *The phenomena of rupture and flow in solids*, 163–198 (Philosophical transactions of the royal society of London).

[226] Field, J.E. and Freeman, C.J., 1981. Strength and fracture properties of diamond. *Philosophical Magazine A*, 43(3), pp.595-618.

[227] Ogata, S. and Li, J., 2009. Toughness scale from first principles. *Journal of Applied Physics*, *106*(11).

[228] Bridgman, P.W., 1947. The effect of hydrostatic pressure on the fracture of brittle substances. *Journal of Applied Physics*, *18*(2), pp.246-258.

[229] Humble, P. and Hannink, R.H.J., 1978. Plastic deformation of diamond at room temperature. *Nature*, *273*(5657), pp.37-39.

[230] Sumiya, H., Yamaguchi, K. and Ogata, S., 2006. Deformation microstructure of high-quality synthetic diamond crystal subjected to Knoop indentation. *Applied physics letters*, 88(16).

[231] Mao, H.K., Bell, P.M., Dunn, K.J., Chrenko, R.M. and DeVries, R.C., 1979. Absolute pressure measurements and analysis of diamonds subjected to maximum static pressures of 1.3–1.7 Mbar. *Review of Scientific Instruments*, *50*(8), pp.1002-1009.

[232] Weidner, D.J., Wang, Y. and Vaughan, M.T., 1994. Strength of diamond. *Science*, 266(5184), pp.419-422.

[233] Wilks, J. and Wilks, E., 1991. *Properties and applications of diamond.*

[234] Banerjee, A., Bernoulli, D., Zhang, H., Yuen, M.F., Liu, J., Dong, J., Ding, F., Lu, J., Dao, M., Zhang, W. and Lu, Y., 2018. Ultralarge elastic deformation of nanoscale diamond. *Science*, 360(6386), pp.300-302.

[235] Nie, A., Bu, Y., Li, P., Zhang, Y., Jin, T., Liu, J., Su, Z., Wang, Y., He, J., Liu, Z. and Wang, H., 2019. Approaching diamond's theoretical elasticity and strength limits. *Nature communications*, *10*(1), p.5533.

[236] Wheeler, J.M., Raghavan, R., Wehrs, J., Zhang, Y., Erni, R. and Michler, J., 2016. Approaching the limits of strength: measuring the uniaxial compressive strength of diamond at small scales. *Nano letters*, *16*(1), pp.812-816.

[237] Liu, B.Y., Liu, F., Yang, N., Zhai, X.B., Zhang, L., Yang, Y., Li, B., Li, J., Ma, E., Nie, J.F. and Shan, Z.W., 2019. Large plasticity in magnesium mediated by pyramidal dislocations. *Science*, 365(6448), pp.73-75.

[238] Li, A.C., Li, B., Rudd, R.E. and Meyers, M.A., 2023. Dislocation generation in diamond under extreme loading. *Matter*, *6*(9), pp.3040-3056.

[239] Eggert, J.H., Hicks, D.G., Celliers, P.M., Bradley, D.K., McWilliams, R.S., Jeanloz, R., Miller, J.E., Boehly, T.R. and Collins, G.W., 2010. Melting temperature of diamond at ultrahigh pressure. *Nature Physics*, *6*(1), pp.40-43.

[240] Dubrovinsky, L., Dubrovinskaia, N., Prakapenka, V.B. and Abakumov, A.M., 2012. Implementation of micro-ball nanodiamond anvils for high-pressure studies above 6 Mbar. *Nature communications*, *3*(1), p.1163.

[241] Kaminsky, F.V. and Kaminsky, F.V., 2017. Carbonatitic Lower-Mantle Mineral Association. *The Earth's Lower Mantle: Composition and Structure*, pp.205-228.

[242] Sharp, T., 2014. Bridgmanite—named at last. *Science*, *346*(6213), pp.1057-1058.

[243] Tschauner, O., Ma, C., Beckett, J.R., Prescher, C., Prakapenka, V.B. and Rossman, G.R., 2014. Discovery of bridgmanite, the most abundant mineral in Earth, in a shocked meteorite. *Science*, *346*(6213), pp.1100-1102.

[244] Tschauner, O., Huang, S., Yang, S., Humayun, M., Liu, W., Gilbert Corder, S.N., Bechtel, H.A., Tischler, J. and Rossman, G.R., 2021. Discovery of davemaoite, CaSiO3-perovskite, as a mineral from the lower mantle. *Science*, *374*(6569), pp.891-894.

[245] Wang, Y. and Liebermann, R.C., 1993. Electron microscopy study of domain structure due to phase transitions in natural perovskite. *Physics and Chemistry of Minerals*, 20(3), pp.147-158.

[246] Redfern, S.A., 1996. High-temperature structural phase transitions in perovskite. *Journal of Physics: Condensed Matter*, 8(43), p.8267.

[247] Couper, S., Speziale, S., Marquardt, H., Liermann, H.P. and Miyagi, L., 2020. Does heterogeneous strain act as a control on seismic anisotropy in Earth's lower mantle?. *Frontiers in Earth Science*, 8, p.540449.

[248] Doukhan, N. and Doukhan, J.C., 1986. Dislocations in perovskites BaTiO3 and CaTiO3. *Physics and chemistry of minerals*, *13*(6), pp.403-410.

[249] Besson, P., Poirier, J.P. and Price, G.D., 1996. Dislocations in CaTiO3 perovskite deformed at high-temperature: a transmission electron microscopy study. *Physics and chemistry of minerals*, *23*(6), pp.337-344.

[250] Souza, J.A. and Rino, J.P., 2011. A molecular dynamics study of structural and dynamical correlations of CaTiO3. *Acta Materialia*, *59*(4), pp.1409-1423.

[251] Ferré, D., Carrez, P. and Cordier, P., 2009. Peierls dislocation modelling in perovskite (CaTiO3): comparison with tausonite (SrTiO3) and MgSiO3 perovskite. *Physics and chemistry of minerals*, *36*(4), pp.233-239.

[252] Wright, K., Price, G.D. and Poirier, J.P., 1992. High-temperature creep of the perovskites CaTiO3 and NaNbO3. *Physics of the earth and planetary interiors*, *74*(1-2), pp.9-22.

[253] Li, P., Karato, S.I. and Wang, Z., 1996. High-temperature creep in fine-grained polycrystalline CaTiO 3, an analogue material of (Mg, Fe) SiO 3 perovskite. *Physics of the earth and planetary interiors*, *95*(1-2), pp.19-36.

[254] Levy, M.R., 2005. Chapter 3: perovskite perfect lattice. *Cryst. Struct. Defect Prop. Predict. Ceram. Mater*, pp.79-114.

[255] Xu, C., Xu, B., Yang, Y., Dong, H., Oganov, A.R., Wang, S., Duan, W., Gu, B. and Bellaiche, L., 2015. Prediction of a stable post-post-perovskite structure from first principles. *Physical Review B*, *91*(2), p.020101.

[256] Guennou, M., Bouvier, P., Krikler, B., Kreisel, J., Haumont, R. and Garbarino, G., 2010. High-pressure investigation of CaTiO 3 up to 60 GPa using X-ray diffraction and Raman spectroscopy. *Physical Review B—Condensed Matter and Materials Physics*, *82*(13), p.134101.

[257] Truffet, B., Fiquet, G., Morard, G., Baron, M.A., Miozzi, F., Harmand, M., Ravasio, A., Mezouar, M. and Guyot, F., 2023. High pressure dissociation of CaTiO3 perovskite into CaO and CaTi2O5. *Physics of the Earth and Planetary Interiors*, *334*, p.106968.

[258] Remington, B.A., Park, H., Prisbrey, S.T., Pollaine, S.M., Cavallo, R.M., Rudd, R.E., Lorenz, K.T., Becker, R., Bernier, J., Barton, N. and Arsenlis, T., 2009. *Progress towards materials science above 1000 GPa (10 Mbar) on the NIF laser* (Vol. 1, No. LLNL-CONF-411555). Lawrence Livermore National Lab.(LLNL), Livermore, CA (United States).

[259] Boioli, F., Carrez, P., Cordier, P., Goryaeva, A., Gouriet, K., Hirel, P., Kraych, A., Mahendran, S., Mussi, A., Nzogang, B.C. and Reali, R., 2018. *Multiscale modeling of the mantle rheology*. Cordier Patrick et AM Goryaeva.

[260] Kohlstedt, D.L., Evans, B. and Mackwell, S.J., 1995. Strength of the lithosphere: Constraints imposed by laboratory experiments. *Journal of Geophysical Research: Solid Earth*, 100(B9), pp.17587-17602.

[261] Lindl, J., 1995. Development of the indirect-drive approach to inertial confinement fusion and the target physics basis for ignition and gain. *Physics of plasmas*, *2*(11), pp.3933-4024.

[262] Freund, L., 1972. Crack propagation in an elastic solid subjected to general loading—II. Non-uniform rate of extension. *Journal of the Mechanics and Physics of Solids*, 20(3), pp.141-152.

[263] Aquistapace, F., Castillo-Castro, D., González, R.I., Amigo, N., García Vidable, G., Tramontina, D.R., Valencia, F.J. and Bringa, E.M., 2024. Plasticity in diamond nanoparticles: dislocations and amorphization during loading and dislocation multiplication during unloading. *Journal of Materials Science*, *59*(12), pp.4788-4809.

[264] Li, A.C., Li, B., González-Cataldo, F., Rudd, R.E., Militzer, B., Bringa, E.M. and Meyers, M.A., 2024. Diamond under extremes. *Materials Science and Engineering: R: Reports*, *161*, p.100857.

[265] Cai, W. and Nix, W.D., 2016. *Imperfections in crystalline solids*. Cambridge University Press.

[266] Zhao, S., Hahn, E.N., Kad, B., Remington, B.A., Bringa, E.M. and Meyers, M.A., 2016. Shock compression of [001] single crystal silicon. *The European Physical Journal Special Topics*, *225*, pp.335-341.

[267] Zhao, S., Kad, B., Hahn, E.N., Remington, B.A., Wehrenberg, C.E., Huntington, C.M., Park, H.S., Bringa, E.M., More, K.L. and Meyers, M.A., 2015. Pressure and shear-induced amorphization of silicon. *Extreme Mechanics Letters*, *5*, pp.74-80.

[268] Yaakobi, B., Boehly, T.R., Meyerhofer, D.D., Collins, T.J.B., Remington, B.A., Allen, P.G., Pollaine, S.M., Lorenzana, H.E. and Eggert, J.H., 2005. EXAFS measurement of iron bcc-to-hcp phase transformation in nanosecond-laser shocks. *Physical review letters*, 95(7), p.075501.

[269] Li, B.Y., Li, A.C., Zhao, S. and Meyers, M.A., 2022. Amorphization by mechanical deformation. *Materials Science and Engineering: R: Reports*, *149*, p.100673.

[270] Bu, Y., Su, Z., Huang, J., Tong, K., Li, P., Wang, C., Jin, T., Zhao, S., Zhao, Z., Soldatov, A. and Wang, Y., 2025. Activating deformation twinning in cubic boron nitride. Nature Materials, pp.1-8.

[271] Hemley, R.J., Jephcoat, A.P., Mao, H.K., Ming, L.C. and Manghnani, M.H., 1988. Pressure-induced amorphization of crystalline silica. *Nature*, *334*(6177), pp.52-54.

[272] Hull, D. and Bacon, D.J., 2011. *Introduction to dislocations* (Vol. 37). Elsevier.

[273] Nellis, W.J., 2008, July. Systematics of compression of hard materials. In *Journal of Physics: Conference Series* (Vol. 121, No. 6, p. 062005). IOP Publishing.

[274] Trunin, R.F., Simakov, G.V., Podurets, M.A., Moiseyev, B.N. and Popov, L.V., 1971. Dynamic compressibility of quartz and quartzite at high pressure. *Izv. Acad. Sci. USSR Phys. Solid Earth*, *1*, pp.13-20.

[275] Boudali, A., Abada, A., Khodja, M.D., Amrani, B., Amara, K., Khodja, F.D. and Elias, A., 2010. Calculation of structural, elastic, electronic, and thermal properties of orthorhombic CaTiO3. *Physica B: Condensed Matter*, *405*(18), pp.3879-3884.

[276] Sinelnikov, Y.D., Chen, G. and Liebermann, R.C., 1998. Elasticity of CaTiO 3–CaSiO 3 perovskites. *Physics and Chemistry of Minerals*, *25*, pp.515-521.

[277] Fischer, G.J., Wang, Z. and Karato, S.I., 1993. Elasticity of CaTiO 3, SrTiO 3 and BaTiO 3 perovskites up to 3.0 Gpa: The effect of crystallographic structure. *Physics and Chemistry of Minerals*, *20*, pp.97-103.

[278] Tariq, S., Ahmed, A., Saad, S. and Tariq, S., 2015. Structural, electronic and elastic properties of the cubic CaTiO3 under pressure: A DFT study. *AIP Advances*, *5*(7).

[279] Bridgman, P.W., 1935. Effects of high shearing stress combined with high hydrostatic pressure. *Physical review*, *48*(10), p.825.

[280] Teller, E., 1961. On the speed of reactions at high pressures. *The Journal of Chemical Physics* 36, 901–903.

[281] Chen, H.C., Lasalvia, J.C., Nesterenko, V.F. and Meyers, M.A., 1998. Shear localization and chemical reaction in high-strain, high-strain-rate deformation of Ti–Si powder mixtures. *Acta materialia*, *46*(9), pp.3033-3046.

[282] Bridgman, P.W., 1937, January. Shearing phenomena at high pressures, particularly in inorganic compounds. In *Proceedings of the American Academy of Arts and Sciences* (Vol. 71, No. 9, pp. 387-460). American Academy of Arts & Sciences.

[283] Enikolopian, N.S., 1985. Some aspects of chemistry and physics of plastic flow. *Pure and Applied chemistry*, 57(11), pp.1707-1711.

[284] Levitas, V.I., 2021. Phase transformations, fracture, and other structural changes in inelastic materials. *International Journal of Plasticity*, *140*, p.102914.

[285] Yu, D., Zhang, J., Wang, F., Zhao, M., Du, K., Shu, S., Zou, J. and Wang, Y., 2013. High-symmetry epitaxial growth under solvothermal conditions: a strategy for architectural growth of tubular and nontubular CaTiO3 microstructures with regular geometrical morphologies and tunable dimensions. *Crystal growth & design*, *13*(7), pp.3138-3143.

[286] Poirier, J.P., Beauchesne, S. and Guyot, F., 1989. Deformation mechanisms of crystals with perovskite structure. *Perovskite: a structure of great interest to geophysics and materials science*, *45*, pp.119-123.

[287] Poirier, J.P., 1985. *Creep of crystals: high-temperature deformation processes in metals, ceramics and minerals*. Cambridge University Press.

[288] Mecklenburgh, J., Heidelbach, F., Mariani, E., Mackwell, S. and Seifert, F., 2010. Rheology and microstructure of (Ca0. 9, Sr0. 1) TiO3 perovskite deformed in compression and torsion. *Journal of Geophysical Research: Solid Earth*, *115*(B5).

[289] Meisheng, H., Wenk, H.R. and Sinitsyna, D., 1992. Microstructures in natural perovskites. *American Mineralogist*, *77*(3-4), pp.359-373.

[290] Toupance, N., 1987. Temperature dependence of the elastic constants for solids of cubic symmetry. Application to Germanium and Silicon. *Physica Status Solidi (b)*, *140*(2), pp.361-368.

[291] Wortman, J.J. and Evans, R.A., 1965. Young's modulus, shear modulus, and Poisson's ratio in silicon and germanium. *Journal of applied physics*, *36*(1), pp.153-156.

[292] Zakhariev, Z. and Radev, D., 1988. Properties of polycrystalline boron carbide sintered in the presence of W 2 B 5 without pressing. *Journal of materials science letters*, *7*, pp.695-696.

[293] Clayton, J.D., 2012. Towards a nonlinear elastic representation of finite compression and instability of boron carbide ceramic. *Philosophical Magazine*, *92*(23), pp.2860-2893.

[294] Carnahan, R.D., 1968. Elastic properties of silicon carbide. *Journal of the American Ceramic Society*, *51*(4), pp.223-224.

[295] Clayton, J.D., 2010. Modeling nonlinear electromechanical behavior of shocked silicon carbide. *Journal of Applied Physics*, *107*(1).

[296] Abramson, E.H., Brown, J.M., Slutsky, L.J. and Zaug, J., 1997. The elastic constants of San Carlos olivine to 17 GPa. *Journal of Geophysical Research: Solid Earth*, *102*(B6), pp.12253-12263.

[297] Kumazawa, M. and Anderson, O.L., 1969. Elastic moduli, pressure derivatives, and temperature derivatives of single-crystal olivine and single-crystal forsterite. *Journal of Geophysical Research*, *74*(25), pp.5961-5972.

[298] Stukowski, A. and Albe, K., 2010. Extracting dislocations and non-dislocation crystal defects from atomistic simulation data. *Modelling and Simulation in Materials Science and Engineering*, *18*(8), p.085001.

[299] Maras, E., Trushin, O., Stukowski, A., Ala-Nissila, T. and Jonsson, H., 2016. Global transition path search for dislocation formation in Ge on Si (001). *Computer Physics Communications*, *205*, pp.13-21.

[300] Chen, H., Levitas, V.I., Xiong, L. and Zhang, X., 2021. Stationary dislocation motion at stresses significantly below the Peierls stress: Example of shuffle screw and 60° dislocations in silicon. *Acta Materialia*, *206*, p.116623.

[301] Kamimura, Y., Edagawa, K. and Takeuchi, S., 2013. Experimental evaluation of the Peierls stresses in a variety of crystals and their relation to the crystal structure. *Acta Materialia*, *61*(1), pp.294-309.